

---

# Optimizing bifacial tandem solar cells for realistic operation conditions

---

Dissertation

*zur Erlangung des Grades eines Doktors der Naturwissenschaften  
(Dr. rer. nat.) am Fachbereich Mathematik und Informatik der Freien  
Universität Berlin*

vorgelegt von

Peter Tillmann

Berlin 2022

*“Things that people learn purely out of curiosity can have a revolutionary effect on human affairs.”*

Frederick Seitz

Erstgutachter: Prof. Christof Schütte

Zweitgutachterin : Prof. Christiane Becker

Drittgutachter: Prof. Eugene A. Katz

Tag der Disputation: 25.01.2023

# Contents

<b>Abstract</b>	<b>v</b>
<b>Kurzfassung</b>	<b>vii</b>
<b>List of publications</b>	<b>ix</b>
<b>1 Introduction</b>	<b>1</b>
<b>2 Theoretical background</b>	<b>7</b>
2.1 Single junction solar cells and their limitation . . . . .	7
2.1.1 Photoelectric effect and simple solar cell model . . . . .	7
2.1.2 Equivalent circuit model . . . . .	8
2.2 Multijunction and tandem solar cells . . . . .	10
2.2.1 Electrical connections in tandem solar cells . . . . .	11
2.2.2 Equivalent circuits for tandem solar cells . . . . .	12
2.3 Illumination and optical aspects in solar cell simulations . . . . .	13
2.3.1 Optical simulations . . . . .	14
2.3.2 Textured interfaces . . . . .	15
2.3.3 Bifacial solar cells . . . . .	16
2.3.4 Luminescent coupling . . . . .	18
2.4 Energy yield calculations . . . . .	19
2.5 Numerical methods . . . . .	20
2.5.1 Finite element method for modelling periodic nano textures . .	20
2.5.2 Bayesian optimization . . . . .	22
2.5.3 GenPro4 . . . . .	25
<b>3 The bifacial illumination model</b>	<b>27</b>
3.0.1 Publication . . . . .	29
<b>4 Bifacial operation and luminescent coupling in tandem solar cells</b>	<b>41</b>
4.0.1 Publication . . . . .	44
<b>5 Validated model-chain for energy yield calculations</b>	<b>53</b>
5.0.1 Publication . . . . .	56
<b>6 Improving the textured interface with FEM and bayesian optimization</b>	<b>67</b>
6.0.1 Publication . . . . .	70
<b>7 Optimizing the geometry of bifacial solar cells considering the area costs</b>	<b>85</b>
7.0.1 Publication . . . . .	87
<b>8 Conclusion</b>	<b>97</b>

<b>Danksagung</b>	<b>135</b>
<b>Selbstständigkeitserklärung</b>	<b>137</b>
<b>Bibliography</b>	<b>139</b>

## Abstract

The current mainstream technology based on silicon semiconductors is approaching their theoretical efficiency limits. To further reduce the cost of photovoltaic systems and to increase the power output new approaches are required and bifacial operation and tandem solar cells are regarded as promising concepts. Tandem solar cells combine two different absorber materials for higher efficiencies by better utilizing the broad energy spectrum of sunlight. Bifacial operation allows the conversion of light not only from the front but also from the backside to increase the electricity generation.

In order to receive light at the backside, solar panels need to be installed on mounting structures above ground, as found in large scale free field installations. The light from the back is mostly originating from reflections of the ground, which makes the calculation of the backside irradiance significantly more complex than the frontside irradiance. In this thesis a detailed illumination model was developed to calculate the backside illumination from the geometrical inputs, ground reflectivity, and sun position. The model was complemented with a newly developed toolchain for solar cell energy yield calculations. The toolchain included a temperature dependent diode model with integration of optical simulation tools such as finite element method and ray tracing based methods. The toolchain can be used with different sources of weather data for realistic energy yield calculations and was validated against experimental solar cell data.

Perovskites are a promising material class for tandem solar cells due to their bandgap tunability. In this thesis the impact of bifacial operation on the optimal bandgap of the perovskite top cell is investigated. Depending on the ground albedo, a significant shift in the optimal bandgap of the perovskite top cell can be observed. Investigating the phenomena of luminescent coupling indicates that a further reduction of the perovskite bandgap is possible. This allows the usage of perovskite materials with better conversion efficiencies and long term stability.

Performing energy yield calculations with the validated model chain for a potential upgrade from a standard monofacial PV installation in Jerusalem with high reflective ground reveals a possible increase of 20 % for bifacial silicon, 40 % for a monofacial tandem, and up to 60 % for perovskite/silicon bifacial tandem solar cells.

Other optical aspects are also important for high efficiency multijunction solar cells. This thesis contains an investigation of the design of a metal grating backside reflector utilized in a world record III/V on silicon solar cells. The optical response is calculated with the finite element method and we further improve the design in our simulation with the help of Bayesian optimization, resulting in an improvement of the photocurrent density by 0.37 mA/cm<sup>2</sup> in the silicon junction.

The installation of bifacial solar cells in free field installations opens the questions of the best geometry for the lowest levelized cost of electricity (LCOE). A simple economical model was developed to investigate the trade-offs between energy yield and land usage in terms of LCOE. Procedures based on bayesian optimization were used to minimize the LCOE of bifacial solar power plants and a potential cost reduction of up to 23 % is demonstrated compared to currently used rule-of-thumb estimations.

The tools and results presented in this thesis will help to guide the future design of (tandem) solar cells and find optimal parameters for their integration in power plants. This will help to further reduce the LCOE of photovoltaic systems and support the global transition towards regenerative energies.



## Kurzfassung

Die aktuell verbreitetste Technologie für Solarzellen, die auf Silizium basiert, nähert sich ihrer theoretischen Effizienz-Obergrenze, was neue Ansätze wie bifaziale Solarzellen oder Tandemsolarzellen für weitere Kostensenkungen nötig macht. Tandemsolarzellen kombinieren zwei unterschiedliche Halbleiter, um den Wirkungsgrad durch eine bessere Nutzung des breiten Energiespektrums von Sonnenlicht zu erhöhen. Der bifaziale Betrieb erlaubt es auch Licht von der Rückseite einer Solarzelle zur Stromerzeugung zu nutzen.

Das Licht auf der Rückseite stammt dabei zum großen Teil von Bodenreflektionen, was die Berechnung der Beleuchtung deutlich komplexer macht als auf der Vorderseite. In dieser Arbeit wurde ein detailliertes Modell entwickelt, um die rückseitige Beleuchtung aus dem geometrischen Aufbau, der Albedo des Bodens und dem Sonnenstand zu berechnen. Das Modell wurde mit einer Reihe von neu entwickelten Simulationstools ergänzt, um die vollständige Leistungsberechnungen von Solarzellen zu ermöglichen. Dabei wurden bestehende optische Simulationswerkzeuge integriert. Das Simulationstool kann mit verschiedenen Wetterdaten genutzt werden, um eine realistische Abschätzung der Energieerträge zu erhalten und es wurde mit experimentellen Solarzellen-Daten validiert.

Eine vielversprechende Materialklasse für Tandemsolarzellen sind Perowskite, die sich aufgrund ihrer veränderbaren Bandlücken gut für eine Kombination mit Silizium eignet. In dieser Arbeit wird der Einfluss des bifazialen Betriebs und der lumineszenten Kopplung auf die optimale Bandlücke der Perowskitzelle untersucht. Je nach Szenario kann eine signifikante Verschiebung zu niedrigeren Bandlücken beobachtet werden. Dadurch lassen sich Perovskite-Materialien nutzen die bessere optoelektronische Eigenschaften und eine höhere Langzeitstabilität aufweisen.

Die Durchführung von Energieertragsberechnungen mit der validierten Modellkette für ein potenzielles Upgrade von einer monofazialen Standard-PV-Anlage in Jerusalem mit stark reflektierendem Boden zeigt eine mögliche Steigerung von 20 % für bifaziale Solarzellen, 40 % für ein monofaziales Tandems und bis zu 60 % für bifaziale Perowskit/Silizium-Tandemsolarzellen.

Für hocheffiziente Mehrfachsolarzellen sind weitere optische Aspekte wichtig. Im Rahmen dieser Arbeit wird das Design eines strukturierten Rückseitenreflektors einer III/V auf Silizium Solarzelle mit Weltrekorteffizienz untersucht. Die Optik des Reflektors wird mit der Finite-Elemente-Methode berechnet und das Design mit Hilfe der Bayesschen Optimierung verbessert. In den Simulationen konnte damit eine Steigerung der Photostromdichte um  $0,37 \text{ mA/cm}^2$  in der Siliziumzelle erreicht werden.

Der genaue Aufbau spielt eine wichtige Rolle bei den Stromgestehungskosten eines Solarparks mit bifazialen Solarzellen. Es wurde ein Kostenmodell entwickelt, um die ideale Balance zwischen höheren Erträgen und höheren Kosten durch größere Flächennutzung zu finden. Dazu wird ein Verfahren auf Basis der Bayes'schen Optimierung genutzt, das die Stromgestehungskosten bifazialer Solarparks minimiert. Im Vergleich zu derzeit verwendeten Faustregeln konnte eine Kostensenkung von bis zu 23 % demonstriert werden.

Die Werkzeuge und Ergebnisse aus dieser Arbeit helfen dabei, das zukünftige Design von (Tandem) Solarzellen und ihre Integration in Kraftwerke zu verbessern. Damit lassen sich die Stromgestehungskosten von Photovoltaik-Systemen weiter senken und somit wird ein Beitrag zur Beschleunigung der Energiewende geleistet.





## List of Publications

- K. Jäger, P. Tillmann, and C. Becker (2020),  
 “Detailed illumination model for bifacial solar cells,”  
*Opt. Express*, vol. 28, no. 4, pp. 4751-4762,  
 DOI: 10.1364/OE.383570  
 In this publication a detailed model to calculate the irradiance on a bifacial solar panel in a periodic area is presented. For this publication I developed the python code, together with Klaus Jäger, that was presented and described here. My contribution was focused on providing solutions to run simulations for many timesteps, where the position of the sun and the direct and diffuse irradiance will change. Some parts of the manuscript were written by me, especially the section “Implementation details”.  
 License: CC-BY 4.0 <https://creativecommons.org/licenses/by/4.0>
- P. Tillmann, K. Jäger and C. Becker (2020),  
 “Minimising the levelised cost of electricity for bifacial solar panel arrays using Bayesian optimisation,”  
*Sustainable Energy Fuels*, vol.4, pp.254-264,  
 DOI: 10.1039/C9SE00750D  
 This publication presents yield estimations and optimizations for bifacial solar cells. The main parameters optimized are the tilt angle of the solar cell modules and the distance between rows of modules (row spacing). I contributed the idea to restrict the row spacing by a land cost model and wrote the code and provided the figures related to the optimizations and energy yield and levelized cost of electricity calculations. I mainly wrote the manuscript related to optimizations and energy yield and levelized cost of electricity calculations.  
 License: CC-BY 3.0 <https://creativecommons.org/licenses/by/3.0>
- K. Jäger, P. Tillmann, E. Katz, C. Becker (2021)  
 “Perovskite/silicon tandem solar cells: Effect of luminescent coupling and bifaciality,”  
*Solar RRL*, vol.5, p.2000628,  
 DOI: 10.1002/solr.202000628,  
 This publication is concerned with the energy yield estimation of tandem solar cells with an emphasis on the effects of bifacial operation and luminescent coupling. The original idea of the project was developed by Klaus Jäger while I contributed the idea to investigate the effect of luminescent coupling. Further, I contributed the computer code to run the energy yield estimations based on the earlier developed illumination model and generated the relevant figures. In the manuscript I wrote major parts of the results and discussion section.  
 License: CC-BY 4.0 <https://creativecommons.org/licenses/by/4.0>
- P. Tillmann, B. Bläsi, S. Burger, M. Hammerschmidt, O. Höhn, C. Becker, K. Jäger (2021)  
 “Optimizing metal grating back reflectors for III-V-on-silicon multijunction solar cells,”  
*Opt. Express*, vol. 29, no. 14, pp. 22517-22532,  
 DOI: 10.1364/OE.426761,  
 In this work the geometry metal grating back reflector for a record efficiency multijunction solar cell is optimized with bayesian optimization. The original

idea of the project came from Sven Burger and Klaus Jäger. For this publication I wrote the complete computer code to perform the simulation and optimization, generated the figures and wrote the majority of the manuscript.

License: CC-BY 4.0 <https://creativecommons.org/licenses/by/4.0>

- P. Tillmann, K. Jäger, A. Karsenti, L. Kreinin, C. Becker (2022)  
“Model-Chain Validation for Estimating the Energy Yield of Bifacial Perovskite/  
Silicon Tandem Solar Cells,”  
*Solar RRL*

DOI: 10.1002/solr.202200079,

The manuscript is concerned with establishing a model-chain required to calculate the energy yield of mono- and bifacial tandem solar cells and validate the separate steps with available experimental data. The original idea of the project was initiated by Christiane Becker while the technical details of the required simulation steps were designed by me. For this publication I wrote the computer code based on the bifacial illumination model established earlier. I created the majority of the figures and wrote the majority of the manuscript.

License: CC-BY 4.0 <https://creativecommons.org/licenses/by/4.0>

## Chapter 1

# Introduction

The massive usage of fossil fuels that started with the industrial revolution in the late 18th century has led to a significant increase in carbon dioxide in the atmosphere. Together with other greenhouse gases, this has already caused an increase in the median temperature of 1.1 °C[1]. With the Paris agreement of 2015 most governments in the world have agreed to limit the global temperature increase to a maximum of 2 °C and preferably 1.5 °C[2]. This was an ambitious goal considering that at the time the global temperature had already risen by 1 °C, while the global CO<sub>2</sub> emissions were still rising[3]. If the future emissions of large quantities of CO<sub>2</sub> should be avoided, the global energy supplies have to be transformed towards renewable energies, and photovoltaic power plants will play a major role in this transformation. Driven by a dramatic reduction in the former expensive solar panel prices[4], globally photovoltaic systems have been the fastest-growing electricity source in terms of peak power capacity since 2012[5]. Today, solar cells are the most cost-efficient source of electricity for many regions in the world[6][7].

Fig. 1.1 shows the price development of solar panels and the balance of system (BOS) costs over the last few decades. The price of solar panels has fallen dramatically and shows a learning curve of over 20 %. The learning curve represents the average relative price reduction every time the globally installed peak power of photovoltaic system has doubled. While the price of modules has drastically fallen, the BOS costs could not keep up with the steep cost reduction trend. BOS costs include all investments necessary to build a PV power plant except the solar modules, including the mounting structures, wiring, inverters, labour and land acquisition. And while the solar panels used to be the largest cost fraction for a PV power plant, in modern installations the BOS costs can amount to more than two thirds of the total investment[7], [9]. This results in a situation where further reduction of solar panel prices has less and less impact on the total cost of electricity produced by photovoltaic power plants and other measures are needed to further reduce the system costs. Many of the BOS costs are associated with the number of installed solar panels. This has led the industry to pursue technologies that allow maximising the power rating of solar modules to decrease the cost of labour for the installation, wiring, land usage and construction materials. One major approach was to increase the size of the modules, however, land usage cannot be reduced by using larger modules. Solar cell efficiency is another strategy that has been embraced by the PV industry to generating more electricity with the same space requirements. Therefore it can reduce the BOS costs required per module, subsequently leading to lower cost for the generated electricity.

By improving manufacturing and cell technologies the PV industry was able to improve the efficiency of standard PV panels from around 15 % to 20 % over the last 2 decades[7], [10], with record efficiency of commercial modules reaching 22.8 %[11]. As the power conversion efficiencies of modern silicon based solar cells slowly move closer to their physical limit of 29.4 %[12], new concepts are required to further increase

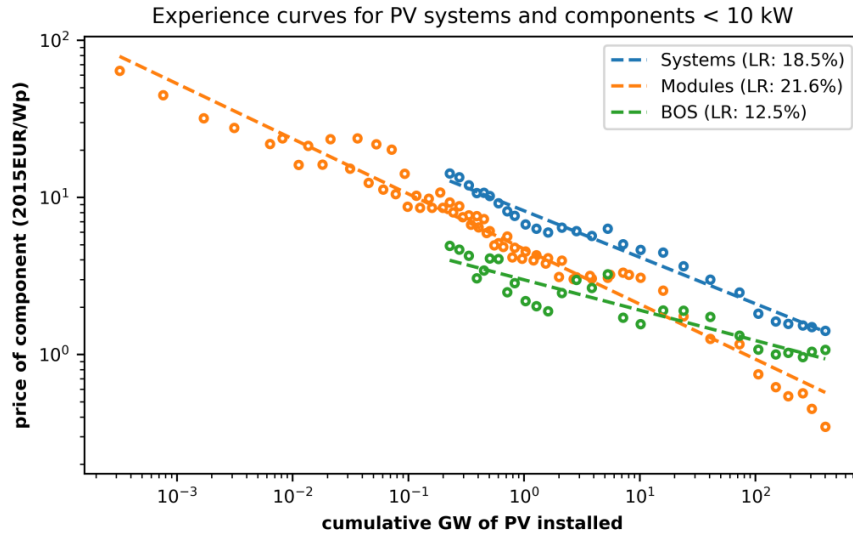


FIGURE 1.1: Inflation adjusted price development of PV components as a function of the cumulative global installations for the Modules, BOS and Systems. The Learning rate (LR) is calculated as the average price reduction for a doubling of the cumulative installation. Reprinted with kind permission from [8]

the power generation of PV power plants. Two promising concepts are the usage of tandem/multijunction solar cells and bifacial operation.

Bifacial solar cells increase the generated electricity by not only converting light received at the front but also on the backside. This was made possible by moving to new cell designs such as PERC (passive emitter rear cell), TOPCon (tunnel oxide passivated contact), HJT (heterojunction technology) and IBC (interdigitated back contact), all of which are all capable of utilising light from the back side[13]–[15]. The widespread usage of cost-efficient PERC solar cells, with a market share of 85 % as of now (2022)[16], has enabled the incredible adoption speed of bifacial solar cells. Bifacial solar cells saw an increase of their global market share from 15 % to over 50 % from 2018 to 2022[16], [17]. The future the market share is projected to reach nearly 80 % by the end of this decade as shown in Fig. 1.2 by the 2022 International Technology Roadmap for Photovoltaic (ITRPV)[16].

Multijunction solar cells on the other hand increase the electricity generation by increasing the efficiency of the light conversion. They use multiple semiconductors with different bandgaps to better utilize the broad energy spectrum of sun light and can reach significantly higher efficiencies, depending on the number of junctions. Tandems are a special case of multijunction solar cells with the combination of two semiconductors, that already reach a theoretical efficiency limit of close to 45 %[18].

Multijunction solar cells based on III/V semiconductors have been researched for a long time. However, the high cost compared to silicon based photovoltaics have limited their usage to niche applications like satellites and concentrated photovoltaics[19], [20]. The upcoming research of perovskite materials is now opening the possibility for large area tandem solar cells that promise high efficiencies while maintaining low manufacturing costs[21], [22]. Since the pioneering work on perovskite semiconductors in 2009, the power conversion efficiency was improved from 3.8 %[23] to over 25 %[24] in 2021. The possibility of tuning the bandgap of the perovskites and the high optoelectronic quality have sparked the interest in using the material in tandem solar cells on top of a silicon bottom cell.

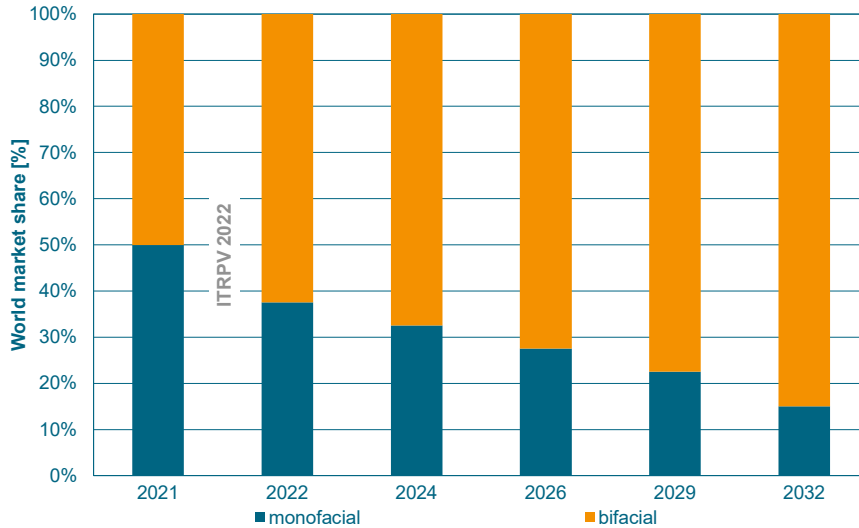


FIGURE 1.2: Estimation for 2021 and projection until 2032 of the market share for bifacial solar cells of the world production by the ITRPV report 2022. Reprinted with kind permission from [16].

Even so bifacial solar panels had tremendous success and tandem solar cells are promising higher efficiencies, they pose some challenges from the perspective of both module manufacturer and solar power plant developer. For planning the design and investment of PV modules, module manufacturing and PV power plants the expected electricity generation over the lifetime (the energy yield) needs to be estimated beforehand. Modeling the irradiance on the front side of solar panels is rather straightforward and for silicon based monofacial solar panels standardized test procedures have been developed. Solar panels typically have power ratings for so called standard testing conditions (STC), with a illumination according to the standardized AM1.5g[25] spectrum and an operation temperature of 25 °C. With the STC power rating good estimations of the energy yield can be made with simple calculations for monofacial solar cells. However, bifacial solar cells are significantly more complex to model because large fractions of the backside illumination come from reflected light from the ground and the surrounding of the modules. Taking these reflections into account requires sophisticated models, with the results being strongly dependent on the specific layout of the PV power plant.

Single junction solar cells are not very sensitive towards changes in the spectral distribution of the irradiance. This allows good estimations based on measurements under the AM1.5g spectrum, even though the spectrum in outdoor condition will vary. In multijunction solar cells, however, the sensitivity for spectral changes can be significant. This is closely related to the electrical configuration of tandem solar cells that can roughly be divided into two categories: monolithic 2-terminal and stacked 4-terminal[26]–[28]. In a monolithic design the two junctions are connected in series and the same electrical current will flow through both subcells. This can lead to significant performance limitations if the subcells absorb a different number of photons because the excess photons of the stronger absorbing junction are mostly lost[29].

The number of absorbed photons in each junction is strongly connected to the spectral distribution of the irradiance and the bandgap of the top cell[30]. The top cell acts as a light filter for the bottom cell and the bandgap determines up to which energy photons will be absorbed in the upper junction. The bandgap is therefore the critical design factor to obtain a balanced photon absorption in the top and bottom cell[31],

[32], a design strategy known as current matching. From theoretical analysis it was deduced that the optimal bandgap of the top cell in combination with a silicon bottom cell would be 1.75 eV for an illumination with AM1.5g[25] spectrum[33]. However, while the rating of solar panels based on silicon under AM1.5g showed good correlation with outdoor performance the same has not been proven for tandem solar cells[31], [34]. In the long term the design of tandem solar cells should be optimized for the operation in outdoor environments and therefore should consider effects such as spectral changes and temperature variations. In case of bifacial operation the exact layout of the power plant needs to be taken into account.

Bifacial and tandem solar cells are both relatively new technologies. In both technologies the outdoor performance is influenced by effects that are not relevant in classical monofacial silicon solar cells. These effects require research to better understand their influence on the power generation of bifacial and tandem solar cells. To further help the understanding of various effects that influence the operation of bifacial and multijunction solar cells this thesis had several primary objectives which can be divided into the following research tasks:

- Development of accurate simulation tools: Simulating bifacial and multijunction solar cells require the creation of comprehensive simulation tools that integrate all relevant effects influencing the performance of solar cells in outdoor conditions. This includes the modeling of (spectral) illumination on the front and backside of solar panels, the absorption characteristics of different cell architectures, and the impact of temperature variations on cell performance.
- Optimal perovskite bandgap for tandem solar cells: The tuneable bandgap of the perovskite top cell is an important design criteria for perovskite-silicon tandem solar cells. Various effects can change the optimal bandgap when comparing standard test conditions to outdoor environments, such as spectral variations or bifacial illumination.
- Optimization of solar cell and power plant design: Using advanced optimization techniques, this task aims to find optimal combinations of design parameters that maximize the performance and electricity cost of solar cell systems.
- Validation of solar cell simulation tools: Validating the models used for energy yield calculations is a crucial step to establish the credibility of the developed simulation tools. This involves comparing the predictions of the models with actual performance data from outdoor mounted solar cells.

Each of these tasks contributes to the overall goal of this thesis, which is to advance our understanding of bifacial and tandem solar cells and to guide future designs of cell architectures and power plants. For this, several simulation tools have been developed to allow a better understanding of bifacial and tandem solar cells. In order for the simulation tools to provide realistic estimations accurate weather data is required that describe the temperature and illumination conditions that are to be expected[35]. Several different databases and simulation tools have been developed to provide spectral and non-spectral irradiance data [36][37][38][39]. One of the most used resources for solar cell simulations is the National Solar Radiation Database (NSRDB) operated by the National Renewable Energy Laboratory (NREL) [38]. It provides a variety of different time series datasets covering North and Central America, including spectrally resolved irradiance data.

The availability of spectral irradiance data is quite limited for regions outside of the coverage of the NSRDB (e.g. Europe). Simulation tools such as the Bird Simple

Spectral Model can be used to compute the spectral irradiance on tilted and horizontal planes by providing basic atmospheric inputs (e.g. ozone content, water vapor) that are available from global weather models[37]. The Bird Simple Spectral Model is a parameterized model based on (time-consuming) radiative transfer calculations and ground measurements and allows for fast calculations for thousands of datapoints. However, it is only usable for clear sky conditions, limiting its overall usability to simulations of sunny days without the influence of clouds.

The NSRDB datasets and the Bird Simple Spectral Model were used for solar cell simulations of tandem solar cells to account for spectral effects in outdoor environments. The irradiance data, which describes the illumination on a horizontal plane, was combined with a detailed illumination model to calculate the irradiance on the front and backside of tilted mono- and bifacial solar cells. The illumination model was developed to accurately calculate the reflection of light from the surrounding while considering partial shading of the ground, depending on the sun position. It can be combined with optical simulations of the solar cell devices based on the finite element method (FEM) and ray tracing based methods. These optical simulations are used to calculate the spectral dependent absorption characteristics of different cell architectures. The optical and illumination simulations are combined with the weather and irradiance data for a realistic estimation of the photocurrent. The influence of the temperature is calculated by using a diode model for the electrical characteristic of the solar cell. Together these tools allow for accurately modeling of the energy yield for realistic operation conditions.

The design of solar cells as well as the geometry of power plants may have many parameters that determine the overall performance of the system. This can make it difficult to find combinations of these parameters for an optimal performance of the system, because typically there are no derivatives of the free parameters available with respect to the different performance metrics. In this thesis, Bayesian optimization is demonstrated as a computational efficient method for these optimization tasks. The simulation and optimization methods and results presented in this thesis allow to optimize the design of PV systems ranging from the structure of the individual solar cells to the layout of power plants. This will help to guide future designs of the cell architectures and power plants and contribute to an accelerated transition of our today's carbon based economy towards renewable energies.

This thesis begins with the theoretical concepts that are required for solar cell modeling presented in the second chapter. This includes introductions to the working principles of solar cells, optical aspects of solar cell designs and numerical simulation and optimization techniques. The following chapters presents the publications on which this cumulative thesis is based, and discuss their relevance in the broader context of this work. The third chapter contains a detailed explanation of the bifacial illumination model. The fourth chapter investigates the effects of bifacial operation and luminescent coupling on the bandgap of perovskite/silicon tandems for idealized solar cells. The fifth chapter focuses on realistic cell performance and validation of the underlying model chain for energy yield calculations of bifacial tandem solar cells. The sixth chapter presents results of an optimization study based on FEM calculations for a backside grating in a multijunction solar cell. The seventh chapter is concerned with the optimization of power plant layouts for bifacial solar cells considering different land cost scenarios. Finally, the main results are summarized and viewed in a larger context in the eighth chapter.





## Chapter 2

# Theoretical background

## 2.1 Single junction solar cells and their limitation

### 2.1.1 Photoelectric effect and simple solar cell model

The basic physical process that allows to convert light into electricity by a semiconductor is the photovoltaic effect, as illustrated in figure 2.1. The characteristic property of a semiconductor is a gap between the valence band and the conduction band. In solid-state physics a band describes states with certain ranges of energetic levels that can be occupied by electrons. The electrons of the material will tend to occupy the lowest energetic level possible and the valence band is the band with the highest energetic states that are still occupied. The conduction band on the other hand is the lowest energetic range where states are available that are not occupied by electrons. The characteristic property of a semiconductor is a gap between the valence and conduction band, a range of energies with no electronic states. This gap is limited by the highest state of the valence band  $E_v$  and the lowest of the conduction band  $E_c$  and is called the bandgap.

If photons of sufficient energy interact with a semiconductor, electrons from the valence band are energetically excited into the conduction band. The elevated electron leaves a vacancy, that can be treated as a positively charge "hole", and a so-called electron-hole pair is formed. Because there are no allowed energetic states between the conduction band and the valence band the excited (elevated) electron can not immediately relax back into the vacancy of the valence band and a metastable state is formed. If the interacting photon carries energy higher than the bandgap of the semiconductor the electrons in the valence band can still be excited from a level

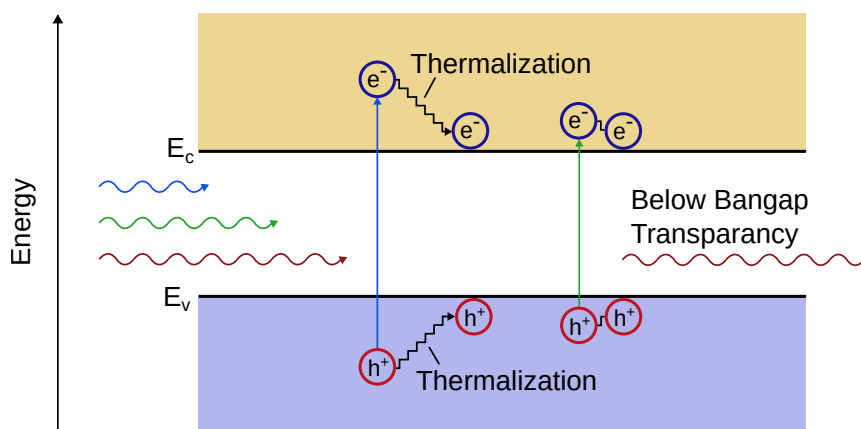


FIGURE 2.1: Schematic illustration of the photovoltaic effect in a semiconductor. Photons with energy significantly higher then the bandgap can excite electrons from below  $E_v$  and/or above  $E_c$ .

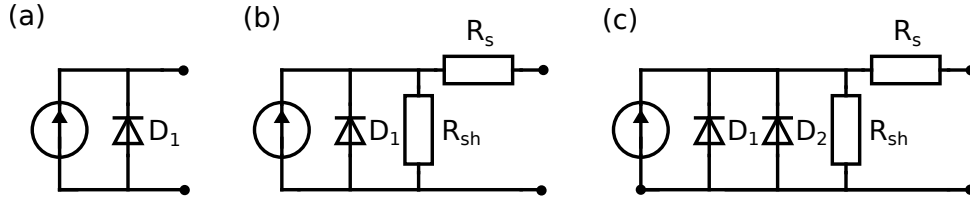


FIGURE 2.2: Equivalent circuits for a one-diode model (a), one-diode model with shunt and series resistances (b) and two-diode model with shunt and series resistances (c).

below the valence band edge  $E_c$  and/or into a state in the conduction band above  $E_c$ . These electrons and holes with energies above and below the respective edge energy levels will quickly lose the excess energy in a process called thermalization. The electron and hole will remain in an energy state close to their respective band edge in a metastable state and can be collected as current to drive an electrical circuit. Due to the thermalization affect the voltage of such a device is limited by the bandgap of the semiconductor and is irrespective of the energy of the radiation as long as it is higher than the bandgap energy. Radiation with photon energies below the bandgap of the semiconductor is not able to excite electrons from the valence to the conduction band and the semiconductor will be transparent to this light. Because radiation from the sun is spectrally distributed over a wide range of energies these two effects already explain major losses in a classical solar cell design and limit the amount of electricity that can be generated from a given radiation source.

### 2.1.2 Equivalent circuit model

For a solar cell, the semiconductor absorber needs two additional layers for separating the electrons and holes, respectively. In a classical silicon solar cell this is achieved by doping the upper and lower side with an element from the III and V main group, respectively to create electron and hole selective contacts. This is also similar to the way a diode is built and the electrical properties of an ideal solar cell can be well described by a current source connected to a diode in parallel. This arrangement is shown in Fig. 2.2 (a) and is also known as an equivalent circuit. Depending on the voltage between the electrical contacts of the equivalent circuit some fraction of the current from the source that is drawn from the source some part of the The current-voltage (IV) characteristic of such an arrangement is described by the Shockley solar cell equation:

$$J(V) = J_{ph} - J_0 \left[ \exp\left(\frac{V}{kT/e}\right) - 1 \right] \quad (2.1)$$

with  $J_{ph}$  as the photocurrent density,  $k$  as Boltzmann constant,  $T$  as the device temperature,  $q$  as electrical charge,  $V$  as the voltage at the connection contacts of the solar cell and  $J_0$  as the dark saturation current density. The photocurrent density  $J_{ph}$  is strongly dependent on the illumination of the solar cell in terms of the photonflux density  $\Phi_f$  as well as the external quantum efficiency (EQE). The EQE describes the collection probability of photons of a certain energy as current of the solar cell. Combining both the photocurrent is:

$$J_{ph} = e \int \text{EQE}(\lambda) \Phi_f(\lambda) d\lambda \quad (2.2)$$

$J_0$  is a characteristic property of a diode and known as the dark saturation current density. The dark saturation current describes the rate at which electrons and holes are recombining and for a good performance of the solar cell this value should be as low as possible, because the electron-hole pairs should be extracted from the semiconductor as electrical current instead of recombining in it. Without an external illumination, an ideal solar cell behaves as an ideal diode and can be described as such. In such an ideal solar cell (or diode) the dark saturation current  $I_0$  is solely driven by the generation of electron-hole pairs from thermal radiation going into the semiconductor itself. The generation of electron-hole pairs by thermal radiation needs to be countered by a rate of recombination in equilibrium. However, electron-hole pairs are only created in the spectral range where the semiconductor can actually absorb, because most of the thermal radiation will consist of photons below the bandgap. Considering the limited absorption with the EQE the dark saturation current density can be calculated as follows:

$$J_{0,\text{ideal}}(T) = e \int EQE(\lambda) \Phi_{\text{BB}}(\lambda, T) d\lambda \quad (2.3)$$

with the elementary charge  $e$ , the photon flux density of the black body radiation  $\Phi_{\text{BB}}$  and the photon wavelength  $\lambda$ . This assumes that all recombination in the solar cell is radiative. In real devices, however, it is often much lower. Using arguments of reciprocity and considering the limited radiative recombination in terms of the external quantum efficiency of electroluminescence  $\text{EQE}_{\text{el}}$  of a real cell a realistic dark saturation current  $J_0$  can be calculated [40]:

$$J_0(T) = \frac{J_{0,\text{ideal}}(T)}{\text{EQE}_{\text{el}}} \quad (2.4)$$

Another effect that limits the performance of solar cells is resistivity. The current that is generated and flows through the solar cell will be subject to electrical resistance losses, which subsequently leads to a voltage drop of the device. On the other hand, the diode effect of the device, that prevents current to flow in the reverse direction, is not perfect and some current will "leak" through. This leak current can often be well described by an ohmic resistance, also known as shunt resistance. Leak current and voltage drop can be accounted for in an equivalent circuit with a resistor in parallel and in series to the electrical load as shown in Fig. 2.5 (b). Both effects can be integrated into eq. 2.1 considering the voltage drop of the cell by the series resistance  $R_s$  and the current loss from the shunt resistance  $R_{\text{sh}}$ :

$$V_{\text{ext}} = V_{\text{int}} - J \cdot R_s \quad (2.5)$$

$$J_{\text{sh}} = \frac{V_{\text{int}}}{R_{\text{sh}}} \quad (2.6)$$

$$J(V_{\text{ext}}) = J_{\text{ph}} - J_0 \left[ \exp\left(\frac{V_{\text{ext}} + J \cdot R_s}{kT/e}\right) - 1 \right] - \frac{V_{\text{ext}} + J \cdot R_s}{R_{\text{sh}}} \quad (2.7)$$

with  $V_{\text{ext}}$  as the voltage usable at the terminals,  $V_{\text{int}}$  as the internal voltage driving the diode and shunt current.

The recombination of electrons and holes in the solar cell can have different mechanisms. Radiative recombination is a fundamental process that can not be prevented and the ideal solar cell equation 2.1 only accounts for this type of recombination. The recombination processes in real devices however is often dominated by a non-radiative process called Shockley-Read-Hall (SRH) recombination. In Shockley-Read-Hall recombination either an electron or a hole is "trapped" in a defect of the semiconductor

crystal. These traps allow the fast recombination of electrons and holes and their energy is transformed into heat. While eq. 2.4 can account for non-radiative recombination the mechanism and therefore the rate of SRH and other non-radiative recombination is quite different. One way to account for different rates of different recombination mechanisms is the introduction of an ideality factor into the diode equation. The ideality factor describes how closely the diode follows the behavior of an ideal diode where only radiative recombination is present. The diode equation with the ideality factor  $n$  is given by:

$$J(V) = J_{\text{ph}} - J_0 \left[ \exp \left( \frac{V}{nkT/e} \right) - 1 \right] \quad (2.8)$$

For the simulation of solar cells the ideality factor is often fitted to match experimental results. Another strategy to account for different recombination mechanisms is the usage of more than one diode (typically two) with a fixed ideality factors (typically 1 and 2) in the equivalent circuit. This requires multiple dark saturation currents that need to be fitted to experimental results and yields the following equation:

$$J(V) = J_{\text{ph}} - J_0 \left[ \exp \left( \frac{V + J \cdot R_{\text{series}}}{1kT/e} \right) - 1 \right] - J_1 \left[ \exp \left( \frac{V + J \cdot R_{\text{series}}}{2kT/e} \right) \right] - \frac{V + J \cdot R_{\text{series}}}{R_{\text{shunt}}} \quad (2.9)$$

For the practical implementation of the various forms of diode equations, it is typically required to invert the formulas to get a function of  $V$  depending on  $J$ . This is typically done by using the LambertW function or other iterative methods[41]–[43]. The code for simulating solar cells that was used in this work however, uses interpolation for inverting the expression. This has the advantage that additional effects, such as luminescent coupling that will be discussed later, are simpler to implement because only the forward function needs to be calculated.

## 2.2 Multijunction and tandem solar cells

To overcome the fundamental physical power conversion efficiency limits of single junctions, multijunction solar cells provide a viable alternative[24]. In a multijunction solar cell multiple absorber materials with different bandgaps are combined into a single device. The special case of multijunction solar cells with two different absorbers is also called a tandem solar cell, inspired by tandem bicycles, where two drivers can combine their separate muscle power. Figure 2.3 shows the fundamental advantage of multijunction solar cells. As discussed above, thermalization and below bandgap transparency are the 2 main sources of efficiency loss in a single junction solar cell. In a multijunction solar cell, the photons with higher energy are absorbed in the higher subcells of the vertical stack of different semiconductor materials. Due to the lower mismatch between photon energy and the bandgap of the semiconductor a higher share of this energy can be utilized by the solar cell. Photons with lower energy will be transmitted into the lower subcells of the multijunction solar cell. As shown in Figure 2.3 (b)-(d) by the colored area the utilisable energy increases with the number of junctions. The largest area increase from increasing the number of junctions by one is going from a single junction to a tandem solar cell.

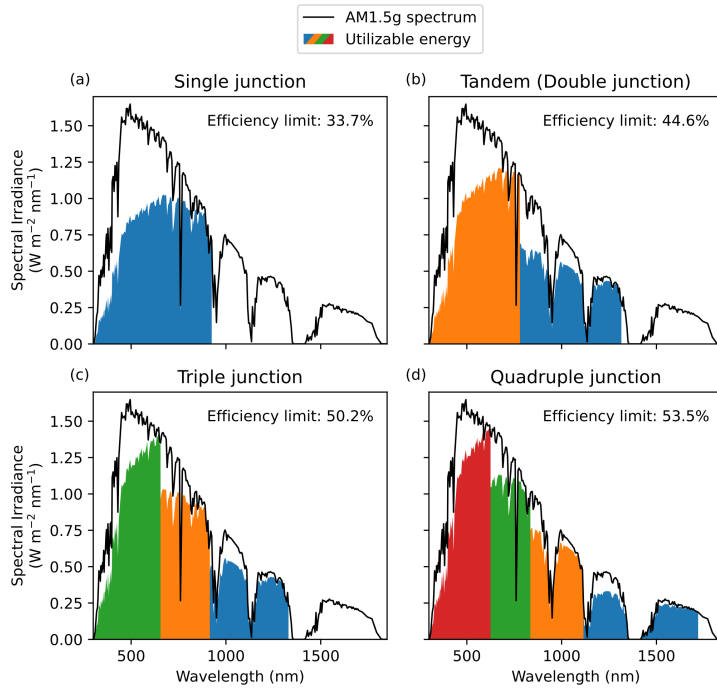


FIGURE 2.3: Utilizable energy of the AM1.5g spectrum when operating a single (a), double (b), triple (c) and quadruple junction solar cell with optimal bandgap combinations. The fraction of energy usable for the different junctions is visualized in different colors. Efficiency limits according to [44].

This increases the efficiency limit from 33.7% from a single junction with optimal bandgap (1.34 eV) to 44.6% for a tandem with bandgaps of 1.58 and 0.94 eV [44]. By addition of more junctions the efficiency limit can be further increase, however effect is becoming increasingly stagnate.

While tandems with high power conversion efficiencies are not a new technology, traditionally they were made from expensive materials and were never able to penetrate larger markets besides space applications and concentrated photovoltaics[19], [20]. The fast progress of perovskite solar cells in terms of efficiency and the available bandgaps of the material made perovskite/silicon tandem solar cells an attractive research field[21], [22].

### 2.2.1 Electrical connections in tandem solar cells

The electrical power generated by the two junctions of a tandem solar cell has to be extracted via electrical connections. There are two main types of connection concepts: two terminal (2T) and four terminal (4T) as shown in Fig. 2.4[45], [46]. In a 2T tandem both junctions are connected in series and the electrical wiring is attached at two endpoints (terminals). One of the endpoints is located at the top of the vertically stacked cells, the other at the bottom. A 4T tandem solar cell on the other hand has a total of four endpoints, two at each junction. Both junctions are connected to separate electrical circuits and are only optically coupled but separated by an electrical insulator.

The main difference between two and four terminal tandem solar cells is the requirement of current matching in the case of two terminals. Because both junctions are electrically connected in series the same current will flow through both cells. If

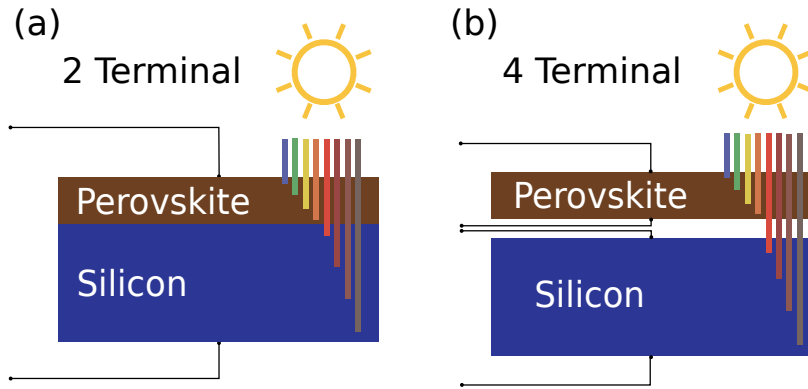


FIGURE 2.4: Wiring scheme in a 2T (a) and a 4T (b) tandem solar cell. The same current will flow through both subcells in the 2T configuration due to the series connection. In 4T configuration both subcells can operate at their individual maximum power point.

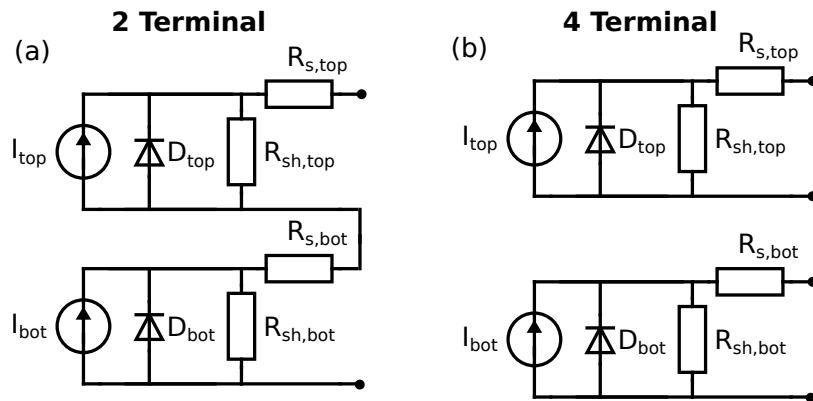


FIGURE 2.5: Equivalent circuits for tandems based on one-diode models in 2T (a) and 4T (b) configuration.

the two junctions generate different photocurrents the overall current of the tandem cell will be limited by the lower photocurrent[47], [48].

Both concepts have certain advantages and disadvantages. So far results from research labs show higher efficiencies for 2T tandems[24], [49]–[51]. And while the commercial development of 4T perovskite/silicon tandem solar cells seems more complex, they have the conceptual advantage of not requiring current matching. This makes the choice of the perovskite bandgap much more flexible[52]. In this thesis the bandgap requirements of 2T and 4T tandem are investigated to guide future research and development of perovskite silicon tandem solar cells.

### 2.2.2 Equivalent circuits for tandem solar cells

Tandem solar cells in 2T or 4T configuration can also be represented by equivalent circuits. Fig. 2.5 shows the equivalent circuits, which are straightforward combinations of the equivalent circuit of a single cell. In the 2T case, the circuits are connected in series while in the 4T case both cells are electrically completely independent.

To calculate the JV characteristic of the 2T tandem solar cell, the current in both junction (top and bottom cell) needs to be same.

$$J_{\text{top}} = J_{\text{bot}} = J_{\text{cell}} \quad (2.10)$$

The power of a solar cell is calculated by the product of the current and the corresponding voltage from the  $JV$  characteristic. For the power of a 2T tandem the voltage of the subcells should be available as a function of the current. The voltage of the cell is then simply the sum of from both subcells, and the power  $P$  and maximum power  $P_{\text{mpp}}$  is given by:

$$\begin{aligned} P_{\text{cell}} &= J_{\text{cell}} (V_{\text{top}} + V_{\text{bot}}), \\ P_{\text{mpp}} &= \max_{J_{\text{cell}}} [P_{\text{cell}}]. \end{aligned} \quad (2.11)$$

For tandem solar cells with 4T configuration the maximum power point calculated independently and the resulting power is the sum of the maximum power of each junction:

$$P_{\text{mpp}} = \max_{J_{\text{Si}}} [J_{\text{Si}} \cdot V_{\text{Si}}(J_{\text{rec,Si}})] + \max_{J_{\text{pero}}} [J_{\text{pero}} \cdot V_{\text{pero}}(J_{\text{rec,pero}})]. \quad (2.12)$$

## 2.3 Illumination and optical aspects in solar cell simulations

Solar cells are optoelectronic devices, meaning they have a combination of optical and electronic properties. In the previous section some models to simulate the electronic characteristics were discussed while this section is concerned with the optical aspects of solar cell simulations.

The optical simulation can roughly be divided into two parts: first the irradiance of light onto the solar cell and second the optical response of the solar cell or solar panel itself. The illumination on the front of the module has two major sources, the direct and diffuse irradiance components from the sky as illustrated in fig. 2.6. The direct irradiance originates from unscattered sunlight, that has a high intensity and narrow angular distribution. If the direct sunlight is not blocked by clouds it typically makes up 80-90 % of the total irradiance that reaches the solar panels[53]. In meteorological measurements it is normally specified as direct normal irradiance (DNI), meaning the irradiance on a plane with the normal of the plane aligned with the beam direction of the direct sunlight. The diffuse light on the other hand has a very wide angular distribution and originates from the complete hemisphere of the sky. The main effects that drive the diffuse irradiance is the Rayleigh scattering responsible for the blue color of the clear sky and the scattering of light at clouds. The diffuse part of the irradiance is typically specified as diffuse horizontal irradiance (DHI), meaning the irradiance on a plane lying flat on the ground (assuming a ground with zero inclination).

While it is quite straight forward to calculate the intensity of the DNI on a tilted plane, the diffuse part of the irradiance requires more sophisticated estimations. The simplest approach is to assume an isotropic distribution of diffuse light over the hemisphere[54]. This is a good approximation for a conformal cloud coverage of the sky and can yield reasonable results for a clear sky[55]. With a clear sky the regions close to the horizon and the area around the solar disc (circumsolar) are typically brighter than the rest of the hemisphere[56]. This led Perez to develop a semiempirical model to account for horizontal and circumsolar brightening for clear skies[53], [57]. For high cloud coverage an isotropic sky model is used and for mixed scenarios both models are weighted depending on the ratio of diffuse and direct irradiance.

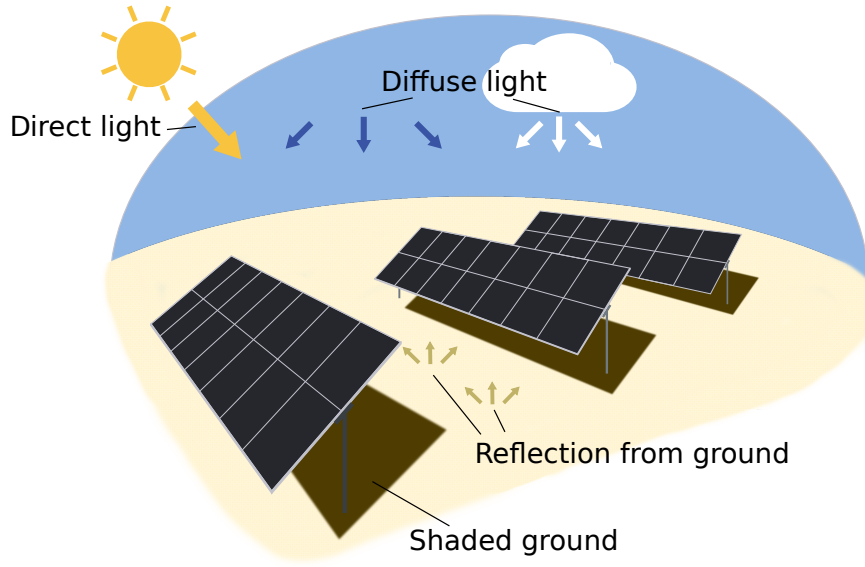


FIGURE 2.6: Illustration of a PV power plant illuminated by direct sunlight, diffuse sky light and diffuse light scattered from clouds. The ground is partially shaded by the models while other regions of the ground reflect a certain part of the sunlight.

### 2.3.1 Optical simulations

Besides illumination, the optical response of the solar cell itself is required for the simulation of the power generation. The optical response relevant for solar cells describes how light reflects, propagates and is absorbed in the active and non-active areas of the cell.

For a simple system, consisting of two different media as shown in 2.7 with a flat interface between, the reflection and transmission of light can be calculated with Fresnel's equations:

$$\begin{aligned}
 R_s &= \left| \frac{n_1 \cos \theta_i - n_2 \cos \theta_t}{n_1 \cos \theta_i + n_2 \cos \theta_t} \right|^2 \\
 R_p &= \left| \frac{n_1 \cos \theta_t - n_2 \cos \theta_i}{n_1 \cos \theta_t + n_2 \cos \theta_i} \right|^2 \\
 T_s &= 1 - R_s \\
 T_p &= 1 - R_p
 \end{aligned} \tag{2.13}$$

where  $R_s$ ,  $R_p$ ,  $T_s$  and  $T_p$  are the reflection and transmission of s and p polarized light, respectively.  $n_1$  and  $n_2$  are the refractive index of the first and second material and  $\theta_i$  and  $\theta_t$  are the angles of incident and transmitted light, respectively. The refractive index defines the optical properties of a material and gives the "light bending ability" of matter. The relationship between  $n_1$  and  $n_2$  and  $\theta_i$  and  $\theta_t$  are given by Snell's law:

$$\frac{\sin \theta_i}{\sin \theta_t} = \frac{n_2}{n_1} \tag{2.14}$$

The absorption of light in the active medium is driving the photocurrent of the solar cell as stated in eq. 2.2. In a homogeneous medium the absorption probability can be



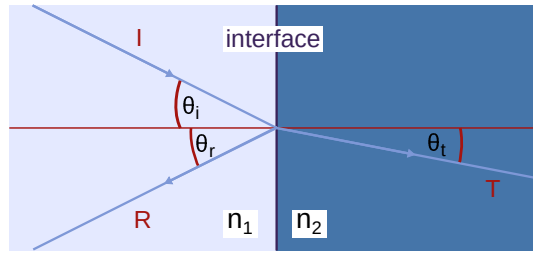


FIGURE 2.7: Illustration of Fresnel's and Snell's law for the transmission (T) and reflection (R) of an incident light beam (I) on a planar interface between two media with a refractive index  $n_1$  and  $n_2$ .

calculated by the Beer-Lambert law:

$$\begin{aligned} I(z) &= I_0 \cdot e^{-\alpha z} \\ A(z) &= I_0 - I(z) \end{aligned} \quad (2.15)$$

where  $\alpha$  is the absorption coefficient,  $I_0$  is the light intensity before entering the absorptive medium and  $A(z)$  and  $I(z)$  are the absorption and the light intensity after traveling a distance  $z$  through the absorbing medium. In an absorptive medium the refractive index is complex valued and the absorption coefficient  $\alpha$  is closely correlated to the imaginary part  $k$  of the refractive index:

$$\alpha \frac{c}{2\omega} = k \quad (2.16)$$

with  $c$  as the speed of light in vacuum and  $\omega$  as the angular frequency of the light.

For the simulation of a solar cell the absorption probability in the active region of the semiconductor of light shining onto the solar cell is required. For this, reflection and transmission at different interfaces and absorption in different layers of the layer stack have to be taken into account. For a stack of layers with only planar interfaces this is possible with the transfer matrix or net radiation method, that gives exact solutions for the propagation and absorption of light in such a system [58]–[60].

### 2.3.2 Textured interfaces

The optical design of a solar cell is focused on maximizing the utilizable photocurrent in the active material. This is achieved by reducing the reflection, reducing parasitic absorption, and trapping weakly absorbed light. Optimizing these properties is also referred to as light management in solar cells[61], [62]. Parasitic absorption is the absorption of light in layers of the solar cell that do not contribute to the photocurrent of the active material. Such layers have a variety of roles, such as providing electrical conductivity or electron or hole selective contacts, and are necessary for a functioning device. It is often difficult to optimize the parasitic absorption because optically beneficial measures (such as decreasing the thickness of parasitic absorbing layers) can hurt the electronic properties of the cell and lead to an overall reduction of the power output.

Reflection occurs when light hits an interface between two media with different refractive indices. Silicon with a refractive index of 3.4 shows a reflection of around 30 % when directly illuminated from air[63]. By texturing the surface of the silicon wafer the reflection can be significantly reduced[64]. Two different effects can reduce the reflection of textured interfaces, depending on the characteristic structure size of the texture. As shown in figure 2.8 for structures larger or equal to the wavelength

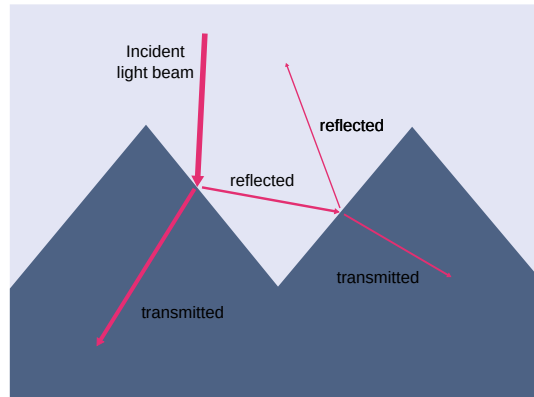


FIGURE 2.8: Schematic illustration of the anti-reflection effect from textured surfaces with feature sizes larger than the wavelength. A reflected beam can interact with the surface a second time with another chance of being transmitted into the substrate.

of the incident light, reflected beams can get a second interaction with the surface to enter the medium[65]. For textures with characteristic structures smaller than the wavelength, the light does not interact like a ray anymore but the wave character is dominant. This results in an interaction where the texture acts as a continuously increasing (or decreasing) refractive index and therefore the graded index effect reduces the reflection, also known as the "moth eye" effect[66], [67]. The third important concept for light management in solar cells is light trapping[68], [69]. Light trapping aims to increase the average path length of light that has entered the cell. In a solar cell based on silicon, the absorption of infrared light with wavelengths above 1050 nm is rather weak but can still contribute to the photocurrent. As shown in fig. 2.9 a scattering structure on the front or backside of the silicon wafer can increase the light path. Subsequent, the absorption of light can be significantly increased between 1050 and 1150 nm. By texturing the front side the anti-reflection and light trapping effect can be combined.

In commercial silicon solar cells, this is practically achieved by etching the silicon with potassium hydroxide that forms randomly oriented pyramids with a size of a few micrometres on the surface of the wafer[70]. In some cases, the relatively large size of potassium hydroxide etched pyramids presents difficulties, especially in the design of multijunction solar cells[62]. Some recent cell designs that reached record power conversion efficiencies are based on periodic structures that can be precisely designed, enabling anti-reflective and light trapping properties but require typically more sophisticated manufacturing steps[49], [68], [69], [71].

Unfortunately, there are no exact and fast methods such as the transfer matrix method for textured interfaces, but sophisticated numerical tools such as the finite element method (FEM)[72], rigorous coupled wave analysis (RCWA)[73], finite-differences time domain[74], or ray tracing[75] are required. In this thesis FEM with the implementation JCMSuite and raytracing with GenPro4[60] are used to simulate the optical response of solar cell designs and are detailed in section 2.5.1 and 2.5.3, respectively.

### 2.3.3 Bifacial solar cells

Conceptually the idea of bifacial solar cells is quite simple. Instead of only converting the light reaching the front side, also light from the back is utilized. This requires

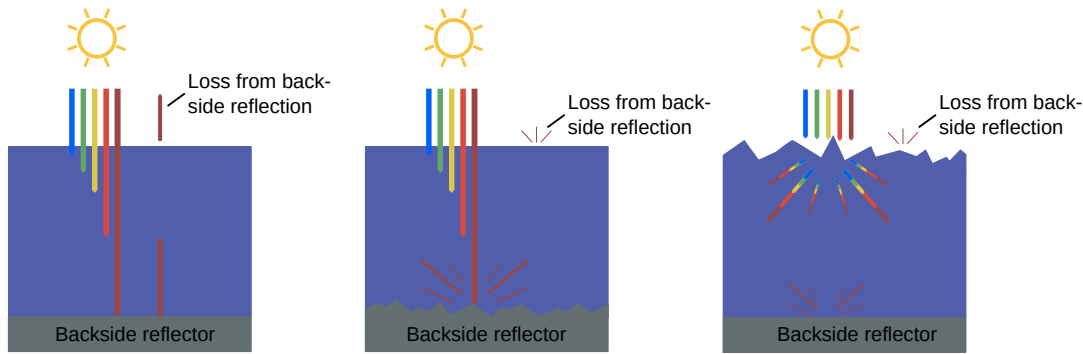


FIGURE 2.9: Illustration of light trapping effect of solar cells by textured interfaces. (a) If no textured interfaces are present in the solar cell the weakly absorbed infrared light can pass through the cell and after being reflected at the backside it can subsequently leave the cell at the top. If either the backside (b) or the frontside (c) is textured the light is scattered into different directions. At the next interaction of the infrared light with the front side most light is reflected back into the cell due to total internal reflection.

a transparent front and backside that is only partly covered with metal contacts. The solar cell market was dominated by BSF-based cells until around 2018[7], [10]. In BSF-based cells the complete backside is covered with aluminium and therefore cannot be used for bifacial operation[76]. With the market penetration of PERC solar cells, that use localized BSFs, the way was cleared for widespread adoption of bifacial solar cells, with an incredible uptake of market share from 15 to over 50 % from 2019 to 2022[17][16].

The precise estimation of the expected energy yield was always a crucial step in planning PV power plants[77]. With the introduction of bifacial solar panels, the complexity of energy yield estimations was further increased[78]. Calculating the irradiance on the modules is a critical step in modelling the system power. This is rather straightforward for monofacial solar panels, where the contribution of direct sunlight is easily calculated from the position of the sun and the inclination angle of the panel. The fraction of diffuse light can be estimated by the portion of the sky that is visible to the front side of the panel, while reflected light from the ground plays only a marginal role in the illumination of the front side[57]. On the other hand, most light reaching the solar panel originates typically from ground reflections as illustrated in fig. 2.6.

The ground itself will not be uniformly illuminated and some parts will be shaded by the solar panels. The shaded areas will depend on the orientation of the solar panels and the position of the sun. Also, depending on the ground position only fractions of the sky will be visible and therefore the irradiance from diffuse light is reduced. Depending on the position on the module the light from ground reflections will also vary.

Several different simulation tools for modelling these effects for backside illumination were developed in the past[79]–[81]. They can roughly be separated into two types, view-factor and ray tracing. View factor models try to find explicit radiative transfer functions between surfaces in the scene. For simple geometric arrangements, they can compute very fast solutions, however, they often ignore multiple reflection effects and are not suited for more complex scenarios. Depending on the implementation edge effects can be taken into account or are ignored to allow faster simulations. Ray tracing on the other hand can accurately model complex scenes, while taking multiple

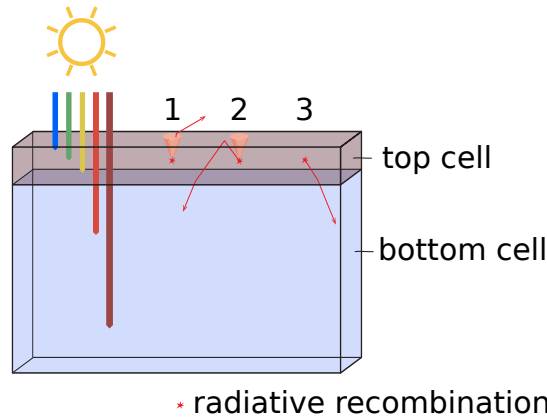


FIGURE 2.10: Illustration of luminescent coupling in a tandem solar cell device. Radiative recombination in the top cell will be emitted isotropically in all directions and can undergo one of the following: (1) Photons are emitted into the narrow escape cone (indicated in light orange) and leave the cell into the air above (and is lost). (2) Photons are emitted into the top direction but outside of the escape cone and will undergo total internal reflection and can be subsequently transmitted into the bottom cell. (3) Photons are emitted towards the bottom cell. Case 2 and 3 will result in an increased photocurrent in the bottom cell.

reflections into account. The disadvantage of ray tracing simulations is the required computation effort, which can take several days of runtime on high-performance computers for very complex scenes[80].

For this thesis, a view-factor based model was developed which assumes a large PV power plant and therefore ignores edge effects. The focus of the development was fast evaluation times and flexibility to easily adapt tandem solar cell simulations. The details of the model are described in chapter 3.

### 2.3.4 Luminescent coupling

In every solar cell, some fraction of the absorbed photocurrent will undergo radiative recombination. The radiative recombination of a semiconductor is emitted isotropically in all directions, and therefore some emission will escape the solar cell. This is a fundamental effect that can not be avoided[40], [82]. In a multijunction solar cells, the radiative recombination in higher layers can also be emitted into lower absorption layers, as shown in fig. 2.10. In the example of a perovskite/silicon tandem solar cell, the photons emitted in the perovskite can undergo one of three processes. Photons emitted into the escape cone (the angular range that does not undergo total internal reflection) can leave the device through the front side shown in case 1 of fig. 2.10. Due to the lower refractive index of air compared to the perovskite most photons emitted into the top direction will undergo total internal reflection on the front side as shown in case 2. In case 3, light emitted into the direction of the bottom cell does not exhibit total internal reflection due to the higher refractive index of the silicon. By absorbing radiative recombination of photons emitted by the perovskite the photocurrent in the silicon can be increased [83], [84]. On the other hand photons generated by the silicon cannot be absorbed in the perovskite, because the photon energy will be close to the bandgap of silicon. Photons emitted by silicon will be therefore in a wavelength range where the perovskite is not able to absorb.

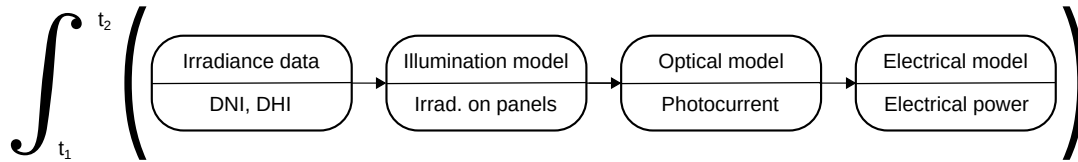


FIGURE 2.11: Example illustration of a model chain for energy yield calculations. Beginning from the irradiance data that typically contains DNI and DHI components the irradiance on the panels is calculated by an illumination model. From the irradiance on the panels, the photocurrent in the junctions of the solar cell are calculated. Finally the electrical model calculates the power, eventually taking other factors such as the temperature into account. The electrical power is calculated for each timestep in the chosen irradiance data set starting from  $t_1$  up to  $t_2$ . Finally the power is integrated over time to give the energy yield of the simulated solar cell.

## 2.4 Energy yield calculations

In the previous sections 2.1 to 2.3 several aspects and models for the optical and electrical behaviour of solar cells have been discussed. Combining these models allows to simulate the power generation of a solar cell. There is little information gained when simulating the power generation under non-standardized circumstances for a single time instance because the weather and irradiance are constantly changing in an outdoor environment. Instead, the power generation is simulated for many different weather conditions that should represent the conditions expected for a solar cells that is installed outside. This procedure is called energy yield calculation and is a powerful method to estimate the expected electricity generation over time. It can be used for evaluating the prospect of new technologies or for cost calculations when designing and dimensioning solar power plants.

For a series of timesteps the power generation is simulated and the yield is calculated by integrating over time:

$$EY = \int_{t_1}^{t_2} P_{SC}(t) dt \quad (2.17)$$

where EY is the energy yield,  $t_1$  and  $t_2$  are the start and end time of the simulated period, respectively, and  $P_{SC}$  is the electrical power of the solar cell.

Energy yield calculations are typically performed by combining several models for different processes that determine the power generation of a solar cell. Fig. 2.11 shows such a chain of models to simulate a solar cell. The basis of each yield calculation is a time series of irradiance data, and together with the sun position the irradiance on the PV panels is calculated. The optical and the electrical characteristics of a specific solar cell are typically separated in two models. These determine the power generation of the solar cell based on the irradiance on the PV panels.

Energy yield calculations can be performed with a wide range of sophistication in the underlying models. And while energy yield calculations can be very useful, it should be considered that the resulting accuracy depends on how well the irradiance data represents the actual irradiance and how well the chosen models represent the actual physics of the solar cell.

## 2.5 Numerical methods

### 2.5.1 Finite element method for modelling periodic nano textures

#### Maxwell's equations

The fundamental processes that determine the behavior of light can be described by Maxwell's equations. Maxwell's equations are partial differential equations that relate electric charge and current densities to the electric and magnetic fields:

$$\begin{aligned}
 \frac{\partial \mathbf{B}}{\partial t} + \nabla \times \mathbf{E} &= 0 \\
 \nabla \cdot \mathbf{D} &= \rho \\
 \frac{\partial \mathbf{D}}{\partial t} - \nabla \times \mathbf{H} &= -\mathbf{j} \\
 \nabla \cdot \mathbf{B} &= 0
 \end{aligned} \tag{2.18}$$

with the magnetic flux density  $\mathbf{B}$ , the electric field strength  $\mathbf{E}$ , the charge density  $\rho$ , the magnetic field strength  $\mathbf{H}$ , electric flux density  $\mathbf{D}$ , and the electrical current density  $\mathbf{j}$ . The relevant optical phenomena of solar cells are the absorption, reflection and transmission by the optical element(s) for a given source (the direction and wavelength of illumination). These can be solved by evaluating the electric field strength using the time harmonic formulation of Maxwell's equations. In the time-harmonic setup, the time dependence of all quantities at a coordinate  $x$  can be described by a harmonic oscillator that depends on the angular frequency  $\omega$ :

$$\mathcal{A}(x, t) = \text{Re} [\mathcal{A}(x)e^{-i\omega t}] \tag{2.19}$$

The constitutive equations relate the magnetic field strength to the magnetic flux density and the electric flux density to the electric field strength by their respective material properties permeability  $\mu$  and permittivity  $\epsilon$  that are scalar in case of isotropic materials:

$$\begin{aligned}
 \mathbf{D} &= \epsilon \mathbf{E} \\
 \mathbf{H} &= \mu \mathbf{B}
 \end{aligned} \tag{2.20}$$

In an absorption simulation, that is the typical basis for a solar cell modeling, the simulated device (the solar cell) is free of internal sources and an external source is defined. In this setup, the constitutive equations allow to combine Maxwell equations into a single equation, where the angular frequency  $\omega$  is depending on the vacuum wavelength of the external light source[85]:

$$\epsilon^{-1} \nabla \times \mu^{-1} \nabla \times \mathbf{E} - \omega^2 \mathbf{E} = 0 \tag{2.21}$$

#### The finite element method

For more complex geometries there are often no exact solutions known to Maxwell's equations and numerical methods are required to approximate the true solution. The finite element method (FEM) is such a numerical method that allows to approximate a solution for partial differential equations, such as the Maxwell's equations, for complex geometrical setups. The approximate solution is achieved by discretizing the investigated geometry into subunits, as shown in fig. 2.12. On these elements, the true function is approximated by a polynomial function up the degree  $p$ . Depending on the dimensionality of the geometry these elements can have different shapes such

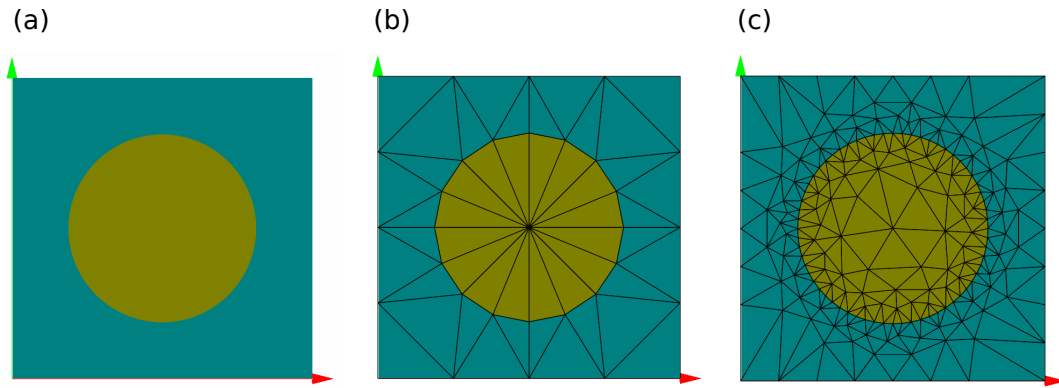


FIGURE 2.12: Example of the approximation of a real geometry by a mesh for a FEM simulation. A circle surrounded by a homogeneous medium as the investigated geometry (a) and the approximation by a course (b) and a fine (c) grid of triangles. Images generated with FEM software JCMsuite[86].

as triangles and rectangles in 2D or tetrahedron and prisms in 3D, and together they form the so called mesh.

FEM is often combined with the Galerkin method, which is detailed below, and for the formalism a few steps and approximations have to be taken to find a solution for the differential equation[87]:

- The differential equation is multiplied by a test function and integrate over the domain of the finite elements to get the so called weak formulation.
- The order  $p$  of the polynomial function for the elements is chosen.
- The integral function over each of the elements is evaluate and assembled to get a system of linear equations
- The system of equations is solved for the unknowns.

In the following these steps are shortly sketched to solve a system for Maxwell's equations. To yield the weak formulation, equation 2.21 is multiplied by a test function  $\mathbf{v}$  and integrated over the domain  $\Omega$ :

$$\int_{\Omega} \mathbf{v}(\nabla \times \mu^{-1} \nabla \times \mathbf{E}) dV - \omega^2 \int_{\Omega} \mathbf{v}(\varepsilon \mathbf{E}) dV = 0 \quad (2.22)$$

Integration by parts finally yields the weak formulation of the time harmonic Maxwell equation:

$$\begin{aligned} \int_{\Omega} (\nabla \times \mathbf{v}) \cdot (\mu^{-1} \nabla \times \mathbf{E}) dV - \int_{d\Omega} \mathbf{v} \mu^{-1} \nabla \times \mathbf{E} \cdot d\mathbf{S} - \omega^2 \varepsilon \int_{\Omega} \mathbf{v} \mathbf{E} \cdot dV &= 0 \\ \Leftrightarrow \int_{\Omega} (\nabla \times \mathbf{v}) \cdot (\mu^{-1} \nabla \times \mathbf{E}) \cdot dV - \omega^2 \varepsilon \int_{\Omega} \mathbf{v} \mathbf{E} dV &= \int_{d\Omega} \mu^{-1} \nabla \times \mathbf{E} \cdot d\mathbf{S} \end{aligned} \quad (2.23)$$

This version can also be compactly expressed as:

$$u(\mathbf{v}, \mathbf{E}) = f(\mathbf{v}) \quad (2.24)$$

where  $f(\mathbf{v})$  is defined by a source term for the incidenting light. Eq. 2.23 and eq. 2.24 are called the weak formulation of the Maxwell equation, because the formulation

does not require the differential equation to hold everywhere, but instead requires it only for the integral over each element. For this, the computational domain  $\Omega$  is discretized into the subspaces  $\Omega_h$ , with the index  $h$  representing each finite element of the mesh. In the next step, which is part of the Galerkin method, each element of the electric field  $E_l$  is replaced by a weighted sum of a set of ansatz functions  $\phi_1, \dots, \phi_N$ . The ansatz functions are typically polynomials of a fixed degree.

$$E_l = \sum_{i=1}^N a_i \phi_i \quad (2.25)$$

In the Galerkin method, the test function  $\mathbf{v}$  is also replaced by the ansatz-function  $\phi_1, \dots, \phi_N$ . This yields the following equation for each element  $h$  of the mesh:

$$\sum_{i=1}^N a_i u(\phi_i, \phi_l) = f(\phi_l) \quad (2.26)$$

which is a set of linear equations with the form:

$$A \cdot \mathbf{a} = \mathbf{f} \quad (2.27)$$

By solving the system of linear equations for the coefficients  $a$  and using the eq. 2.25, the electric field in each element  $\Omega_l$  can be calculated and gives a solution of the Maxwell equation for the defined setup.

The FEM simulations for this thesis were performed with JCMSuite, a software specialized in the modelling of nano-optical systems[86]. It implements a *hp*-FEM, meaning it allows for a combination of refining the mesh and increasing the polynomial degree of the ansatz-functions to increase the accuracy of the numeric solution to Maxwell's equation. This provides a high level of flexibility for tuning the setup, enabling high precision while maintaining low computation times.

### 2.5.2 Bayesian optimization

Bayesian optimization is a powerful and versatile technique to find the minimum (or maximum) of a given target function. It is a so-called “black box” optimization algorithm, because it does not depend on the derivatives or other information of the target function and requires only that the target function can be probed. Bayesian optimization is used for a wide variety of application areas and is often chosen for functions that are computationally expensive to evaluate[88]–[91]. It is a model based optimization algorithm, where the real function space is approximated with a regressive model. The regression model is then used to find promising inputs for the target function to find the optimum. With the new data point, the regression model is updated and the next candidate configuration is computed based on the updated model. The algorithm is called “Bayesian” because the sequential process can be described as calculating a posterior distribution of the target function using the already acquired data as prior likelihood.

#### Gaussian process regression

The typical choice for the regression model is Gaussian process regression, because they are not only modeling the function values but also its uncertainty, which is required by the Bayesian optimization algorithm. The model that approximates the



target function  $f$  defines a probability distribution for an input  $f(x)$ . The probability distribution is given by a Gaussian with a mean and standard deviation:

$$P(f(x)|x) = \mathcal{N}(\mu(x), \sigma^2(x)) \quad (2.28)$$

with  $\mathcal{N}$  denoting the normal distribution, based on the mean  $\mu$  and the standard deviation  $\sigma$ .

For the estimation of  $\mu(x)$  and  $\sigma(x)$  the Gaussian process has to be fitted to the available observation data. Given a set of observations  $f(\chi_1), f(\chi_2), \dots, f(\chi_t)$  the model is formed by a multivariate normal distribution, that is defined by a mean vector  $Y$  and a covariance matrix  $\Sigma$ . The covariance matrix represents the closeness or correlation of the observations to each other in terms of their input parameters  $\chi$ . It is calculated via a kernel function  $k$  that measures the distance of two data points depending on the input parameters  $\chi_1$  and  $\chi_2$ . The underlying assumption is that functions tend to be smooth and similar behavior is expected from the target function. Therefore data points that are close to each other in the input space should correlate more to each other than points which are further apart, with the kernel function  $k$  quantifying the closeness. The resulting covariance matrix  $\Sigma$  for the observations  $\chi_1$  to  $\chi_t$  is given by:

$$\Sigma = \begin{bmatrix} k(\chi, \chi_1) & \cdots & k(\chi_1, \chi_t) \\ \vdots & \ddots & \vdots \\ k(\chi_t, \chi_1) & \cdots & k(\chi_t, \chi_t) \end{bmatrix} \quad (2.29)$$

and the mean vector  $Y$  of the existing observations is given by:

$$Y = \begin{bmatrix} f(\chi_1) \\ \vdots \\ f(\chi_t) \end{bmatrix} \quad (2.30)$$

In order to draw conclusions about new data points the conditional distribution of the multivariate Gaussian distribution (of the existing observations) is used. This again gives a Gaussian distribution  $P(f(x)|x, \chi_1 \dots \chi_t, f(\chi_1 \dots \chi_t))$  and for the calculation the covariance between the existing observations and data point  $x$ , is required:

$$\Lambda = [ k(x, \chi_1) \quad k(x, \chi_2) \quad \cdots \quad k(x, \chi_t) ] \quad (2.31)$$

The prediction for the normal distribution of the new datapoint  $x$  can then be calculated with:

$$\begin{aligned} \mu(x) &= \Lambda^T \Sigma^{-1} Y \\ \sigma^2(x) &= k(x, x) - \Lambda^T \Sigma^{-1} \Lambda \end{aligned} \quad (2.32)$$

### Squared exponential kernel function

One important choice when using Gaussian process regression is the kernel function  $k$ . Many different functions are possible and in the simplest form it could be the inverse of the euclidean distance between the input parameters  $\chi$ . However, the typical choice is the squared exponential covariance function[92]. It has a bell curve and weights short range interactions higher than long range. It is given by:

$$k_{SE}(\chi_1, \chi_2) = \sigma_f^2 \cdot \exp\left(-\frac{\|\chi_1 - \chi_2\|^2}{2l^2}\right) \quad (2.33)$$

The squared exponential covariance function itself has the two hyperparameters  $l^2$  and  $\sigma_f^2$ .  $l^2$  can be interpreted as the characteristic length scale for which interactions between observations correlate to each other while  $\sigma_f^2$  can be interpreted as a parameter for the overall variance and therefore uncertainty of the regression. These two hyperparameter have to be scaled to appropriate values for the available observation data in order for the Gaussian process, and subsequent the Bayesian optimization, to give good results.

### Acquisition function

The last important choice for the Bayesian optimization algorithm is the acquisition function. The acquisition function selects input configurations that should minimize (or maximize) the function value based on the interpolated mean and uncertainty of the underlying model. One popular choice for an acquisition function is expected improvement[92]. Expected improvement evaluates possible configurations by the expectation value of the improvement based on the prediction for configuration  $x$ . The improvement is defined as the difference between the prediction of the Gaussian Process  $P$  and the currently known best observation  $f^*$ .

$$\begin{aligned} I(x) &= \max(f^* - P, 0) \\ P &\sim \mathcal{N}(\mu(x), \sigma(x)) \end{aligned} \quad (2.34)$$

There is no negative improvement, therefore the minimum of the improvement is 0. The expected improvement is the expectation value of the improvement, that is given by the integral of over the improvement times its likelihood:

$$EI(x) = \int_{-\infty}^{\infty} I(x)\phi(\epsilon)d\epsilon \quad (2.35)$$

With  $\phi$  as the probability density function of the normal distribution. Using equation 2.34 and reparametrization  $P \sim \mu + \sigma\mathcal{N}(0, 1)$ :

$$EI(x) = \int_{-\infty}^{(f^* - \mu)/\sigma} (f^* - \mu - \sigma\epsilon)\phi(\epsilon)d\epsilon \quad (2.36)$$

by transforming and solving the integral the final form of expected improvement is given by:

$$EI(x) = (f^* - \mu)\Phi\left(\frac{f^* - \mu}{\sigma}\right) + \sigma\phi\left(\frac{f^* - \mu}{\sigma}\right) \quad (2.37)$$

with  $\Phi$  being the cumulative density function of a normal distribution.

### Application of Bayesian optimization

Bayesian optimization is an iterative process, where in each cycle a new best configuration is searched for. In each cycle the following four steps are repeated:

- Use Gaussian process model to predict mean and standard deviation of the parameter landscape.
- Based on the predicted mean and standard deviation, find the best new candidate configuration  $x^*$ , quantified by the acquisition function(e.g. expected improvement).
- Calculate the value  $y = f(x^*)$ .

- Update the Gaussian process model with the new datapoint  $y, x^*$ .

This process can be repeated until a certain computation budget is exhausted or a convergence criteria is reached.

In optimization the trade-off between exploration (exploring configurations far from known ones) and exploitation (evaluating configurations close to already known good values) is very important. In Bayesian optimization the trade-off can be controlled over the acquisition and kernel function. In general, Bayesian optimization is considered to be highly efficient in terms of convergence with number of function evaluations[93], however different studies show mixed results when comparing against other black box optimization algorithms[94], [95]. In a study by Scheider *et al.*, on the other hand, Bayesian optimization showed the fastest convergence when compared with particle swarm, differential evolution and downhill simplex in the optimization of several nano-optical systems[96].

### 2.5.3 GenPro4

GenPro4 is a software package designed for optical simulations of single-junction and multi-junction solar cells[60]. It is based on a generalized net-radiation method that includes formalisms for the scattering of light at textured interfaces.

The net radiation method balances the radiation flux at each interface of the solar cell stack, considering the reflection, transmission and absorption between the layers. At each interface  $i$ , four components have to be balanced as shown in fig. 2.13: the incoming flux  $q_i^a$ , the reflected flux  $q_i^b$ , the transmitted flux  $q_i^d$  and the back-reflection from the next layer  $q_i^c$ . Refer to Figure 2.13 for an illustration of the power flux components at the interfaces of an optical system with three interfaces. The components can be calculated from the reflectance  $r$ , the interface transmittance  $t$  (the fraction of power flux transmitted through an interface) and the layer transmittance  $\tau$  (the fraction of power flux remaining after traveling through a layer).

$$\begin{cases} q_i^a = \tau_i \cdot q_{i-1}^d \\ q_i^b = r_i \cdot q_i^a + t_i \cdot q_i^c \\ q_i^c = \tau_{i+1} \cdot q_{i+1}^b \\ q_i^d = t_i \cdot q_i^a + r_i \cdot q_i^c \end{cases} \quad (2.38)$$

Reflectance and transmittance at the individual interfaces are determined by Fresnel's law (eq. 2.13) and the absorption in the layers by the Beer-Lambert law (eq. 2.15). These equations form a set of linear equations, which can be solved to find the absorption in each layer, as well as the transmission and reflection of the entire solar cell stack.

Genpro4 generalizes this idea for textured layers that scatter light in multiple directions. This is done by discretizing the hemisphere from where an interface can be illuminated, into ranges of the zenith angles while averaging over the azimuth. This leads  $r$ ,  $t$  and  $\tau$  to become matrices, that connect different incoming to outgoing directions (with  $\tau$  being a diagonal matrix, since the incoming direction is always equal to the outgoing one) and the power flux components  $q$  to become vectors. With the discretized hemisphere again a set of linear equations can be formulated and solved for the transmittance, absorption and reflection. However, the interface parameter  $r$  and  $t$  can no longer be calculated from Fresnel's equations but more sophisticated methods are required. GenPro4 includes a solver for calculating the scattering matrices with the use of a ray tracing algorithm. This requires a topological model of the interface and can be imported from atomic force microscopy data.

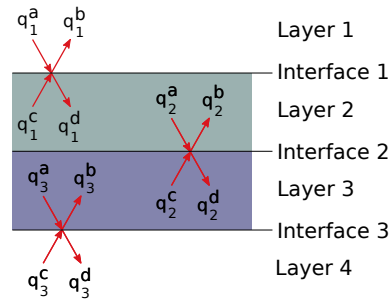


FIGURE 2.13: Illustration of the power flux components  $q$  at the interfaces of an optical system with a total of 3 interfaces.

The ray tracing algorithm ignores wave effects and therefore the structure size of the interface should be larger than the wavelength to achieve reasonable results. The main advantage of ray tracing, compared to more rigorous methods such as FEM, is the computation speed. It was validated to show good results for random pyramids that are etched into silicon[97]. GenPro4 also includes a method for rough surfaces with feature sizes below the wavelength size, however this model is not used for this thesis.

## Chapter 3

# The bifacial illumination model

Bifacial solar cells can deliver in the range of 5-15 % higher energy yields compared to classical monofacial panels[98]–[100]. As bifacial solar cells are most useful in field installation they are typically found in large solar power plants where the solar cell modules are arranged in wide rows, with many rows behind each other. The exact gain that can be realized by a solar power plant depends on many factors, notably the type of ground the plant is built on, the height of solar cell rows and the distance between rows[101]. These factors contribute to the variability in yield increase observed with bifacial solar cells. However, when planning a photovoltaic power plant it is important to have accurate estimations of the expected electricity production that allows accurate financial planning[77]. With the detailed illumination model presented in this work we provide the means for such accurate energy yield estimations.

The light received at the backside of the solar panels is mainly reflected from the ground[101]. The ground is unevenly illuminated due to the absorption of direct sunlight by the solar panels, resulting in only certain ground areas between the rows of solar panels being illuminated.

Depending on the location of the solar panel or the ground, different fractions of direct and diffuse light will be blocked by other rows of solar cells. This also leads to a partially inhomogeneous illumination along the vertical extent of the solar panels. In our manuscript we describe in detail all the relevant calculations necessary to accurately model the irradiance on bifacial solar cells and account for the spatial inhomogeneity along the module. We assume that the rows are infinitely wide and infinitely many rows are in front and behind the modeled unit cell. This allows to treat the problem in two dimensions, greatly simplifying the necessary calculations and allowing much faster evaluation speeds.

In the context of this work, the illumination model is the basis for all energy yield calculations presented in this thesis. The illumination model itself however does not model the optical behavior inside the solar panels, focusing instead solely on the irradiance received on the exterior of the modules. Designed for flexibility and rapid computation, the model includes several new features not present in the original version.

### *Supporting information*

The computer code underlying the article has been published and is accessible under <https://doi.org/10.5281/zenodo.3543570>



## Detailed illumination model for bifacial solar cells

KLAUS JÄGER,<sup>1,2,\*</sup>  PETER TILLMANN,<sup>1,2</sup> AND CHRISTIANE BECKER<sup>1</sup>

<sup>1</sup>Helmholtz-Zentrum Berlin für Materialien und Energie, Albert-Einstein-Straße 16, 12489 Berlin, Germany

<sup>2</sup>Zuse Institute Berlin, Takustraße 7, 14195 Berlin, Germany

\*klaus.jaeger@helmholtz-berlin.de

**Abstract:** We present a detailed illumination model for bifacial photovoltaic modules in a large PV field. The model considers direct light and diffuse light from the sky and treats the illumination of the ground in detail, where it discriminates between illumination of the ground arising from diffuse and direct light. The model calculates the irradiance components on arbitrarily many positions along the module. This is relevant for finding the minimal irradiance, which determines the PV module performance for many PV modules. Finally, we discuss several examples. The code for the model is available online (DOI: 10.5281/zenodo.3543570).

Published by The Optical Society under the terms of the [Creative Commons Attribution 4.0 License](#). Further distribution of this work must maintain attribution to the author(s) and the published article's title, journal citation, and DOI.

### 1. Introduction

Solar energy is the most abundant of all sustainable energy technologies [1]. Further, the cost of photovoltaics (PV) has decreased rapidly in the last decade [2]. Therefore, many studies suggest that the largest fraction of global energy needs in a sustainable carbon-free economy can be covered by photovoltaic solar energy [3,4].

Currently, most photovoltaic modules use monofacial solar cells, which only can utilize light that hits the cell at the front. In contrast to that, bifacial solar cells can also convert light impinging at the back and therefore increase the energy yield significantly. Because of novel silicon solar cell technologies using passivated emitter rear contacts (PERC/PERT/PERL) or IBC contacting schemes, bifacial solar cell operation becomes feasible and indeed, they are expected to have 60% market-share by 2029 [5–7].

To estimate the energy yield of bifacial modules it is vital to develop detailed illumination models, especially because the largest fraction of light that hits the module at the back arises from the ground. Several different illumination models were developed in recent years [8]. Sometimes, modules are treated as isolated and shadowing of module rows in front or behind is not considered [9], which overestimates the irradiation onto the ground. Already several authors developed detailed shadowing models of the ground [10–12], however, often variations of the irradiance along the module are neglected [12]. Calcabrini and coworkers developed a simplified model for front illumination using a sky view factor, which quantifies the landscape around the PV module, and a sun coverage factor, which they define ‘at a location with a raised horizon as the ratio between time that the sun is behind the module or blocked by the skyline per year and the annual sunshine duration at the same location with a clear horizon’ [13].

In a recent publication we minimized the levelized cost of electricity (LCOE) of large PV fields of bifacial modules using a Bayesian optimization algorithm [14]. In the present manuscript, we detail the illumination model, which we used in the preceding manuscript. The model, which is described in section 2 considers direct light and diffuse light from the sky and contains a detailed illumination model of the ground, where the model discriminates between illumination of the ground arising from diffuse and direct light. The model calculates the irradiance components on

arbitrarily many positions along the module, which is relevant for finding the minimal irradiance, which determines the PV module performance for many PV modules. Finally, we discuss several examples in section 3.

## 2. Illumination model

With the illumination model we calculate the irradiance onto a solar module, which is placed somewhere in a big PV-field. We assume this field to be so big that effects from the boundaries can be neglected. Further, we assume the modules to be homogeneous: we neglect effects from the module boundaries or module space in between solar cells. Hence, we can treat this problem as 2-dimensional with periodic boundary conditions, as illustrated in Fig. 1. As input we use the *direct normal irradiance* (DNI) and the *diffuse horizontal irradiance* (DHI), which we obtain from freely available weather databases, and the solar position. In [14], DNI and DHI were adapted according to the Perez model to account for the diffuse irradiance more accurately [15].

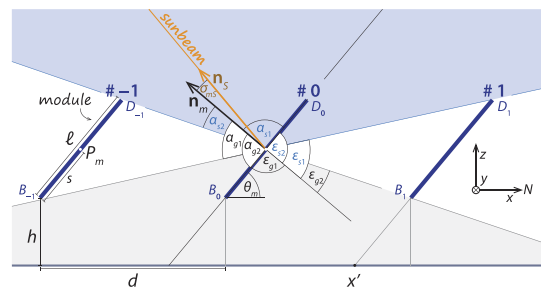


**Fig. 1.** Illustrating the irradiance components, which reach the module on the front and back sides; the front components are summarized in Table 1. Here, we assume w.l.o.g. that the PV system is located on the northern hemisphere and oriented towards South,  $\phi_m = 180^\circ$ . For better visibility, the point  $P_m$ , on which the irradiance components are evaluated, is not depicted on module #0 but on # - 1.

**Table 1. Irradiance components constituting the illumination of a solar module with  $s = \overline{BP}_m$ , where  $P_m$  is defined in Fig. 1. These components have to be considered for front and back sides – hence eight components in total.**

direct irradiance from the sky	$J_{\text{dir}}^{\text{sky}}(s)$
diffuse irradiance from the sky	$J_{\text{diff}}^{\text{sky}}(s)$
diffuse irradiance from the ground...	
... originating from direct sunlight	$J_{\text{dir}}^{\text{gr}}(s)$
... originating from diffuse skylight	$J_{\text{diff}}^{\text{gr}}(s)$

For the front and back sides of the module, we have to consider four irradiance components each – hence eight components in total. These components are summed up in Table 1 and depicted in Fig. 1. In this model we assume the solar modules to be completely black, meaning they do not reflect any light that could reach another module.

The total irradiance (or intensity; given in watt per m<sup>2</sup>) on front is given by

$$I_f(s) = I_{\text{dir},f}^{\text{sky}}(s) + I_{\text{diff},f}^{\text{sky}}(s) + I_{\text{dir},f}^{\text{gr.}}(s) + I_{\text{diff},f}^{\text{gr.}}(s), \quad (1)$$

and similar for the back side with a subscript *b* instead of *f*.

In section 2.1 we will derive expressions for the four components impinging onto the solar module from the sky. Expressions for the components impinging from the ground are derived in section 2.2. Table 2 shows the input parameters required for calculating the components.

**Table 2. Input parameters for the illumination model.**

<b>Module parameters</b> (depicted in Fig. 1)	
$\ell$	module length (m)
$d$	module spacing (m)
$h$	module height above the ground (m)
$\theta_m$	module tilt angle
$\phi_m$	module azimuth angle
<b>Solar and environmental parameters</b>	
DNI	direct normal irradiance (W/m <sup>2</sup> ) <sup>‡</sup>
DHI	diffuse horizontal irradiance (W/m <sup>2</sup> ) <sup>‡</sup>
$\theta_S$	zenith angle of the Sun
$a_S$	solar altitude, connected to zenith via $a_S = 90^\circ - \theta_S$
$\phi_S$	azimuth of the Sun
$A$	albedo of the ground
<sup>‡</sup> This parameter also can be spectral. Then, the unit would be W/(m <sup>2</sup> nm) and we would use the spectral irradiance $[I_\lambda] = \text{W}/(\text{m}^2\text{nm})$ and the spectral radiance $[L_\lambda] = \text{W}/(\text{sr}\cdot\text{m}^2\text{nm})$	
<b>Numerical parameters</b>	
$N_g$	number of points at which irradiance on the ground is evaluated in the interval $[0, d]$
$N_m$	number of points at which irradiance is evaluated on the module
$N_\alpha$	number of directions at which light impinging onto the module is discretized

The irradiance  $I$  is based on the more fundamental notion *radiance*  $L$  (in watt per steradian per m<sup>2</sup>), which is connected to the irradiance via

$$I(\mathbf{r}) = \int_{\Omega} L(\mathbf{r}, \theta, \phi) \cos \theta \, d\Omega, \quad (2)$$

where  $\mathbf{r}$  defines the coordinates on the surface on which  $I$  and  $L$  are evaluated [16].  $\theta$  and  $\phi$  denote the polar angle and azimuth, where  $\theta$  is defined such that it denotes the angle between the evaluated ray and the normal to the surface at  $\mathbf{r}$ . The term  $\cos \theta$  arises from Lambert's cosine law, which accounts for the decreasing irradiance of a beam of light which strikes a surface under increasing angle, because the radiant power is distributed across a larger area. The solid angle element is given by  $d\Omega = \sin \theta \, d\theta \, d\phi$ .

For the following derivation we define dimensionless *geometrical distribution functions* as

$$t_{\text{dir}}(s) := \frac{I_{\text{dir}}(s)}{\text{DNI}} \quad \text{and} \quad t_{\text{diff}}(s) := \frac{I_{\text{diff}}(s)}{\text{DHI}} \quad (3)$$

for the components arising from direct sunlight and diffuse skylight, respectively. Here we omitted the superscripts "sky" and "gr." as well as "f" and "b". DNI is the *direct normal irradiance* and DHI denotes the *diffuse horizontal irradiance*; see also Table 2.



### 2.1. Irradiance components from the sky

The *direct irradiance components from the sky* are given by

$$I_{\text{dir},f}^{\text{sky}}(s) = \begin{cases} \text{DNI} \cdot \cos \sigma_{mS}, & \text{if } \cos \sigma_{mS} > 0, \\ 0, & \text{if } \cos \sigma_{mS} \leq 0, \end{cases} \quad (4a)$$

$$I_{\text{dir},b}^{\text{sky}}(s) = \begin{cases} \text{DNI} \cdot |\cos \sigma_{mS}|, & \text{if } \cos \sigma_{mS} < 0, \\ 0, & \text{if } \cos \sigma_{mS} \geq 0. \end{cases} \quad (4b)$$

where the cosine between sunlight and module normal is calculated with

$$\cos \sigma_{mS} = \mathbf{n}_m \cdot \mathbf{n}_S = \begin{pmatrix} \cos \phi_m \sin \theta_m \\ \sin \phi_m \sin \theta_m \\ \cos \theta_m \end{pmatrix} \cdot \begin{pmatrix} \cos(-\phi_S) \sin \theta_S \\ \sin(-\phi_S) \sin \theta_S \\ \cos \theta_S \end{pmatrix}. \quad (5)$$

The  $-\phi_S$  arises from the fact that the solar azimuth  $\phi_S$  has a negative (clockwise) orientation in the right-handed coordinate system defined in Fig. 1. Hence, it increases from 0 at North ( $x$ -direction) to  $\frac{\pi}{2}$  at East ( $-y$ -direction) and  $\pi$  at South. Note that  $\cos \theta_{mS} > 0$  when direct sunlight hits the front of the module and  $< 0$  when it hits the back. For modules facing South ( $\theta_m = 180^\circ$ ), the latter can occur in the mornings and the evenings in the half year between the vernal equinox and the autumnal equinox. Further, our algorithm checks whether the position  $s$  on the module is shadowed by the row of modules in front. In that case,  $I_{\text{dir},f}^{\text{sky}}(s) = 0$ .

For the *diffuse irradiance from the sky*  $I_{\text{diff},f}^{\text{sky}}(s)$  on the module front we have to consider the angular range from which light can reach the module. This concept is also known as view factors (VF) in literature [8]. Generally speaking, diffuse light can reach the module front from an opening that spans from the top of the front row  $D_{-1}$  to the plane of the module itself, marked by the topmost point  $D_0$ . In the example in Fig. 1, point  $P_m$  on module #0 is illuminated by light from directions within  $\langle D_{-1}P_mD_0$ . With respect to the module normal, this range is constrained by the angles  $\alpha_{s1} = -\pi/2$  and  $\alpha_{s2}(s)$ . However, diffuse light does not only reach the module from directions within the  $xz$ -plane but from a *spherical wedge* as explained in the appendix. Under the assumption that diffuse light arrives isotropically from the upper hemisphere and using Eqs. (22) and (24) we find

$$I_{\text{diff},f}^{\text{sky}}(s) = \text{DHI} \cdot \text{SVF}_f^{\text{sky}} = \frac{\text{DHI}}{2} [\sin \alpha_{s2}(s) - \sin \alpha_{s1}] = \frac{\text{DHI}}{2} [\sin \alpha_{s2}(s) + 1]. \quad (6a)$$

For the *diffuse irradiance from the sky*  $I_{\text{diff},b}^{\text{sky}}(s)$ , the SVF for  $P_m$  is restricted by  $\langle D_0P_mD_1$ . With respect to the module normal, this range is constrained by the angles  $\epsilon_{s1}(s)$  and  $\epsilon_{s2} = \pi/2$ .

$$I_{\text{diff},b}^{\text{sky}}(s) = \text{DHI} \cdot \text{SVF}_b^{\text{sky}} = \frac{\text{DHI}}{2} [\sin \epsilon_{s2} - \sin \epsilon_{s1}(s)] = \frac{\text{DHI}}{2} [1 - \sin \epsilon_{s1}(s)] \quad (6b)$$

### 2.2. Irradiance components from the ground

As illustrated in Fig. 2, the ground receives direct and diffuse light from the sky, where we introduce the irradiances  $G_{\text{dir}}(x_g)$  and  $G_{\text{diff}}(x_g)$ . We assume the ground to be a Lambertian reflector with albedo  $A$ . Under this assumption the ground emits isotropically with the radiance

$L^{\text{gr}}(x_g)$ , which is connected to the irradiance  $G(x_g)$  via

$$L^{\text{gr}}(x_g) = \frac{A}{\pi} G(x_g), \quad (7)$$

where we omitted the subscripts “diff” and “dir”. Similar to Eq. (3) we define *geometrical distribution functions* on the ground:

$$\gamma_{\text{dir}} := \frac{G_{\text{dir}}}{\text{DNI}}, \quad \text{and} \quad \gamma_{\text{diff}} := \frac{G_{\text{diff}}}{\text{DHI}} = \text{SVF}_g. \quad (8)$$

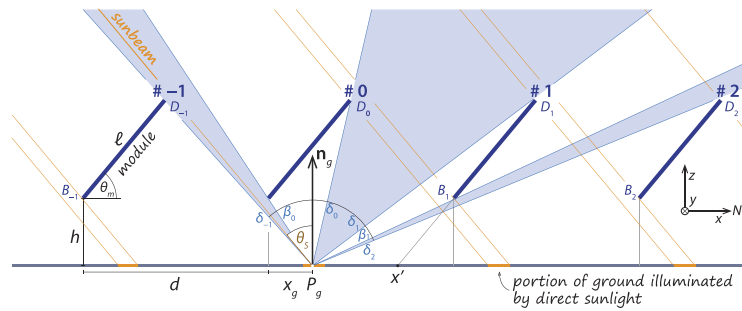


**Fig. 2.** Illustrating the irradiance components, which reach the ground under a large field of PV modules. Here, we assume w.l.o.g. that the PV system is located on the northern hemisphere and oriented towards South.

The *direct* geometrical distribution function is position dependent and takes values of 0 for shaded areas (no direct sunlight) and the projection of the direct irradiance on the ground otherwise:

$$\gamma_{\text{dir}}(x_g) = \begin{cases} \cos \theta_S, & \text{if direct sunlight hits ground at } x_g, \\ 0, & \text{if a module blocks direct light at } x_g, \end{cases} \quad (9)$$

hence  $\gamma_{\text{dir}}$  is independent of the azimuth of the Sun  $\phi_S$ . In Fig. 2 the fractions of the ground, which can be reached by direct sunlight, are marked in orange. Depending on the geometrical module parameters and the position of the Sun, the illuminated area may lay completely within the unit cell as in the example in Fig. 2, it may extend from one unit cell into the next as in Fig. 3 or no direct light can reach the ground. The latter can occur when the module spacing  $d$  decreases or when the zenith angle  $\theta_S$  is large, which means that the Sun has a low altitude.

The *diffuse* geometrical distribution function describes the fraction of the sky that is visible at a certain location on the ground. For the example shown in Fig. 2, light can reach  $P_g$  from three ranges:  $\angle D_{-1}P_gB_0$ ,  $\angle D_0P_gD_1$  and  $\angle B_1P_gD_2$ . Using Eq. (22), we find

$$\gamma_{\text{diff}}(x_g) = \frac{1}{2} [ (\sin \delta_{-1} - \sin \beta_0) + (\sin \delta_0 - \sin \delta_1) + (\sin \beta_1 - \sin \delta_2) ]. \quad (10)$$

If  $|\delta_{-1}| \leq |\beta_0|$  no light reaches the ground from between modules # - 1 and #0. If  $x_g > x'$ , we have to use the ranges  $\angle D_0P_gB_1$  and  $\angle D_1P_gD_2$  instead of the ones mentioned above.

Now we derive expressions for the irradiance components, which illuminate the module from the ground:  $I_{\text{dir},f}^{\text{gr}}$ ,  $I_{\text{diff},f}^{\text{gr}}$ ,  $I_{\text{dir},b}^{\text{gr}}$  and  $I_{\text{diff},b}^{\text{gr}}$ . The following derivation is valid for both components

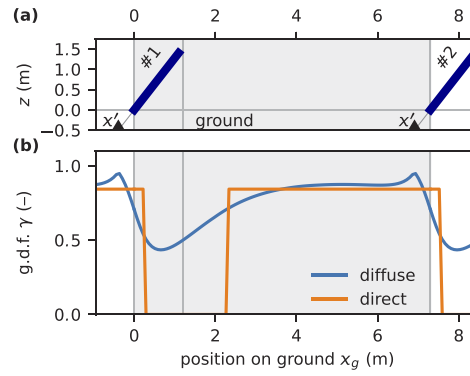


**Fig. 3.** An example for (a) a module configuration and (b) the corresponding diffuse and direct geometrical distribution functions  $\gamma$  on the ground, as defined in Eq. (8). The following parameters were used:  $\ell = 1.96$  m,  $d = 7.30$  m,  $h = 0.50$  m and  $\theta_m = 52^\circ$ . The solar position for the direct component was  $a_S = 31.9^\circ$  and  $\phi_S = 144.1^\circ$  (Berlin, 20 June 2019, 11:52 am CEST). The number of positions  $x_g$  on the ground, on which the functions are evaluated, is controlled by the parameter  $N_g$ , which was 101 in this example. The unit cell is represented as shaded area.

originating either from direct sunlight or diffuse skylight. Hence, we omit the subscripts “dir” and “diff” in the following. As illustrated in Fig. 1, the relevant angular range is given by  $\langle B_{-1}P_mB_0$  for the front and  $\langle B_0P_mB_1$  for the back, respectively. With respect to the module normal, this range is constrained by the angles  $\alpha_{g1}(s)$  and  $\alpha_{g2} = \pi/2$  for the front and by the angles  $\epsilon_{g1} = -\pi/2$  and  $\epsilon_{g2}(s)$  for the back. The diffuse irradiance components from the ground can be calculated using Eq. (21) in the appendix,

$$I_f^{\text{gr.}}(s) = \frac{\pi}{2} \int_{\alpha_{g1}(s)}^{\alpha_{g2}} L^{\text{gr.}} [x_f^g(s, \alpha)] \cos \alpha \, d\alpha, \quad (11a)$$

$$I_b^{\text{gr.}}(s) = \frac{\pi}{2} \int_{\epsilon_{g1}}^{\epsilon_{g2}(s)} L^{\text{gr.}} [x_b^g(s, \epsilon)] \cos \epsilon \, d\epsilon. \quad (11b)$$

As illustrated in Fig. 2,  $x_g(s, \alpha)$  and  $x_g(s, \epsilon)$  are the coordinates of the respective points  $P_g(s, \alpha)$  and  $P_g(s, \epsilon)$  on the ground, which are defined such that the angles between the line  $\overline{P_gP_m}$  and the module normal  $\mathbf{n}_m$  are equal to  $\alpha$  or  $\epsilon$ , respectively. Using  $\phi_m = 180^\circ$ , we find

$$x_g(s, \alpha) = s \cdot \cos \theta_m + (h + s \cdot \sin \theta_m) \tan(\theta_m + \alpha), \quad (12a)$$

$$x_g(s, \epsilon) = s \cdot \cos \theta_m + (h + s \cdot \sin \theta_m) \tan(\theta_m - \epsilon). \quad (12b)$$

Applying the definitions from Eqs. (3) and (8) together with Eq. (7) to Eqs. (11) yields

$$I_f^{\text{gr.}}(s) = \frac{A}{2} \int_{\alpha_{g1}(s)}^{\alpha_{g2}} \gamma [x_g(s, \alpha)] \cos \alpha \, d\alpha, \quad (13a)$$

$$I_b^{\text{gr.}}(s) = \frac{A}{2} \int_{\epsilon_{g1}}^{\epsilon_{g2}(s)} \gamma [x_g(s, \epsilon)] \cos \epsilon \, d\epsilon. \quad (13b)$$

### 2.3. Implementation details

The implementation is written in Python and utilizes the NumPy scientific computing package fast tensor operations. The code was implemented with the fast evaluation of time-series data for energy yield calculations in mind. For a fixed-array geometry and changing solar positions only the geometric distribution functions for direct light  $t_{\text{dir}}$  have to be calculated separately for every timestep while the different  $t_{\text{diff}}$  are time independent:

$$I_{\text{dir}}(s, t) := \text{DNI}(t) \cdot t_{\text{dir}}(s, t) \quad \text{and} \quad I_{\text{diff}}(s, t) := \text{DHI}(t) \cdot t_{\text{diff}}(s) \quad (14)$$

The irradiance of direct and diffuse light from the sky, which directly hit the solar modules, can be calculated with simple geometric functions. These numeric functions are evaluated very fast with vectorized code.

To account for reflected light from the ground the integral in Eq. (13) would need to be solved for every timestep. To avoid this, the ground is discretized into a finite amount of elements  $N_g$ . Within each element the radiance is assumed to be constant. This allows to reformulate Eq. (13) into a sum over all elements visible to the module. By introducing the ground view factor  $\text{VF}_g$  the geometrical calculations are not depending on the timestamp anymore, which is very beneficial for the speed of numerical evaluation:

$$I(s, t) = \frac{A}{2} \int_{\alpha_{g1}(s)}^{\alpha_{g2}} \gamma [x_g(s, \alpha), t] \cos \alpha \, d\alpha = \sum_{i=1}^n \gamma [x_g(s, \alpha_i), t] \cdot \text{VF}_g^i \quad (15)$$

where the  $\text{VF}_g$  is given by

$$\text{VF}_g^i = \int_{\alpha_i}^{\alpha_{i+1}} \cos \alpha \, d\alpha = \sin \alpha_{i+1} - \sin \alpha_i \quad (16)$$

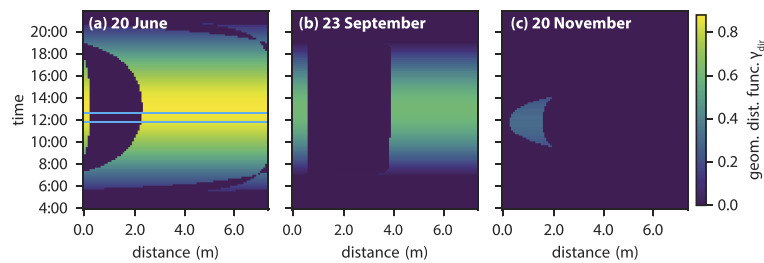
The numerical implementation allows to perform a one year simulation with irradiance data in one-hour intervals (4400 data points) in less than 1 s on normal personal computer. The code was published on [github](#) and can be accessed online [17].

### 3. Some examples

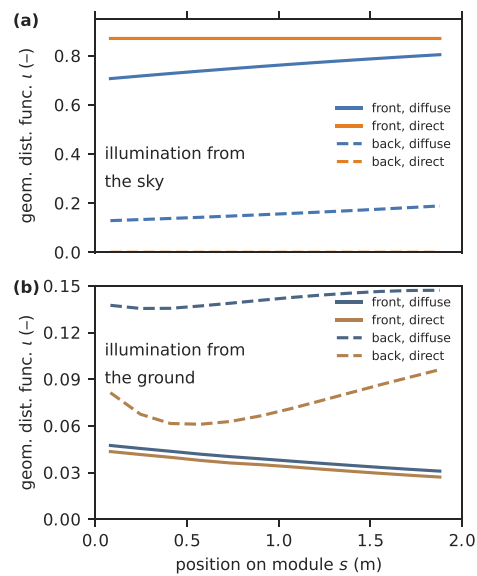
In this section we demonstrate the model with a few examples. We assume a PV system which is located in Berlin, Germany (52.5°N, 13.25°E). Based on a rule-of-thumb rule we set the module tilt approximately to the geographical latitude,  $\theta_m = 52^\circ$  and determine the distance such that a module does not shade a module behind on 21 December, 12 noon [11,18]. For modules with  $\ell = 1.96$  m length this leads to a distance between module rows of  $d = 7.3$  m. A sketch of this configuration is shown in Fig. 3(a). The solar positions are calculated using the Python package `pysolar` [19].

Figure 3(b) shows the geometrical distribution functions  $\gamma$  for direct and diffuse components on the ground for 20 June 2019, 11:52 am CEST.  $\gamma_{\text{diff}}$  is minimal below the module where the angle covered by the module is largest; and maximal at  $x'$ , because here the ground sees (almost) no shadow from module #1.

Figure 4 shows how the direct geometrical distribution function on the ground  $\gamma_{\text{dir}}$  develops during three days (20 June, 23 September and 20 November 2019). For 20 June, a large fraction of the ground is illuminated throughout the day. After sunrise and before sunset the Sun is below the module plane and direct sunlight hits the module back. During short amounts of time in the morning and evening the Sun lies in the module plane and no direct sunlight hits the module. At these times the shadow on the ground vanishes (around 7 am and 7 pm). In between these times the Sun is above the plane and direct light hits the module front. On 23 September, the length of



**Fig. 4.** Illumination of the ground by direct sunlight on three days: (a) 20 June, (b) 23 September, and (c) 20 November 2019. The color corresponds to the geometrical distribution function  $\gamma_{\text{dir}}$  and is equivalent to  $\cos(\theta_S)$ , if it is not zero due to shadowing [see Eq. (9)]. The following parameters were used:  $\ell = 1.96$  m,  $d = 7.30$  m,  $h = 0.50$  m and  $\theta_m = 52^\circ$ . The lines in (a) correspond to the timestamps also used in Figs. 3(b), 5 and 6. The number of positions  $x_g$  on the ground, on which the functions are evaluated, is controlled by the parameter  $N_g$ , which was 101 in this example.



**Fig. 5.** Example of geometrical distribution functions  $\iota$  on the module for light the module receives (a) from the sky and (b) the ground. The following parameters were used:  $\ell = 1.96$  m,  $d = 7.30$  m,  $h = 0.50$  m,  $\theta_m = 52^\circ$ , and albedo  $A = 30\%$ . The solar position for the direct components was  $a_S = 31.9^\circ$  and  $\phi_S = 144.1^\circ$  (Berlin, 20 June 2019, 11:52 am CEST). For the calculation we used DHI = 1 and DNI = 1. The number of positions  $s$  along the module, on which the functions are evaluated, is controlled by the parameter  $N_m$ , which is 12 in this example.

the shadow is almost the same during the whole day: the module tilt ( $52^\circ$ ) is almost the same as the latitude of Berlin ( $52.5^\circ$ ) - hence at equinox the ecliptic is practically normal to the module plane. On 20 November, only short stretches of the ground are illuminated.

Figure 5 shows an example for the eight geometrical distribution functions  $\iota$  corresponding to the irradiance components hitting the PV module on its front and back sides. While the functions originating from the sky (a) are stronger on the front side, the components originating from the ground (b) are stronger on the back side. This can be understood by the opening angles: the opening angle towards the sky is larger on the front side, but the opening angle of the ground is larger at the back. The largest relative variations are observed for the ground component at the module back side originating from direct sunlight: it is strongest for short  $s$ -values. This can be understood when looking at Fig. 3(b): the ground is illuminated by sunlight directly below the module.

In Fig. 6 we look at two examples on how the irradiance distribution along the module varies depending on the irradiation conditions. We utilized irradiation data measured at the *Hochschule für Technik und Wirtschaft Berlin* on 20 June 2019. DNI data was measured with the SHP1 pyrheliometer and DHI data was obtained with the SMP1 pyranometer [20]. Figure 6(a) shows results for 11:52 am CEST. Then, no DNI ( $0 \text{ W/m}^2$ ) was measured while DHI was  $144 \text{ W/m}^2$  - hence clouds covered the Sun. As discussed in [14], for many PV modules, such as

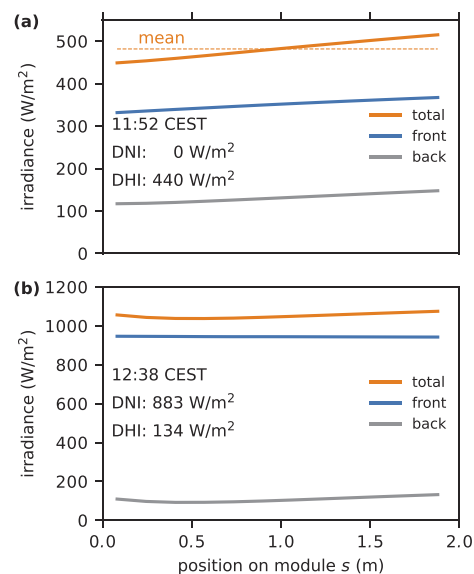


**Fig. 6.** Examples of irradiation onto the module for irradiation conditions in Berlin on 20 June 2019 at (a) 11:52 am and (b) 12:38 pm CEST. The following parameters were used:  $\ell = 1.96 \text{ m}$ ,  $d = 7.350 \text{ m}$ ,  $h = 0.50 \text{ m}$ ,  $\theta_m = 52^\circ$ , and albedo  $A = 30\%$ . The radiation data was obtained from HTW Berlin weather station [20]. The number of positions  $s$  along the module, on which the functions are evaluated, is controlled by the parameter  $N_m$ , which is 12 in this example. In (a), also an example for the total irradiance mean is shown, which would be calculated by models based on a view factor approach.

silicon modules composed of several single solar cells connected in series, the overall module performance is not determined by the mean irradiance but by the lowest irradiance observed by the module. Both the front and total irradiation are lowest at the lower end of the module. The total irradiance at the upper end is 10.7% higher than at the lower end. Figure 6(b) shows the situation 46 minute later, at 12:38 pm. Then, the DNI ( $883 \text{ W/m}^2$ ) is much higher than the DHI ( $134 \text{ W/m}^2$ ) – direct sunlight hits the PV module. Here, the irradiation onto the module front is almost independent of the module position, the maximum variations in total irradiance are below 0.5%. The total irradiation, which would be relevant for bifacial modules, is minimal at  $s \approx 0.57 \text{ m}$

The varying position of the irradiance minimum shows that it is very relevant to determine the irradiance components as functions along the module position  $s$ , which is automatically done by the model presented in this manuscript. Models based on view factors often have only mean irradiances as output, which might overestimate the final module performance.

#### 4. Conclusions and outlook

Accurate illumination models are crucial for yield estimations of PV power plants with bifacial solar cells. In this manuscript, we derived a detailed model that takes all relevant irradiation components onto PV modules into account and allows for a quick calculation. The code can be accessed online [17]. The irradiation components are calculated locally resolved along the module, which enables the user to determine the minimal irradiance, which is dependent on the illumination conditions, as illustrated in Fig. 6. This is relevant for accurately estimating the performance for many types of PV modules.

In a next step, we will expand the model such that the irradiance components onto the module are angular resolved. This is especially relevant when connecting the illumination model to optical models of solar cells. Further, it would be desirable to experimentally assess the model described in this manuscript in the future.

#### 5. Appendix. Integration of radiance across a spherical wedge

As shown in Fig. 1, the different diffuse components reach a point  $P_m$  on the solar module from certain angular ranges. However, diffuse light does not only reach the module from directions within the  $xz$ -plane, but from a spherical wedge, as illustrated in Fig. 7.

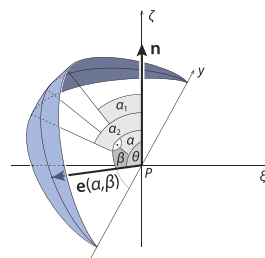


**Fig. 7.** The spherical wedge indicating the directions from which diffuse light can reach the module. Here, the wedge angle is  $(\alpha_2 - \alpha_1)$ , where  $\alpha_1$  and  $\alpha_2$  denote angles with respect to the normal direction  $\mathbf{n}$ . Depending on the application,  $\mathbf{n}$  is either the module normal  $\mathbf{n}_m$  or the normal to the ground  $\mathbf{n}_g$ . When  $\mathbf{n} = \mathbf{n}_g$ , the directions  $\xi$  and  $\zeta$  coincide with  $x$  and  $z$  in Fig. 1. When  $\mathbf{n} = \mathbf{n}_m$ ,  $\xi$  and  $\zeta$  are rotated with respect to  $x$  and  $z$  by the module tilt angle  $\theta_m$ . The  $xz$ - and  $\xi\zeta$ -planes always coincide.

The irradiance can be calculated with

$$I(P) = \int_{\Omega} L(\alpha, \beta) \cos \theta \, d\Omega, \quad (17)$$

where  $\Omega$  is the set of solid angles defined by the wedge and  $\theta$  is the angle spanned between the directional unit vector  $\mathbf{e}(\alpha, \beta)$  and the normal  $\mathbf{n}$ . With the spherical coordinate system defined in Fig. 7, we have

$$d\Omega = \sin \beta \, d\alpha \, d\beta. \quad (18)$$

The cosine factor can be expressed as

$$\cos \theta = \mathbf{n} \cdot \mathbf{e}(\alpha, \beta) = \begin{pmatrix} 0 \\ 0 \\ 1 \end{pmatrix} \cdot \begin{pmatrix} \sin \beta \sin \alpha \\ \cos \beta \\ \sin \beta \cos \alpha \end{pmatrix} = \sin \beta \cos \alpha. \quad (19)$$

Hence, we find for the irradiance

$$I(P) = \int_{\alpha=\alpha_1}^{\alpha_2} \int_{\beta=0}^{\pi} L(\alpha, \beta) \cos \alpha \sin^2 \beta \, d\alpha \, d\beta. \quad (20)$$

As we assume that the PV field is so big that boundary effects can be neglected. As a consequence, the illumination is invariant under translation along the y-axis and the problem can be treated as 2-dimensional. Therefore, the radiance does not depend on  $\beta$ ,  $L(\alpha, \beta) \equiv L(\alpha)$ . Integrating over  $\beta$  leads to

$$I(P) = \frac{\pi}{2} \int_{\alpha_1}^{\alpha_2} L(\alpha) \cos \alpha \, d\alpha. \quad (21)$$

When the radiance is isotropic,  $L(\alpha) \equiv L$ , we have

$$I(P) = \frac{L\pi}{2} (\sin \alpha_2 - \sin \alpha_1). \quad (22)$$

For small angle intervals it is sometimes useful to work with the angles  $\alpha = 0.5(\alpha_1 + \alpha_2)$  and  $\delta = \alpha_2 - \alpha_1$ . Then, Eq. (22) becomes

$$I(P) = L\pi \cos \alpha \sin \frac{\delta}{2}. \quad (23)$$

In our model, the diffuse light from the sky is given as *diffuse horizontal irradiance* DHI. In this work we assume the diffuse skylight to be isotropic, hence the diffuse sky radiance  $L_s$  is independent of the direction. With Eq. (22), we find

$$L_s = \frac{1}{\pi} \text{DHI}, \quad (24)$$

where we used  $\alpha_1 = -\frac{\pi}{2}$  and  $\alpha_2 = \frac{\pi}{2}$ .

### Funding

Helmholtz Einstein International Berlin Research School in Data Science (HEIBRiDS); Helmholtz Association via Helmholtz Excellence Network SOLARMATH (ExNet-0042-Phase-2-3).



### Acknowledgments

We thank Lev Kreinin and Asher Karsenti from SolAround for fruitful discussions regarding the illumination model for bifacial solar cells. The results were obtained at the Berlin Joint Lab for Optical Simulations for Energy Research (BerOSE) of Helmholtz-Zentrum Berlin für Materialien und Energie, Zuse Institute Berlin and Freie Universität Berlin, and within the Helmholtz Excellence Network SOLARMATH, a strategic collaboration of the DFG Excellence Cluster MATH+ and Helmholtz-Zentrum Berlin für Materialien und Energie.

### Disclosures

The authors declare no conflict of interest.

### References

1. F. Creutzig, P. Agoston, J. C. Goldschmidt, G. Luderer, G. Nemet, and R. C. Pietzcker, "The underestimated potential of solar energy to mitigate climate change," *Nat. Energy* **2**(9), 17140 (2017).
2. N. M. Haegel, H. Atwater, T. Barnes, C. Breyer, A. Burrell, Y.-M. Chiang, S. D. Wolf, B. Dimmler, D. Feldman, S. Glunz, J. C. Goldschmidt, D. Hochschild, R. Inzunza, I. Kaizuka, B. Kroposki, S. Kurtz, S. Leu, R. Margolis, K. Matsubara, A. Metz, W. K. Metzger, M. Morjaria, S. Niki, S. Nowak, I. M. Peters, S. Philipps, T. Reindl, A. Richter, D. Rose, K. Sakurai, R. Schlatmann, M. Shikano, W. Sinke, R. Sinton, B. Stanbery, M. Topic, W. Tumas, Y. Ueda, J. van de Lagemaat, P. Verlinden, M. Vetter, E. Warren, M. Werner, M. Yamaguchi, and A. W. Bett, "Terawatt-scale photovoltaics: Transform global energy," *Science* **364**(6443), 836–838 (2019).
3. M. Z. Jacobson, M. A. Delucchi, Z. A. Bauer, S. C. Goodman, W. E. Chapman, M. A. Cameron, C. Bozonnat, L. Chobadi, H. A. Clonts, P. Enevoldsen, J. R. Erwin, S. N. Fobi, O. K. Goldstrom, E. M. Hennessy, J. Liu, J. Lo, C. B. Meyer, S. B. Morris, K. R. Moy, P. L. O'Neill, I. Petkov, S. Redfern, R. Schucker, M. A. Sontag, J. Wang, E. Weiner, and A. S. Yachanin, "100% Clean and Renewable Wind, Water, and Sunlight All-Sector Energy Roadmaps for 139 Countries of the World," *Joule* **1**(1), 108–121 (2017).
4. M. Child, C. Kemfert, D. Bogdanov, and C. Breyer, "Flexible electricity generation, grid exchange and storage for the transition to a 100% renewable energy system in Europe," *Renew. Energy* **139**, 80–101 (2019).
5. T. Dullweber, C. Kranz, R. Peibst, U. Baumann, H. Hannebauer, A. Fülle, S. Steckemetz, T. Weber, M. Kutzer, M. Müller, G. Fischer, P. Palinginis, and H. Neuhaus, "PERC+: industrial PERC solar cells with rear Al grid enabling bifaciality and reduced Al paste consumption," *Prog. Photovoltaics* **24**(12), 1487–1498 (2016).
6. S. Chunduri and M. Schmela, "Bifacial Solar Technology Report 2018 edition," Tech. rep., TaiYang News (2018).
7. "International Technology Roadmap for Photovoltaic (ITRPV), Tenth edition," Tech. rep., VDMA (2019).
8. T. S. Liang, M. Pravettoni, C. Deline, J. S. Stein, R. Kopecek, J. P. Singh, W. Luo, Y. Wang, A. G. Aberle, and Y. S. Khoo, "A review of crystalline silicon bifacial photovoltaic performance characterisation and simulation," *Energy Environ. Sci.* **12**(1), 116–148 (2019).
9. R. Schmagier, M. Langenhorst, J. Lehr, U. Lemmer, B. S. Richards, and U. W. Paetzold, "Methodology of energy yield modelling of perovskite-based multi-junction photovoltaics," *Opt. Express* **27**(8), A507–A523 (2019).
10. U. A. Yusufoglu, T. M. Pletzer, L. J. Koduvelikulathu, C. Comparotto, R. Kopecek, and H. Kurz, "Analysis of the Annual Performance of Bifacial Modules and Optimization Methods," *IEEE J. Photovolt.* **5**(1), 320–328 (2015).
11. L. Kreinin, A. Karsenty, D. Grobgeld, and N. Eisenberg, "PV systems based on bifacial modules: Performance simulation vs. design factors," in *Proceedings of the 43rd IEEE Photovoltaic Specialists Conference (PVSC)*, (IEEE, 2016), pp. 2688–2691.
12. B. Marion, S. MacAlpine, C. Deline, A. Asgharzadeh, F. Toor, D. Riley, J. Stein, and C. Hansen, "A practical irradiance model for bifacial PV modules," in *Proceedings of the 44th IEEE Photovoltaic Specialist Conference (PVSC)*, (IEEE, 2017), pp. 1537–1542.
13. A. Calcabrini, H. Ziar, O. Isabella, and M. Zeman, "A simplified skyline-based method for estimating the annual solar energy potential in urban environments," *Nat. Energy* **4**(3), 206–215 (2019).
14. P. Tillmann, K. Jäger, and C. Becker, "Minimising levelised cost of electricity of bifacial solar panel arrays using bayesian optimisation," *Sustain. Energy Fuels* **4**(1), 254–264 (2020).
15. R. Perez, R. Stewart, R. Seals, and T. Guertin, "The development and verification of the Perez diffuse radiation model," Tech. rep., Sandia National Laboratories (SNL), Albuquerque, NM, and Livermore, CA (United States) (1988).
16. J. E. Harvey, C. L. Vernold, A. Krywonos, and P. L. Thompson, "Diffracted radiance: A fundamental quantity in nonparaxial scalar diffraction theory," *Appl. Opt.* **38**(31), 6469–6481 (1999).
17. P. Tillmann and K. Jäger, Bifacial illumination model, (2019). DOI: 10.5281/zenodo.3543570.
18. P. Grana, "The new rules for latitude and solar system design," (2018). <https://www.solarpowerworldonline.com/2018/08/new-rules-for-latitude-and-solar-system-design/>.
19. B. Stafford, "Pysolar," (2018). DOI: 10.5281/zenodo.1461066.
20. V. Quaschnig, T. Tjaden, J. Weniger, and J. Bergner, "HTW weather station," (2019). [https://wetter.htw-berlin.de/History/DIF\\_SMP5\\_DIR\\_SHP1/2019-06-20/2019-06-21](https://wetter.htw-berlin.de/History/DIF_SMP5_DIR_SHP1/2019-06-20/2019-06-21).



## Chapter 4

# Bifacial operation and luminescent coupling in tandem solar cells

Tandem solar cells promise to further improve the power conversion efficiency of solar cells and ultimately reduce the cost of electricity generation. Perovskite is a material class that has seen tremendous progress in terms of efficiency and scalability and the combination in a tandem solar cell with a silicon subcell has reached 29.80 % [24] which is significantly higher than the record silicon cell with 26.7 percent [102].

The electrical connection scheme in a tandem solar cell has a major impact on the overall design requirements [26]. In a 4 terminal (4T) connection, the two sub cells are only mechanically stacked and optically coupled, but are electrically completely separated. This requires a more complex wiring scheme and an optically transparent but electrically insulating interlayer. The alternative of a 2 terminal (2T) tandem solar cell has only two electrical contacts, one on top and one at the bottom of the cell stack. Both cells are connected in series which requires that both subcells are operated with the same current. To maximise the power conversion efficiency of a 2T tandem solar cell both absorbers should generate the same photocurrent [18]. Because the top cell acts as an optical filter from the perspective of the bottom cell the design of the top cell is the critical factor to accomplish this task. The bandgap of the perovskite junction will determine the absorption edge, beyond which photons with higher wavelength will pass through the material, their energy insufficient to overcome the bandgap. A lower perovskite bandgap will therefore lead to a higher photocurrent in the top cell because more photons can be absorbed. The optimisation of the perovskite bandgap is therefore a crucial step in designing a tandem solar cell to achieve current matching between the top and bottom absorbers [103]. In 4 terminal tandem solar cells the two subcells are electrical independent and therefore do not require current matching and the bandgap is therefore a less critical design choice.

Solar cells are often tested and subsequently optimised using a standardized light spectrum called AM1.5g. This gives a good indication of the expected performance for single junction solar cells, however for 2T tandem solar cells outdoor results can significantly differ [31]. Over the course of the day and different cloud conditions the spectral distribution of light can vary significantly. These changes in spectral distribution can have an impact on the optimal bandgap of a tandem solar cell. We therefore model the solar cell performance using typical meteorological year (TMY) spectral data from the NSRDB to have a more realistic estimation of the bandgap effects.

In this journal paper we investigate the potential effects of bifacial illumination and luminescent coupling on the design of tandem solar cells. By using a silicon subcell that is capable of bifacial power conversation the tandem will also be capable of utilising light from the backside. As the bottom cell has a lower bandgap, all light from the backside will be exclusively absorbed in the bottom absorber. Depending on

the electrical wiring in a 2T or 4T setup this will have a strong impact on the design requirements of the perovskite top cell. The current matching requirement in a 2T tandem will require a higher absorption share in the top cell of light from the front side in a bifacial compared to a monofacial setup. Luminescent coupling is an effect well known from multijunction solar cells[84], [104]. Recombination of electron hole pairs in the top cell can lead to generation of photons that potentially can be absorbed in the bottom cell. From an optical perspective most photons that are generated in the top cell will be absorbed in the bottom cell because of the contrast of the refractive index towards the top and bottom. Perovskites have a higher refractive index compared to the air above the cell. Because the generation of photons by luminescent recombination can be assumed to be isotropic[105], many photons will be emitted into directions that will undergo total internal reflection on the top side of the cell. Because silicon has a higher refractive index than perovskite there is no total internal reflection for light emitted in the top cell towards the bottom cell, while light that is reflected at the top interface can further travel into the silicon as well. Both, luminescent coupling and bifacial operation can have an influence on the optimal bandgap on the perovskite because they increase the photocurrent in the silicon bottom cell. In this work we quantify the impact on the optimal bandgap for different levels of luminescent coupling efficiencies and ground albedo. The simulated tandem solar cells are idealized to investigate general trends without the results being tied to specific cell architectures. We find that both effects allow for lower perovskite bandgaps in 2T configurations compared to tandem solar cells with monofacial illumination and without the consideration of luminescent coupling.

#### *Supporting information*

The supporting information document published with this manuscript can be accessed under <https://doi.org/10.1002/solr.202000628>

# Perovskite/Silicon Tandem Solar Cells: Effect of Luminescent Coupling and Bifaciality

Klaus Jäger,\* Peter Tillmann, Eugene A. Katz, and Christiane Becker

The power conversion efficiency of the market-dominating silicon photovoltaics approaches its theoretical limit. Bifacial solar operation with harvesting additional light impinging on the module back and the perovskite/silicon tandem device architecture are among the most promising approaches for further increasing the energy yield from a limited area. Herein, the energy output of perovskite/silicon tandem solar cells in monofacial and bifacial operation is calculated, for the first time considering luminescent coupling (LC) between two sub-cells. For energy yield calculations, idealized solar cells are studied at both standard testing as well as realistic weather conditions in combination with a detailed illumination model for periodic solar panel arrays. Typical experimental photoluminescent quantum yield values reveal that more than 50% of excess electron–hole pairs in the perovskite top cell can be utilized by the silicon bottom cell by means of LC. As a result, LC strongly relaxes the constraints on the top-cell bandgap in monolithic tandem devices. In combination with bifacial operation, the optimum perovskite bandgap shifts from 1.71 eV to the range 1.60–1.65 eV, where already high-quality perovskite materials exist. The results are very important for developing optimal perovskite materials for tandem solar cells.

## 1. Introduction

Monofacial silicon solar cells currently dominate the photovoltaic (PV) market.<sup>[1]</sup> Their practical efficiencies meanwhile approach the theoretical limit of around 29.4%,<sup>[2]</sup> such that innovative

technologies and concepts are required to increase the energy yield on limited areas. One approach is using bifacial solar systems that not only utilize light, which falls onto the front side of the PV module, but also light reach the back side,<sup>[3,4]</sup> as shown in Figure 1. Bifacial PV power plants demonstrated >20% enhanced annual energy yield in comparison to a monofacial power plant of a similar size.<sup>[5]</sup> Modern silicon solar cell concepts with passivated emitter rear contact (PERC), heterojunction (SHJ), or integrated back contact (IBC) enable bifacial solar cell operation at low additional cost. Due to these reasons, the International Technology Roadmap for Photovoltaics predicts nearly 70% market share for bifacial solar cells in 2030.<sup>[1]</sup>

A second method to increase the energy output from a PV system on limited area is the multi-junction approach where multiple solar cells with different bandgaps are stacked on top of each other. These different materials exhibit complementary


electronic bandgaps such that the high-energy photons of solar irradiation are absorbed by the high-bandgap materials on top, whereas the low-energy photons are absorbed by the lower bandgap material at the bottom. As a result, the excess photon energy losses are reduced and conversion efficiencies increase, significantly overcoming the efficiency limit of silicon single-junction solar cells.

A currently widely investigated technology for large-scale applications is the combination of silicon and perovskite solar cells in a tandem device.<sup>[6]</sup> High efficiencies, a tunable bandgap, external photoluminescent quantum yields up to 10%<sup>[7]</sup> and low-cost fabrication processes make perovskites an attractive tandem partner for established silicon PVs. The current record efficiencies for perovskite/silicon tandem solar cells are 29.15%<sup>[8]</sup> for monolithic two-terminal (2T) and 28.2%<sup>[9]</sup> for stacked four-terminal (4T) devices, respectively, bearing the potential for power conversion efficiencies (PCEs) as high as  $\approx 44\%$ <sup>[10]</sup> assuming radiative recombination the only recombination channel and standard test conditions (STC), i.e., 25 °C temperature and 1000 W m<sup>-2</sup> solar irradiance with AM1.5g spectral distribution.<sup>[11]</sup> The monolithic tandem configuration has (among others) the advantage of requiring only two external contacts and one maximum power point (MPP) tracker, enabling module-related costs comparable to single-junction devices.<sup>[12]</sup> Under STC, the theoretical power output of silicon-based monolithic tandem solar cells, however, reveals a sharp maximum at a

Dr. K. Jäger, P. Tillmann, Prof. C. Becker  
Department Optics for Solar Energy  
Helmholtz-Zentrum Berlin für Materialien und Energie GmbH  
Albert-Einstein-Straße 16, Berlin 12489, Germany  
E-mail: klaus.jaeger@helmholtz-berlin.de

Dr. K. Jäger, P. Tillmann  
Computational Nano Optics  
Zuse Institute Berlin  
Takustraße 7, Berlin 14195, Germany

Prof. E. A. Katz  
Department of Solar Energy and Environmental Physics  
The Jacob Blaustein Institutes for Desert Research  
Ben-Gurion University of the Negev  
Sede Boqer Campus, Beersheba 8499000, Israel

 The ORCID identification number(s) for the author(s) of this article can be found under <https://doi.org/10.1002/solr.202000628>.

© 2021 The Authors. Solar RRL published by Wiley-VCH GmbH. This is an open access article under the terms of the Creative Commons Attribution License, which permits use, distribution and reproduction in any medium, provided the original work is properly cited.

DOI: 10.1002/solr.202000628

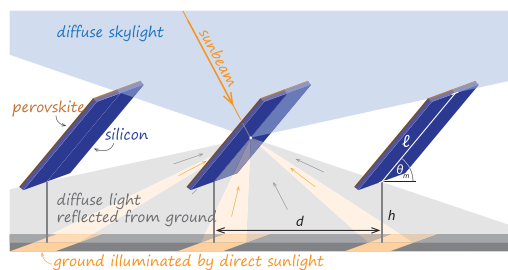


**Figure 1.** Illustrating the illumination components reaching a bifacial solar module in a large PV field: both the front and back sides can be illuminated by direct sunlight, diffuse skylight, and light from the ground, which can originate from direct sunlight or diffuse skylight. The PVs field is characterized by the module length  $l$ , height of the modules above the ground  $h$ , module tilt angle  $\theta_m$ , distance between rows of modules  $d$ , and albedo of the ground  $A$ .<sup>[29]</sup>

top-cell bandgap around 1.71 eV, limiting the choice of available perovskite top cell materials. The reason for the sharp optimum is the current matching requirement in a monolithic series-connected tandem device, i.e., the top cell bandgap has to be tuned such that the numbers of generated electrons are the same for the top cell and the bottom cell. However, perovskites with bandgaps above 1.7 eV often suffer from low electronic quality resulting in reduced solar-cell efficiencies.<sup>[13]</sup>

Recently, bifacial perovskite/silicon tandem solar cells were extensively investigated.<sup>[14–18]</sup> In particular, Onno et al. found that the range of appropriate top-cell bandgaps broadens in a bifacial tandem-cell configuration.<sup>[15]</sup> This is in line with thermodynamic consideration by Khan et al.<sup>[19]</sup> Additional photons absorbed in the silicon bottom cell from rear-side illumination allow for a lower bandgap of the (perovskite) top cell at current-matching conditions.

One aspect of perovskite-based tandem PV operation has not been considered so far: luminescent (or radiative) coupling between the different subcells in the device, i.e., the reabsorption of luminescent photons emitted by the high-bandgap top cell in the low-bandgap bottom cell. This effect is well-known in multi-junction solar cells based on III–V semiconductors where luminescent-coupling efficiencies above 30% were reported.<sup>[20]</sup> Already in 2002, Brown and Green identified luminescent coupling (LC) as a means to reduce spectral mismatch in 2T tandem solar cells.<sup>[21]</sup> Although the effect of LC is negligible at current-matching conditions, a considerable positive effect appears in noncurrent-matched, bottom-cell limited devices.<sup>[22–25]</sup> Similar to bifacial cell operation LC, i.e., the reabsorption of luminescent photons emitted by the high-bandgap cell in the low-bandgap cell, results in more photons absorbed in the silicon bottom cell, as shown in **Figure 2a**. To the best of our knowledge, LC has not been investigated experimentally for perovskite-based multi-junction solar cells yet.

In this study, we theoretically investigate how bifacial illumination and LC affect the performance of perovskite/silicon tandem solar cells. We use idealized solar-cell models for these calculations: Shockley–Queisser's (SQ) detailed balance limit<sup>[26]</sup> for the perovskite top cell and the Richter limit<sup>[2]</sup> for the silicon

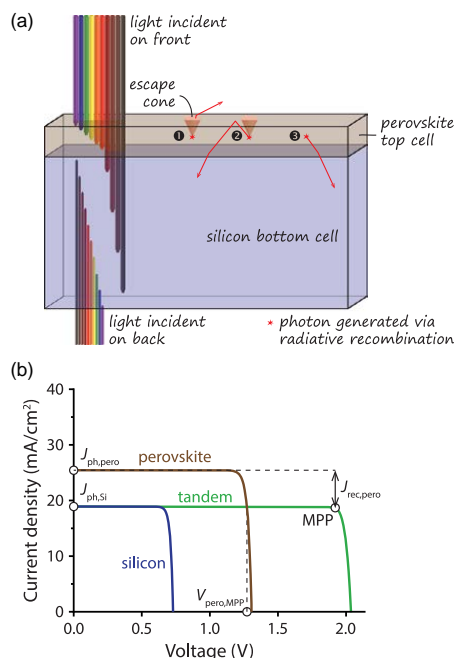


**Figure 2.** a) Illustrating LC in a perovskite/silicon tandem solar cell. A photon, which is generated in the perovskite top cell via radiative recombination can 1) either leave the perovskite cell if its direction is within the escape cone, or 2) it undergoes total internal reflection and is redirected downward such that it can enter the silicon cell, just as 3) a photon that is emitted into the lower hemisphere. More details can be found in Section S3, Supporting Information. b) An example for  $J$ – $V$  curves of a bottom-cell limited tandem cell (green) and the perovskite (brown) and silicon (blue) subcells illuminated under STC. Here, the perovskite is simulated with a bandgap of 1.6 eV and generates a higher photocurrent density  $J_{ph,pero}$  than the silicon subcell with  $J_{ph,Si}$ . At the MPP of the tandem cell, significantly less current density is extracted from the perovskite cell than generated. The excess current density  $J_{rec,pero}$  can be reutilized via LC to increase the photocurrent density of the silicon subcell.

bottom cell, which also incorporates Auger recombination. For the perovskite cell operation under one Sun, Auger recombination is negligible.<sup>[27]</sup> Using these models, we first assess how illumination from the back side and LC affect the tandem-cell performance under STCs. Then, we use optical simulations<sup>[28]</sup> to estimate how much of light from radiative recombination in the perovskite leaves the cell toward the Sun in a single-junction cell configuration and how much will reach the silicon subcell in a tandem stack. This allows us to relate measured external quantum photoluminescence efficiency in a single-junction perovskite cell to the reasonable internal quantum efficiency, and subsequently to evaluate which range of luminescent-coupling efficiencies is realistic in tandem devices. Finally, we estimate the energy yield using weather data from a climatic zone with high diffuse illumination ratio. For this, we apply a detailed illumination model, which takes direct sunlight, diffuse skylight, shadowing by other modules and reflection from the ground into consideration.<sup>[29]</sup> We finally

discuss how all the realistic deviations from STCs considered in this study—1) bifacial irradiation, 2) LC, and 3) weather conditions with high diffuse illumination ratio—influence the constraints for the perovskite top cell bandgap.

## 2. Modeling Details

### 2.1. Electrical Solar Cell Model

To calculate the current density–voltage ( $J$ – $V$ ) characteristic of the PV modules, the irradiance values on the front and back sides are used as input for the electrical model. In this article, we use highly idealized solar cell models:

For the perovskite top cell, we assume that all photons with energy higher than the cell bandgap are absorbed and every absorbed photon generates one electron–hole pair. Hence, the maximum achievable photocurrent density is given by

$$J_{\text{ph,pero}} = e \int_0^{\lambda_{\text{pero}}} \Phi_f(\lambda) d\lambda \quad (1)$$

where  $e$  is the elementary charge,  $\Phi_f$  is the photon flux reaching the module at the front, and  $\lambda_{\text{pero}}$  is the wavelength corresponding to the perovskite bandgap. In a monolithic tandem device, this value is only achieved in case of a limiting top cell, i.e., less or equal photons absorbed in the perovskite than in the silicon. The  $J$ – $V$  characteristic is calculated according to the SQ limit,<sup>[26]</sup> where only radiative recombination is considered. In the SQ limit, both external (ELQE) and internal (ILQE) luminescence quantum efficiencies are equal to 100%. The former is the number of photons emitted into free space relative to the number of electron–hole pairs generated by light absorption in a solar cell. The latter is a ratio between the number of electron–hole pairs recombined radiatively to the entire number of the recombined pairs. The SQ limit is briefly summarized in Section S1, Supporting Information.

For the silicon bottom cell, the perovskite top-cell acts as a filter for the short wavelengths up to the perovskite bandgap. However, the perovskite cell also may emit light, which can be utilized by the bottom cell via LC, which is discussed later. In addition, Auger recombination must be considered for a silicon cell. We implement this using an idealized model by Richter et al.;<sup>[2]</sup> the details are given in the Section S2, Supporting Information.

In a high-end solar cell made of a direct bandgap semiconductor, a significant fraction of the absorbed photons, which are not extracted as electrical current, will be re-emitted as light via radiative recombination. An electrically independent solar cell operated at MPP only has a small recombination current because almost all charge carriers are extracted. However, in a 2 T tandem cell, where the top and bottom cells are electrically connected in series, the same current density flows through bottom and top cell. If the generated photocurrent density and the extracted current density deviate strongly from each other, as shown in Figure 2b, significant recombination will be present in the top cell. If the recombination is radiative, the re-emitted light from the top cell can be absorbed and utilized by the bottom cell, which is known as LC. In perovskite/silicon tandem solar cells, we only need to consider light emitted by the perovskite cell, which can

be absorbed by the silicon bottom. The silicon cell itself will hardly emit light because of the indirect bandgap of silicon. Furthermore, the energy of the emitted photons would be close to the silicon bandgap and hence cannot be absorbed by perovskite with a larger bandgap than silicon. For the maximum achievable short-circuit current density in the Si bottom cell, we find

$$J_{\text{ph,Si}}(V_{\text{pero}}) = e \int_{\lambda_{\text{pero}}}^{\lambda_{\text{Si}}} A(\lambda) \Phi_f(\lambda) d\lambda + e \int_0^{\lambda_{\text{Si}}} A(\lambda) \Phi_b(\lambda) d\lambda + \eta_{\text{LC}} [J_{\text{ph,pero}} - J_{\text{pero}}(V_{\text{pero}})] \quad (2)$$

with the absorption in silicon  $A(\lambda)$ , which we calculate according to the Tiedje–Yablonovitch limit for a silicon wafer thickness of 300  $\mu\text{m}$  as described in Section S2, Supporting Information.  $J_{\text{pero}}(V_{\text{pero}})$  is the current density at the working point of the perovskite cell. The term  $[J_{\text{ph,pero}} - J_{\text{pero}}(V_{\text{pero}})]$  corresponds to excess electron–hole pairs generated in the perovskite top cell, which cannot be extracted from the monolithic tandem device, e.g., due to a limiting bottom cell. These excess electron–hole pairs can recombine radiatively and be reabsorbed by the silicon with  $\eta_{\text{LC}}$  being the efficiency of this LC. Here, we also accounted for light that hits the solar cell at the back,  $\Phi_b$ . For monofacial cells, we have  $\Phi_b \equiv 0$ . Furthermore,  $\lambda_{\text{Si}}$  is the wavelength corresponding to the silicon bandgap. More details about LC are given in the Section S3, Supporting Information.

As we assume zero series resistance and infinitely large shunt resistance of the cells, for both subcells the electric current density  $J$  can be directly calculated from the photocurrent density  $J_{\text{ph}}$  and the voltage-dependent recombination current density  $J_{\text{rec}}$

$$J = J_{\text{ph}} - J_{\text{rec}}(V) \quad (3)$$

where details about  $J_{\text{rec}}$  for the perovskite and silicon subcells are given in Section S1 and S2, Supporting Information, respectively.

For 2 T cells, where the same current density flows through both cells, we have

$$J_{\text{cell}} = J_{\text{ph,Si}} - J_{\text{rec,Si}}(V_{\text{Si}}) = J_{\text{ph,pero}} - J_{\text{rec,pero}}(V_{\text{pero}}) \quad (4)$$

We calculate the  $J$ – $V$  characteristic of the tandem solar cell by numerically inverting the expressions  $J_{\text{rec,Si}}(V_{\text{Si}})$  and  $J_{\text{rec,pero}}(V_{\text{pero}})$  such that we have functions of  $J_{\text{rec,pero}}$  and  $J_{\text{rec,Si}}$ , respectively. From the  $J$ – $V$  curve, the output power density of the cell can be directly calculated as

$$P_{\text{cell}} = J_{\text{cell}} [V_{\text{Si}}(J_{\text{rec,Si}}) + V_{\text{pero}}(J_{\text{rec,pero}})] \quad (5)$$

$$P_{\text{mpp}} = \max_{J_{\text{cell}}} (P_{\text{cell}})$$

Tandem solar cells can also be built in 4 T configuration, where the two subcells are electrically independent and can operate at their individual MPPs

$$P_{\text{mpp}} = \max_{J_{\text{Si}}} [J_{\text{Si}} \cdot V_{\text{Si}}(J_{\text{rec,Si}})] + \max_{J_{\text{pero}}} [J_{\text{pero}} \cdot V_{\text{pero}}(J_{\text{rec,pero}})] \quad (6)$$

## 2.2. Optical Model

To estimate the effect of LC in realistic perovskite-tandem solar cells, we apply optical modeling. In this article, we use the MATLAB-based tool GenPro4, which can calculate the absorption profile in solar-cell structures using the net radiation method.<sup>[28]</sup> This tool treats light coherently in thin layers but incoherently in thick layers. Because GenPro4 only can treat light that falls onto a layer stack from the exterior, we split the simulations in two: one simulation treating the layer stack above the perovskite layer, the other layer stack treating the layers below. Details on these calculations are given in Section S4, Supporting Information.

## 2.3. Energy Yield Calculation

We calculate the overall energy yield for different scenarios using a simulation approach that combines several sub-models. For calculating the spectral irradiance at the front and back sides of a solar module in a big PV field, we use a recently developed illumination model.<sup>[29,30]</sup> The PV field is considered so large that boundary effects can be neglected. As schematically illustrated in Figure 1, the illumination model considers four components reaching the module front: direct sunlight, diffuse skylight, diffuse light from the ground, which originates from direct sunlight reaching the ground and diffuse skylight reaching the ground. Furthermore, the same four components must be considered reaching the back-side of the module. Hence the illumination model considers eight components in total.

The illumination model uses the following input parameters: first, the geometrical parameters of the PV field, which are shown in Figure 1: module length  $\ell$ , mounting height  $h$ , module spacing  $d$ , and tilt angle  $\theta_m$ . Second, the albedo (i.e., the reflectivity) of the ground, which is highly dependent on the material properties of the ground. Although grass typically exhibits albedo values around 20%, gray and white gravel have albedo values of 30% and 50%, respectively, and snow reaches albedo values up to 70%.<sup>[31]</sup> In this work, we assume the albedo to be independent of the wavelength with  $A = 30\%$ , which is a rather conservative estimate with realistic room for improvement. Third, the (spectral) direct normal incidence (DNI) and the diffuse horizontal incidence (DHI) for different instants of time. We retrieve these data from the National Solar Radiation Data Base (NSRDB) operated by NREL.<sup>[32]</sup> They publish hourly spectral direct and diffuse irradiance for a typical meteorological year (TMY).

With the spectral irradiance on the front and back sides, we can calculate the generated photocurrent densities in the top and bottom cells using Equation (1) and (2). We calculate the full  $J-V$  characteristics for every hour in the TMY data set and take the appropriate maximum to get the maximum power output of the cell according to Equation (S14) and (S15), Supporting Information. By integrating over all hourly data points in the data set for one year, we obtain the annual energy yield.

## 3. Results and Discussion

### 3.1. Tandem-Cell Operation Under Standard Testing Conditions

Figure 3 shows the effect of the top cell bandgap on the maximum output power density of a 2T tandem solar cell for various levels of a) backside illumination and b) LC under standard testing conditions. Without either backside illumination or LC, the optimal bandgap of the perovskite cell for maximum power

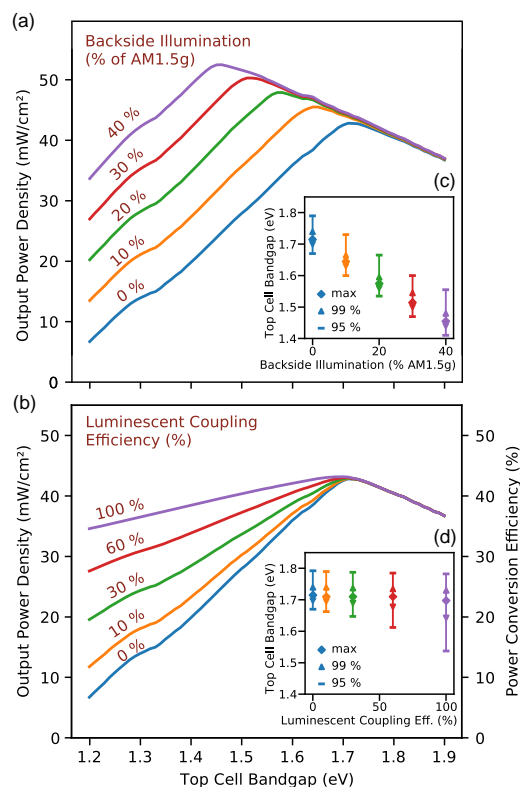


**Figure 3.** Maximum output power density of 2T tandem solar cells as function of the top-cell bandgap for different levels of a) backside illumination and b) LC efficiencies under STCs. The insets show the optimal top-cell bandgap for different levels of c) backside illumination and d) LC efficiencies under STCs. The diamonds mark the ideal bandgap with maximum power output; the arrowheads and the dash marks span the ranges where at least 99% and 95% of the maximum output power density are achieved. Note: For the graph with varying backside illumination, no LC is assumed, and for varying LC efficiencies, no backside illumination is present. The bottom cell bandgap is 1.12 eV in all cases. For bifacial solar cells we use the output power density instead of the power conversion efficiency, because the power density of the light illuminating the solar cell, depends on the assumed albedo.



output density is 1.71 eV, where the same current densities are generated in the top and bottom cells. For other top-cell bandgaps, the generated current densities differ from each other. Only the lower current density can flow through the solar cell, while the excess current density is lost, which reduces the overall PCE of the tandem solar cell. For a silicon-based tandem solar cell, the bandgap of the top cell absorber is critical to achieve current matching between the subcells. For a top-cell bandgap higher than the optimum, the current density generated in the top cell is below that generated in the bottom cell; the tandem cell is said to be “top-cell limited”. For a top-cell bandgap lower than the optimum, the bottom-cell current density is lower; the cell is “bottom-cell limited”.

With higher levels of backside illumination, as shown in Figure 3a, the maximum power output density increases and the optimum top-cell bandgap shifts toward lower bandgaps. The backside illumination is exclusively absorbed in the bottom cell and cannot reach the top cell, leading to more generated electron–hole pairs in the bottom-cell. To match the photocurrent densities between the two subcells, the top-cell bandgap needs to be lowered, such that it can absorb more light. For top-cell bandgaps larger than 1.71 eV, increased back-side illumination hardly affects the overall output power density, because here the tandem device is top-cell limited and the additional photocurrent generated in the bottom cell cannot be utilized.

As shown in Figure 3b, increasing the LC efficiency does not shift the position and height of the maximum output power density; however, the power output is increased for bandgaps below the optimum. For top-cell bandgaps above the optimum, LC does not affect the performance, because here the cells are top-cell limited and the excess current in the bottom cell cannot be utilized for LC.

Figure 3c,d summarize these results. For a given scenario of backside illumination or LC, the optimal bandgap and the range of 99% and 95% of the maximum output power density are shown. With increasing backside illumination, the optimal top-cell bandgap shifts to lower values, while sensitivity is unchanged. For LC, the optimal bandgap remains unchanged, but the 99%- and 95% bands broaden toward lower bandgaps.

### 3.2. Estimating Reasonable Values of Luminescent-Coupling Efficiency

Now, as we have studied how LC can improve the performance of bottom-cell limited tandem solar cells (see Figure 3b,d), we investigate, which LC efficiencies are realistic in perovskite/silicon tandem solar cells from an optical point of view.

Increasing the PCE of solar cells toward the theoretical limit can be realized by improving the ELQE of the cell in open circuit (OC), or in the other words—by suppressing non-radiative recombination.<sup>[33,34]</sup> Despite the direct bandgap of metal halide perovskite semiconductors, initially reported ELQE values for perovskite solar cells were extremely low ( $\approx 10^{-4}\%$ ).<sup>[35]</sup> Then, tremendous growth was demonstrated for perovskite solar cells reaching an ELQE of 0.5%.<sup>[36]</sup> which is equal to the record for silicon cells.<sup>[37]</sup> Recently, Liu et al. realized a single-junction perovskite solar cell with 8.4% ELQE<sup>[7]</sup>. Note that record ELQE values of the champion GaAs cells do not exceed 25%,<sup>[38,39]</sup> even

though ILQE values of 99.7% have experimentally been shown for GaAs devices.<sup>[40]</sup>

As a first step to estimate the LC efficiency for a cell with the experimentally measured 8.4% ELQE, we calculate the fraction  $E_i^{\text{int}}$  of light generated in the perovskite layer, which leaves the solar cell structure, using the optical simulation tool GenPro4. We assume a perovskite thickness of 400 nm and an emission wavelength of 795 nm, which corresponds to the bandgap of the perovskite methylammonium lead iodide (MAPbI<sub>3</sub>) of 1.56 eV, in accordance with the device architecture used by Liu et al.<sup>[7]</sup> As shown in the Section S4, Supporting Information, we revealed  $E_i^{\text{int}} = 7.8\%$  for this configuration, which is independent of the emission depths in the perovskite layer. The rest of the generated light cannot leave the solar cell structure, because it either radiates in directions outside the emission cone, which has an opening angle of 23.8° for MAPbI<sub>3</sub> at 795 nm,<sup>[41]</sup> or it is absorbed before it can leave the solar cell. The experimental ELQE (8.4%) being larger than the numerical value  $E_i^{\text{int}} = 7.8\%$  shows that a high ILQE was achieved. For semiconductors with high ILQE, photon recycling,<sup>[42]</sup> i.e., the reabsorption of previously emitted photons within the perovskite, can increase the ELQE to values higher than what would be expected from the optical simulations, where photon recycling was neglected.<sup>[43]</sup> An experimental proof of internal photon recycling in perovskite solar cells was given by Pazos–Outón et al.<sup>[44]</sup> Furthermore, Braly et al. demonstrated perovskite films with 90% ILQE.<sup>[45]</sup>

We can estimate the ILQE using a simple model for a cell in open-circuit condition where the charge carriers created by the external light source can undergo a chain of emission and reabsorption events. In a first step, the charge carriers can either recombine radiatively with probability ILQE or nonradiatively with probability  $(1 - \text{ILQE})$ . In the next step, the emitted photons can either leave the cell with probability  $E_i^{\text{int}}$ , be absorbed parasitically in nonactive areas with probability  $A_{\text{para}}$  or reabsorbed in the perovskite with probability  $A_{\text{pero}} = 1 - E_i^{\text{int}} - A_{\text{para}}$ .  $A_{\text{pero}}$ ,  $E_i^{\text{int}}$ , and  $A_{\text{para}}$  can be extracted from the optical simulations described in the Supporting Information I. The reabsorbed light can undergo the same processes as the directly absorbed light from an external light source. This chain of events can be represented as a geometric series to calculate the ELQE

$$\begin{aligned} \text{ELQE} &= E_i^{\text{int}} \cdot \text{ILQE} [1 + A_{\text{pero}} \cdot \text{ILQE} + (A_{\text{pero}} \cdot \text{ILQE})^2 + \dots] \\ &= \frac{E_i^{\text{int}} \cdot \text{ILQE}}{1 - A_{\text{pero}} \cdot \text{ILQE}} \end{aligned} \quad (7)$$

This function can be inverted to retrieve ILQE

$$\text{ILQE} = \left( \frac{E_i^{\text{int}}}{\text{ELQE}} + A_{\text{pero}} \right)^{-1} \quad (8)$$

Using Equation (8), we estimate the ILQE of the best cell from Liu et al.<sup>[7]</sup> to be around 65%. This is in line with simulations from Cho et al. on perovskite-based light emitting diodes, where they calculate that an ILQE of 60% is sufficient to reach an ELQE equal to the purely optical expectation if photon recycling is considered.<sup>[43]</sup>

Figure 4b shows the perovskite/silicon tandem solar cell structure, which we used to study coupling of emitted light by the

perovskite layer into silicon. This structure is based on recent high-end tandem solar cells,<sup>[46,47]</sup> but in contrast to them, we used MAPbI<sub>3</sub> as perovskite material to be consistent with the single-junction results discussed earlier. For an emission wavelength of 795 nm, 76% of the light generated in perovskite reaches the silicon layer, as shown in Figure 4b. This value is almost independent from the emission depths in the perovskite layer, as shown in the Section S4, Supporting Information. Only 4% of the generated light leave the solar cell structure into air and 17% are reabsorbed in the perovskite layer, which can contribute to photon recycling. More details of the optical tandem-cell simulations are shown in Figure S2, Supporting Information.

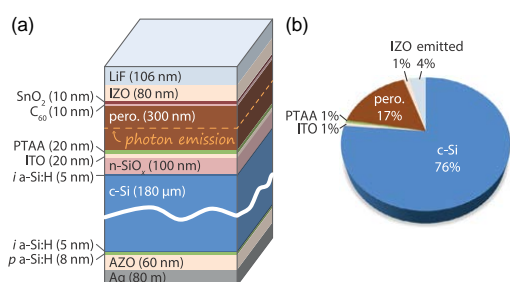


**Figure 4.** a) The tandem solar cell structure used for estimating the fraction of photons, which are generated in the perovskite layer and reach the silicon wafer. The structure is based on recent high-end perovskite/silicon tandem solar cells.<sup>[46,47]</sup> The dotted line indicates the middle of the perovskite layer (150 nm depths). In our calculations, we assumed the light emission from this depth. b) Relative distribution of photons with 795 nm wavelength, which are isotropically emitted in the center of the perovskite layer. Although around 76% are absorbed by the silicon wafer, around 17% are reabsorbed by the emitting perovskite layer. Only  $\approx 4\%$  leave the solar cell structure.

We can estimate an upper bound for the luminescence coupling efficiency  $\eta_{\text{LC}}^{\text{max}}$  by replacing  $E_{\text{int}}^{\text{int}}$  with  $A_{\text{Si}}$  in Equation (7)

$$\eta_{\text{LC}}^{\text{max}} = \frac{A_{\text{Si}} \cdot \text{ILQE}}{1 - A_{\text{pero}} \cdot \text{ILQE}} \quad (9)$$

For estimating  $\eta_{\text{LC}}^{\text{max}}$ , we use the values for 150 nm emission depths, shown in Figure 4b:  $A_{\text{Si}} = 0.763$  and  $A_{\text{pero}} = 0.171$ . Assuming  $\text{ILQE} = 65\%$ , just as for the single-junction cell discussed earlier, we find  $\eta_{\text{LC}}^{\text{max}} \approx 56\%$ . However, it should be noted that Liu et al. measured the ELQE with an illumination of one sun without charge-carrier extraction (open-circuit condition, in which all photo-generated carriers should recombine). When charge carriers are extracted in solar cell operation, the ratio of radiative to nonradiative recombination might change considerably.<sup>[48]</sup> Further research is needed to assess realistic radiative efficiencies at low recombination currents. In any case, we provide a positive answer on the fundamental question: a significant fraction of light emitted by the perovskite sub-cell can reach the silicon wafer. This can change a paradigm in developing optimal perovskite materials for efficient tandem solar cells.

### 3.3. Energy Yield Under Realistic Weather Conditions

Under realistic conditions, the illumination on a solar module in a large PV field consisting of periodic rows of solar panels will significantly differ from standard testing conditions. The spectral distribution and irradiance of light in the outdoors is constantly changing and the illumination on the backside is highly dependent on the layout of the PV field. **Figure 5** shows the result of energy-yield calculations for bifacial and monofacial tandem solar modules for different bandgaps and varying levels of albedo in Seattle, USA and compares the performance of 2T and 4T solar cells. The 4T cells show only a small dependence on the top-cell bandgap with the optimum at the upper limit of the

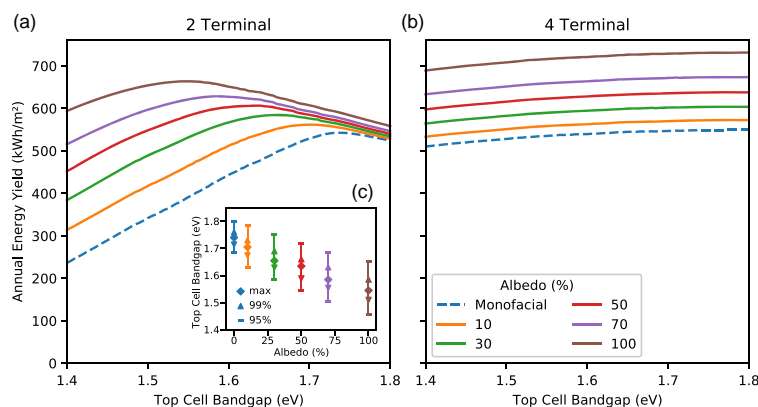


**Figure 5.** Energy yield for bifacial and monofacial tandem power plants simulated for Seattle with a) 2 T and b) 4 T cells connection for different albedo values. The inset c) shows the optimal top-cell bandgap for different levels of albedo. The diamonds mark the ideal bandgap with maximum energy yield; the arrowheads and the dash marks span the ranges where at least 99% and 95% of the maximum energy yield is achieved. All simulations were performed with a module distance  $d = 8$  m and mounting height of  $h = 0.5$  m. The tilt angle was optimized for every data point. Monofacial tandems are simulated with albedo  $A = 0\%$ .

**Table 1.** Results from energy-yield calculations of 2 T tandem cells for different albedo scenarios using average meteorological year data for Seattle with module height  $h = 0.5$  m and module distance  $d = 8$  m.

Type	Albedo [%]	Bifacial gain [%] <sup>a)</sup>	Opt. bandgap [eV]	Energy yield [kWh m <sup>-2</sup> a <sup>-1</sup> ]
Monofacial	0	–	1.74	543
Bifacial	10	5.5	1.70	562
	30	12.7	1.66	584
	50	19.7	1.64	606
	70	27.1	1.59	628
	100	37.4	1.54	664

<sup>a)</sup>“Bifacial Gain” denotes the gain in irradiance.

simulated range (1.8 eV) and a monotonic decrease toward 1.5 eV. Increasing the albedo increases the energy yield but leaves character of the bandgap dependence unchanged.

In contrast, the 2 T cells are strongly affected by changing the top-cell bandgap. Similar to the results for STC (Figure 3a), there is a well-defined maximum for the bandgap with reduced energy yield for higher or lower values. The ideal top cell bandgap for monofacial cells shifts from of 1.71 eV for STC to 1.74 eV for Seattle.

With increasing albedo, the optimal top-cell bandgap shifts to lower values. The additional light impinging onto the backside is exclusively absorbed by the bottom cell. Reducing the bandgap of the top cell will increase their photocurrent density at the cost of the bottom cell. Thus, the two subcells can be made current-matched again by reducing the top-cell bandgap.

**Table 1** summarizes the results from the energy-yield calculations for PV modules with 2 T tandem cells for different albedo values. For a realistic albedo of  $A = 30\%$  corresponding to gray cement,<sup>[49]</sup> the optimal bandgap shows a shift of 0.08 eV with respect to a monofacial cell. In this scenario, the energy yield is increased by 7.5%, which is significantly smaller than the 12.7% gain of irradiance. One reason for the increase in energy yield being smaller than the increase in irradiance is that light reaching the back side can only be utilized with the single-junction PCE of the bottom cell. Furthermore, for 2 T tandem solar cells decreasing the top-cell bandgap to ensure current matching reduces the overall open-circuit voltage and hence the PCE.

However, considering the electronic material quality of state-of-the-art perovskites,<sup>[13]</sup> the effect of bandgap-shift might be relevant. Although in principle organic/inorganic perovskites can be fabricated with continuously tunable bandgaps,<sup>[13,50]</sup> not all bandgap-materials can be fabricated with the same electronic quality. Fabricating high-quality perovskite semiconductors with bandgaps in the range of 1.70–1.75 eV is still a very challenging task and previous results show higher quality semiconductors in the region of 1.60–1.65 eV.<sup>[12]</sup>

Operation of perovskite/silicon tandem solar cells in bifacial configuration allows to utilize 1.60–1.65 eV bandgap perovskites for optimal performance. This enables using current high-quality perovskite absorber layers in the tandem device.

**Figure 6** shows the effect of the top-cell bandgap on the annual energy yield for mono- and bifacial 2 T tandem PV modules simulated for Seattle, USA, with various levels of LC. With an

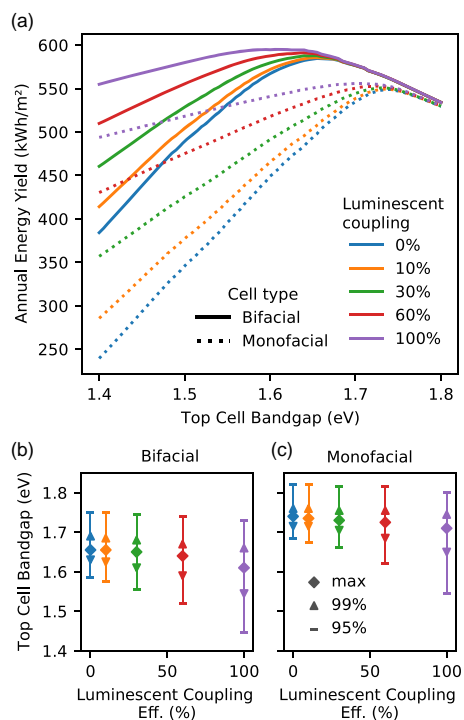


**Figure 6.** a) Annual energy yield for mono- and bifacial 2 T perovskite/silicon tandem solar cell modules simulated for Seattle with various levels of LC. The subfigures shows the optimal top-cell bandgap for different levels of LC of b) bifacial and c) monofacial tandem cells. The diamonds mark the ideal bandgap with maximum energy yield; the arrowheads and the dash marks span the ranges where at least 99% and 95% of the maximum energy yield is achieved. All simulations were performed with a module distance  $d = 8$  m and  $d = 0.5$  m mounting height. Bifacial operation is calculated with albedo  $A = 30\%$ . The module tilt angle  $\theta_m$  was optimized for every data point.

increasing LC efficiency, the energy yield becomes more and more independent from the bandgap of the top cell. Also, the maximum energy yield increases slightly and shifts a bit toward lower bandgaps. As the spectral distribution of outdoor illumination changes with time, there will always be situations where the top or bottom cells generate different photocurrent densities. Therefore, the optimal top-cell bandgap for outdoor performance will always be a compromise, which delivers the best balance over time.<sup>[51]</sup> With increasing LC efficiency, the losses from periods, where the cell is bottom-cell limited, will become smaller, while losses from top-cell limitation are not affected.<sup>[52]</sup> This explains the shift of the optimal bandgap to lower values, where the overall absorption in the top cell is increased. As an example, the energy yield of perovskite/silicon tandem solar cells with 1.64 eV bandgap triple-cation perovskite top cell is found to increase by 21.5% when additionally considering a LC efficiency of 30% and bifacial operation on a 30% reflective ground.

4 T tandem solar cells barely show any performance improvement because of LC, as both subcells are operated individually at their MPP, where only very little radiative recombination is present.

#### 4. Conclusion

In conclusion, we calculated the energy yield of perovskite/silicon tandem solar cells considering LC between the two sub-cells and bifacial illumination of the device. To do so, we first studied idealized solar cells using the SQ limit and Richter's limit for the perovskite and the silicon sub-cells, respectively. We found that additional backside illumination around 10–20% is sufficient to shift the optimum perovskite top-cell bandgap in 2 T tandem solar cells from 1.71 eV to the 1.60–1.64 eV range. We further found that LC can strongly reduce the current-mismatch if the tandem solar cell is bottom-cell limited.

As a second step, we performed optical simulations to evaluate the relevance of LC for perovskite/silicon tandem solar cells. On the basis of experimental photoluminescent quantum yield values, we found that more than 50% of excess electron–hole pairs generated in the perovskite top cell can be reused by the silicon bottom cell. Particularly for configurations with perovskite top-cell bandgaps below the current matching optimum, this significantly enhances the energy yield.

Finally, we performed energy-yield calculations based on typical meteorological year (TMY3) weather data of Seattle, USA, and applied an illumination model considering the spectral irradiance at the front and back sides of a solar module in a big PV field. In agreement with the calculations using standard testing conditions, we found that the operation of perovskite/silicon tandem solar cells in bifacial configuration allows to utilize 1.60–1.65 eV bandgap perovskites for optimal performance and LC further minimizes the impact of current-mismatch in case of (silicon) bottom-cell limited devices, i.e., less photons absorbed in the silicon than in the perovskite absorber layer. The results are very important for developing the optimum perovskite material for tandem solar cells.

#### Supporting Information

Supporting Information is available from the Wiley Online Library or from the author.

#### Acknowledgements

K.J. and P.T. contributed equally to this work. P.T. thanks the Helmholtz Einstein International Berlin Research School in Data Science (HEIBRIDES) for funding. The authors acknowledge the support from the SNaPSHoTs project in the framework of the German–Israeli bilateral R&D cooperation in the field of applied nanotechnology (grant no. 011O1806) funded by the German Federal Ministry for Education and Research (BMBF) and the National Technological Innovation Authority of the State of Israel. The results were obtained at the Berlin Joint Lab for Optical Simulations for Energy Research (BerOSE) and the Helmholtz Excellence Cluster SOLARMATH of Helmholtz-Zentrum Berlin für Materialien und Energie, Zuse Institute Berlin and Freie Universität Berlin. Open access funding enabled and organized by Projekt DEAL.

#### Conflict of Interest

The authors declare no conflict of interest.

#### Keywords

energy yields, luminescent coupling, perovskite/silicon tandem solar cells

Received: October 7, 2020

Revised: December 4, 2020

Published online: December 12, 2020

- [1] ITRPV, 11th edition of the international technology roadmap photovoltaics, Technical report, VDMA, 2020, <https://itrvp.vdma.org> (accessed: August 2020).
- [2] A. Richter, M. Hermle, S. W. Glunz, *IEEE J. Photovolt.* **2013**, *3*, 1184.
- [3] R. Kopecek, J. Libal, *Nat. Energy* **2018**, *3*, 443.
- [4] T. S. Liang, M. Pravettoni, C. Deline, J. S. Stein, R. Kopecek, J. P. Singh, W. Luo, Y. Wang, A. G. Aberle, Y. S. Khoo, *Energy Environ. Sci.* **2019**, *12*, 116.
- [5] N. Ishikawa, S. Nishiyama, presented at *3rd Biji PV Workshop*, Miyazaki, Japan, September 2016.
- [6] J. Werner, B. Niesen, C. Ballif, *Adv. Mater. Interfaces* **2018**, *5*, 1700731.
- [7] Z. Liu, L. Krückemeier, B. Krogmeier, B. Klingebiel, J. A. Márquez, S. Levchenko, S. Öz, S. Mathur, U. Rau, T. Unold, T. Kirchartz, *ACS Energy Letters* **2019**, *4*, 110.
- [8] A. Al-Ashouri, E. Köhnen, B. Li, A. Magomedov, H. Hempel, P. Caprioglio, J. A. Márquez, A. B. M. Vilches, E. Kasparavicius, J. A. Smith, N. Phung, D. Menzel, M. Grischek, L. Kegelmann, D. Skroblin, C. Gollwitzer, T. Malinauskas, M. Jošt, G. Matič, B. Rech, R. Schlatmann, M. Topič, L. Korte, A. Abate, B. Stannowski, D. Neher, M. Stollerfoht, T. Unold, V. Getautis, S. Albrecht, *Science* **2020**, *370*, 1300.
- [9] B. Chen, S.-W. Baek, Y. Hou, E. Aydin, M. D. Bastiani, B. Scheffel, A. Proppe, Z. Huang, M. Wei, Y.-K. Wang, E.-H. Jung, T. G. Allen, E. V. Kerschaver, F. P. G. de Arquer, M. I. Saidaminov, S. Hoogland, S. D. Wolf, E. H. Sargent, *Nat. Commun.* **2020**, *11*, 1257.
- [10] T. Leijtens, K. A. Bush, R. Prasanna, M. D. McGehee, *Nat. Energy* **2018**, *3*, 828.
- [11] IEC:60904-3: Photovoltaic devices – Part 3: Measurement principles for terrestrial photovoltaic (PV) solar devices with reference spectral irradiance data, 2008.
- [12] M. Jošt, L. Kegelmann, L. Korte, S. Albrecht, *Adv. Energy Mater.* **2020**, 1904102.
- [13] E. L. Unger, L. Kegelmann, K. Suchan, D. Sörell, L. Korte, S. Albrecht, *J. Mater. Chem.A* **2017**, *5*, 11401.
- [14] R. Schmagier, M. Langenhorst, J. Lehr, U. Lemmer, B. S. Richards, U. W. Paetzold, *Opt. Express* **2019**, *27*, A507.
- [15] A. Onno, N. Rodkey, A. Asgharzadeh, S. Manzoor, Z. J. Yu, F. Toor, Z. C. Holman, *Joule* **2020**, *4*, 580.
- [16] H. Imran, I. Durrani, M. Kamran, T. M. Abdolkader, M. Faryad, N. Z. Butt, *IEEE J. Photovolt.* **2018**, *8*, 1222.
- [17] O. Dupre, A. Tuomiranta, Q. Jeangros, M. Boccard, P.-J. Alet, C. Ballif, *IEEE J. Photovolt.* **2020**, *10*, 714.
- [18] R. Asadpour, R. V. K. Chavali, M. Ryyan Khan, M. A. Alam, *Appl. Phys. Lett.* **2015**, *106*, 243902.
- [19] M. Ryyan Khan, M. A. Alam, *Appl. Phys. Lett.* **2015**, *107*, 223502.
- [20] A. W. Walker, O. Höhn, D. N. Micha, L. Wagner, H. Helmers, A. W. Bett, F. Dimroth, *J. Photon. Energy* **2015**, *5*, 053087.

- [21] A. Brown, M. Green, in *Conf. Record of the Twenty-Ninth IEEE Photovoltaic Specialists Conf.*, IEEE, Piscataway, NJ **2020**, pp. 868–871.
- [22] M. A. Steiner, J. F. Geisz, *Appl. Phys. Lett.* **2012**, *100*, 251106.
- [23] M. Z. Shvarts, M. A. Mintairov, V. M. Emelyanov, V. V. Evstropov, V. M. Lantratov, N. K. Timoshina, *AIP Conf. Proc.* **2013**, *1556*, 147.
- [24] N. L. A. Chan, T. Thomas, M. Fuhrer, N. J. Ekins-Daukes, *IEEE J. Photovolt.* **2014**, *4*, 1306.
- [25] D. J. Friedman, J. F. Geisz, M. A. Steiner, *IEEE J. Photovolt.* **2014**, *4*, 986.
- [26] W. Shockley, H. J. Queisser, *J. Appl. Phys.* **1961**, *32*, 510.
- [27] Z. Wang, Q. Lin, B. Wenger, M. G. Christoforo, Y.-H. Lin, M. T. Klug, M. B. Johnston, L. M. Herz, H. J. Snaith, *Nat. Energy* **2018**, *3*, 855.
- [28] R. Santbergen, T. Meguro, T. Suezaki, G. Koizumi, K. Yamamoto, M. Zeman, *IEEE J. Photovolt.* **2017**, *7*, 919.
- [29] K. Jäger, P. Tillmann, C. Becker, *Optics Express* **2020**, *28*, 4751.
- [30] P. Tillmann, K. Jäger, C. Becker, *Sustain. Energy Fuels* **2020**, *4*, 254.
- [31] S. Chunduri, M. Schmela, Bifacial solar technology report 2018 edition, Technical report, TaiYang News, **2018**.
- [32] S. Wilcox, W. Marion, Users manual for TMY3 data sets, Technical Report NREL/TP-581-43156, National Renewable Energy Laboratory, **2008**.
- [33] U. Rau, *Phys. Rev. B Condens. Matter Mater. Phys.* **2007**, *76*, 085303.
- [34] O. D. Miller, E. Yablonovitch, S. R. Kurtz, *IEEE J. Photovolt.* **2012**, *2*, 303.
- [35] K. Tvingstedt, O. Malinkiewicz, A. Baumann, C. Deibel, H. J. Snaith, V. Dyakonov, H. J. Bolink, *Sci. Rep.* **2014**, *4*, 1.
- [36] D. Bi, W. Tress, M. I. Dar, P. Gao, J. Luo, C. Renevier, K. Schenk, A. Abate, F. Giordano, J. P. Correa Baena, J. D. Decoppet, S. M. Zakeeruddin, M. K. Nazeeruddin, M. Grätzel, A. Hagfeldt, *Sci. Adv.* **2016**, *2*, e1501170.
- [37] M. A. Green, *Progr. Photovolt. Res. Appl.* **2012**, *20*, 472.
- [38] B. M. Kayes, H. Nie, R. Twist, S. G. Spruytte, F. Reinhardt, I. C. Kizilyalli, G. S. Higashi, in *Conf. Record of the IEEE Photovoltaic Specialists Conf.*, IEEE, Piscataway, NJ **2011**, pp. 000004–000008.
- [39] A. Braun, E. A. Katz, D. Feuermann, B. M. Kayes, J. M. Gordon, *Energy Environ. Sci.* **2013**, *6*, 1499.
- [40] I. Schnitzer, E. Yablonovitch, C. Caneau, T. J. Gmitter, *Appl. Phys. Lett.* **1993**, *62*, 131.
- [41] J. A. Guerra, A. Tejada, L. Korte, L. Kegelmann, J. A. Töfflinger, S. Albrecht, B. Rech, R. Weingärtner, *J. Appl. Phys.* **2017**, *121*, 173104.
- [42] R. Brenes, M. Laitz, J. Jean, D. W. Dequillettes, V. Bulović, *Phys. Rev. Appl.* **2019**, *12*, 014017.
- [43] C. Cho, B. Zhao, G. D. Tainter, J. Y. Lee, R. H. Friend, D. Di, F. Deschler, N. C. Greenham, *Nat. Commun.* **2020**, *11*, 611.
- [44] L. M. Pazos-Outón, M. Szumilo, R. Lamboll, J. M. Richter, M. Crespo-Quesada, M. Abdi-Jalebi, H. J. Beeson, M. Vru ini, M. Alsari, H. J. Snaith, B. Ehrler, R. H. Friend, F. Deschler, *Science* **2016**, *351*, 1430.
- [45] I. L. Braly, D. W. deQuillettes, L. M. Pazos-Outón, S. Burke, M. E. Ziffer, D. S. Ginger, H. W. Hillhouse, *Nat. Photon.* **2018**, *12*, 355.
- [46] M. Jošt, E. Köhnen, A. B. Morales-Vilches, B. Lipovšek, K. Jäger, B. Maccio, A. Al-Ashouri, J. Krč, L. Korte, B. Rech, R. Schlattmann, M. Topič, B. Stannowski, S. Albrecht, *Energy Environ. Sci.* **2018**, *11*, 3511.
- [47] E. Köhnen, M. Jošt, A. B. Morales-Vilches, P. Tockhorn, A. Al-Ashouri, B. Maccio, L. Kegelmann, L. Korte, B. Rech, R. Schlattmann, B. Stannowski, S. Albrecht, *Sustain. Energy Fuels* **2019**, *3*, 1995.
- [48] J. Jia, Y. Miao, Y. Kang, Y. Huo, M. Mazouchi, Y. Chen, L. Zhao, H. Deng, P. Supaniratisai, S. H. AlQahtani, J. S. Harris, *Opt. Express* **2015**, *23*, A219.
- [49] R. Levinson, H. Akbari, *Cement Concrete Res.* **2002**, *32*, 1679.
- [50] G. E. Eperon, S. D. Stranks, C. Menelaou, M. B. Johnston, L. M. Herz, H. J. Snaith, *Energy Environ. Sci.* **2014**, *7*, 982.
- [51] M. T. Hörantner, H. J. Snaith, *Energy Environ. Sci.* **2017**, *10*, 1983.
- [52] B. M. Yu Jeco, K. Yoshida, R. Tamaki, N. Ahsan, Y. Okada, in *33rd European Photovoltaic Solar Energy Conf. and Exhibition*, WIP, München, Germany **2017**, pp. 1236–1240.



## Chapter 5

# Validated model-chain for energy yield calculations

While the usage of idealised solar cells for simulations can help to identify general trends they have limited value in calculating realistic energy yield estimations. The highest efficiency for a perovskite/silicon tandem solar cell measured until now is 29.8% [24], still significantly lower than the theoretical limit of 42% [18]. For a realistic estimation of a solar cell performance effects of parasitic absorption, reflection losses, non-radiative recombination and temperature need to be considered [35]. This requires the interaction of several simulation steps containing a tool for irradiance on the module, optical response of the solar cell and electrical characteristics. While there are numerous studies investigating the potential energy yield of perovskite/silicon tandem solar cells, only few studies have outdoor data to validate their models. Although outdoor performance data is already scarce for monofacial tandem solar cells, only one study has reported outdoor measurements of bifacial perovskite/silicon tandem solar cells [106]. Bifacial solar cells add the additional challenge that they are typically mounted in rows of solar panels, while small area solar cells from academic research are often installed on test benches on rooftops. Because the irradiance on the backside of a solar cell is strongly dependent on the surrounding geometries it remains unclear how realistic these kinds of test scenarios are for bifacial tandem solar cells. With this work we try to bridge the gap between unvalidated energy yield estimations and missing outdoor performance data by utilising available data from single junction silicon solar cells to validate our simulation tools. The company SolAround provided solar cell performance and irradiance data for 3 days (2 sunny, 1 cloudy) for a rooftop installation in Jerusalem, Israel. The installation contains several rows of mono- and bifacial solar cells in a geometry closely resembling solar panel arrays typically seen in large PV power plants. Additionally, the cell temperatures of the solar cells is measured at the backside of the modules, allowing for an accurate modelling of their electrical characteristics.

For this work we combine our illumination model for irradiance of bifacial solar cells, the optical response of the cell in terms of reflectance and absorptance is simulated with GenPro4 [60] and finally a simple one-diode model is used as the electrical model. We show that the short circuit current generated by a solar cell is highly linear with the irradiance on the module front, with spectral effects and temperature exhibiting no significant effects. After simulating the irradiance on the front and back side with the illumination model we convert the irradiance into the module current by multiplying with the STC rated short circuit current. Using this simple approach the illumination model is validated and we find good agreement between simulation and measurement. We further use the available data of short circuit current, fill factor, open circuit voltage and maximum power measured for the rooftop mounted solar

panels to validate our optical simulation based on Genpro4 and the electrical model based on a temperature dependent one-diode model equivalent circuit.

subsequently, in the second part of the manuscript the model-chain is used to estimate the performance of bifacial perovskite/silicon tandem solar cells for realistic operation conditions. With the previous validation steps we could increase our confidence in the modelling results and can conferme several previously reported trends in our works[107] and studies from De Bastiani *et al.*[106] and Onno *et al.*[108]. The trend for lower optimal perovskite bandgaps under bifacial operation is noteworthy, because it allows the utilisation of perovskite composition that showed better optoelectronic properties and long term stability[103][109].

#### *Supporting information*

The supporting information document published with this manuscript can be accessed under <https://doi.org/10.1002/solr.202200079>



# Model-Chain Validation for Estimating the Energy Yield of Bifacial Perovskite/Silicon Tandem Solar Cells

Peter Tillmann, Klaus Jäger, Asher Karsenti, Lev Kreinin, and Christiane Becker\*

The power conversion efficiency of conventional silicon solar cells approaches its theoretical limit. Bifacial operation and the perovskite/silicon tandem device architecture are promising approaches for increasing the energy yield of photovoltaic modules. Here, an energy yield calculation tool for (bifacial) perovskite/silicon tandem solar cells is presented. It uses a chain of models for irradiance, optical absorption, and temperature-dependent electrical performance. Each step is validated with irradiance and performance data from a rooftop installation with mono- and bifacial silicon solar cells in Jerusalem, Israel. Selecting the data for two days (one in summer, one in winter) and considering the high-reflective ground of this particular installation (albedo 60%) a 20% increased energy yield for a bifacial module with respect to a monofacial module is modeled. This result matches well with experimental data. When “upgrading” the silicon solar cell to a perovskite/silicon tandem solar cell, the case study predicts up to 40% additional energy yield. Combining the concepts of bifacial solar operation and perovskite/silicon tandem solar cells results in up to 60% increased energy with a high albedo ground, and is therefore a promising approach to further decrease the levelized cost of electricity for photovoltaic electricity generation.

Technology Roadmap for Photovoltaics revised the prediction on market share for bifacial cell technology for a certain date upwards year by year and meanwhile predicts a share of more than 75% bifacial cells in 2031.<sup>[3]</sup> Particularly passivated emitter rear cell (PERC) and rear totally diffused (PERT) silicon cells allow for bifacial operation, and hence more power generation at nearly zero additional costs. This enables the reduction of the levelized cost of electricity (LCOE) at a fast pace<sup>[4]</sup> and opens up new application fields such as agricultural PV<sup>[5]</sup> and floating PV.<sup>[6]</sup>

Accurate modeling of the energy yield of bifacial solar power plants is of utmost importance as it allows to estimate the LCOE at a certain location, which is a crucial figure-of-merit to judge the bankability of planned solar power plants. Modeling the energy yield from monofacial solar modules based on weather data, such as direct and diffuse solar irradiance, temperature, wind speed, and the geometrical arrangement and surroundings of the module, has been well-developed in the past decades. However, modeling the rear-side irradiance on a solar module is still regarded as challenging,<sup>[7]</sup> particularly on so-called “variable” days with quickly changing cloud coverage, and more general, on shorter time scales.<sup>[8]</sup> The reason is that the rear side of a solar module mainly receives light reflected from the ground with a timely variable pattern of directly illuminated and shadowed areas seeing more or less from the diffuse skylight. In 2019, Pelaez et al. compared five different bifacial illumination models<sup>[9]</sup> either based on ray tracing,<sup>[10]</sup> a view factor model,<sup>[11]</sup> or an empirical model based on a large amount of field data,<sup>[12]</sup> all predicting the front and irradiance on sunny days within reasonable errors. However, when taking the next step toward multijunction solar cells one has to look more closely and accurate modeling of bifacial irradiance at short time scales becomes even more important.

In case of two-terminal tandem devices, which are the preferred configuration in terms of minimized balance-of-system costs and low parasitic absorption losses in contact layers, current matching is required for maximal power output. Both, the PV system and the solar cells, have to be designed in such a way that an equal number of photons is absorbed in the top and bottom cells, respectively, because otherwise the whole device is limited by the subcell absorbing fewer photons. While variable weather conditions tend to average out in bifacial single-junction devices, variations of front and rear side illumination can significantly


## 1. Introduction

The market share of bifacial photovoltaic (PV) modules has grown remarkably in recent years. Bifacial modules not only utilize light impinging onto the front side of the PV module, but also light reaching the backside.<sup>[1,2]</sup> The International

P. Tillmann, K. Jäger, C. Becker  
Department Optics for Solar Energy  
Helmholtz-Zentrum Berlin für Materialien und Energie  
12489 Berlin, Germany  
E-mail: christiane.becker@helmholtz-berlin.de

P. Tillmann, K. Jäger  
Computational Nano Optics  
Zuse Institute Berlin  
14195 Berlin, Germany

A. Karsenti, L. Kreinin  
Lev Academic Center  
SolAround Ltd.  
Jerusalem 9611001, Israel

 The ORCID identification number(s) for the author(s) of this article can be found under <https://doi.org/10.1002/solr.202200079>.

© 2022 The Authors. Solar RRL published by Wiley-VCH GmbH. This is an open access article under the terms of the Creative Commons Attribution License, which permits use, distribution and reproduction in any medium, provided the original work is properly cited.

DOI: 10.1002/solr.202200079

disturb current-matching in bifacial tandem solar cells.<sup>[13]</sup> Various theoretical energy-yield calculation models were developed for the currently widely discussed two-terminal perovskite/silicon tandem solar cells<sup>[14]</sup> in bifacial operation.<sup>[13,15–18]</sup> However, only very little experimental data of bifacial two-terminal perovskite/silicon tandem solar cells on outdoor test fields have been published so far.<sup>[19]</sup> Hence, in the medium term, the prediction of the energy yield of this technology will still rely on simulations. More important is to validate the rear-side illumination models by experimental field data, e.g., from bifacial silicon single-junction solar cells at the specific location of interest, to enable reasonable predictions for bifacial tandem solar cells as well.

In this study, we combine several models to calculate the energy yield of the investigated devices. Each step in the chain of models is validated with data from a mono- and a bifacial silicon solar module. In the first step, we apply an illumination model for bifacial solar modules arranged as an infinitely extended array based on view-factor considerations.<sup>[20]</sup> We compare the simulations with the measured data from a bifacial solar cell module installed in a small power plant located on a rooftop in Jerusalem, Israel, on two sunny days (one in winter and one in summer) as well as one “variable” day with quickly changing cloud coverage. Comparing the measured generated current with the modeled combined irradiance from the front and rear sides of the module allows to validate the optical view factor model nearly independently from module temperature and wind speed. In a second step, we implement a temperature-dependent electrical model to compare measured and simulated generated power. Finally, we use our validated bifacial solar cell model to predict the energy yield of perovskite/silicon tandem solar cells with the perovskite top cell on the front side, and also the configuration with perovskite cells “sandwiching” the silicon bottom cell on both, front and rear side.

## 2. Experimental Data and Numerical Methods

### 2.1. Experimental Data Basis

The experimental data used in this work was recorded on a rooftop installation in Jerusalem, Israel, provided by SolAround Ltd. Figure 1a shows the rooftop installation, made of four rows of solar panels mounted in landscape orientation with three panels per row. A high-albedo plastic foil under the solar panels is used

to increase the amount of light reflected onto the back side of the modules. The installation includes mono- and bifacial modules and sensors for measuring the global, diffuse and direct irradiance. K-type thermocouples are installed at the back side of solar panels to measure the cell temperature. The temperature sensor should give a good estimate of the operation conditions of the solar cells, but the actual cell temperature is likely slightly higher than the temperature measured at the back side of the panel. From the solar panels, the short-circuit current ( $I_{sc}$ ), open-circuit voltage ( $V_{oc}$ ), maximum power, and fill factor ( $FF$ ) are measured each minute. Three days of data are available, August 26, 2019 (sunny summer day), February 15, 2020 (sunny winter day), and February 19, 2020 (cloudy/variable winter day). The parameters used to represent the rooftop installation are summarized in Table 1.

### 2.2. Numerical Methods

#### 2.2.1. Bifacial Illumination Model

The first step to calculate the characteristics of the bifacial solar cells is to simulate the irradiance on the front and back sides. For the irradiance simulation, we employ a recently developed view factor illumination model,<sup>[20,21]</sup> which was specifically designed for bifacial solar cells. In that model, the PV field is considered so large that boundary effects can be neglected. The geometry of the solar panels is simplified (the panels are assumed to be perfectly flat, with no frame) and the front and back side are modeled as perfectly black. These assumptions are used in many view-factor models and typically lead to an underestimation of the back side irradiance of 5–20%.<sup>[22,23]</sup> Figure 1b shows the schematic illustration of the components reaching the module front and back each: direct sunlight, diffuse skylight, diffuse light from the ground originating from direct sunlight reaching the ground, and diffuse light from the ground originating from diffuse skylight reaching the ground. To describe the geometry of the PV installation under investigation the model requires the module length  $\ell$ , mounting height  $h$ , module spacing  $d$ , and tilt angle  $\theta_m$ . Second, also the albedo (i.e., the reflectivity) of the ground is required (see Table 1).

For the rooftop location in Jerusalem, no spectrally resolved solar irradiance data is available. However, broadband direct and diffuse irradiance are measured by pyranometers with a time resolution of one minute. To emulate the spectral information

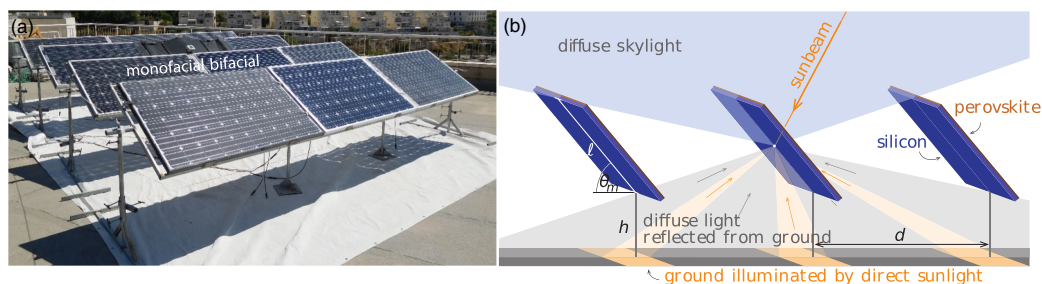


**Figure 1.** a) Photograph of the mono- and bifacial silicon solar panel rooftop installation located in Jerusalem, Israel, delivering the experimental data for model validation. All data for monofacial cells is measured with the left module in the second row, bifacial data is measured with the module in the middle of the second row. b) Schematic representation of the bifacial irradiance model used in this study. Adapted under terms of the CC-BY license.<sup>[18]</sup> Copyright 2021, The Authors. Solar RRL published by Wiley-VCH GmbH.

**Table 1.** Experimental parameters of the solar panel rooftop installation in Jerusalem.

Model parameters		
$l$	module length [m]	1.0
$d$	module spacing [m]	1.9
$h$	module height above the ground [m]	0.8
$\theta_m$	module tilt angle	30°
$A$	albedo of the ground	60%
Solar cell parameters at standard test conditions (STC)		
Front-side illumination		
$V_{OC}$	Open-circuit voltage [V]	38.8
$I_{SC}$	Short-circuit current [A]	9.83
FF	FF [%]	74
$P$	Power [W]	283
Rear-side illumination		
$V_{OC}$	Open-circuit voltage [V]	38.6
$I_{SC}$	Short-circuit current [A]	8.35
FF	FF [%]	74
$P$	Power [W]	242
	Bifaciality (Ratio rear to front power)	85%
	Number of cells per module	60
	Cell active area (unshaded by wires) [cm <sup>2</sup> ]	240
Outdoor solar panel field data		
$V_{OC}$	Open-circuit voltage [V]	
$I_{SC}$	Short-circuit current [A]	
FF	FF [%]	
$P$	Power at maximum power point [W]	
Measured solar and temperature data		
DHI	Diffuse horizontal irradiance [W m <sup>-2</sup> ]	K&Z CMP11 Pyranometer with shadow ring
GHI	Global horizontal irradiance [W m <sup>-2</sup> ]	K&Z CMP11 Pyranometer
POA	Irradiance in the plane of the module front side [W m <sup>-2</sup> ]	Phox SOZ-03 silicon reference cell
$T_c$	Cell temperature	Type K thermocouple at back side of the module

needed to calculate the photocurrent we use spectrl2, a model based on radiative transfer simulations developed by Bird and Riordan.<sup>[24]</sup> spectrl2 calculates the direct and diffuse spectral irradiance based on the solar position and several atmospheric parameters, such as precipitable water, ozone concentration, and aerosol optical depth. This model is only suitable for clear-sky conditions and therefore only applicable for describing the two sunny days August 26, 2019 and February 15, 2020.

### 2.2.2. Optical Solar Cell Model

We use the MATLAB-based software package GenPro4<sup>[25]</sup> to calculate the optical absorption, reflection, and transmission of the investigated cell architectures. GenPro4 uses the

net-radiation method for multilayer stacks and ray tracing for simulating scattering by pyramidal interfaces. As input, we provide detailed layer stacks, the type of interface (planar or textured), and the complex refractive index ( $nk$ -data) for the used materials. All detailed layer stacks and references for the used  $nk$ -data are summarized in the Supporting Information (SI) Section S5.

To study how the perovskite bandgap affects the solar-cell performance, we performed a wavelength shift of the available  $nk$  dataset for perovskite.<sup>[26]</sup> This estimation is justified by experimental data.<sup>[27]</sup>

We calculated the photocurrent densities as functions of the absorption and the spectral irradiance using

$$J_{ph} = e \int_{300\text{ nm}}^{1200\text{ nm}} A(\lambda) \Phi_f(\lambda) d\lambda \quad (1)$$

where  $e$  is the elementary charge,  $A(\lambda)$  is the absorption in the considered absorber layer, and  $\Phi_f$  is the photon flux reaching the module. The photon flux can be calculated from the spectral irradiance according to

$$\Phi_f(\lambda) = E_\lambda \frac{\lambda}{hc} \quad (2)$$

with the spectral irradiance  $E_\lambda$ , the Planck constant  $h$  and the speed of light  $c$ .

### 2.2.3. Temperature-Dependent One-Diode Model

An electrical model is used to calculate the power output of a solar cell from the absorbed photocurrent. To get a realistic estimation of the power output different factors such as the electrical resistance and temperature have to be accounted for. In this work, we use a one-diode model to calculate the current-voltage characteristics ( $IV$ -curves) of each solar cell. The one-diode model assumes an equivalent circuit, where an ideal current source is connected in parallel to a diode and optionally one or two resistors to model the series and shunt resistance of the solar cell. We use the following equation in our work

$$J(V) = J_{ph} - J_0 \left[ \exp\left(\frac{V + J \cdot R_{series}}{kT/e}\right) - 1 \right] - \frac{V + J \cdot R_{series}}{R_{shunt}} \quad (3)$$

with the dark saturation current density  $J_0$ , elementary charge  $e$ , the Boltzmann constant  $k$ , the temperature  $T$ , photon current density  $J_{ph}$ , series resistance  $R_{series}$ , and shunt resistance  $R_{shunt}$ . This form of the one-diode equation has three parameters that determine the  $IV$ -curve for a given illumination and temperature: series resistance, shunt resistance, and dark saturation current. These parameters can typically be extracted from the measured  $IV$ -curve by fitting the one-diode equation to match the experiment. While series and shunt resistance are only slightly dependent on temperature (we assume it to be constant for simplicity) the dark saturation current is strongly dependent on the temperature. Therefore, we are not fitting the dark saturation current directly. Using the integrated overlap of the blackbody radiation and the external quantum efficiency (EQE) of a junction an idealized but temperature-dependent dark saturation current can be computed<sup>[28,29]</sup>

$$J_{0,\text{ideal}}(T) = e \int_0^\infty \text{EQE}(\lambda) \Phi_{\text{BB}}(\lambda, T) d\lambda \quad (4)$$

with the elementary charge  $e$  and the photon flux of the black body radiation  $\Phi_{\text{BB}}$ . Using arguments of reciprocity and considering the limited external quantum efficiency  $\text{EQE}_{\text{el}}$  of a real cell a realistic and temperature-dependent dark saturation current  $J_0$  can be calculated.<sup>[28]</sup>

$$J_0(T) = \frac{J_{0,\text{ideal}}(T)}{\text{EQE}_{\text{el}}} \quad (5)$$

For details of the approach please see Supporting Information Section S1. It should be noted that we assume a constant ideality factor for the diode of  $n = 1$ .

### 3. Results

#### 3.1. Validation of the Bifacial Illumination Model

In a first step, we aim to validate the optical bifacial illumination model by comparing simulated with experimental data. The illumination model calculates the intensities of the direct and diffuse light that are received at the front and back side of the

solar modules. While the illumination on the backside is not directly measured we can use the short-circuit current of a bifacial module as a proxy.

Figure 2a shows the dependence between the plane-of-array irradiance on the front side of the solar cell modules and the short-circuit current measured on a monofacial PERT silicon solar cell module. The plane-of-array irradiance is directly measured by a reference cell mounted in the same plane as the solar cell modules. The silicon solar module is rated for a short-circuit current  $I_{\text{SC}}$  of 9.83 A at standard testing conditions (STC), i.e.,  $1000 \text{ W m}^{-2}$  irradiance. The red line shows the linear dependence of the short-circuit current on the irradiance calibrated with the STC measurement. The blue dots represent the short-circuit current measured over the course of August 26, 2019 and February 15, 2020. This shows that the short-circuit current  $I_{\text{SC}}$  is an excellent proxy for the irradiance. Here, the data points from February 19, 2020 are excluded because the timestamps of the irradiance and the short-circuit current are not perfectly aligned (in the temporal sense), and therefore can diverge considerably in rapidly changing cloud coverage.

Because of the nearly linear response of the short-circuit current with respect to the plane-of-array irradiance, we use a constant factor determined by the short circuit current measured at STC for the model validation of this section

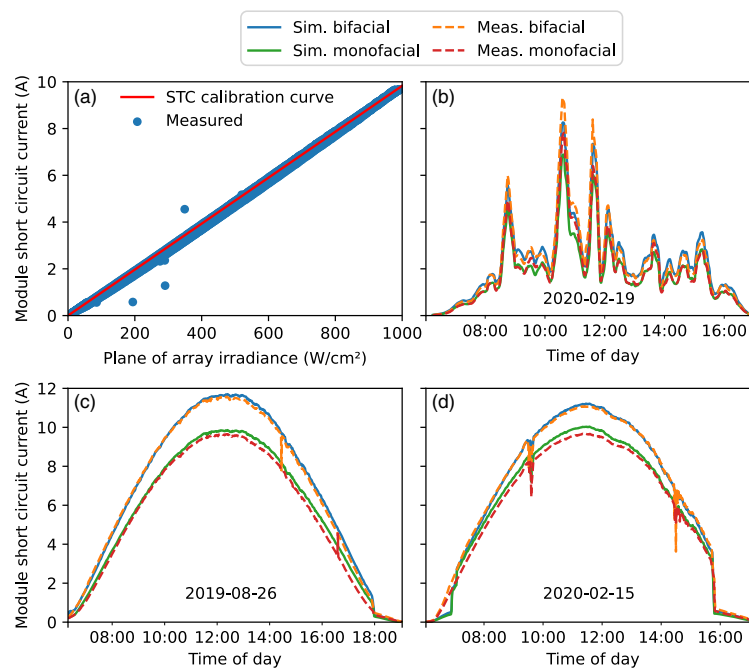


**Figure 2.** Validation of the bifacial illumination model. a) Correlation between measured module short-circuit current and measured plane of array irradiance (blue symbols), and calibration curve from solar cell characteristics at standard testing conditions (STC (red line)). b–d) Comparison of measured and modeled short-circuit current for mono- and bifacial solar modules at one variable day (b) and two sunny days (b), (c) by combining the bifacial irradiance model with the STC calibration curve. In part (b) a 15 min rolling average is shown. The output of the irradiance model depends on the DNI and DHI readings, position of the sun and the photovoltaic (PV) installation geometry detailed in Table 1.

$$\begin{aligned} J_{\text{ph,front}} &= \frac{9.83A}{1000W} \cdot E_{\text{front}} \\ J_{\text{ph,back}} &= \frac{8.35A}{1000W} \cdot E_{\text{back}} \\ J_{\text{ph,bifacial}} &= J_{\text{ph,front}} + J_{\text{ph,back}} \end{aligned} \quad (6)$$

with  $E_{\text{front}}$  and  $E_{\text{back}}$  as the irradiance calculated by the irradiance model for the front and back side respectively. These calculations are based on the pyranometer readings for the DNI and DHI, as well as the position of the sun (in terms of azimuth and zenith angle) and the geometry of the PV installation detailed in Table 1.

Figure 2b–d shows the simulated and measured module short-circuit current for a bifacial and monofacial silicon module on August 26, 2019, February 15, 2020, and February 19, 2020, respectively. For the 2 days with clear-sky conditions, the calculated curves are very close to the measured lines, showing a good agreement between measurement and simulation. The variable day (February 19) is much more demanding. The results shown are 15 min rolling average because the very fast changes in irradiance otherwise would render the graphic unreadable. Because the timestamps of the irradiance are not perfectly aligned with the short-circuit current measurements some divergence between simulation (based on the irradiance) and measurement is to be expected. Also, the underlying assumption of the illumination model (all direct sunlight originates from a point source while the diffuse light is distributed isotropically over the hemisphere) is less valid for situations with rapidly changing cloud coverage. Nonetheless, the illumination model is still able to reproduce the general trends of the short-circuit current. However, some higher differences are visible between model and measurement, especially for times with high and quickly changing irradiance.

### 3.2. Validation of the Optical Solar Cell and Spectral Models

As detailed in Section 2.2, we use a three-step modeling approach to calculate the generated photocurrent density in each junction of the photovoltaic devices. First, we simulate the optical absorption profile of the investigated solar cell using the material stack as input. Second, we generate spectral information from broadband irradiance measurement and weight them with the results of the bifacial illumination model. Third, we combine spectral absorption and spectral irradiance to calculate the photocurrent density in the relevant junctions of the solar cell devices according to Equation (1).

Figure 3a shows the layer stack used for calculating absorption, reflection, and transmission of the bifacial SolAround PERT solar cell. The details of the layer stack and the used  $nk$ -data are found in the Supporting Information, Section S5. Figure 3b,c shows the result of the optical GenPro4 simulation with front side and back side illumination, respectively.

Figure 3d shows selected examples of the calculated spectral direct irradiance for different times on August 26, 2020. A spectrum according to AM1.5g is added as a reference. A red shift is clearly visible for the early morning spectrum at 7:10 am resulting from the increased scattering of short-wavelength light due to the prolonged light path through the atmosphere. At 8:50, the

spectrum is already close to the 10:30 and 12:10 spectra, which are very similar and nearly identical to the AM1.5 reference spectrum.

To compare the calculated photocurrent with the measured short-circuit current, the area of the solar cell and the number of cells in one module has to be considered. For a cell, we assume an active area (area of the cell that actively contributes to the absorption) of  $240 \text{ cm}^2$  and 60 cells per module.

Figure 3e shows the photocurrent of the simulated mono- and bifacial PERT solar module and the measured short circuit current. Simulation and measurement are in good agreement and the results are very similar to the simulated short-circuit current based on STC measurements.

### 3.3. Validation of the Temperature-Dependent One-Diode Model

We use a one-diode model to calculate the  $IV$ -curves for a given temperature and absorbed photocurrent. From the  $IV$ -curve the open-circuit voltage,  $FF$ , and maximum power point are derived. The details of the model are described in the numerical method section above. The measured values for  $V_{\text{OC}}$  and  $FF$  of silicon PERT solar cells mounted at the rooftop installation were fitted to acquire the necessary parameters for the one-diode model. We found  $R_{\text{series}} = 1.9 \Omega \text{ cm}^2$ ,  $R_{\text{shunt}} = 1000 \Omega \text{ cm}^2$  and  $\text{EQE}_{\text{el}} = 0.16\%$ .

Both the open-circuit voltage and the  $FF$  strongly depend on the temperature according to the one diode model (see Figure S4 in the Supporting Information). The level of irradiance also influences the  $FF$  and open-circuit voltage. Higher levels of irradiance have a positive impact on the open-circuit voltage while the  $FF$  has a peak, depending on the series and shunt resistance of the cell. Higher temperatures always reduce  $FF$  and open-circuit voltage. A more detailed discussion of these effects is given in the Supporting Information, Section S3.

Figure 4 shows the measured module temperature ( $T_m$ ) and global horizontal irradiance (GHI) (a), the measured and simulated power output  $P$  (b), the  $FF$  (c), and the open-circuit voltage  $V_{\text{OC}}$  (d). Overall measured and simulated parameters of the solar cell agree very well. Over the course of the morning temperature and irradiance gradually increase. While the increasing irradiance leads to increasing  $V_{\text{OC}}$  higher cell temperatures reduces it. These competing trends of temperature and irradiance on the  $FF$  and  $V_{\text{OC}}$  are well reproduced by the model and result in good agreement for the power simulation of the solar cell modules. Larger differences are found only for very low levels of light intensity in the morning and times when either the irradiance sensor and/or the solar panels are shaded in the evening. This confirms that the chosen simulation approach is well suited to reproduce the measured power output of the silicon based PERT modules produced by SolAround. In Section S3.1 of the Supporting Information, we show the results for the simulation of the bifacial solar cell and discuss the differences for modeled and simulated results. The main differences between results for the bifacial and monofacial solar cells are an unexpected high  $FF$  measured for the bifacial solar cell when using the same cell parameters as used for the monofacial cells. We additionally benchmarked a two-diode model assuming a constant,

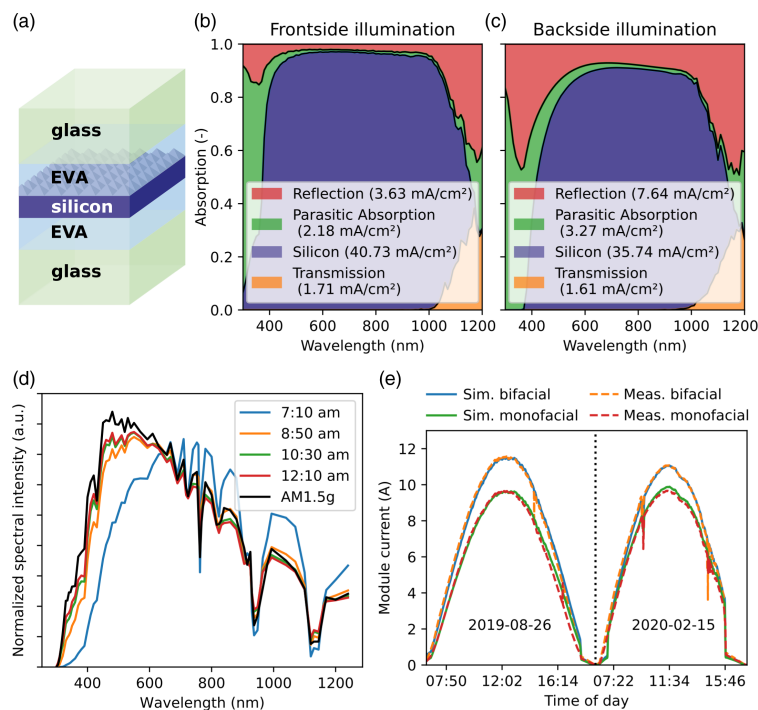


**Figure 3.** Validation of optical solar cell modelling. a) Layer stack of the frontside textured passivated rear totally diffused (PERT) bifacial solar cells used to simulate absorptance, transmittance and reflectance for b) frontside and c) back side illumination with the software GenPro4. For a better clarity, the thin contact, passivation and doping layers or not show here; the respective parasitic absorption is summarized in green in part (b) and (c). The detailed layer stack can be found in the Supporting Information Section S5. d) Examples of modeled spectral direct normal irradiance according to the model spectrl2<sup>[24]</sup> for different times on August 26, 2020 and AM1.5g spectrum for comparison. e) Comparison of measured and modeled short-circuit current for mono- and bifacial solar modules on two sunny days by combining the bifacial irradiance model (separately validated in Figure 2), spectrl2 and optical simulations using GenPro4.

temperature-independent dark saturation current for the second diode. The parameters were fitted for a JV curve recorded under STC and results are shown in S2 and S3 in the Supporting Information. Due to the ambivalent results from the comparison of the one- and two-diode model we used the simpler one-diode model for the remainder of this work.

### 3.4. Energy Yield Predictions for Bifacial Perovskite/silicon Tandem Solar Cells

In this section, we estimate the energy yield that would be obtained if the bifacial solar panel array located on a rooftop in Jerusalem, Israel, did not consist of mono- or bifacial silicon solar modules, but of perovskite/silicon tandem solar cells of different configurations. We introduce 2- and 4-terminal connected perovskite-on-silicon tandem solar cells, simulate the 2-day energy yield for bifacial and monofacial devices and discuss the effects of the perovskite bandgap. Later in this section, we propose a 4-terminal architecture with three junctions, two

perovskite junctions surrounding a silicon junction in the middle, like a “sandwich,” and discuss its performance prospects.

**Figure 5** illustrates the 2-terminal connected and 4-terminal connected tandem solar cells. The solar cell stack for 2-terminal connected tandem solar cells is based on work by Al-Ashouri et al.<sup>[14]</sup> that marks the highest perovskite/silicon tandem solar cell efficiency with published details of the layer stack. These tandem cells use a MeO-2PACz self-assembled monolayer (SAM) as selective contact for hole transport. This layer is shown for completeness in Figure 5 but it is not considered in the optical simulation because it is unlikely to affect the optical response due to its very small thickness (1–2 nm). Here we focus on tandem solar cells where the perovskite cell is processed on the polished side of the silicon bottom cell and the textured side facing downwards. This approach enables spin-coating deposition of the top cell, which shows the highest efficiencies published so far.<sup>[14]</sup> From an industrial manufacturing point of view, double-sided textured silicon bottom cells might be favorable in the future<sup>[30–32]</sup> and our modeling approach is fully applicable to these kinds of cell technologies as well.<sup>[33]</sup>

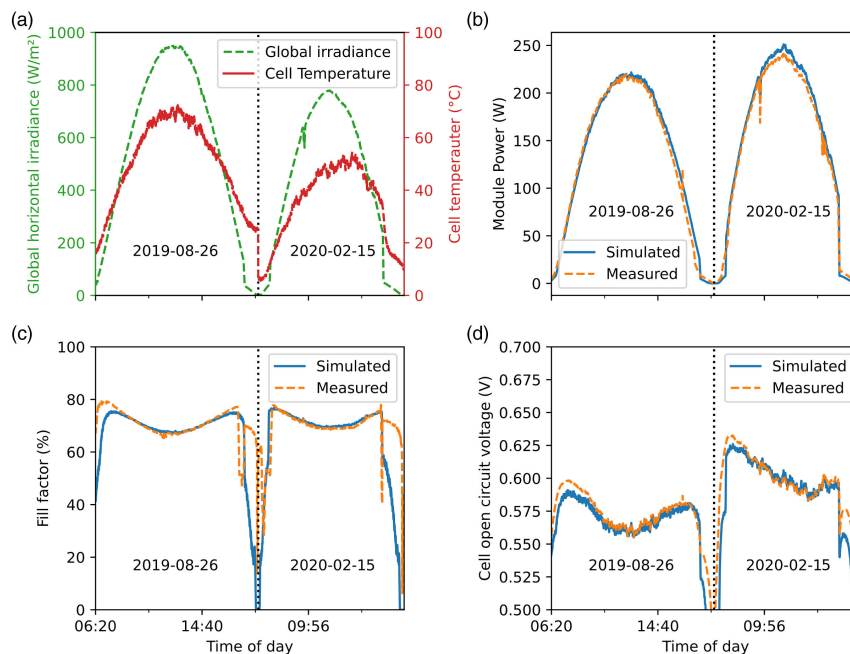


**Figure 4.** Measured sensor data and parameters of monofacial solar cells over the course of August 26, 2019 and February 15, 2020. a) Measured global horizontal irradiance and cell temperature. Comparison of simulated (one-diode model) and measured b) module power, c) fill factor (FF), and d) open-circuit voltage.

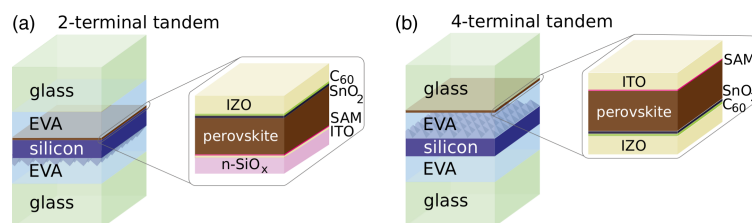


**Figure 5.** Schematic of the simulated bifacial tandem stack in a) 2-terminal and b) 4-terminal configuration. One side of the silicon exhibits a pyramidal texture, the other side is planar. In the case of the 2-terminal tandem the perovskite is assumed to be processed on the planar side of the silicon bottom cell while in the 4-terminal configuration the texture is pointed upwards to minimize reflection losses under top illumination. The self-assembled monolayer (SAM) is shown for completeness but ignored in the optical simulations due to its very small thickness (1–2 nm). The detailed stacks including all considered interlayers can be found in Supporting Information Section S5.

In this study, we adapt the silicon bottom cell architecture and use cell parameters of the SolAround solar cells. The PERT cells from SolAround are based on *p*-type silicon wafers and textured at the front side. For the simulation of tandem stacks a silicon oxide interlayer was added (shown as  $n\text{-SiO}_x$  in the layer stacks). This silicon oxide interlayer is highly doped (for electrical conductivity) and was used by Al-Ashouri et al. to reduce the reflection between the perovskite and silicon subcell.

For the cell parameters of the perovskite subcell ( $\text{EQE}_{\text{el}}$ ,  $R_{\text{shunt}}$ ,  $R_{\text{series}}$ ) we fit results published by Jošt et al.<sup>[34]</sup> on the temperature dependence of the efficiency and  $V_{\text{OC}}$  of the perovskite solar cell. Details of the fitting results can be found in the Supporting Information Section S4.

For the 4-terminal tandem, we assume a stack consisting of a perovskite top cell as used by Jošt et al. processed on the front glass and, separated by a layer of EVA, the silicon bottom cell

with the textured side to the front. The copper contact of the perovskite is replaced with a 200 nm thick layer of indium zinc oxide (IZO) for transparency in the infrared region. This approach likely leads to a too optimistic estimation of the performance of the 4-terminal tandem cell because the lateral current flow through the IZO layer will cause a higher series resistance compared to the copper contact of the reference. However, we do not account for this difference because it is not quantitatively accessible.

All fitted values for  $\text{EQE}_{\text{el}}$  and resistivity for the 2- and 4-terminal configurations are summarized in Table 2. The details of the stacks with all relevant interlayers (transparent conductive oxides, charge carrier transport layers, anti-reflective coatings)

**Table 2.** Summary of the fitted cells parameters ( $R_{\text{series}}$ ,  $R_{\text{shunt}}$ , and  $\text{EQE}_{\text{el}}$ ) for different cell types and simulation results ( $\eta$ ,  $V_{\text{oc}}$ , and  $J_{\text{ph}}$ ) for standard testing conditions (25 °C, AM1.5g illumination). Where appropriate separate values for top and bottom cells of the tandems have been indicated with top cell value/bottom cell value.

	$R_{\text{series}}$ [ $\Omega \text{ cm}^2$ ]	$R_{\text{shunt}}$ [ $\Omega \text{ cm}^2$ ]	$\text{EQE}_{\text{el}}$ [%]	$\eta_{\text{STC}}$ [%]	$V_{\text{oc}}$ [V]	$J_{\text{ph}}$ [ $\text{mA cm}^{-2}$ ]
Silicon	1.9	1000	0.16	19.3	0.655	40.7
Perovskite	6	1000	0.12	18.3	1.103	22.1
T tandem	6	1000/1000	0.16/0.12	25.3	1.735	18.8
T tandem	6/1.9	1000/1000	0.16/0.12	24.9	1.114/0.619	19.9/17.5

and the corresponding absorption spectra calculated with GenPro4 are found in the Supporting Information, Section S5. The generated photocurrent density in the silicon and perovskite junctions is in line with state-of-the-art 2-terminal<sup>[14]</sup> and 4-terminal<sup>[35]</sup> perovskite on silicon tandem cells. However, the power conversion is 3–4 percentage points (p.p.) below the values reported in these research articles. This is mainly due to the usage of silicon cell parameters of solar modules produced with standard industrial processes while research articles often use high-end silicon cells that are only available on small scales. Also, the parameters for the perovskite cell correspond to a lower efficiency then would be found for small-scale record cells.

For all simulations of tandem solar cells, we assume that the modules are mounted in the same rooftop installation shown in Figure 1 with the geometry detailed in Table 1 and the same albedo of 60%. Figure 6 shows the calculated photocurrent density generated in the (a + c) perovskite and (b + d) silicon junction in a bifacial (top row) and a monofacial (bottom row) tandem for different perovskite bandgaps. Overall the photocurrent density follows the irradiance over the course of the day with the highest levels around midday. Decreasing the perovskite bandgap increases the photocurrent density because more photons with energies above the bandgap can be utilized. As a consequence, the photocurrent density in the silicon junction decreases with lower perovskite bandgaps. While the perovskite junction is unchanged for mono- or bifacial operation the silicon junction generates significantly higher current densities with

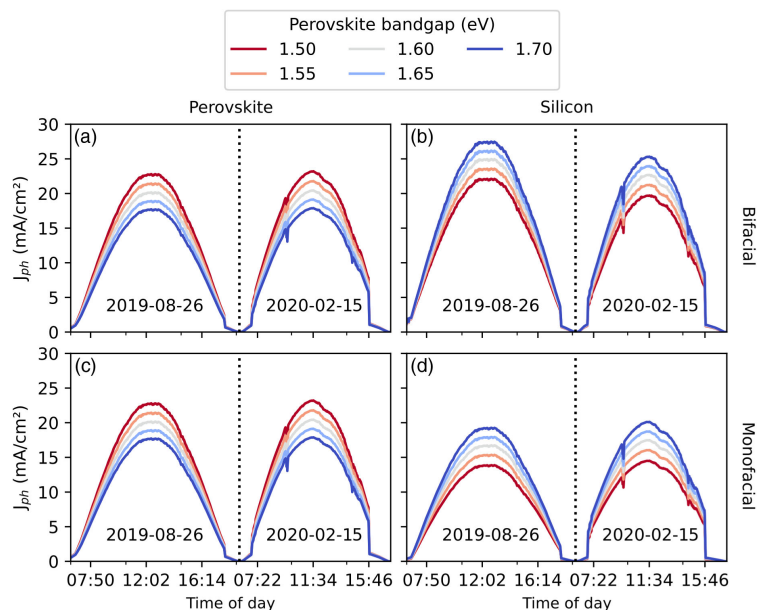


**Figure 6.** Absorbed photocurrent density  $J_{\text{ph}}$  of the (left) perovskite and (right) silicon subcell of 2-terminal perovskite/silicon tandem solar cells over the course of 26 August 2019 and 15 February 2020. The upper row (a,b) and lower rows (c,d) show results for a bifacial and for a monofacial tandem device, respectively. The geometrical parameters of the solar panel array as well as the albedo (60%) are identical to the parameters of the Jerusalem rooftop installation as specified in Table 1.



back side illumination. The light reaching the back of the bifacial tandem is exclusively absorbed in the silicon cell. This is because silicon has a lower bandgap than perovskite. All light that is transmitted because of photon energies below the bandgap of the silicon is also below the bandgap of the perovskite and therefore can not be absorbed there either.

With a perovskite bandgap of 1.55 eV the bifacial device generates roughly the same photocurrent density in the perovskite and silicon junctions and hence is at current-matching conditions. For the monofacial tandem solar cell, the optimal perovskite bandgap is significantly higher. Because of the missing additional photons from the back side, the perovskite top cell needs to transmit more light into the silicon subcell to ensure current-matching conditions. For a bandgap of around 1.65 eV, both junctions generate roughly equal current densities.

Figure 7 shows the simulated energy yield over the two days (August 26, 2019 and February 15, 2020) of available data for one module of mono- or bifacial silicon cells (green), 2-terminal (blue) and 4-terminal (orange) perovskite/silicon tandem cells for different perovskite bandgaps (in case of the tandems). The monofacial silicon cell yields around 3.3 kWh on these two days while the bifacial equivalent yields 3.9 kWh, an increase of roughly 20%. The energy yield of the monofacial 2-terminal tandem module strongly depends on the perovskite bandgap, with an optimal bandgap of 1.66 eV. The optimal bandgap of the bifacial 2-terminal tandem is shifted to 1.56 eV and an overall increased electrical yield is found. Overall, mono- and bifacial 4-terminal tandem cells show a lower dependence on the perovskite bandgap with the optimum at the maximum of the chosen perovskite bandgap range. The optimal bandgap does not change under bifacial operation. We choose a range of 1.5–1.7 eV because in this range high-quality perovskite materials have been demonstrated while perovskite cells with higher bandgaps can be difficult to manufacture.<sup>[36]</sup>

At their individual optimal bandgap, 2-terminal tandem solar cells show a slightly higher module yield compared to the

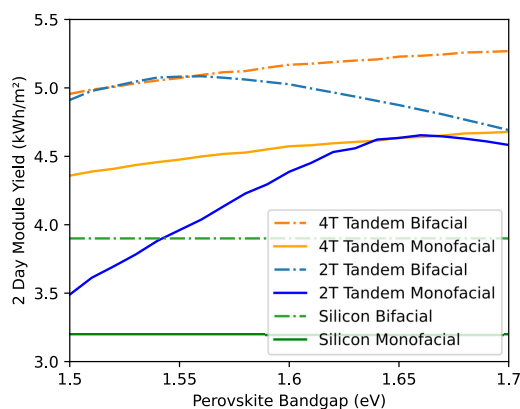


**Figure 7.** Simulated two-day (August 26, 2019 and February 15, 2020) energy yield of one module for different solar cell technologies as function of the perovskite bandgap (in case of tandems). The geometrical parameters of the solar panel array as well as the albedo (60%) are identical to the parameters of the Jerusalem rooftop installation as specified in Table 1.

corresponding 4-terminal configuration at the same bandgap. However, the 4-terminal configurations have a higher energy yield at the maximum bandgap. Please note that the results shown in Figure 7 should only be regarded as a rough estimation of optimum perovskite bandgaps. We regarded the  $EQE_{el}$  as a constant parameter in our simulations neglecting its dependence on temperature, injection, and particularly, the perovskite bandgap. This might lead to an underestimation of the tandem energy yield for lower-bandgap perovskites where much higher  $EQE_{el}$  values have been reported,<sup>[37]</sup> and to an overestimation of the yield when the tandem solar cells comprise wide-bandgap perovskite top cells, which often suffer from photo-induced phase segregation deteriorating the open-circuit voltage.<sup>[38]</sup> This might especially impact 4-terminal tandem solar cells where an optimum perovskite bandgap at the upper edge of the investigated range was found. For more detailed energy yield calculations the individual performance of the perovskite top cell in terms of  $EQE_{el}$  has to be considered.

The addition of a perovskite, wide-bandgap top cell atop a silicon bottom cell enables obtaining higher power conversion efficiencies owing to a reduction of thermalization losses of high energy photons. As this concept might also work for light impinging on the backside of the solar module, we also propose a triple-junction, 4-terminal perovskite/silicon-perovskite “sandwich” architecture. Figure 8a shows the schematic stack of this solar cell configuration. The top perovskite and the middle silicon cell are connected in series and form two electrical contacts (terminals) of the cell. The bottom perovskite is insulated by a layer of EVA, similar to the perovskite cell in the conventional 4-terminal tandem, and is connected with two separate terminals. The two top junctions will absorb similar photocurrent densities when the perovskite bandgap is chosen properly while the bottom perovskite will only absorb a fraction of the light due to the significantly lower irradiance at the back side of the module. Figure 8b shows the effect of the top and bottom perovskite bandgap and the 2-day energy yield. The effect of the top cell bandgap is much larger and an optimum is found at around 1.63 eV. The optimal bottom cell bandgap is found at the lower bound at 1.50 eV. It seems to be beneficial to absorb as much light as possible in the bottom perovskite junction. Figure 8c shows the calculated photocurrent density in the top-, middle- and bottom-junctions over the course of August 26, 2019 for a “sandwich” solar cell with a top and bottom cell bandgap of 1.63 and 1.50 eV, respectively. The photocurrent density of the top perovskite and the silicon junction is quite well matched, resulting in optimal utilization of the impinging light. In contrast, the bottom perovskite cell absorbs only a fraction of the photocurrent densities due to the lower irradiance at the back side of the module. Figure 8d shows the *IV*-curves of the “sandwich” at 1 pm on August 26, 2019. Due to the low intensity of light absorbed in the bottom perovskite junction, the open-circuit voltage is rather low, and therefore the power conversion efficiency is reduced.

### 3.5. Discussion

In this final section, we compare the results and discuss the prospects of different cell designs. Figure 9 shows the combined energy yield of the two sunny days (August 26, 2019 and

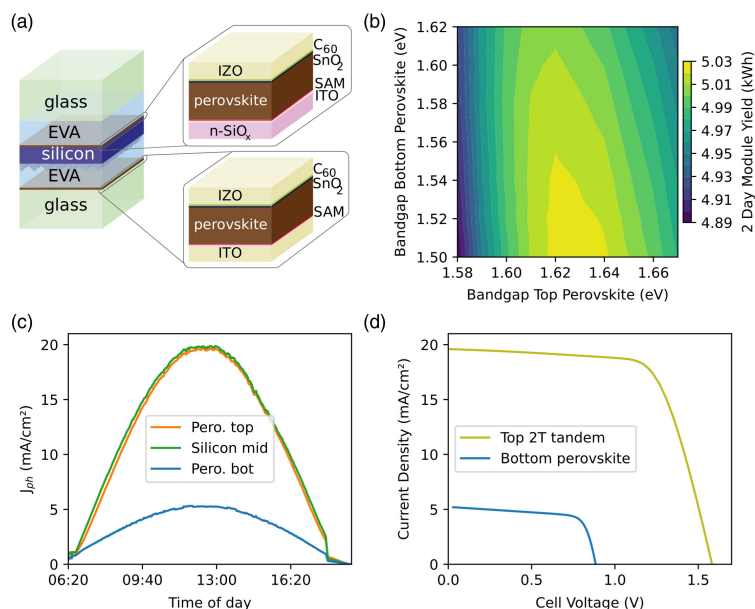


**Figure 8.** Simulation setup and results for 4-terminal sandwich configuration. a) Stack of the simulated “sandwich” solar cell. The upper perovskite and the silicon cell form a 2-terminal tandem, the lower perovskite is electrically independent with its own 2-connection terminals. b) Two-day energy yield for various bandgaps of the top (x-axis) and bottom (y-axis) perovskite. c) Absorbed photocurrent density  $J_{ph}$  over the course of August 26, 2019 for the three junctions of the device. d) Example IV-curves for August 26, 2019, 13:00. Because top perovskite and silicon subcells are connected in series they share one IV-curve as a tandem.

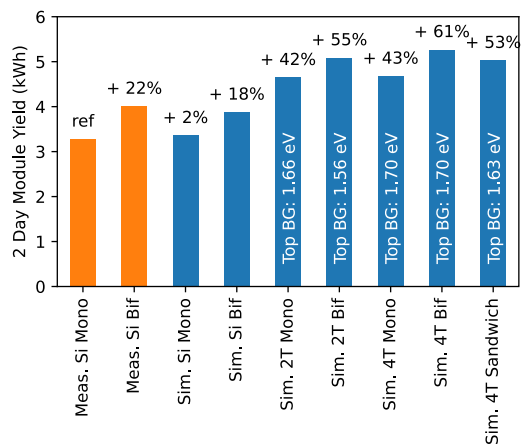


**Figure 9.** Two-day (August 26, 2019 and February 15, 2020) energy yield comparison of one module for all investigated solar cell architectures. The first two bars show the experimental result for mono and bifacial silicon solar cells. For all tandem solar cells the best performing perovskite bandgap was selected. The shown relative gains in percentage all refer to the experimental monofacial result.

February 15, 2020) with measured data for one module on the Jerusalem rooftop solar panel array installation, and with simulated estimates for different solar cell technologies. The first two bars show the measured energy yield of the monofacial and bifacial PERT silicon solar cell module. Compared to the monofacial module (reference) the bifacial module yielded 22% higher energy outputs. It has to be noted that the most common surfaces below bifacial solar power plants exhibit lower albedo values than 60% as in the case of the specific Jerusalem rooftop installation. Therefore, and considering the short timeframe of this study, the bifacial gain cannot be generalized and the +20% should be regarded as an upper bound for the bifacial energy yield gain. Simulated results for the silicon cells show similar numbers, however, the difference between the monofacial and the bifacial is lower, with only 16% gain due to bifaciality. We use the same cell parameters for the mono- and bifacial module, however, the *FF* of the bifacial cell seems to be higher (See Figures S5 and S6 in the Supporting Information). This results in an underestimation of the generated power and explains some of the differences between simulated and measured bifacial gain. Another factor can be found in the assumption of the model, where rows are infinitely wide and infinitely many rows are present. In the rooftop installation, however, there are only four rows with three modules each, where some light will shine in from the sides or the front, which is not considered by our model.

When switching to monofacial perovskite-on-silicon tandem technology, the results show an increase in the energy yield of 42%, which is significantly higher than the gain possible with silicon bifacial technology. This result is comparable with a study by Lehr et al.<sup>[16]</sup> who calculated around 40% increased energy yield for a monofacial tandem solar cell. The bifacial 2-terminal tandem is even able to produce 54% more energy than the silicon reference. This is a 13 p.p. increase with bifaciality, compared to the 16 p.p. from the simulated silicon cell results. This is in agreement with our earlier study<sup>[18]</sup> and findings by Onno et al.<sup>[13]</sup>. Because of the lower perovskite bandgap for current-matching in the bifacial tandem solar module, the voltage of the cell is also reduced. The lower cell voltage reduces the power conversion efficiency of light received at the front side compared to a monofacial tandem with a higher bandgap, and therefore the yield gain of 13 p.p. with bifaciality is the lowest for all considered technologies.

Because the perovskite and the silicon subcells are electrically independent in the 4-terminal configuration, the bifacial operation does not affect the consideration of the perovskite top cell bandgap. This results in a 43% and 61% higher energy yield for the mono- and bifacial 4-terminal tandem, respectively, an increase of 18 p.p. by bifacial operation. This shows that 4-terminal tandems can utilize bifacial operation slightly better than 2-terminal connections.

Finally, we discuss the results for the 4-terminal “sandwich,” a design that includes two perovskite junctions with a silicon cell in between. Such a configuration is only sensible in bifacial operation because under monofacial operation no light would reach the bottom perovskite cell. Our results suggest that such a device does not improve the energy yield compared to conventional tandem devices. Both, the standard bifacial 2-terminal and 4-terminal tandem solar cells, show higher energy yields. The increased complexity and cost of an additional perovskite junction do not translate into higher energy gains. This is because of the low voltage of the bottom perovskite cell associated with the low light intensity at the back side of the solar cell module.

#### 4. Conclusion

In this work, we presented measured and simulated results for a solar panel array installed on a rooftop in Jerusalem, Israel. Irradiance and solar cell performance data for two sunny days, one in summer, one in winter, were available. We used the experimental performance data of the PERT silicon solar cells to validate the different steps in our model chain. We validated the illumination on the front and back side of the model, the absorbed photocurrent based on optical simulations of the solar cell stack, and finally the electrical performance calculated from a temperature-dependent one-diode model to model the cells open-circuit voltage, FF, and power at maximum power point.

In this study, we confirm earlier findings, that bifacial operation significantly alters the ideal bandgap for 2-terminal tandem solar cells, favoring the potentially more stable lower perovskite bandgaps, while 4-terminal tandem solar cells only show a weak dependence on the bandgap.

Finally, we compared the measured and simulated energy yield of PERT silicon solar cells for two days, and calculated

the expected gain for a situation where the conventional silicon solar panels were replaced by 2-terminal and 4-terminal perovskite/silicon tandem solar cells in mono- and bifacial configuration at the same location. Assuming that current results for small-area perovskites cells can be scaled up in the future, monofacial 2- and 4-terminal tandems could result in 40–45% higher energy yields than monofacial silicon solar cells. Using bifacial tandem solar cells and albedo increasing measures can further increase the power output, with even 54–63% energy yield gain compared to a monofacial silicon solar module. A 4-terminal “sandwich” configuration was introduced, with two perovskite junctions surrounding one silicon cell in the center, but no additional gain was found. The low light intensity in the bottom perovskite possibly limits the performance and overall the device showed no gain compared to classical 2- or 4-terminal tandem cells.

#### Supporting Information

Supporting Information is available from the Wiley Online Library or from the author.

#### Acknowledgements

P.T. thanks the Helmholtz Einstein International Berlin Research School in Data Science (HEIBRIDS) for funding. The authors acknowledge the support from the SNaPSHOTs project in the framework of the German–Israeli bilateral R&D cooperation in the field of applied nanotechnology (grant no. 011O1806) funded by the German Federal Ministry for Education and Research (BMBF) and the National Technological Innovation Authority of the State of Israel. The results were obtained at the Berlin Joint Lab for Optical Simulations for Energy Research (BerOSE) and the Helmholtz Excellence Cluster SOLARMATH of Helmholtz-Zentrum Berlin für Materialien und Energie, Zuse Institute Berlin and Freie Universität Berlin (grant no. ExNet-0042-Phase-2-3).

Open Access funding enabled and organized by Projekt DEAL.

#### Conflict of Interest

The authors declare no conflict of interest.

#### Data Availability Statement

The data that support the findings of this study are available from the corresponding author upon reasonable request.

#### Keywords

bifacial solar cells, energy yield calculations, perovskite/silicon tandem solar cells

Received: January 27, 2022

Revised: May 3, 2022

Published online: June 23, 2022

[1] R. Kopecek, J. Libal, *Nat. Energy* **2018**, *3*, 443.

[2] T. S. Liang, M. Pravettoni, C. Deline, J. S. Stein, R. Kopecek, J. P. Singh, W. Luo, Y. Wang, A. G. Aberle, Y. S. Khoo, *Energy Environ. Sci.* **2019**, *12*, 116.

- [3] ITRPV, *Technical Report, VDMA 2021*, itrpv.vdma.org (accessed: July 2021).
- [4] R. Kopecek, J. Libal, *Energies* **2021**, *14*, 2076, number: 8 Publisher: Multidisciplinary Digital Publishing Institute.
- [5] A. Weselek, A. Ehmann, S. Zikeli, I. Lewandowski, S. Schindele, P. Högy, *Agron. Sustainable Dev.* **2019**, *39*, 35.
- [6] G. M. Tina, F. Bontempo Scavo, L. Merlo, F. Bizzarri, *Appl. Energy* **2021**, *281*, 116084.
- [7] T. Katsaounis, K. Kotsovos, I. Gereige, A. Basaheeh, M. Abdullah, A. Khayat, E. Al-Habshi, A. Al-Saggaf, A. E. Tzavaras, *Renewable Energy* **2019**, *143*, 1285.
- [8] D. Berrian, J. Libal, *Prog. Photovoltaics Res. Appl.* **2020**, *28*, 609.
- [9] S. A. Pelaez, C. Deline, S. M. MacAlpine, B. Marion, J. S. Stein, R. K. Kostuk, *IEEE J. Photovoltaics* **2019**, *9*, 82, conference Name: IEEE Journal of Photovoltaics.
- [10] C. W. Hansen, J. S. Stein, C. Deline, S. MacAlpine, B. Marion, A. Asgharzadeh, F. Toor, in *2016 IEEE 43rd Photovoltaic Specialists Conf. (PVSC)*, IEEE, Portland, OR, USA **2016**, pp. 0138–0143, <https://doi.org/10.1109/PVSC.2016.7749564>.
- [11] B. Marion, S. MacAlpine, C. Deline, A. Asgharzadeh, F. Toor, D. Riley, J. Stein, C. Hansen, in *2017 IEEE 44th Photovoltaic Specialist Conf. (PVSC)*, IEEE, Piscataway, NJ **2017**.
- [12] J. E. Castillo-Aguilella, P. S. Hauser, *IEEE Access* **2016**, *4*, 498, conference Name: IEEE Access.
- [13] A. Onno, N. Rodkey, A. Asgharzadeh, S. Manzoor, Z. J. Yu, F. Toor, Z. C. Holman, *Joule* **2020**, *4*, 580.
- [14] A. Al-Ashouri, E. Köhnen, B. Li, A. Magomedov, H. Hempel, P. Caprioglio, J. A. Márquez, A. B. M. Vilches, E. Kasparavicius, J. A. Smith, N. Phung, D. Menzel, M. Grischek, L. Kegelmann, D. Skroblin, C. Gollwitzer, T. Malinauskas, M. Jošt, G. Matič, B. Rech, R. Schlatmann, M. Topič, L. Korte, A. Abate, B. Stannowski, D. Neher, M. Stollerfoht, T. Unold, V. Getautis, S. Albrecht *Science* **2020**, *370*, 1300.
- [15] R. Schmager, M. Langenhorst, J. Lehr, U. Lemmer, B. S. Richards, U. W. Paetzold, *Opt. Express* **2019**, *27*, A507, publisher: Optical Society of America
- [16] J. Lehr, M. Langenhorst, R. Schmager, F. Gota, S. Kirner, U. Lemmer, B. S. Richards, C. Case, U. W. Paetzold, *Sol. Energy Mater. Sol. Cells* **2020**, *208*, 110367.
- [17] O. Dupré, A. Tuomiranta, Q. Jeangros, M. Boccard, P.-J. Alet, C. Ballif, *IEEE J. Photovoltaics* **2020**, *10*, 714.
- [18] K. Jäger, P. Tillmann, E. A. Katz, C. Becker, *Sol. RRL* **2021**, *5*, 2000628.
- [19] M. De Bastiani, A. J. Mirabelli, Y. Hou, F. Gota, E. Aydin, T. G. Allen, J. Troughton, A. S. Subbiah, F. H. Isikgor, J. Liu, L. Xu, B. Chen, E. Van Kerschaver, D. Baran, B. Fraboni, M. F. Salvador, U. W. Paetzold, E. H. Sargent, S. De Wolf, *Nat. Energy* **2021**, *6*, 167.
- [20] K. Jäger, P. Tillmann, C. Becker, *Opt. Express* **2020**, *28*, 4751.
- [21] P. Tillmann, K. Jäger, C. Becker, *Sustainable Energy Fuels* **2019**, *4*, 254.
- [22] S. A. Pelaez, C. Deline, B. Marion, B. Sekulic, J. Parker, B. McDanold, J. S. Stein, in *Conf. Record of the IEEE Photovoltaic Specialists Conf.*, Vol. *2020-June*, IEEE, Calgary, AB, Canada, ISBN 9781728161150, ISSN 01608371, **2020**, pp. 1757–1759, <https://doi.org/10.1109/PVSC45281.2020.9300379>.
- [23] N. Riedel-Lyngskær, D. Berrian, D. Alvarez Mira, A. Aguilar Protti, P. B. Poulsen, J. Libal, J. Vedde, *Appl. Sci.* **2020**, *10*, 8487.
- [24] R. E. Bird, C. Riordan, *J. Clim. Appl. Meteorol.* **1986**, *25*, 87.
- [25] R. Santbergen, T. Meguro, T. Suezaki, G. Koizumi, K. Yamamoto, M. Zeman, *IEEE J. Photovoltaics* **2017**, *7*, 919.
- [26] K. Jäger, L. Korte, B. Rech, S. Albrecht, *Opt. Express* **2017**, *25*, A473.
- [27] D. P. McMeekin, G. Sadoughi, W. Rehman, C. E. Eperon, M. Saliba, M. T. Hörantner, A. Haghighirad, N. Sakai, L. Korte, B. Rech, M. B. Johnston, L. M. Herz, H. J. Snaith, *Science* **2016**, *351*, 151.
- [28] U. Rau, *Phys. Rev. B* **2007**, *76*, 085303.
- [29] M. T. Hörantner, H. J. Snaith, *Energy Environ. Sci.* **2017**, *10*, 1983.
- [30] B. Chen, S.-W. Baek, Y. Hou, E. Aydin, M. D. Bastiani, B. Scheffel, A. Proppe, Z. Huang, M. Wei, Y.-K. Wang, E.-H. Jung, T. G. Allen, E. V. Kerschaver, F. P. G. de Arquer, M. I. Saidaminov, S. Hoogland, S. D. Wolf, E. H. Sargent, *Nat. Commun.* **2020**, *11*, 1257.
- [31] Y. Hou, E. Aydin, M. De Bastiani, C. Xiao, F. H. Isikgor, D. J. Xue, B. Chen, H. Chen, B. Bahrami, A. H. Chowdhury, A. Johnston, S. W. Baek, Z. Huang, M. Wei, Y. Dong, J. Troughton, R. Jalmood, A. J. Mirabelli, T. G. Allen, E. Van Kerschaver, M. I. Saidaminov, D. Baran, Q. Qiao, K. Zhu, S. De Wolf, E. H. Sargent, *Science* **2020**, *367*, 1135.
- [32] F. Sahli, J. Werner, B. A. Kamino, M. Bräuningner, R. Monnard, B. Paviet-Salomon, L. Barraud, L. Ding, J. J. Diaz Leon, D. Sacchetto, G. Cattaneo, M. Despeisse, M. Boccard, S. Nicolay, Q. Jeangros, B. Niesen, C. Ballif, *Nat. Mater.* **2018**, *17*, 820.
- [33] R. Santbergen, M. R. Vogt, R. Mishima, R. Mishima, M. Hino, H. Uzu, D. Adachi, K. Yamamoto, M. Zeman, O. Isabella, *Opt. Express* **2022**, *30*, 5608.
- [34] M. Jošt, B. Lipovšek, B. Glažar, A. Al-Ashouri, K. Brecl, G. Matič, A. Magomedov, V. Getautis, M. Topič, S. Albrecht, *Adv. Mater.* **2020**, *10*, 2000454.
- [35] A. Rohatgi, K. Zhu, J. Tong, D. H. Kim, E. Reichmanis, B. Rounsaville, V. Prakash, Y. W. Ok, *IEEE J. Photovoltaics* **2020**, *10*, 417.
- [36] M. Jošt, L. Kegelmann, L. Korte, S. Albrecht, *Adv. Mater.* **2020**, *10*, 1904102.
- [37] J. J. Yoo, G. Seo, M. R. Chua, T. G. Park, Y. Lu, F. Rotermund, Y. K. Kim, C. S. Moon, N. J. Jeon, J. P. Correa-Baena, V. Bulović, S. S. Shin, M. G. Bawendi, J. Seo, *Nature* **2021**, *590*, 587.
- [38] E. L. Unger, L. Kegelmann, K. Suchan, D. Sörell, L. Korte, S. Albrecht, *J. Mater. Chem. A* **2017**, *5*, 11401.

## Chapter 6

# Improving the textured interface with FEM and bayeasian optimisation

Perovskites are a promising semiconductor material for solar cell applications in general and tandems in particular. However, multijunction solar cells have been known for several decades and their first commercial usage was in 1997 with the Hughes HS 601HP satellite mission [20]. Traditionally, the high efficiency multijunction solar cells were based in III/V semiconductor materials such as GaAs. While all record efficiency solar cells are using III/V semiconductors[24] the technology is associated with very high manufacturing costs and has so far restricted the adoption to niche applications[19]. Recent successes of researchers at Fraunhofer ISE have renewed interest in multijunction solar cells with top cells from III/V semiconductors on a silicon bottom cell. Combining III/V materials for the top cell with a silicon bottom cell promises the combination of the excellent controllability of III/V semiconductors with the low cost of silicon solar cells. In 2018 Cariou *et al.* presented a III/V on silicon multijunction solar cell with an efficiency of 33.3 %[71], a record at that time, that has meanwhile improved to 35.9 %[24]. The multijunction solar cells are based on a silicon bottom cell with tunnel oxide passivated contacts (TOPcon) and had excellent electrical properties. The planar reference cell only achieved a power convergence efficiency of 31.4 % due to weak absorption of infrared light. By using a metal grating as light trapping structure at the backside of the silicon solar cell the absorption in the infrared region could be improved significantly, leading to the efficiency of 33.3 %.

We first simulate the optical characteristics of the metal grating at the backside of the solar cell and calculate the spectrally resolved absorptance of the solar cells. Comparison of the simulation results with the measured EQE shows a reasonable agreement. Based on the original structure 4 geometrical parameters were derived to optimise the generated photocurrent in the silicon junction of the solar cell. Analysing the sensitivity of the photocurrent towards the geometrical parameters reveal that the most relevant parameters should be highly controllable with laser-interference lithography, the method used to create the texture in the work of Cariou *et al.*. The used techniques are not limited to a specific solar cell design but are applicable to other technologies and with this manuscript we demonstrate a case study how a combination of FEM with Bayesian optimisation can be used to guide the design of optical components in a multijunction solar cell.

### *Supporting information*

The data from the FEM and transfer matrix calculations as well as the measured data used in this publication can be accessed under <https://data.helmholtz-berlin.de/pub/ND000006>

The python code used to recalculate the presented results and reproduce the figures from the manuscript can be access under <https://zenodo.org/record/5013230>



## Optimizing metal grating back reflectors for III-V-on-silicon multijunction solar cells

PETER TILLMANN,<sup>1,2</sup> BENEDIKT BLÄSI,<sup>3</sup> SVEN BURGER,<sup>2,4</sup>   
 MARTIN HAMMERSCHMIDT,<sup>2,4</sup> OLIVER HÖHN,<sup>3</sup> CHRISTIANE  
 BECKER,<sup>1</sup> AND KLAUS JÄGER<sup>1,2,\*</sup>

<sup>1</sup>Dept. Optics for Solar Energy, Helmholtz-Zentrum Berlin für Materialien und Energie, Albert-Einstein-Straße 16, 12489 Berlin, Germany

<sup>2</sup>Computational Nano Optics, Zuse Institute Berlin, Takustraße 7, 14195 Berlin, Germany

<sup>3</sup>Fraunhofer Institute for Solar Energy Systems ISE, Heidenhofstr. 2, 79110 Freiburg, Germany

<sup>4</sup>JCMwave GmbH, 14050 Berlin, Germany

\*klaus.jaeger@helmholtz-berlin.de

**Abstract:** Multi-junction solar cells allow to utilize sunlight more effectively than single junction solar cells. In this work, we present optical simulations of III-V-on-silicon solar cells with a metal grating at the back, which experimentally have reached more than 33% power conversion efficiency. First, we perform simulations with the finite element method and compare them with experimental data to validate our model. We find that accurately modeling the investigated geometrical structure is necessary for best agreement between simulation and experimental measurements. Then, we optimize the grating for maximized light trapping using a computationally efficient Bayesian optimization algorithm. The photo current density of the limiting silicon bottom cell is improved from 13.48 mA/cm<sup>2</sup> for the experimental grating to 13.85 mA/cm<sup>2</sup> for the optimized metal grating. Investigation of all geometrical optimization parameters of the grating (period, height, . . . ) shows that the structure is most sensitive towards the period, a parameter highly controllable in manufacturing by inference lithography. The results show a pathway to exceed the current world record efficiency of the III-V-on-silicon solar cell technology.

Published by The Optical Society under the terms of the [Creative Commons Attribution 4.0 License](https://creativecommons.org/licenses/by/4.0/). Further distribution of this work must maintain attribution to the author(s) and the published article's title, journal citation, and DOI.

### 1. Introduction

The power conversion efficiency of single-junction silicon solar cells is limited to around 29.4% [1]. With the record efficiency of 26.7% [2] there is little room for improvement. The most substantial factor in the limited conversion is the poor utilization of the solar spectrum. The high energy of short-wavelength radiation is only partially utilized by a silicon semiconductor while a large fraction is lost by thermalization. Combining multiple semiconductors in a multijunction solar cell substantially increases the possible efficiency to 49.8% [3] when using a silicon subcell in a triple junction solar cell.

Cariou *et al.* demonstrated a III-V-on-silicon triple junction solar cell with a power conversion efficiency (PCE) of 31.4% and all planar interfaces [4]. The cell was produced by wafer bonding of an epitaxial grown III-V tandem solar cell with a tunnel-oxide passivated contacts (TOPCon) silicon solar cell. The electrical properties of the cell were excellent, however the absorption of IR light was low because silicon is only weakly absorbing between 1000 nm and 1200 nm.

Light management is important to maximize the absorption of incident light in solar cells. Random pyramid-shaped structures are the industrial standard for silicon solar cells and can often be utilized for silicon-based multi-junction solar cells as well [5]. The pyramids prolong the

average light path in the solar cell and therefore increase the absorption in the weakly absorbing regime of silicon, which is called light trapping.

However TOPCon passivation is not compatible with the standard process for random pyramid texturing. Instead, Cariou *et al.* introduced a square-shaped metal grating back reflector fabricated by nano-imprint lithography. This back reflector allowed them to significantly increase the absorbed photocurrent density in the silicon subcell while retaining the excellent passivation properties of the TOPCon. The triple junction solar cell yielded 33.3% PCE [4]. A record at that time, it was meanwhile improved PCE values exceeding 34% [6].

Metal gratings as light-trapping textures were first proposed by Kiess and Morf [7] and more recent studies demonstrated their applicability in highly efficient silicon solar cells [8–10]. Peters *et al.* investigated the influence of the grating geometry on the performance gain of the metal grating [11]. Further, Cordaro *et al.* investigated silver nano-discs in a hexagonal lattice as back reflectors in III-V-on-silicon cells [12].

Metal gratings deflect a fraction of the light, which reaches the back of the solar cell, away from the zeroth reflection order. If the period of the diffraction grating is shorter than the vacuum wavelength, the diffracted light experiences total internal reflection at the front side of the solar cell [see Appendix A]. Hence, absorptance of a solar cell can be substantially improved in the weakly absorbing regime.

In this work we optically simulate triple-junction solar cells with back side gratings similar to the layer stack used by Cariou *et al.* We compare our simulated results with EQE and reflectance measurements to validate the model and show the importance of the geometrical details of the textured interface. Then, we use Bayesian optimization to find geometric parameters that maximize the absorbed photocurrent in the silicon subcell. Bayesian optimization is well suited to find a global extremum of functions where no gradient information is available and which require long computation times [13]. It was used for a variety of applications such as robotics [14], hyper-parameter tuning [15], optical systems [16] and solar cells [17–19].

Next, we discuss the sensitivity of the optimized structure towards the parameters and how this might affect an experimental realization. Last, we briefly discuss alternative optimization targets and how these might effect the final performance of a solar cell with a metal grating as back reflector.

## 2. Modelling optical response of the solar cell with metal grating back reflector

In this section we explain our simulation approach in detail and show results for solar cells with a planar silicon-silver interface and with two different geometrical models of the textured interface. We compare our results with external quantum efficiency (EQE) and reflectance measurements and discuss the importance of the modeling details for the textured interface.

### 2.1. Investigated setup

Figure 1(a) shows a schematic illustration of the solar cell stack simulated in our work. The solar cell consists of three junctions. The upper two junctions are based on direct bandgap materials (GaInP and GaAs) produced by epitaxial growth on the front. These two junctions are combined with a silicon subcell by wafer-bonding. A silver contact is evaporated onto the back of the solar cell that also acts as a reflector for weakly absorbed infrared light.

In a second setup Cariou *et al.* implemented a textured metal grating as back contact. The grating was prepared by nano-imprint lithography (NIL). For the preparation, SU8 photoresist [20] was spin coated onto the poly-Si contact at the back. The photoresist was UV cured after texturing with a PDMS stamp, replicated from a master created by interference lithography [21]. The surface was then treated by reactive ion etching to remove any photoresist between the structures. Finally the grating resulted from filling the gaps of the photoresist with evaporated



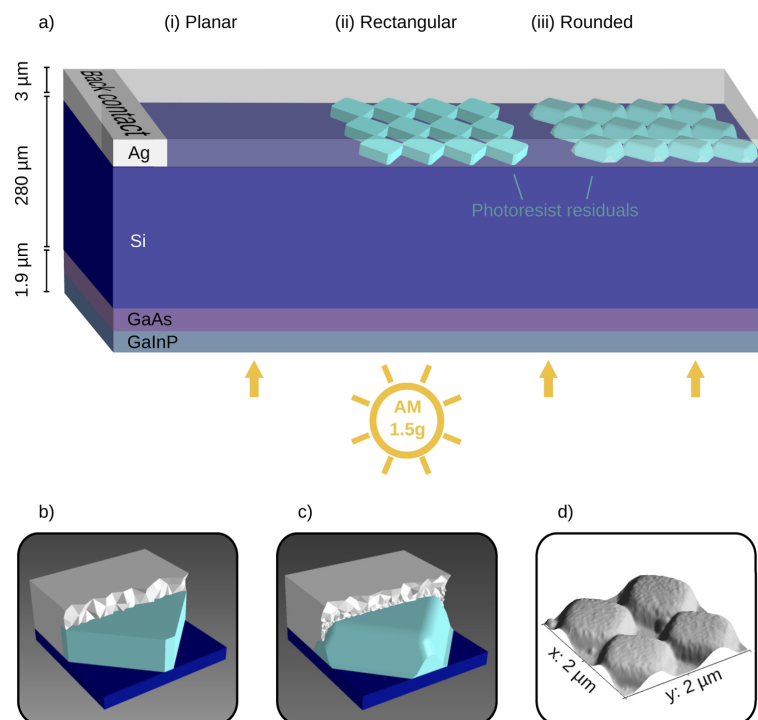


**Fig. 1. Layer stack and interface structures of the optical system.** (a) Schematic illustration of triple junction solar cell stack with three different Si-Ag interface configurations: (i) without periodic grating (planar interface), (ii) idealized grating with rectangular shaped photoresist residuals, (iii) more realistic grating with rounded photoresist residuals. The stack is shown upside down and the incident of the illumination is at the bottom. The rectangular and rounded structures are both used to model the photoresist residuals that remain after nano imprint lithography texturing at the backside of the silicon cell. Mesh grid of the rectangular (b) and round (c) structure as used in the simulation software. (d) Atomic force microscope image of the experimentally implemented grating after NIL patterning of the photo resist before metal evaporation. In the planar samples no photoresist is used in the production process. For more details of the solar cell stack please refer to [4].

silver. Figure 1(d) shows an atomic force microscope image of the surface after texturing the photoresist before the metal contact is evaporated.

Two different model structures are used to simulate the textured solar cell. The rectangular structure shown in Fig. 1(b) is modeled with rectangular side walls (with respect to the base) and approximates the photoresist by intersecting cuboids. This approach is similar to other simulation studies on metal gratings for solar cell applications [22,23]. Reducing the complexity of the texture to cuboids can be necessary because of limitations of the used optical simulation method and might be chosen for ease of implementation. However, this simplification neglects several features of the experimental structure that are visible in electron microscopy images:

- The sidewalls of the photoresist residuals are not perpendicular but have an angle of around  $65^\circ$  between the sidewall and the silicon base.
- Edges and vertices are not sharp but rounded.
- The point of intersection between the cuboid elements is lowered compared to the flat top area.

The rounded structure shown in Fig. 1(c) represents the experimental implemented texture as close as possible. The period of both grating models is 1000 nm and the photoresist structure has a height of 250 nm. The edge length of the cuboid in the rectangular structure is 760 nm. The photoresist residual in the rounded model has a length of 870 nm at the base and 650 nm at the top, resulting in a sidewall angle of around  $65^\circ$ . The edges and vertices of the photoresist block were rounded with a radius of 50 nm, where applicable. All parameters for the simulated geometries were estimated from SEM images.

## 2.2. Numerical simulation of the absorption profile

For simulating the absorption and, subsequently, the absorbed photocurrent density under normal incident AM1.5g [24] illumination we divide the multijunction solar cell stack into three sections.

The transmission, reflection and absorption spectra of the anti-reflective coating, GaInP and GaAs junction, bonding layer and interface to the silicon wafer were previously simulated using a coherent transfer matrix method (TMM) [25]. Due to intellectual property concerns the exact details of the this top layer stack cannot be disclosed.

The absorption in the silicon wafer is calculated with the Beer-Lambert law. The top and bottom silicon tunnel passivated contacts and the polysilicon layers are not considered, instead, the silicon cell is treated as a homogeneous layer.

For modeling of the backside grating we use the finite element method (FEM) software JCMsuite [26]. The optical response was simulated between 950 nm and 1200 nm with a resolution of 10 nm. Below 950 nm almost all light is absorbed in one of the junctions and does not reach the back of the cell.

For computational efficiency, the optical response of the grating is computed for all sources belonging to the same Bloch group [27] in a single simulation. Because the grating is the only non-planar interface in the solar cell stack all diffracted light will remain within orders of the same Bloch group. Consequently, in order to simulate the optical response of the complete solar cell stack only one FEM simulation is required per simulated wavelength. From the FEM Simulation the full scattering matrix of the metal grating is obtained. The scattering matrix connects each incoming to each outgoing diffraction channel. The individual interaction, that takes  $s$  and  $p$  polarization into account, can be described by a Jones matrix with 4 elements. The full scattering matrix (for one wavelength) therefore consists of  $4N \times N$  elements, where  $N$  is the number of propagating diffraction orders. Each interaction with the metal grating redistributes the propagating light into the individual channels of the diffraction orders. Between interactions of the metal grating the absorption of light in the silicon wafer (according to Beer-Lambert law)

and potential transmission and absorption losses in the front layers (from TMM simulation) are calculated. The final result for each wavelength is an absorptance in silicon, parasitic absorptance in the metal and front layers and reflection loss. More details on such formalisms are given in Ref. [28].

From the absorption profile of the three active junctions we calculate the photocurrent. Due to the excellent electric properties of the Si subcell we assume a collection probability of 100%. Therefore the photocurrent in the  $i$ -th subcells is given by

$$J_{\text{ph},i} = e \int_{300 \text{ nm}}^{1200 \text{ nm}} A_i(\lambda) \Phi_{\text{AM 1.5g}}(\lambda) d\lambda \quad (1)$$

with  $e$  as elementary charge,  $A_i(\lambda)$  as the wavelength dependent absorption in the  $i$ -th layer and  $\Phi_{\text{AM 1.5g}}(\lambda)$  as spectral photon flux under AM 1.5g illumination.

### 2.3. Model validation by comparing experimental and simulated solar cell performance

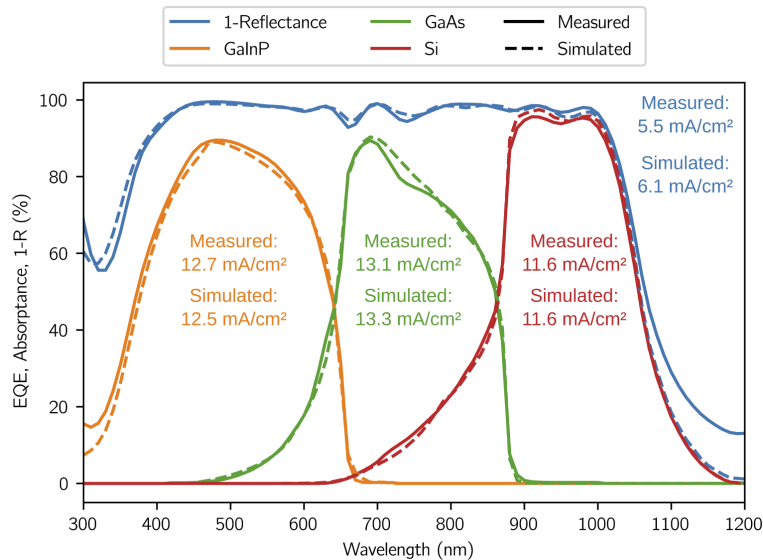
In order to validate our simulation model, we first compare the simulated absorption profiles with experimental external quantum efficiency (EQE) of a fully planar GaInP/GaAs/Si triple junction solar cell device (Fig. 2). To compensate the shading from front contact fingers the incidence light is reduced by 1% for the calculation of the simulated absorption profile. Due to the high reflectivity of the silver front contact fingers 1% of the illumination is added to the simulated reflectance. We assume a collection probability of 100%, allowing us to directly compare measured EQE and simulated absorption profiles.

Experiment and simulation of EQE and absorptance show a very good agreement with only minor deviations in the UV ( $< 350 \text{ nm}$ ) and around  $750 \text{ nm}$ . The reflection also shows good agreement over a wide range of the spectrum, however above  $1000 \text{ nm}$  an overestimation is visible in the simulation. A possible explanation is parasitic absorption in the n-doped polysilicon of the selective top contact, which is not considered in the TMM layer stack. The parasitic absorption in the polysilicon of the selective contact is typically most relevant for wavelength regions below  $500 \text{ nm}$ . However, for strongly doped layers the absorption can increase above  $1000 \text{ nm}$  due to free carrier absorption and can accumulate to several hundred  $\text{nA/cm}^2$  current density [29].

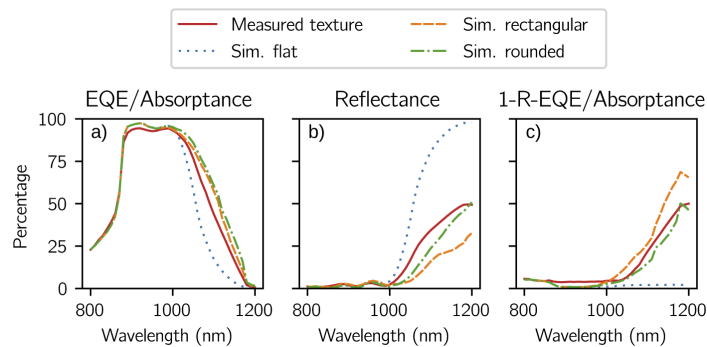
The best planar triple-junction solar cells reached a power conversion efficiency of 31.4% under standard test conditions (STC). The Si junction absorbs a photocurrent density of  $11.6 \text{ mA/cm}^2$  which is significantly less compared to the GaInP and GaAs with  $12.7 \text{ mA/cm}^2$  and  $13.1 \text{ mA/cm}^2$ , respectively, and therefore limiting the short-circuit current density of the complete cell to  $11.6 \text{ mA/cm}^2$ . The reflection losses for light above  $1050 \text{ nm}$  are very large, with over 60% at  $1100 \text{ nm}$ , because of the low absorption coefficient of silicon in this wavelength region. Most of the reflected light is not directly reflected at the illuminated side of the solar cell but passes the cell, is reflected at the silver back contact and subsequently leaves the cell at the front.

Figure 3 shows the EQE/absorptance, reflectance and parasitic absorption losses of the measured cell with periodic metal grating as back reflector, and the respective simulations using a planar rear contact, as well as a periodic grids comprised of rectangular and rounded features. Implementing a textured interface at the back side significantly improves the absorption for wavelengths longer than  $1000 \text{ nm}$ . All simulated absorption profiles slightly overestimate around  $900 \text{ nm}$  due to an underestimation of the parasitic absorption in the top layer stack not considered appropriately by the TMM calculation. Moreover, the simulated textures overestimate the absorptance in the range from  $1050$  to  $1150 \text{ nm}$ . The EQE curve of the rectangular texture is very close to the rounded one and slightly closer to the measured EQE of the real device. However, the two simulated textures show significant differences in reflectance and parasitic absorption.

Table 1 shows the photocurrent density of the silicon subcell and the equivalent current density for the reflection and parasitic absorption above  $1000 \text{ nm}$  for simulations and measurements of



**Fig. 2.** Comparison of experiment and simulation for a planar GaInP/GaAs/Si triple junction solar cell (without metal grating). Measured external quantum efficiency (EQE) (solid lines) and modeled absorbance (dashed lines) of the GaInP, GaAs and Si subcells in the triple junction device with planar rear side, as well as  $(1 - R)$  of the whole device. For the simulated absorbance and reflectance we compensate 1% shading arising from contact fingers at the sun-facing front side of the device.



**Fig. 3.** Comparing simulation and measurement results of the textured cell with planar simulation as reference. (a) EQE measurement and simulated absorbance of the silicon subcell, as well as (b) reflectance ( $R$ ) and (c) parasitic absorption (calculated from  $1 - R - \text{EQE}/\text{absorbance}$ ) of the GaInP/GaAs/Si triple junction solar cell with periodic grating at the rear side. The solid line represents data from the measured cell, dashed and dotted lines show results from simulations.

the textured and planar cells. For the simulated cells the difference to the experimental result is shown in brackets.

**Table 1. Overview of experimental and simulation results for the photocurrent density of the Si-junction  $J_{ph}$ , reflection  $J_{ph, refl}$  and parasitic absorption  $J_{ph, para}$ . Reflection and parasitic absorption are integrated for wavelengths from 1000 nm to 1200 nm to highlight the effect of the metal grating. For the simulated results the differences compared to the experimental results are shown in brackets.**

	$J_{ph}$ (mA/cm <sup>2</sup> )	$J_{ph, refl}$ (mA/cm <sup>2</sup> )	$J_{ph, para}$ (mA/cm <sup>2</sup> )
Planar (Exp)	11.6	4.3	0.9
Planar (Sim)	11.6 (0)	5.0 (+0.7)	0.2 (-0.7)
Texture (Exp)	12.7	2.2	1.7
Rounded texture (Sim)	13.5 (+0.8)	1.7 (-0.5)	1.4 (-0.3)
Rectangular texture (Sim)	13.2 (+0.5)	1.1 (-1.1)	2.3 (+0.6)

The rectangular texture shows a reflectance loss that is about half that of the measured cell with a cumulative reflection of 1.1 mA/cm<sup>2</sup> compared to 2.2 mA/cm<sup>2</sup> for the measured cell. The rounded texture is closer to experiment but still underestimates the reflection by 0.5 mA/cm<sup>2</sup>. The underestimation of reflection is likely due to an overestimation of the diffraction efficiency of the silver grating. In other words, the amount of light that is reflected back into the zeroth order, which can escape from the solar cell stack, is underestimated in the simulations.

The simulated absorption profiles of the rounded and rectangular texture are close to each other because the rectangular texture partially compensates the strong underestimation in reflectance by overestimating the parasitic absorption. While the parasitic absorption is slightly underestimated in the rounded simulation with a difference of -0.3 mA/cm<sup>2</sup> compared to the measurement, the rectangular model shows an overestimation of 0.6 mA/cm<sup>2</sup>.

In summary, in terms of absorptance the rounded and rectangular models perform very similar but a more detailed analysis of reflectance and parasitic absorption shows significant differences and a better agreement between rounded model and experimental measurements. These results highlight the importance of accurately modeling the scattering geometry. There are several possible explanations for the difference in absorption, reflectance and parasitic absorption between the rounded model and the experimental cell: The experimental cell has a micro-rough interface between photoresist and silver that is not present in the model. It seems plausible that this roughness could introduce additional parasitic absorption and decrease the resulting EQE. However, Hauser *et al.* showed with an identical structure that a different etching process yielding very smooth surfaces does not change the EQE [30]. Another possible explanation is the uncertainty of the refractive index data for silver. Published datasets show significant differences in the wavelength region of 1000 nm even so they are determined using planar interfaces [31]. Evaporating silver onto a micro-structured substrate might introduce additional uncertainties on the optical properties of the resulting film.

### 3. Optimizing the metal grating back reflector

As discussed above, the metal grating implemented by Cariou *et al.* significantly increased the absorbed photocurrent density in the silicon subcell from 11.6 to 12.7 mA/cm<sup>2</sup>, improving the overall power conversion efficiency from 31.4% to 33.3%. The grating showed high diffraction efficiency (defined as the fraction of the light diffracted into non-zero orders) without degrading the excellent passivating properties of the contact layers [25]. However, two major loss mechanisms limit the quantum efficiency, when a metallic diffraction grating is used as backside reflector. First, on every interaction with the grating a certain fraction of light will be parasitically absorbed by the metal. Second, another fraction of the light will be redirected into the zeroth order and

can subsequently leave the solar cell at the front side. For a high-performance grating the amount of parasitic absorption in the metal and the escape of light through the zeroth order channel must be minimal. The following optimization aims at finding a grating geometry, where these losses are minimized.

Based on the rounded structure introduced in Section 2., we simultaneously optimized four geometrical parameters to maximize the absorbed photocurrent density in the silicon junction using a Bayesian optimization algorithm [32]. The choice of an optimal optimization algorithm strongly depends on the underlying problem. While Bayesian optimization is often regarded as highly efficient in terms of needed function evaluations [33] different benchmarking studies showed mixed results when compared to other global optimization procedures [34,35]. However, a study by Schneider *et al.* found that Bayesian optimization was highly suitable for numerical optimization of nano-optical systems and significantly outperformed particle swarm, differential evolution and downhill simplex in each investigated setup [32].

In principle, Bayesian optimization consists of two steps: first, an interpolation model approximates the target function and its uncertainty (based on previously evaluated data points). Second, an acquisition function determines the next query point from the interpolation model. After evaluating the function for the queried data point the interpolation model is updated and the next step can be computed with the acquisition function. This cycle is repeated until a specified number of steps or a convergence criterion is reached. The software package for Bayesian optimization provided by JCMSuite was used with a Gaussian process as interpolation model and expected improvement as acquisition function [32].

Table 2 shows the range and constraints of the parameters used to optimize the performance of the silver grating. The bottom width is restricted to be smaller than the period. With increasing size of the bottom width the area of the silicon backside that is covered by the photoresist residuals also increases. However there needs to be a certain contact area between the silicon wafer and the silver back contact. Because of the rotation of  $45^\circ$  between the base of the photoresist residual and the unit cell the minimal contact area between silicon and silver is 17.5% by enforcing that the bottom width is equal or smaller than the period. To prevent an overhanging side wall of the photoresist (to ensure manufacturability) the top width is restricted to be smaller than the bottom width.

**Table 2. Free optimization parameters and their ranges and constraints.**

	Range (nm)	Constraint
Height	100–500	—
Period	100–1400	—
Bottom Width	100–1400	< Period
Top Width	100–1400	< Bottom Width < Period

The optimization procedure was split into two phases: first, 100 random geometries were simulated to provide an overview of the parameter landscape. This is not strictly necessary for the optimization but can help with the subsequent analysis of the results. Additionally, Bayesian optimization also benefits from knowing random geometries. In the second phase, 400 iterations of Bayesian optimization were performed. Figure 4 shows the FEM unit cell of the experimentally derived configuration (left) and the unit cell of the optimized grating (right). Table 3 shows the parameters and the resulting photocurrent generated in the silicon sub cell of both configurations.

Compared to the experimental structure the optimized version is slightly higher and has a smaller period, a smaller bottom width and a considerably smaller top width. The contact area of the optimized configuration was reduced to about 20% from 30% of the experimental structure due to the changes of bottom width and period. Also the sidewall angle is less steep in the

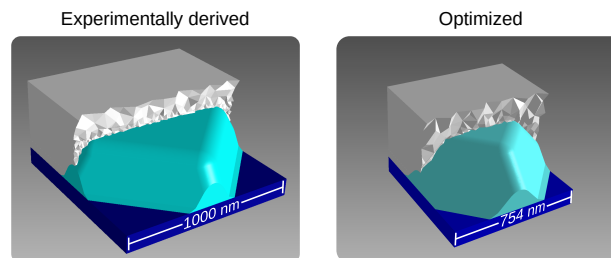


**Fig. 4.** Structure of the FEM unit cell for the simulation of the experimentally derived configuration (left) and the structure yielding the highest photocurrent in the Si junction after optimization.

**Table 3. Parameter range and constraints of the optimization.**

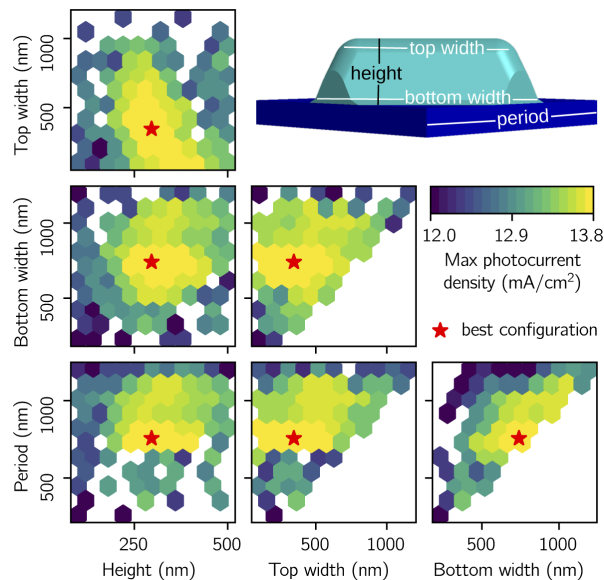
	Height (nm)	Period (nm)	Bottom Width (nm)	Top Width (nm)	Photocurrent density (mA/cm <sup>2</sup> )
Experimentally derived	250	1000	870	650	<b>13.48</b>
Optimized	296	755	740	345	<b>13.86</b>

optimum than in the experimentally derived configuration. Looking from the top onto the unit cell, the area covered by the sidewalls is dominating and only smaller areas are covered by the planar top of the photoresist residual and the silicon-silver interface.

Figure 5 shows the optimization landscape where each of the six hexbin plots represents a combination of two geometrical parameters. Each hexagonal element shows the maximum photocurrent density generated in the silicon subcell and the red star marks the configuration with the highest photocurrent density. Due to the parameter constraints no configuration in the bottom right is sampled for combinations involving bottom width, top width and period because bottom width and top width are restricted to be lower than the period.

Overall, there seems to be a weak interdependence between the different parameters. For combinations of bottom width/height, top width/height, period/height and period/top width choosing one parameter has only small or no effect on the optimal choice of the second parameter. The only pairs showing visible interdependence are top width/height and period/bottom width. The top width/height pair has a negative correlation, resulting in a lower top width with increasing height for optimal combinations. Hence, the structure tends to have a somewhat stable sidewall angle for optimal variations of either top/width or height. On the other hand, period and bottom width are positively correlated. High performing configurations tend to be close to the diagonal, which results in a high covering ratio of photoresist on the silicon wafer. This might even negatively affect the electrical performance of the solar cell due to an increasing series resistance of the back contact resulting from a smaller contact area of the silver with the silicon wafer.

For a period above 1000 nm the gratings are trapping a decreasing fraction of light and in turn the absorbed photocurrent is reduced. In order to trap light diffracted into the first order (or higher) by total internal reflection the period of the grating has to be smaller than the free space wavelength (see Appendix A). Because the backside grating typically strongly diffracts into the first order and the relevant wavelength for light trapping starts above 1000 nm, gratings with a period larger than 1000 nm show low light-trapping performance. Because the parameters top width and bottom width are constraint to be smaller than the period they also lead to weak performance above 1000 nm.



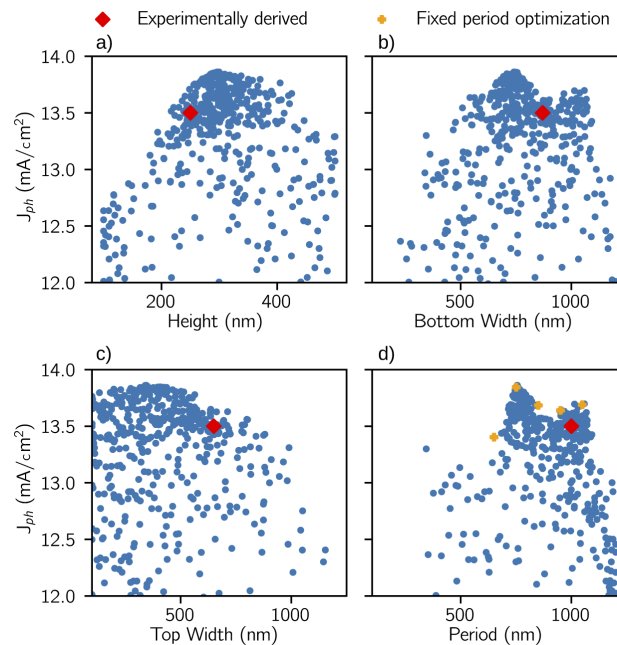
**Fig. 5.** Illustrating the dependence of the photocurrent density on the geometrical parameters and their interdependence for all configurations simulated during the optimization procedure. The six subfigures show each a combination of two parameters where every hexagon represents the maximum photocurrent that was achieved within its extent.

Figure 6 shows the photocurrent density of each configuration as a function of the four geometric parameters. The height shows a broad maximum with very efficient scattering structures for heights between 250 and 350 nm. The top width shows also a broad maximum with an even wider range of 150–500 nm. The period has two distinct sharp maxima, with a local optimum around 1000 nm and the global optimum at around 750 nm. The parameter setting corresponding to the experimental structure by Cariou *et al.* is located in the local maximum of 1000 nm and improvements of the current density might be achieved by switching to a period of 750 nm. The presence of distinct maxima for different periods is similar to results from Peters *et al.* where the height and period of related structures were optimized and local maximum were found around a period of 350 and 730 nm and the global maximum was at 990 nm [11].

To verify the double peak characteristic and exclude the possibility of an optimisation artefact we ran five additional optimizations with a fixed period between 650 and 1050 nm. For each period we performed calculations with 10 random configurations and 40 optimization iterations each. The optimal photocurrent density of these experiments is marked with orange crosses in Fig. 6 d) and confirms the double peak characteristics. The so-found optima lay on top or very close to the existing datapoints of the optimization without constrained period. The datapoint at 950 nm lays in the photocurrent density "valley" between the global maximum at 750 nm and the local maximum at 1050 nm.

The graph for the photocurrent density as a function of the bottom width also shows a double peak, however because the period and the bottom width are not completely independent of each





**Fig. 6.** Photocurrent density  $J_{ph}$  generated in the silicon subcell in dependence of the geometric parameters (a) height, (b) bottom width, (c) top width, and (d) period for all configurations simulated during optimization. The red diamond marks the simulation that was performed with the parameters from the experimentally derived configuration. The orange crosses mark the optimum from optimizations with a fixed period.

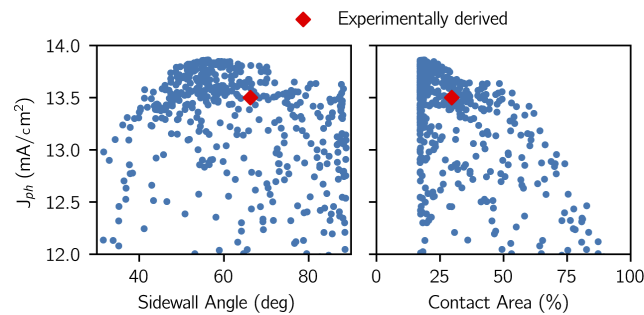
other (the bottom width needs to be smaller than the period) this pattern might just reflect the interdependence between the two parameters as already visible in Fig. 5.

Figure 7 shows scatter plots of the sidewall angle and the contact area, two parameters that can be derived from the other four parameters. Even though the optimized structure shown in Fig. 4 clearly has less steep side walls compared to the experimental structure the side wall angle does not seem to be a critical parameter. This agrees with the broad maximum of the top width. While period and bottom width should be close to 750 nm for optimal performance the top width can be between 150–500 nm without a negative effect on the photocurrent density.

The contact area depends on the ratio of period and bottom width. Because the photocurrent density strongly depends on both these parameters the contact area also shows a narrow maximum at around 20%. In an experimental cell this might have a negative impact on the contact resistance.

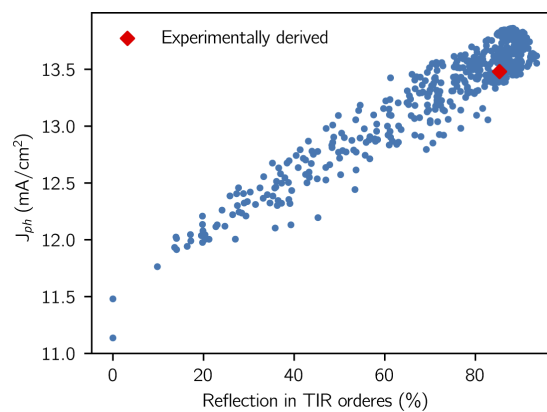
To further analyse the relevant properties that determine the performance of the metal gratings, we investigate the effect of total internal reflection (TIR) of diffracted light. Light diffracted at the backside grating into a non-zero order will often experience TIR (see Appendix A) and therefore its pathway and absorption in the silicon will be increased.

Figure 8 shows the photocurrent density as a function of reflections into TIR orders (averaged over 1000–1200 nm wavelength). The percentage of light directed into TIR orders strongly correlates with the resulting photocurrent density. However, if only configurations with TIR



**Fig. 7.** Photocurrent density  $J_{ph}$  over sidewall angle (a) and electrical contact area between silver back and silicon wafer (b) for all simulated configuration. The red diamond marks the simulation that was performed with the parameters from the experimentally derived configuration.

orders above 80% are considered, the correlation is significantly lower. For reflectance values around 90% a variation of the photocurrent density of around 0.5 mA/cm<sup>2</sup> can be observed. The reason for this is that the light in the TIR orders can be diffracted into an outcoupling direction at further interactions with the grating. Because of the reciprocity of optical systems, the incoupling efficiency for a specific order is equal to its outcoupling efficiency (e.g. if 10% of the light from normal incidence (order zero) is directed into one channel of the first order, 10% of the light incident from that channel will be directed into the zeroth order during the next interaction). If the diffracted light is concentrated into few orders with high efficiency on the first interaction with the grating the same efficiency will apply to out coupling into the zeros order on the second interaction.



**Fig. 8.** Photocurrent density  $J_{ph}$  vs reflection into total internal reflected (TIR) orders for all configuration simulated during optimization. The reflection is averaged over the wavelength range of 1000–1200 nm. The red diamond marks the simulation that was performed with the parameters from the experimentally derived configuration.

Therefore, the reflectance into TIR orders is a suitable parameter to discriminate between good and bad performing metal grating configurations but is not sufficient to distinguish between good and excellent gratings. The metal grating configuration with the highest TIR order reflectance of 94.0% shows a photocurrent density of 13.6 mA/cm<sup>2</sup>, compared to 13.5 mA/cm<sup>2</sup> for the experimentally derived and 13.8 mA/cm<sup>2</sup> for the optimized configuration. If the TIR reflectance were chosen as sole optimization criterion the current gain would have been limited to about one third compared to a full computation of the photocurrent density.

#### 4. Conclusions

In this work, we performed optical simulations of III-V-on-silicon multijunction solar cells with a silver grating at the back. Two main loss mechanisms limiting the light trapping efficiency were identified: parasitic absorption in the silver back contact and back-reflected light escaping through the zeroth-order diffraction. We showed the importance of accurately modeling the used structure to best reproduce the experimental results with optical simulations.

By applying a Bayesian optimization algorithm we optimized the geometric structure of the metal grating to increase the absorbed photocurrent density in the silicon junction—so far the limiting junction of the monolithic triple junction device. The obtained geometrical parameters of the optimized metal grating partly deviated considerably from the initial experimental configuration. In our simulations we were able to improve the photocurrent density from 13.48 mA/cm<sup>2</sup> for the experimentally derived grating geometry to 13.86 mA/cm<sup>2</sup> for the optimized grating. This corresponds to a gain of 0.37 mA/cm<sup>2</sup> or a relative increase of the photocurrent density in the silicon junction by 2.8%.

Further, we analyzed the sensitivity of the optimized metal grating structure with respect to four geometrical parameters: period, height, as well as top and bottom width of the grating features. We found that the period is the most important parameter. From an experimental perspective it is a well controllable parameter.

Finally, we investigated the dependence of the photocurrent density in the silicon subcell on the TIR order reflection of the metal grating. We found a strong correlation. However, to identify high performing metal gratings the TIR order reflection does not suffice.

#### Appendix A — Light trapping by total reflection of diffracted light

The diffractive grating at the back of the solar cell scatters normally incident light away from the interface normal. If the diffraction angle is sufficiently large already light from the first order is trapped by total internal reflection. Figure 9 illustrates the setup and condition for total internal reflection, which is present, when the period of the grating is larger than the vacuum wavelength of the illuminating light. This relationship can be derived by combining the critical angle for total reflection, which is derived from Snell's law of refraction, with the formula for constructive interference at a grating. The constructive interference of the propagating light in the silicon media of the wafer is given by

$$m \frac{\lambda_{Air}}{n_{Si}} = m \lambda_{Si} = d \sin(\theta_d) \quad (2)$$

with  $m$  as reflection order,  $\lambda$  as wavelength,  $n$  as refractive index,  $d$  as the lattice constant and  $\theta_d$  as the diffraction angle. The critical angle for total reflection from the silicon wafer into the air above the cell is given by

$$\sin(\theta_c) = \frac{n_{Air}}{n_{Si}} = \frac{1}{n_{Si}} \quad (3)$$

with  $\theta_c$  as critical angle and  $n$  as refractive index. Combining Eqs. (2) and (3) shows that the diffraction angle  $\theta_d$  is equal to the critical angle  $\theta_c$  for total reflection if the free space wavelength

$\lambda$  is equal to the lattice constant  $d$ .

$$m = 1 \Rightarrow \sin(\theta_c) = \frac{d}{\lambda_{\text{Air}}} \sin(\theta_d)$$

$$\lambda = d \Rightarrow \sin(\theta_c) = \sin(\theta_d)$$

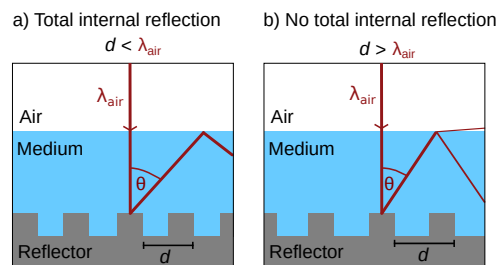


**Fig. 9. Illustrating the trapping of light by total internal reflection.** (a) If the period  $d$  of the metal grating is smaller than the vacuum wavelength first (and higher) order diffracted light will be trapped by total internal reflection. (b) If the period  $d$  of the metal grating is larger than the vacuum wavelength some proportion of the first order diffracted light will escape at the medium/air interface.

**Funding.** Helmholtz Einstein International Berlin Research School in Data Science; Bundesministerium für Wirtschaft und Technologie (0324247); Bundesministerium für Bildung und Forschung (05M20ZBM); Helmholtz Excellence Network SOLARMATH (ExNet-0042-Phase-2-3).

**Acknowledgements.** We thank Philipp-Immanuel Schneider from JCMwave for advice in the implementation and interpretation of Bayesian optimization results. The results were obtained at the Berlin Joint Lab for Optical Simulations for Energy Research (BerOSE) of Helmholtz-Zentrum Berlin für Materialien und Energie, Zuse Institute Berlin, and Freie Universität Berlin.

**Disclosures.** The authors declare no conflict of interest.

**Data availability.** Data underlying the results presented in this paper is available [36]. Python code that allows to generate the figures in this paper from the raw data and recalculate the photocurrent density in the SI junction is available [37].

## References

1. A. Richter, M. Hermle, and S. W. Glunz, "Reassessment of the Limiting Efficiency for Crystalline Silicon Solar Cells," *IEEE J. Photovoltaics* **3**(4), 1184–1191 (2013).
2. K. Yoshikawa, H. Kawasaki, W. Yoshida, T. Irie, K. Konishi, K. Nakano, T. Uto, D. Adachi, M. Kanematsu, H. Uzu, and K. Yamamoto, "Silicon heterojunction solar cell with interdigitated back contacts for a photoconversion efficiency over 26%," *Nat. Energy* **2**(5), 17032 (2017).
3. S. Abdul Hadi, E. A. Fitzgerald, and A. Nayfeh, "Theoretical efficiency limit for a two-terminal multi-junction step-cell using detailed balance method," *J. Appl. Phys.* **119**(7), 073104 (2016).
4. R. Cariou, J. Benick, F. Feldmann, O. Höhn, H. Hauser, P. Beutel, N. Razek, M. Wimplinger, B. Bläsi, D. Lackner, M. Hermle, G. Siefert, S. W. Glunz, A. W. Bett, and F. Dimroth, "III–V-on-silicon solar cells reaching 33% photoconversion efficiency in two-terminal configuration," *Nat. Energy* **3**(4), 326–333 (2018).
5. S. Fan, Z. J. Yu, R. D. Hool, P. Dhingra, W. Weigand, M. Kim, E. D. Ratta, B. D. Li, Y. Sun, Z. C. Holman, and M. L. Lee, "Current-Matched III–V/Si Epitaxial Tandem Solar Cells with 25.0% Efficiency," *Cell Rep. Phys. Sci.* **1**(9), 100208 (2020).
6. S. Glunz, F. Dimroth, M. Hermle, J. Benick, F. Predan, B. Bläsi, A. Fell, A. Richter, H. Hauser, O. Höhn, D. Lackner, P. Schygulla, and R. Müller, "Silicon-Based Monolithic Triple-Junction Solar Cells with Conversion Efficiency >34%," *37th European Photovoltaic Solar Energy Conference and Exhibition* pp. 574–578 (2020).
7. H. Kiess and R. Morf, "Light Trapping In Solar Cells And Determination Of The Absorbed Energy By Calorimetry," in *Optical Materials Technology for Energy Efficiency and Solar Energy Conversion VIII*, vol. 1149 C.-G. Granqvist and C. M. Lampert, eds. (SPIE, 1989), p. 124.

8. J. Eisenlohr, N. Tucher, H. Hauser, M. Graf, J. Benick, B. Bläsi, J. C. Goldschmidt, and M. Hermle, "Efficiency increase of crystalline silicon solar cells with nanoimprinted rear side gratings for enhanced light trapping," *Sol. Energy Mater. Sol. Cells* **155**, 288–293 (2016).
9. B. Bläsi, N. Tucher, J. Eisenlohr, B. G. Lee, J. Benick, H. Hauser, M. Hermle, and J. C. Goldschmidt, "Rear side gratings for silicon solar cells: efficiency enhancement finally demonstrated," in *Photonics for Solar Energy Systems VI*, vol. 9898 R. B. Wehrspohn, A. Gombert, and A. N. Sprafke, eds. (SPIE, 2016), p. 98980A.
10. O. Höhn, H. Hauser, N. Tucher, R. Müller, and B. Bläsi, "Modeling and realization of photonic structures for silicon-based tandem solar cells," in *Physics, Simulation, and Photonic Engineering of Photovoltaic Devices IX*, vol. 11275 A. Freundlich, M. Sugiyama, and S. Collin, eds. (SPIE, 2020), p. 1.
11. M. Peters, M. Rüdiger, H. Hauser, M. Hermle, and B. Bläsi, "Diffraction gratings for crystalline silicon solar cells—optimum parameters and loss mechanisms," *Prog. Photovolt: Res. Appl.* **20**(7), 862–873 (2012).
12. C. E. A. Cordaro, N. Tucher, S. Tabernig, H. Hauser, O. Höhn, R. Müller, B. Bläsi, and A. Polman, "Plasmonic and Mie scattering in nanopatterned back reflectors for III–V-on-silicon solar cells (Conference Presentation)," in *Photonics for Solar Energy Systems VIII*, vol. 11366 J. C. Goldschmidt, A. N. Sprafke, and G. Pandraud, eds. (SPIE, 2020), p. 6.
13. B. Shahriari, K. Swersky, Z. Wang, R. P. Adams, and N. de Freitas, "Taking the Human Out of the Loop: A Review of Bayesian Optimization," *Proc. IEEE* **104**(1), 148–175 (2016).
14. A. Cully, J. Clune, D. Tarapore, and J.-B. Mouret, "Robots that can adapt like animals," *Nature* **521**(7553), 503–507 (2015).
15. J. Snoek, H. Larochelle, and R. P. Adams, "Practical Bayesian Optimization of Machine Learning Algorithms," (2012).
16. P.-I. Schneider, X. G. Santiago, C. Rockstuhl, and S. Burger, "Global optimization of complex optical structures using Bayesian optimization based on Gaussian processes," *Proc. SPIE* **103350**, 103350O (2017).
17. H. C. Herbol, W. Hu, P. Frazier, P. Clancy, and M. Poloczek, "Efficient search of compositional space for hybrid organic–inorganic perovskites via Bayesian optimization," *npj Comput. Mater.* **4**(1), 51 (2018).
18. H. Abdelrahman, F. Berkenkamp, J. Poland, and A. Krause, "Bayesian optimization for maximum power point tracking in photovoltaic power plants," in *2016 European Control Conference, ECC 2016*, (Institute of Electrical and Electronics Engineers Inc., 2017), pp. 2078–2083.
19. P. Tillmann, K. Jäger, and C. Becker, "Minimising levelised cost of electricity of bifacial solar panel arrays using bayesian optimisation," *Sustainable Energy Fuels* **4**(1), 254–264 (2020).
20. J. M. Shaw, J. D. Gelorme, N. C. LaBianca, W. E. Conley, and S. J. Holmes, "Negative photoresists for optical lithography," *IBM J. Res. Dev.* **41**(1.2), 81–94 (1997).
21. A. J. Wolf, H. Hauser, V. Kübler, C. Walk, O. Höhn, and B. Bläsi, "Origination of nano- and microstructures on large areas by interference lithography," in *Microelectronic Engineering*, vol. 98 (Elsevier, 2012), pp. 293–296.
22. A. Mellor, I. Tobias, A. Mart, and A. Luque, "A numerical study of Bi-periodic binary diffraction gratings for solar cell applications," *Sol. Energy Mater. Sol. Cells* **95**(12), 3527–3535 (2011).
23. M. Wellenzohn and R. Hainberger, "Light trapping by backside diffraction gratings in silicon solar cells revisited," *Opt. Express* **20**(S1), A20 (2012).
24. "IEC:60904-3: Photovoltaic devices - Part 3: Measurement principles for terrestrial photovoltaic (PV) solar devices with reference spectral irradiance data," (2008).
25. B. Bläsi, O. Höhn, H. Hauser, R. Cariou, J. Benick, F. Feldmann, P. Beutel, D. Lackner, M. Hermle, G. Siefert, S. W. Glunz, A. W. Bett, F. Dimroth, and N. Tucher, "Photonic structures for III–V//Si multijunction solar cells with efficiency >33%," in *Photonics for Solar Energy Systems VII*, vol. 10688 R. B. Wehrspohn and A. N. Sprafke, eds. (SPIE, 2018), p. 2.
26. J. Pomplun, S. Burger, L. Zschiedrich, and F. Schmidt, "Adaptive finite element method for simulation of optical nano structures," *Phys. Status Solidi B* **244**(10), 3419–3434 (2007).
27. S. Bloch, "Application of the dilogarithm function in algebraic k-theory and algebraic geometry," *Proc. Intern. Symp. on Algebraic Geometry, Kyoto, 1977* (1978).
28. K. Jäger, G. Köppel, M. Hammerschmidt, S. Burger, and C. Becker, "On accurate simulations of thin-film solar cells with a thick glass superstrate," *Opt. Express* **26**(2), A99 (2018).
29. S. Reiter, N. Koper, R. Reineke-Koch, Y. Larionova, M. Turcu, J. Krügener, D. Tetzlaff, T. Wietler, U. Höhne, J. D. Köhler, R. Brendel, and R. Peibst, "Parasitic Absorption in Polycrystalline Si-layers for Carrier-selective Front Junctions," in *Energy Procedia*, vol. 92 (Elsevier Ltd, 2016), pp. 199–204.
30. H. Hauser, O. Höhn, R. Müller, N. Tucher, K. Mühlbach, R. da Silva Freitas, J. Benick, M. Hermle, and B. Bläsi, "Polymer-Based Rear Side Light Trapping Structures for Silicon-Based Tandem Solar Cells," *36th European Photovoltaic Solar Energy Conference and Exhibition* pp. 749–752 (2019).
31. Y. Jiang, S. Pillai, and M. A. Green, "Re-evaluation of literature values of silver optical constants," *Opt. Express* **23**(3), 2133 (2015).
32. P. I. Schneider, X. Garcia Santiago, V. Soltwisch, M. Hammerschmidt, S. Burger, and C. Rockstuhl, "Benchmarking Five Global Optimization Approaches for Nano-optical Shape Optimization and Parameter Reconstruction," *ACS Photonics* **6**(11), 2726–2733 (2019).
33. R. L. Riche and V. Picheny, "Revisiting bayesian optimization in the light of the coco benchmark," (2021). ArXiv: 2103.16649.

34. O. S. Steinholtz, "A Comparative Study of Black-box Optimization Algorithms for Tuning of Hyper-parameters in Deep Neural Networks," Tech. rep., Luleå University of Technology, Department of Engineering Sciences and Mathematics. (2018).
35. T. D. H. D. S. Group, C. Balázs, M. van Beekveld, S. Caron, B. M. Dillon, B. Farmer, A. Fowlie, E. C. Garrido-Merchán, W. Handley, L. Hendriks, G. Jóhannesson, A. Leinweber, J. Mamuzić, G. D. Martinez, S. Otten, P. Scott, R. R. de Austri, Z. Searle, B. Stienen, J. Vanschoren, and M. White, "A comparison of optimisation algorithms for high-dimensional particle and astrophysics applications," (2021). ArXiv: 2103.16649.
36. P. Tillmann, B. Bläsi, S. Burger, M. Hammerschmidt, O. Höhn, C. Becker, and K. Jäger, "Data underlying 'Optimizing metal grating back reflectors for III-V-on-silicon multijunction solar cells'," HZB Data Service: 2021, <https://doi.org/10.5442/ND000006>.
37. P. Tillmann, B. Bläsi, S. Burger, M. Hammerschmidt, O. Höhn, C. Becker, and K. Jäger, "Python code reproducing results from 'Optimizing metal grating back reflectors for III-V-on-silicon multijunction solar cells'," Version 1, Zenodo 22 June 2021, <https://doi.org/10.5281/zenodo.5013230>.

## Chapter 7

# Optimizing the geometry of bifacial solar cells considering the area costs

The usage of bifacial solar cells is increasingly becoming mainstream because they help to increase the electricity production per used module with little to no additional manufacturing cost[110]. Because bifacial modules require illumination at the backside to increase the yield, they are mostly found in large PV free field installations, where wide rows of modules are placed in front of each other. Two critical parameters that determine the bifacial gain in such installations are the tilt angle of the modules and the distance between rows of modules[101]. There is an optimal tilt angle in terms of energy yield if the other geometrical parameters are fixed. The same is not true for the row to row distance (also called row spacing), where the energy yield will always increase for larger distances[99]. It is, however, impractical and cost inefficient to use very wide row spacings and cover large areas with only a few modules. To balance the trade-off between land usage and higher energy yield we use an economical model that includes costs of land usage. We calculate the levelized cost of electricity over the lifetime of a PV power plant and optimize the geometry of the solar cell rows using Bayesian optimization. To calculate the energy yield a very simple solar cell model is used where we assume a fixed power convergence efficiency of 20 % at the front and 18 % at the back side. With this manuscript, we show the practical usability of the bifacial illumination model. We model the optimal geometry for several locations across a wide range of climate zones, assuming different land costs scenarios. This shows a clear trend of lower row spacing and lower tilt angles in higher land cost scenarios. Although the solar cell model was quite simple, we show that a detailed analysis of the land usage weighted against energy yield gains can significantly improve the economic viability of a bifacial PV power plant. Together with other tools developed during this thesis, this allows to model the energy yield of bifacial PV power plants and optimize the geometry for lowest LCOE.

### *Supporting information*

The supporting information document published with this manuscript can be accessed under <https://doi.org/10.1039/C9SE00750D>



Cite this: *Sustainable Energy Fuels*,  
2020, 4, 254

## Minimising the levelised cost of electricity for bifacial solar panel arrays using Bayesian optimisation†

Peter Tillmann, ‡<sup>ab</sup> Klaus Jäger ‡<sup>ab</sup> and Christiane Becker ‡<sup>ab</sup>\*<sup>a</sup>

Bifacial solar module technology is a quickly growing market in the photovoltaics (PV) sector. By utilising light impinging on both, front and back sides of the module, actual limitations of conventional monofacial solar modules can be overcome at almost no additional costs. Optimising large-scale bifacial solar power plants with regard to minimum levelised cost of electricity (LCOE), however, is challenging due to the vast amount of free parameters such as module inclination angle and distance, module and land costs, character of the surroundings, weather conditions and geographic position. We present a detailed illumination model for bifacial PV modules in a large PV field and calculate the annual energy yield exemplary for four locations with different climates. By applying the Bayesian optimisation algorithm we determine the global minimum of the LCOE for bifacial and monofacial PV fields at these two locations considering land costs in the model. We find that currently established design guidelines for mono- and bifacial solar farms often do not yield the minimum LCOE. Our algorithm finds solar panel configurations yielding up to 23% lower LCOE compared to the established configuration with the module tilt angle equal to the latitude and the module distance chosen such that no mutual shading of neighboring solar panels occurs at winter solstice. Our algorithm enables the user to extract clear design guidelines for mono- and bifacial large-scale solar power plants for most regions on Earth and further accelerates the development of competitively viable photovoltaic systems.

Received 4th September 2019  
Accepted 3rd November 2019

DOI: 10.1039/c9se00750d

rsc.li/sustainable-energy

### 1. Introduction

The record power conversion efficiency (PCE) of monofacial silicon solar cells – currently the dominant solar-cell technology – is 26.7%<sup>1</sup> and approaches the physical limit of around 29.4%, which was calculated by Richter *et al.*<sup>2</sup> Photovoltaic (PV) systems consisting of bifacial solar modules can generate a significantly higher annual energy yield (EY) than systems using conventional monofacial PV modules, because bifacial solar modules not only utilize light impinging onto their front, but also illumination onto their rear side.<sup>3,4</sup> Furthermore, advanced solar-cell concepts such as PERC, PERT, PERL (passivated emitter rear contact/totally-diffused/locally-diffused) and IBC (interdigitated back contact) can easily be manufactured as bifacial solar cells.<sup>5</sup> Kopecek and Libal see bifacial solar cells as the concept with the ‘highest potential to increase the output power of PV systems at the lowest additional cost’.<sup>3</sup> Indeed, the bifacial solar cell market has been gathering pace for a couple of years and

several major PV companies, such as Sanyo,<sup>6</sup> Yingli,<sup>7</sup> PVG solutions, bSolar/SolAround,<sup>8</sup> and Trina Solar<sup>9</sup> introduced bifacial modules. The tenth edition of the International Technology Roadmap for Photovoltaics (ITRPV) predicts a global market share of more than 50% for bifacial modules in 2029.<sup>10</sup> Large-scale bifacial PV power plants already have been realised and showed a higher energy yield than their monofacial counterparts.<sup>11</sup>

The levelised cost of electricity (LCOE) is a very relevant economic metric of a solar power plant.<sup>12</sup> The performance of bifacial solar modules is heavily affected by their surroundings, because they can accept light from almost every direction. Hence, a vast amount of parameters influence the resulting LCOE, for example the module and land costs, module distance and inclination angle, albedo of the ground, geographical position and the weather conditions at the location of the solar farm. Liang *et al.* recently identified comprehensive simulation models for energy yield analysis as one of the key enabling factors.<sup>4</sup> As an example, we briefly discuss how only two free parameters – land cost and module distance – affect the resulting LCOE, which makes it challenging to identify the sweet spot yielding a minimum LCOE: if two rows of tilted solar modules are installed close to each other, many modules can be installed per area. However, at too small distances shadowing will limit the rear side irradiance and consequently the total

<sup>a</sup>Helmholtz-Zentrum Berlin für Materialien und Energie, Albert-Einstein-Strasse 16, D-12489 Berlin, Germany. E-mail: christiane.becker@helmholtz-berlin.de

<sup>b</sup>Zuse Institute Berlin, Takustraße 7, D-14195 Berlin, Germany

† Electronic supplementary information (ESI) available. See DOI: 10.1039/c9se00750d

‡ These authors contributed equally to this work.





energy yield.<sup>13,14</sup> In contrast, putting the rows of modules far apart from each other maximizes the irradiance at the rear side and the energy yield per module. The number of modules installed per area, however, is lower and the overall energy yield of the solar farm decreases. The module inclination angle is a third free parameter, closely connected to the two aforementioned module distance and land cost, and obviously affects shadowing of neighboring solar panel rows and hence energy yield and LCOE of a bifacial solar farm, too.

Historically, the module inclination angle was usually set to the geographical latitude of the solar farm location, and the module distance was either set to a fixed value based on experience<sup>15</sup> or to the minimum module distance without mutual shadowing on the day of winter solstice at 9 am<sup>16</sup> or noon.<sup>17</sup> However, it has turned out that these rule-of-thumb estimates often do not lead to a minimised LCOE.<sup>18</sup> One reason is that these models did not consider the cost of land. Recently Patel *et al.* considered land costs when optimising bifacial solar farms.<sup>16</sup> However, also in this study the module distance and inclination angle were preset according to above mentioned winter solstice rule. Considering the enormous market growth of bifacial solar cell technology, finding the optimum configuration yielding minimum LCOE is highly desired. With the PV system costs in \$ per Watt peak (Wp), land costs in \$ per area and the geographic location of the solar farm as known input variables, inversely finding the optimal geometrical configuration of a bifacial PV field is a computational challenging multi-dimensional optimisation task.

In this study, we apply a multi-parameter Bayesian optimisation in order to minimise the LCOE of large-scale bifacial solar power plants. We present a comprehensive illumination model for bifacial solar arrays and calculate the annual energy yield (EY) based on TMY3 (Typical Meteorological Year 3) data for four exemplary locations near Seattle, Dallas, Mojave Desert and Havana. We calculate optimal module inclination angles and module distances yielding minimal LCOE for various module to land cost ratios. We find that our calculated optima strongly depend on both the module to land cost ratio and the geographical location. We conclude that currently used rule-of-thumb estimates for optimal module distance and tilting angle must be reconsidered. Our method enables the user to extract clear design guidelines for mono- and bifacial large-scale solar power plants principally anywhere on Earth.

## 2. Illumination model

With the illumination model we calculate the irradiance onto a solar module, which is placed somewhere in a big PV-field. We assume this field to be so big that effects from its boundaries can be neglected, but for smaller fields this might be a relevant effect caused by higher irradiance on the edges due to decreased self-shading. Further, we assume the modules to be homogeneous: we neglect effects from the module boundaries or module space in between the solar cells. Hence, we can treat this problem as 2-dimensional with periodic boundary conditions, as illustrated in Fig. 1. A similar approach was pursued for example by Marion *et al.*<sup>19</sup> In the current model we assume

the solar modules to be completely black, which means they do not reflect any light which could reach another module.

The PV field is irradiated from direct sunlight under the Direct Normal Irradiance (DNI)<sup>§</sup> and the direction  $n_s$ , which is determined by the solar azimuth  $\phi_s$  and the solar zenith  $\theta_s$ . The latter is connected to the solar altitude  $a_s$  (the height above the ground) via  $a_s = 90^\circ - \theta_s$ . Further, the PV field receives diffuse light from the sky, which is given as Diffuse Horizontal Irradiance (DHI). However, for calculating the total irradiance onto the module, also light reflected from the ground and shadowing by the other modules must be taken into account.

Due to the typical geometry of a power plant the specular reflected DNI from the front side will seldom reach the back side of the front row. The diffuse reflectivity of the module should be significantly lower. In the current model we therefore assume the solar modules to be completely black and to not reflect any light. This might lead to a slight underestimation of the illumination.

Fig. 1 shows the different components of light, which can reach the front of a PV module at point  $P_m$ . The numbers 1–4 correspond to the numbers in the figure – illumination on the sky is w.l.o.g. indicated for module #2 while illumination from the ground is indicated w.l.o.g. for module #5.

(1) Direct sunlight hits the modules under the direction  $n_s$ . It leads to the irradiance component  $I_{\text{dir},f}^{\text{sky}}(s) = \text{DNI} \cos \sigma_{\text{ms}}$ , where  $s$  is the distance between the lower end of the module  $B_2$  and  $P_m$ ,  $s = B_2 P_m$ , and  $\sigma_{\text{ms}}$  is the angle between the module surface normal and the direct incident sunlight.

(2) Diffuse skylight  $I_{\text{diff},f}^{\text{sky}}(s)$  hits the module at  $P_m$  from directions within the wedge determined by  $\langle D_1 P_m, D_2 \rangle$ . Diffuse light does not only reach the module from directions within the  $xz$ -plane but from a spherical wedge, which is closely linked to the sky view factor as for example used by Calcabrini *et al.*<sup>20</sup>

(3)  $I_{\text{dir},f}^{\text{gr}}(s)$  denotes direct sunlight that hits the module after it was reflected from the ground.

(4) Finally,  $I_{\text{diff},f}^{\text{gr}}(s)$  denotes diffuse skylight that hits the module after it was reflected from the ground.

All four components are summarized in Table 1. Table 2 denotes all parameters that are used as input to the model.

The total irradiance (or intensity) on front is given by

$$I_f(s) = I_{\text{dir},f}^{\text{sky}}(s) + I_{\text{diff},f}^{\text{sky}}(s) + I_{\text{dir},f}^{\text{gr}}(s) + I_{\text{diff},f}^{\text{gr}}(s), \quad (1)$$

and similar for the back side with a subscript b instead of f. In total, we hence consider eight illumination components on our module.

As noted above, the incident light is given as DNI and DHI. The nonuniform irradiance distribution on the module front and back surfaces has to be considered.<sup>21,22</sup> For the further treatment, it is therefore convenient to define unit-less geometrical distribution functions as for the components arising from direct sunlight and diffuse skylight, respectively. The geometrical distribution functions are closely related to the concept of view factors, which is often used for such illumination models.<sup>4,20,23</sup> Usually, view factors are defined such that

<sup>§</sup> The irradiance or intensity is the radiant power a surface receives per area.



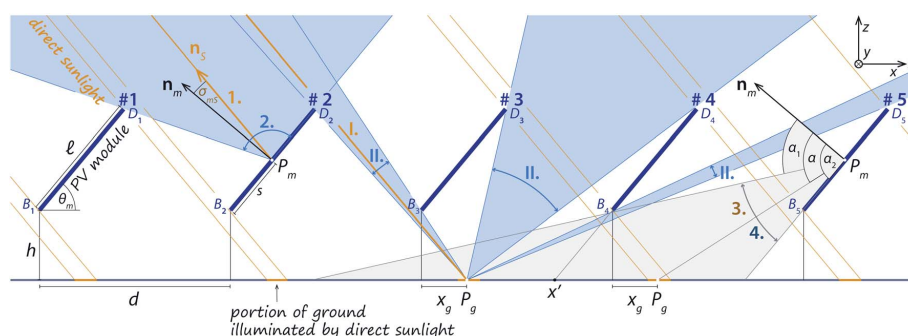


**Fig. 1** Illustrating the geometrical configuration of a (periodic) PV field and the illumination components, which reach each module on the front. The modules are labeled with #1–#5. At #1, the geometrical parameters  $h$ ,  $d$  and  $\theta_m$  are illustrated –  $d$  is the horizontal length of a unit cell. At #2, the two irradiance components illuminating the module from the sky at  $P_m$  are indicated: 1. direct and 2. diffuse. Below #3, the I. direct and II. diffuse illumination of point  $P_g$  on the ground are illustrated – here diffuse illumination origins from three angular intervals. On #5 the angular range of light reaching  $P_m$  from the ground is indicated. It consists of 3. direct and 4. diffuse light being reflected from the ground. Components 1.–4. are summarized in Table 1. Here, we assume w.l.o.g. that the PV system is located on the northern hemisphere and oriented towards South.

**Table 1** The four irradiance components which constitute the illumination of a solar module in dependence of the position  $P_m$  on the module as defined in Fig. 1, where  $s$  is the distance  $\overline{BP_m}$ . These components have to be considered for front and back sides – hence eight components in total. The numbers correspond to the numbers in Fig. 1

1.	Direct irradiance from the sky + circumsolar brightening	$I_{\text{dir}}^{\text{sky}}(s)$
2.	Diffuse irradiance from the sky	$I_{\text{diff}}^{\text{sky}}(s)$
3.	Diffuse irradiance from the ground originating from direct sunlight + circumsolar brightening	$I_{\text{dir}}^{\text{gr}}(s)$
4.	Diffuse irradiance from the ground originating from diffuse skylight	$I_{\text{diff}}^{\text{gr}}(s)$

**Table 2** The input parameters required to calculate the different parameters of the PV system

Module parameters (depicted in Fig. 1)	
$\ell$	Module length (m)
$w$	Module width (m)
$d$	Module spacing (m)
$h$	Module height above the ground (m)
$\theta_m$	Module tilt angle
Solar parameters	
DNI	Direct normal irradiance ( $\text{W m}^{-2}$ ) <sup>a</sup>
DHI	Diffuse horizontal irradiance ( $\text{W m}^{-2}$ ) <sup>a</sup>
$\theta_s$	Zenith angle of the sun (connected to solar altitude $a_s$ via $a_s = 90^\circ - \theta_s$ )
$\phi_s$	Azimuth of the Sun
$A$	Albedo of the ground
Economical parameters	
$c_p$	Peak power related system costs ( $\text{\$ per kWp}$ )
$c_L$	Land consumption related costs ( $\text{\$ per m}^2$ )

<sup>a</sup> This parameter also can be spectral. Then, the unit would be  $\text{W (m}^2 \text{ nm)}^{-1}$ .

they describe the radiation from one area onto another area, hence they give the average radiation onto the area, e.g. a module. However, we do not seek the mean irradiation on a module but the minimal irradiation. This is because of the electric properties of PV modules, as described in Section 3.1.

$$t_{\text{dir},f}(s) := \frac{I_{\text{dir},f}(s)}{\text{DNI}} \quad \text{and} \quad t_{\text{diff},f}(s) := \frac{I_{\text{diff},f}(s)}{\text{DHI}} \quad (2)$$

In eqn (2) we omitted the superscripts “sky” and “gr.”. The calculation of the components  $t_{\text{dir},f}^{\text{sky}}(s)$  and  $t_{\text{diff},f}^{\text{gr}}(s)$  requires the integration over geometrical distribution functions on the ground  $\gamma_{\text{dir}}(x_g)$  and  $\gamma_{\text{diff}}(x_g)$ , where  $x_g$  is the coordinate of the point  $P_g$  on the ground.

In particular, we have where we omitted the subscripts “diff” and “dir”. The coordinate  $x_g(s, \alpha)$ , on which  $\gamma_{\text{dir}}$  and  $\gamma_{\text{diff}}$  are evaluated, is defined such that the angle between the line  $\overline{P_g P_m}$  and the module normal  $n_m$  is equal to  $\alpha$  – the integration parameter. In Fig. 1 the fractions of the ground, which are illuminated by direct sunlight, are marked in orange.

$$t_f^{\text{gr}}(s) = \frac{A}{2} \int_{\alpha_1(s)}^{\alpha_2} \gamma[x_g(s, \alpha)] \cos \alpha d\alpha, \quad (3)$$

Fig. 2 shows an example for illumination onto the ground: subfigure (a) illustrates the position of the solar modules #1 and #2. Subfigure (b) shows the geometrical distribution functions on the ground.  $\gamma_{\text{diff}}$  is minimal below the module where the angle covered by the module is largest; and maximal at  $x'$ , because here the ground sees least shadow from module #1.

Depending on the geometrical module parameters and the position of the Sun, the directly illuminated area (1) may lay completely within the unit cell as in the examples in Fig. 1 and



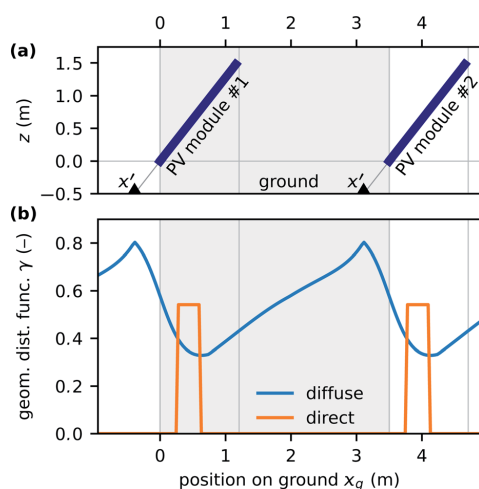


Fig. 2 An example for (a) a module configuration and (b) the corresponding diffuse and direct geometrical distribution functions at the ground  $\gamma_{\text{diff}}$  and  $\gamma_{\text{dir}}$ . The following parameters were used:  $\ell = 1.96$  m,  $d = 3.50$  m,  $h = 0.50$  m and  $\theta_m = 52^\circ$ . The solar position for the direct component was  $\theta_s = 57.2^\circ$  and  $\phi_s = 143.3^\circ$  (Berlin, 20 September 2019, 11:00 CEST). The unit cell is represented as shaded area.

2, (2) it may extend from one unit cell into the next or (3) no direct light can reach the ground. The latter can occur when the module spacing  $d$  decreases or when the solar altitude  $a_s$  is low.

Fig. 3 shows the eight geometrical distribution functions  $\iota$  corresponding to the irradiance components hitting the PV module on its front and back sides. While the functions originating from the sky (a) are stronger on the front side, the components originating from the ground (b) are stronger on the back side. This can be understood by the opening angles: the opening angle towards the sky is larger on the front side, but the opening angle of the ground is larger at the back.

All calculations presented in this work were performed with Python using numpy as numerical library for fast tensor operations.

### 3. Annual energy yield

#### 3.1. Calculating the energy yield

We calculate the annual electrical energy yield EY by feeding the illumination model described in Section 2 with irradiance data. To demonstrate the features of the model, we use TMY3 (Typical Meteorological Year 3) data for this work. TMY3 data is well suited to estimate the solar energy yield for thousands of different locations.<sup>24</sup> Amongst other parameters, the TMY3 data contain hourly DHI( $t$ ) and DNI( $t$ ) values. The overall EY given in [EY] = kW h per m<sup>2</sup> and year is the sum of the energy yields harvested over the course of a year at the module front and back sides,  $\text{EY} = \text{EY}_f + \text{EY}_b$ , which are calculated with

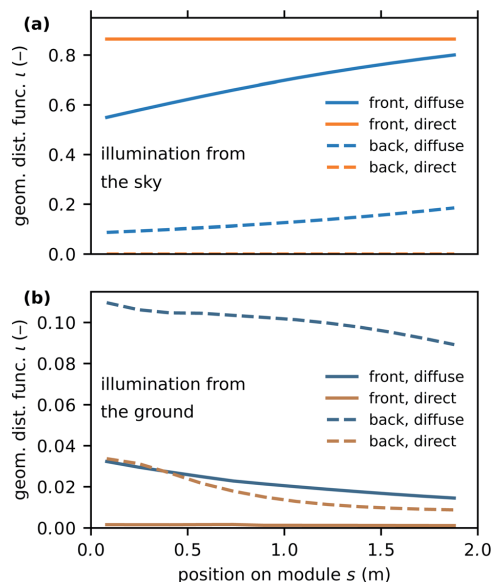


Fig. 3 Geometrical distribution functions on the module for light the module receives (a) from the sky and (b) the ground. The following parameters were used:  $\ell = 1.96$  m,  $d = 3.50$  m,  $h = 0.50$  m,  $\theta_m = 52^\circ$ , and albedo  $A = 30\%$ . The solar position for the direct components was  $\theta_s = 57.2^\circ$  and  $\phi_s = 143.3^\circ$  (Berlin, 20 September 2019, 11:00 CEST).

$$\text{EY}_f = \eta_f \left\{ \sum_t \left[ \iota_{\text{dir},f}^{\text{sky}}(\hat{s}_i, t_i) + \iota_{\text{dir},f}^{\text{gr.}}(\hat{s}_i, t_i) \right] \text{DNI}(t_i) \Delta t + \sum_i \left[ \iota_{\text{diff},f}^{\text{sky}}(\hat{s}_i) + \iota_{\text{diff},f}^{\text{gr.}}(\hat{s}_i) \right] \text{DHI}(t_i) \Delta t \right\}, \quad (4)$$

and  $\text{EY}_b$  with a subscript b instead of f. TMY3 data is available at the time stamps  $t_i$  and  $\Delta t$  is the time between two time stamps, which is typically 1 h for TMY3 data.  $\eta_f$  and  $\eta_b$  denote the power conversion efficiency for light impinging on the front and back sides of the solar module, respectively. By setting  $\eta_f = \eta_b = 1$ , eqn (4) delivers the annual radiant exposure on the front  $H_f$  (and similarly  $H_b$ ). As we aim at for an optimisation of the site-specific geometry of a solar park in a general way and not only for a specific solar module type, we assume a constant mean efficiency with  $\eta_f = 0.20$  and  $\eta_b = 0.18$ , and hence a bifaciality factor of 0.9.<sup>5</sup> The following optimisation results on solar panel arrays can therefore be understood as site-specific design guideline for any solar module type with efficiencies in this range. In reality, the power conversion efficiency is certainly not a constant but depends on multiple module specific factors such as module temperature, irradiance and angle of incidence.<sup>25,26</sup>

The  $\iota$ -functions are evaluated on the position  $\hat{s}_i \in \mathcal{P}_m$ , where  $\mathcal{P}_m = \{s_1, s_2, \dots, s_{N_m}\}$  is the set of all considered positions along the module. In a conventional PV module, all cells are



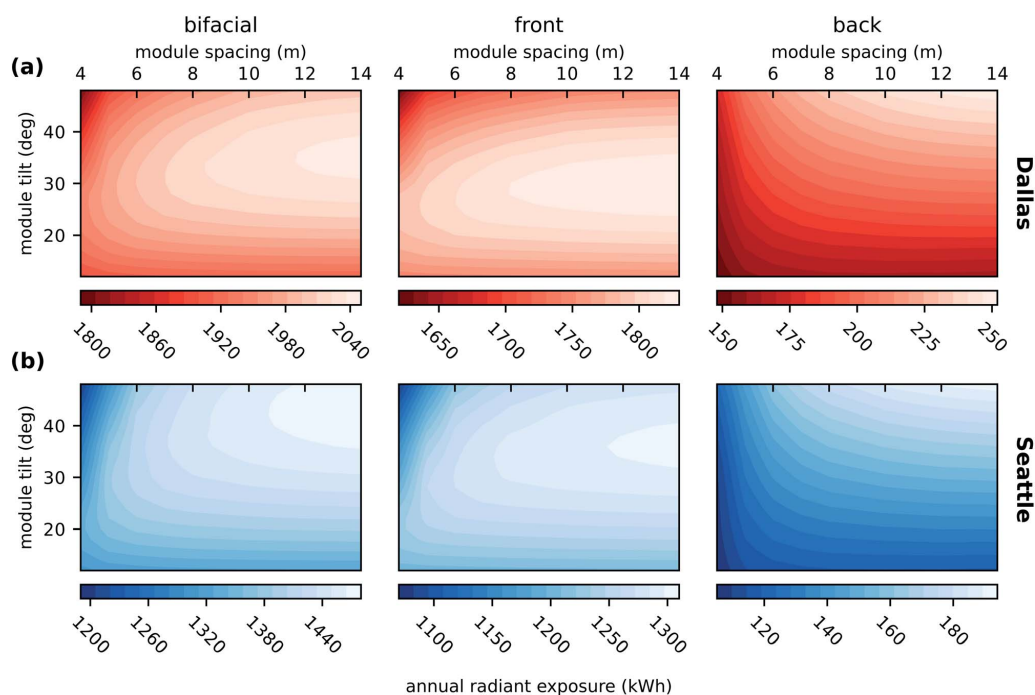


Fig. 4 Annual radiant exposure for bifacial modules and the contributions from front and back sides in a large PV field as a function of module spacing  $d$  and module tilt  $\theta_m$ . Results are shown for Dallas, TX, (top row) and Seattle, WA, (bottom row). The annual radiation yield is calculated using eqn (4) with  $\eta_f = \eta_b = 1$ . Simulated with  $m$  module height  $h = 0.5$  m and albedo  $A = 30\%$ .

electrically connected in series and therefore the cell generating the lowest current limits the overall module current. To take this into account, we determine  $\hat{s}_i$  such that

$$(I_f + I_b)(\hat{s}_i, t_i) \leq (I_f + I_b)(s, t_i) \quad (5)$$

for all  $s \in P_m$ . This means that the position on the module with the lowest irradiance, which is proportional to the solar cell current, determines the overall module performance. For high-end solar modules, the module performance might be higher depending on how bypass diodes are implemented. Therefore, our condition establishes a lower bound of the module performance under certain illumination conditions.

To model the diffuse irradiance we use the Perez model, that is widely used for solar cell simulations. The Perez model distinguishes three different components of diffuse irradiance to calculate the intensity on a tilted plane: isotropic dome, circumsolar brightening and horizontal brightening. For modeling the illumination the circumsolar brightening component is added to the direct normal irradiance because it is centred at the position of the sun. The horizontal brightening is shaded by rows in front and back and is therefore not considered to calculate the final irradiance. For the isotropic dome irradiation

on the module, the corresponding geometrical distribution functions  $i^{\text{diff}}(s)$  need to be calculated only once.

For the components arising from direct sunlight, also the geometrical distribution functions  $i^{\text{dir}}(s, t_i)$  are time-dependent, because they depend on the position of the Sun ( $\theta_{s,i}$ ,  $\phi_{s,i}$ ),<sup>¶</sup> which we calculate using the Python package Pysolar.<sup>28</sup>

### 3.2. Results and discussion

As an example, we discuss results for two locations with different climates: first, Dallas/Fort Worth area, Texas (TX), USA (Denton, 195 m elevation, 33.21° N, 97.13° W) with a humid subtropical climate (Köppen–Geiger classification Cfa<sup>29</sup>) with hot, humid summers and cool winters. Secondly, Seattle, Washington (WA), USA (Boeing Field, 47.68° N, 122.25° W) with a warm-temperate (Mediterranean) climate (Köppen–Geiger classification Csb<sup>29</sup>) with relatively dry summers and cool wet winters. Fig. S1<sup>†</sup> shows climate diagrams for these two locations.

In the ESI,<sup>†</sup> we also show results for Daggett, USA (Mojave desert, 585 m elevation, 34.87° N, 116.78° W) with a hot desert climate (Köppen–Geiger classification BWh<sup>29</sup>) and Havana,

<sup>¶</sup> See for example ref. 27, appendix E.



Cuba (Casa Blanca, 50 m elevation, 23.17° N, 82.35° W) with a tropical climate (Köppen–Geiger classification A<sup>29</sup>).

Fig. 4 shows the annual radiant exposure in (a) Dallas and (b) Seattle for bifacial PV modules (left) in a big PV field and the contributions from the front (middle) and back sides (right). The data shown in the figure are calculated like the energy yield according to eqn (4), where we set  $\eta_f = \eta_b = 1$ . We see that  $H$  generally increases with the module spacing. However, it is not economical to have a too large distance between the rows as we will see when considering the electricity cost in Section 4.

For Dallas, the optimal angle for monofacial modules, which only can utilize front illumination, is about 28°; it is mainly determined by direct sunlight. For back illumination,  $H$  increases significantly with the module inclination angle  $\theta_m$ : hardly any direct light reaches the module at the back, but contributions from diffuse sky and reflected from the ground increase with  $\theta_m$ . Increasing the module tilt further reduces the shaded area on the ground and therefore increases ground illumination. The optimal module tilt for a bifacial module is a compromise between the optimal tilt for the front and beneficial higher tilt angles for back contribution. Overall, the optimal module tilt for bifacial modules is significantly higher than for monofacial modules. Here it is about 36°.

Overall, the trends for Seattle are comparable to those for Dallas. However, we can identify differences: the overall radiant exposure is much lower because Seattle sees around 2170 annual Sun hours, compared to about 2850 h in Dallas.<sup>30</sup> Further, the optimal tilt for monofacial and bifacial modules is 32° and 44°, respectively, which is explained by the higher latitude of Seattle.

For the front side illumination we see the interesting effect that, while the latitude of Seattle and Dallas differ by 14.5°, the respective optimal tilt angles only differ by 4°. This is probably because of the higher contribution on the annual radiant exposure from the summer months in Seattle compared to Dallas. While in Seattle May to September contribute 77% of the annual radiant exposure this is only 65% in Dallas. Because the module irradiance during the summer months (with higher elevation angles of the Sun) benefits from lower tilt angle  $\theta_m$

values this can explain the difference of latitude to optimal tilt angles. The higher fraction of diffuse light in Seattle that also benefits the radiant exposure on the front side for small  $\theta_m$  might additionally increase this effect.

Fig. 5 shows how much the different irradiation components contribute to the annual radiant exposure for a bifacial module with  $d = 10$  m module spacing,  $\theta_m = 34^\circ$  tilt and albedo  $A = 30\%$  in Dallas: about 74% of the total exposure arises from direct sunlight impinging onto the module front, 14% are due to diffuse skylight impinging onto the front but the fraction of light that reaches the front from the ground is almost negligible. However, of the 10.5% exposure received by the back, around 88% is reflected from the ground. Hence, the albedo only has little influence onto the energy yield of monofacial modules but is very relevant for bifacial modules. Fig. S4† shows corresponding results for Seattle. Compared to Dallas, Seattle shows 1.4% per larger contribution by the back side. While the front side receives radiation with a ratio of 3.5 : 1 of direct to diffuse light, for the back side, this ratio is close to 1 : 1. These results show that four factors drive the gain of bifacial modules instead of monofacial modules: the albedo of the ground, the module tilt angle, the module spacing and the overall fraction of diffuse light.

Also the mounting height  $h$  affects the bifacial gain. Increasing the mounting height monotonically raises the energy yield. Therefore it is difficult to optimise this parameter without knowing additional technical and commercial constraints. However, we find that the bifacial gain starts to saturate for a height above 0.5 m, which is in agreement with work from Kreinin *et al.*<sup>17</sup> Since a mounting height of  $h = 0.5$  m seems realistic all simulations in our work are performed with this mounting height.

#### 4. Minimising the electricity cost

In Section 3 we discussed how to calculate the annual electrical energy yield and we analysed how the annual radiant exposure on the modules depends on the module spacing and tilt for two examples: Dallas and Seattle. In this section, we are going to

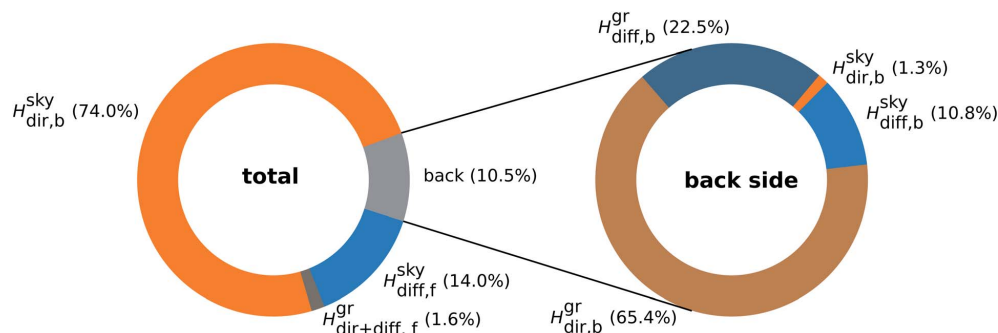


Fig. 5 (left) Different annual radiant exposure components for a bifacial solar cell in Dallas. (right) Detailed picture for the back side. Simulated with module spacing  $d = 10$  m, module tilt  $\theta_m = 34^\circ$ , module height  $h = 0.5$  m and albedo  $A = 30\%$ .



derive a simple model for the electricity cost and perform some cost optimisations.

$$\text{LCOE} = \frac{\ell I_p \eta_f c_p + d c_L}{\ell EY T}, \quad (12)$$

#### 4.1. Levelised cost of electricity

As a measure for the electricity cost we use the levelised cost of electricity (LCOE), which is a key metric for electricity generation facilities. In the simplest case, the LCOE is given as the total cost  $C_F$  spent in the facility during its lifetime  $T$  (in years) divided by the total amount of electric energy  $E_{\text{total}}$  generated in that time. Using the yield of a meteorological representative year allows to calculate the total yield by multiplying the annual power production with the lifetime of the facility.

$$\text{LCOE} = \frac{C_F}{E_{\text{total}}} = \frac{C_F}{E_F T}, \quad (6)$$

where  $E_F$  is the electric energy generated by the PV field in one year. In more involved models also costs of capital and discount rates are taken into account. ||

The total cost can be split into two components, associated with the peak power  $C_P$  (including modules, inverters, mounting *etc.*) and the land consumption  $C_L$  (lease, fences, cables *etc.*) of the facility.

$$C_F = C_P + C_L \quad (7)$$

By considering a facility with a PV-field of  $M$  rows with  $N$  modules each the costs can be calculated per unit cell,

$$C_F = (C_{P,m} + C_{L,m})MN. \quad (8)$$

The peak-power related costs per module  $C_{P,m}$  are calculated with

$$C_{P,m} = c_p \eta_f I_p \ell w \quad (9)$$

where  $c_p$  denotes the peak-power associated costs given in [ $c_p$ ] = \$ per kWp, which we use as input parameter.  $I_p = 1 \text{ kW m}^{-2}$  is the peak irradiance as used for standardized PV characterization<sup>31</sup> and  $w$  and  $\ell$  denote the module width and length, respectively.  $\eta_f$  denotes the power conversion efficiency on the front side of the solar cell.

The cost of land consumption per module depends on module width  $w$  and spacing  $d$ ,

$$C_{L,m} = c_L d w \quad (10)$$

with the land cost  $c_L$  given in [ $c_L$ ] = \$ per  $\text{m}^2$ , which is an input parameter.

The annual generated electric energy of the PV field is given by with the annual yield EY according to eqn (4).

$$E_F = EY \ell w MN, \quad (11)$$

Combining eqn (6)–(11) and simplifying leads to the expression which is independent of the field dimensions  $M$  and  $N$  and the module width  $w$ .

In this study, we assume for the overall costs of the PV system  $c_m = 1000$  \$ per kWp, which includes all costs over the lifetime of the solar park, such as PV module investment, balance of system cost, planning, capital cost and others. The land cost is not included in this quantity. The lifetime is assumed to be  $T = 25$  years, a typical time span for the power warranty of solar cell modules.<sup>27</sup>

In our optimisation, we aim to minimize the LCOE as parameter of the module spacing  $d$  and the solar module tilt  $\theta_m$ . We perform the optimisation for five land-cost scenarios  $c_L$ , in which we assume to include all costs that are related to an increase of area such as lease, cables, fences *etc.* Table 3 gives an overview of the cost scenarios and the resulting fraction of the land costs on the total costs, ( $C_L/C_F$ ).

#### 4.2. Optimisation method

As optimisation method we use Bayesian optimisation, which is well suited to find a global minimum of black box functions, which are expensive to evaluate.<sup>32</sup> Bayesian optimisation has been used in a wide variety of applications such as robotics,<sup>33</sup> hyper parameter tuning<sup>34</sup> or physical systems.<sup>35,36</sup>

In principle, Bayesian optimisation consists of two components: a surrogate model that approximates the black box function and its uncertainty (based on previously evaluated data points) and an acquisition function that determines the next query point from the surrogate model. After evaluating the function for the queried data point the surrogate model is updated and the next step can be computed with the acquisition function. This cycle is repeated until a specified number of steps or a convergences criteria is reached. We use the implementation from scikit-optimize with Gaussian process as surrogate model and expected improvement as acquisition function.<sup>37</sup>

#### 4.3. Optimisation results

Traditionally, the optimal tilt and module spacing are often estimated with the winter solstice rule.<sup>38,39</sup> The optimal distance between two rows of modules is defined as the shortest distance for which the shadow of a row of modules does not hit the next

Table 3 Overview of used cost scenarios. Right column shows the share of land consumption on total costs for different scenarios assuming row spacing  $d = 10$  m, module length  $\ell = 1.96$  m and  $\eta_f = 20\%$

$c_p$ (\$ per kWp)	$c_L$ (\$ per $\text{m}^2$ )	$C_L/C_F$ (%)
1000	1.00	2.5
1000	2.50	6.0
1000	5.00	11.3
1000	10.00	20.3
1000	20.00	33.8

|| See for example ref. 27, chapter 21.



row of modules in a specified solar time window (e.g. 9 am–3 pm) on winter solstice. As a rule of thumb the tilt is often chosen to be equivalent to the latitude of the facility location. However these rules do not consider the economic trade off between land costs and energy yield or typical weather patterns (e.g. foggy winters) that vary for different locations.

Fig. 6 and 7 shows the optimisation results for a field of (a) bifacial and (b) monofacial PV modules in Dallas and Seattle, respectively. Black dots mark evaluated data points, the red dot marks the found optimum and the color map shows the interpolation of the LCOE by the Gaussian process. The blue line indicates the winter solstice rule (9 am).

We see that the optimum shifts to smaller module spacing with increasing land cost. Further, also the optimal module tilt decreases in order to compensate for increased shadowing because of less module spacing. Overall, bifacial installations show larger module spacing and higher tilt angles in optimal configurations compared to monofacial technology. With increasing land costs and therefore reduced optimal module spacing the cost landscape gets increasingly steep. The sensitivity of the optimised parameters increases and using non-optimal geometrical configurations results in increasing yield loss. Seattle shows the same trends for optimal configuration in different cost scenarios. Compared to Dallas optimal tilt and spacing are higher.

Our optimisation results differ significantly from the geometric parameters obtained from the winter solstice rule. For Dallas the winter solstice rule only provides comparable optimal parameters for  $c_L = 5$  \$ per  $m^2$ . In Seattle, the optimal distances are shorter and the optimal module tilts are larger than expected from the winter solstice rule for all cost scenarios. This can be understood when considering the large share of diffuse light during the Seattle winter, which mitigates shading losses significantly.

Table 4 compares the LCOE obtained from optimisation to results for rule-of-thumb geometries (tilt angle = latitude, distance according to 9 am winter solstice rule) for different land cost scenarios. Depending on the location and cost scenario we see a reduction of LCOE of up to 23%. The rule-of-thumb approach shows its weakness especially in Seattle. There is a general trend for higher reductions at high cost scenarios, where the cost landscape is increasingly steep (see Fig. 6 and 7). The optimisation for Havana in general exhibits the smallest reduction of LCOE but compared to the other locations there is no clear trend for higher reductions for higher land costs.

From these results it is clear that the winter solstice rule is not able to properly reflect different economic trade-offs or different illumination conditions over the course of the year. This is especially true when setting the tilt angle to the latitude of the location. For a minimal LCOE module tilt and spacing should be optimised independently from each other. Further,

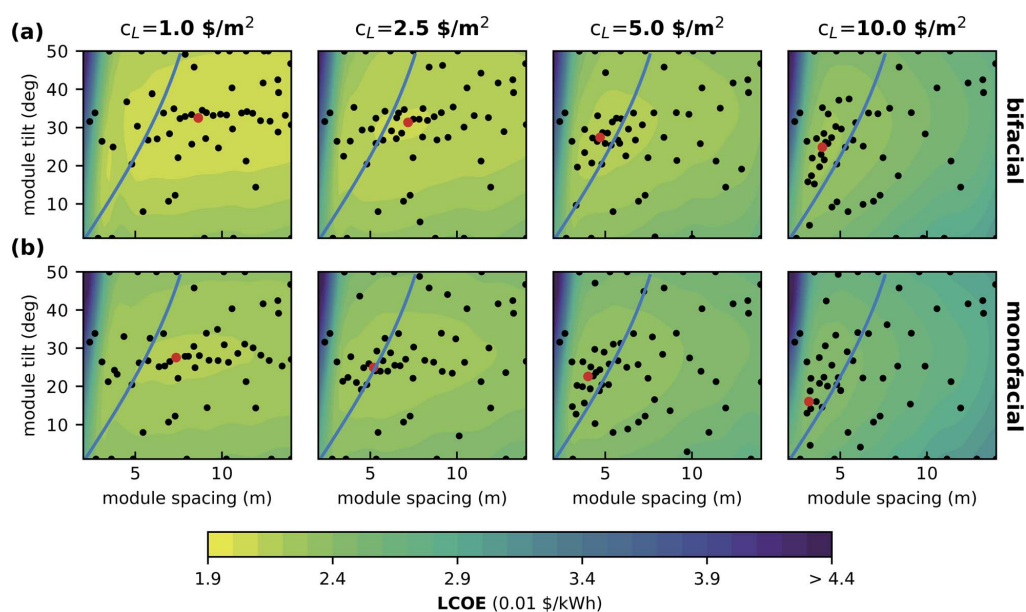


Fig. 6 Results of the Bayesian optimisation for minimising LCOE of (a) bifacial and (b) monofacial PV modules in Dallas with the land cost  $c_L$  scenarios 1, 2.5, 5, and 10 \$ per  $m^2$ . Black dots mark evaluated configurations and the color map corresponds to the interpolation by a Gaussian process. The red dot indicates the minimal LCOE found by the optimisation. The blue curves indicate rule-of-thumb module distance according to 'no shadowing of neighboring modules at winter solstice'. Simulations with albedo  $A = 30\%$ , module height  $h = 0.5$  m and peak power costs  $c_p = 1000$  \$ per kW h.



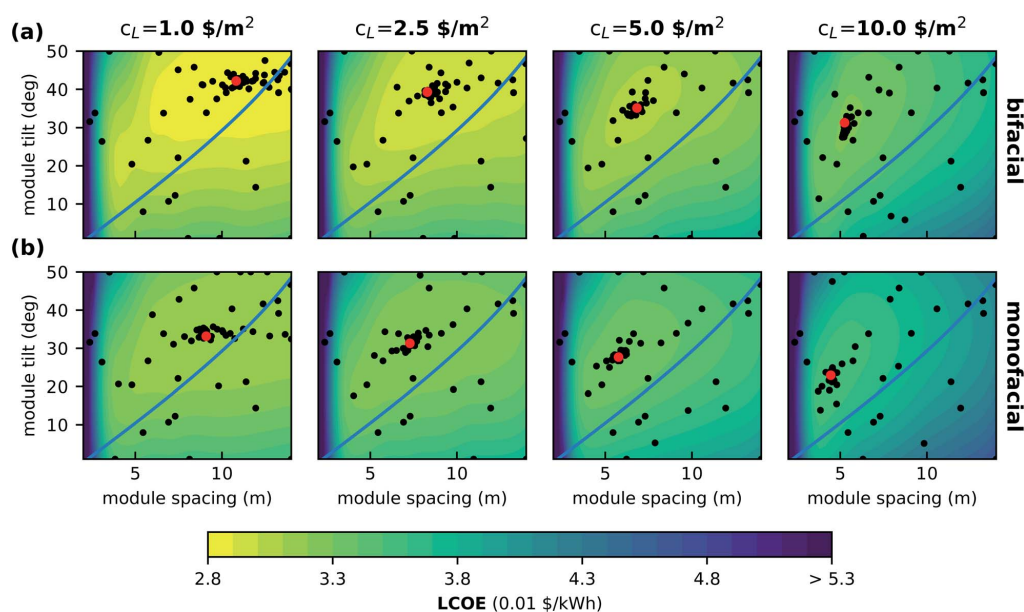


Fig. 7 Results of the Bayesian optimisation for minimising LCOE of (a) bifacial and (b) monofacial PV modules in Seattle with the land cost  $c_L$  scenarios 1, 2.5, 5 and 10 \$ per  $m^2$ . Black dots mark evaluated configurations and the color map corresponds to the interpolation by a Gaussian process. The red dot indicates the minimal LCOE found by the optimisation. The blue curves indicate rule-of-thumb module distance according to 'no shadowing of neighboring modules at winter solstice'. Simulations with albedo  $A = 30\%$ , module height  $h = 0.5$  m and peak power costs  $c_P = 1000$  \$ per kW h.

typical weather patterns and the local economic situation must be taken into account.

#### 4.4. Discussion

The results of all optimisations are summarised in Fig. 8 and Table 5. We see that the optimal LCOE increases slightly with the land cost. Further, in Seattle the LCOE difference between mono- and bifacial modules is larger as in Dallas, Havana or the Mojave Desert. This is caused by the larger module tilt and diffuse light share in Seattle, which increases the fraction of illumination at the module back. Dallas and the Mojave Desert have comparable latitude but show a small difference in bifacial

gain due to the higher diffuse light share in Dallas. As discussed above, the optimal module tilt decreases with increased land consumption cost  $c_L$ .

In general, we see that for a utility scale solar cell plant both, the module tilt and the distance between rows, affect the annual energy yield. Increasing the distance increases the energy yield and the costs per module while tilt can be optimised cost-neutral. The optimal distance between rows is a compromise between increasing costs with higher land use for higher distances and lower energy yield due to shading for lower distances. This is true also for monofacial modules but due to the increased relevance of light reflected from the ground it is more relevant for bifacial modules.

Table 4 Comparing LCOE results for bifacial modules with optimised tilt and distance vs. rule-of-thumb parameters (module tilt equal latitude and distance according to 9 am winter solstice rule) for Dallas, Havana, Mojave and Seattle. Simulations with albedo  $A = 30\%$ , module height  $h = 0.5$  m and peak power costs  $c_P = 1000$  \$ per kW h

$c_L$ (\$ per $m^2$ )	LCOE (cents) optimised				Rule-of-thumb				Reduction (%)			
	DALL.	HAVA.	MOJA.	SEAT.	DALL.	HAVA.	MOJA.	SEAT.	DALL.	HAVA.	MOJA.	SEAT.
1.0	2.04	1.84	1.57	2.83	2.05	1.87	1.58	2.85	0.5	1.6	0.6	0.7
2.5	2.10	1.89	1.61	2.93	2.10	1.89	1.62	3.00	0.0	0.0	0.6	2.3
5.0	2.17	1.94	1.67	3.07	2.18	1.94	1.68	3.24	0.5	0.0	0.6	5.2
10.0	2.28	2.02	1.77	3.28	2.33	2.04	1.80	3.74	2.1	1.0	1.7	12.3
20.0	2.47	2.17	1.92	3.62	2.63	2.23	2.06	4.73	6.1	2.7	6.8	23.5





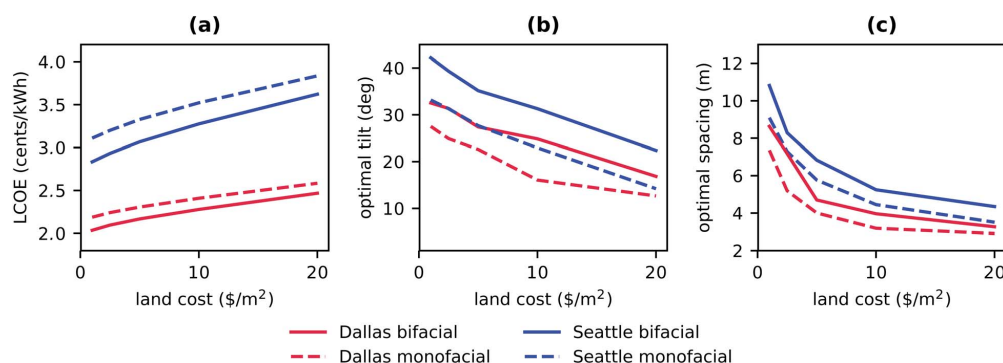


Fig. 8 Results of the optimisation for different land cost scenarios in Dallas (red lines) and Seattle (blue lines): (a) lowest LCOE and (b) optimal module tilt and (c) optimal spacing. Simulations with albedo  $A = 30\%$ , module height  $h = 0.5$  m and peak power costs  $c_p = 1000$  \$ per kW h.

Table 5 Fraction of land cost ( $C_L/C_F$ ), module distance  $d$  and bifacial gain for optimised configurations in different cost scenarios. Simulations with albedo  $A = 30\%$ , module height  $h = 0.5$  m and peak power costs  $c_p = 1000$  \$ per kW h

$c_L$ (\$ per m <sup>2</sup> )	$C_L/C_F$ (%)				$d$ (m)				Bif. gain (%)			
	DALL.	HAVA.	MOJA.	SEAT.	DALL.	HAVA.	MOJA.	SEAT.	DALL.	HAVA.	MOJA.	SEAT.
1.0	2.2	2.0	2.1	2.7	8.6	8.2	8.5	10.8	11.4	11.3	10.7	13.6
2.5	4.4	3.3	4.2	5.0	7.2	5.3	6.9	8.3	11.0	10.1	10.3	12.7
5.0	5.7	4.7	6.1	8.0	4.7	3.9	5.1	6.8	9.6	9.0	9.4	11.7
10.0	9.2	7.8	9.6	11.8	4.0	3.3	4.2	5.2	8.8	7.9	8.4	10.5
20.0	14.3	13.9	15.1	18.2	3.3	3.2	3.5	4.3	7.3	7.5	7.3	9.2

The optimal configuration for bifacial solar cells depends on the radiation conditions and the albedo of the facility location. With increasing latitude (and therefore lower solar elevation angles), albedo and diffuse light contribution the bifacial gain will be increased and therefore make this type of PV technology more attractive for utility scale developers.

Cost optimisations for PV installation are quickly outdated because PV module prices have been decreasing for many years and land cost is very volatile. However the optimal installation geometry only depends on the ratio of land cost related to total costs and not absolute values. Hence, at a scenario of  $c_L = 10$  \$ per m<sup>2</sup> and  $c_p = 1500$  \$ per kWp yields the same optimisation result as  $c_L = 5$  \$ per m<sup>2</sup> and  $c_p = 750$  \$ per kWp.

## 5. Conclusions

We developed a detailed model to calculate the irradiation onto both sides of a PV module, which is located in a large PV field. With this model, we could estimate the annual energy yield for monofacial and bifacial PV modules as a function of the module spacing and the module tilt. We assume a constant power conversion efficiency and a simple approach to calculate the levelised cost of electricity allowing for a technology independent modeling. Combined with a Bayesian optimisation algorithm, this allowed us to minimise the LCOE as a function of module spacing and module tilt for different land consumption

scenarios. Due to the general approach the presented LCOE have the character of an example. It can be refined by implementation of module specific derating factors such as the temperature and incident angle dependent conversion efficiency behaviour.

Our results basically show that the bifacial gain and optimal geometry depend on the specific location and cost scenario. The bifacial gain can be expected to increase for locations with higher latitude and higher diffuse light share.

The usually used rule of thumb, no shadowing at winter-solstice and module tilt angle equal to the geographical latitude, leads to suboptimal module spacing and tilt combinations, because it does not account for economic trade-offs and the influence of the local climate. In contrast, optimising the parameters in Seattle can lead to a 23% reduction of LCOE for high land cost scenarios. This shows the significance of site-specific and land-cost dependent optimisation and helps users to identify the configurations yielding minimal LCOE.

## Conflicts of interest

There are no conflicts to declare.

## Acknowledgements

We thank Lev Kreinin and Asher Karsenti from SolAround for fruitful discussions regarding the illumination model for



bifacial solar cells. P. T. thanks the Helmholtz Einstein International Berlin Research School in Data Science (HEIBRID) for funding. The results were obtained at the Berlin Joint Lab for Optical Simulations for Energy Research (BerOSE) and the Helmholtz Excellence Cluster SOLARMATH of Helmholtz-Zentrum Berlin für Materialien und Energie, Zuse Institute Berlin and Freie Universität Berlin.

## Notes and references

- 1 K. Yoshikawa, H. Kawasaki, W. Yoshida, T. Irie, K. Konishi, K. Nakano, T. Uto, D. Adachi, M. Kanematsu, H. Uzu and K. Yamamoto, *Nat. Energy*, 2017, 2, 17032.
- 2 A. Richter, M. Hermle and S. W. Glunz, *IEEE J. Photovoltaics*, 2013, 3, 1184–1191.
- 3 R. Kopecek and J. Libal, *Nat. Energy*, 2018, 3, 443–446.
- 4 T. S. Liang, M. Pravettoni, C. Deline, J. S. Stein, R. Kopecek, J. P. Singh, W. Luo, Y. Wang, A. G. Aberle and Y. S. Khoo, *Energy Environ. Sci.*, 2019, 12, 116–148.
- 5 S. Chunduri and M. Schmela, *Bifacial Solar Technology Report 2018 Edition, Taiyang news technical report*, 2018.
- 6 Sanyo, *Sanyo Canada launches first bifacial solar module* -, 2009, <https://www.greenlaunches.com/alternative-energy/sanyo-canada-launches-first-bifacial-solar-module.php>.
- 7 Yingli, *Yingli's PANDA BIFACIAL Module Became the World's First Bifacial Module Certified by CGC, UL, and TUV Rheinland*, 2018, <http://ir.yinglisolar.com/news-releases/news-release-details/yingli-panda-bifacial-module-became-worlds-first-bifacial>.
- 8 bSolar, *bSolar launches High-Efficiency Bifacial Silicon Solar Cells*, 2012, <https://www.photovoltaik.eu/article-449463-30021/b-solar-launches-high-efficiency-bifacial-silicon-solar-cells-.html>.
- 9 TrinaSolar, *Trina Solar to launch N-type i-TOPCON double-glass bifacial modules*, 2019, <https://solarpv.expert/2019/06/14/trina-solar-to-launch-n-type-i-topcon-double-glass-bifacial-modules/>.
- 10 ITRPV, *10th Edition of the International Technology Roadmap Photovoltaics, Vdma technical report*, 2019.
- 11 N. Ishikawa and S. Nishiyama, *presented at the 3rd Bifacial PV Workshop*, Miyazaki, Japan, 2016.
- 12 F. Fertig, S. Nold, N. Wöhrle, J. Greulich, I. Hädrich, K. Krauß, M. Mittag, D. Biro, S. Rein and R. Preu, *Prog. Photovoltaics Res. Appl.*, 2016, 24, 800–817.
- 13 J. Appelbaum, *Renewable Energy*, 2016, 85, 338–343.
- 14 M. R. Khan, E. Sakr, X. Sun, P. Bermel and M. A. Alam, *Appl. Energy*, 2019, 241, 592–598.
- 15 I. Shoukry, J. Libal, R. Kopecek, E. Weffringhaus and J. Werner, *Energy Procedia*, 2016, 92, 600–608.
- 16 M. T. Patel, M. R. Khan, X. Sun and M. A. Alam, *Appl. Energy*, 2019, 247, 467–479.
- 17 L. Kreinin, A. Karsenty, D. Grobgeld and N. Eisenberg, *2016 IEEE 43rd Photovoltaic Specialists Conference (PVSC)*, 2016, pp. 2688–2691.
- 18 P. Grana, *The new rules for latitude and solar system design*, 2018, <https://www.solarpowerworldonline.com/2018/08/new-rules-for-latitude-and-solar-system-design/>.
- 19 B. Marion, S. MacAlpine, C. Deline, A. Asgharzadeh, F. Toor, D. Riley, J. Stein and C. Hansen, *2017 IEEE 44th Photovoltaic Specialist Conference (PVSC)*, 2017.
- 20 A. Calcabrini, H. Ziar, O. Isabella and M. Zeman, *Nat. Energy*, 2019, 4, 206–215.
- 21 U. A. Yusufoglu, T. M. Pletzer, L. J. Koduvelikulathu, C. Comparotto, R. Kopecek and H. Kurz, *IEEE J. Photovoltaics*, 2015, 5, 320–328.
- 22 L. Kreinin, N. Bordin, A. Karsenty, A. Drori, D. Grobgeld and N. Eisenberg, *2010 35th IEEE Photovoltaic Specialists Conference*, 2010, pp. 002171–002175.
- 23 X. Sun, M. R. Khan, C. Deline and M. A. Alam, *Appl. Energy*, 2018, 212, 1601–1610.
- 24 S. Wilcox and W. Marion, *Users manual for TMY3 data sets, National Renewable Energy Laboratory Technical Report NREL/TP-581-43156*, National Renewable Energy Laboratory Golden, CO, 2008.
- 25 N. Martin and J. M. Ruiz, *Prog. Photovoltaics Res. Appl.*, 2005, 13, 75–84.
- 26 M. Jazayeri, S. Uysal and K. Jazayeri, *2013 High Capacity Optical Networks and Emerging/Enabling Technologies*, 2013, pp. 44–50.
- 27 A. H. M. Smets, K. Jäger, O. Isabella, R. A. C. M. M. van Swaaij and M. Zeman, *Solar energy: The physics and engineering of photovoltaic conversion technologies and systems*, UIT Cambridge, 2016.
- 28 B. Stafford, *Pysolar*, 2018, DOI: 10.5281/zenodo.1461066.
- 29 M. Kottek, J. Grieser, C. Beck, B. Rudolf and F. Rubel, *Meteorol. Z.*, 2006, 15, 259–263.
- 30 L. Ozborn, *Average Annual Sunshine in American Cities*, 2019, <https://www.currentresults.com/Weather/US/average-annual-sunshine-by-city.php>.
- 31 ISO 9845-1:1992, *International organization for standardization technical report*, 1992.
- 32 B. Shahriari, K. Swersky, Z. Wang, R. P. Adams and N. de Freitas, *Proc. IEEE*, 2016, 104, 148–175.
- 33 A. Cully, J. Clune, D. Tarapore and J.-B. Mouret, *Nature*, 2015, 521, 503–507.
- 34 J. Snoek, H. Larochelle and R. P. Adams, *Practical Bayesian Optimization of Machine Learning Algorithms*, 2012, <http://papers.nips.cc/paper/4522-practical-bayesian-optimization>.
- 35 P.-I. Schneider, X. G. Santiago, C. Rockstuhl and S. Burger, *Proc. SPIE*, 2017, 103350, 103350O.
- 36 H. C. Herbol, W. Hu, P. Frazier, P. Clancy and M. Poloczek, *npj Comput. Mater.*, 2018, 4, 51.
- 37 T. Head, MechCoder, G. Louppe, I. Shcherbatyi, Fcharras, Z. Vínicius, Cmmalone, C. Schröder, Nel215, N. Campos, T. Young, S. Cereda, T. Fan, Rene-Rex, Kejia (KJ) Shi, J. Schwabedal, Carlosdanielcsantos, Hvass-Labs, M. Pak, F. Callaway, L. Estève, L. Besson, M. Cherti, K. Pfannschmidt, F. Linzberger, C. Cauet, A. Gut, A. Mueller and A. Fabisch, *Scikit-Optimize/Scikit-Optimize: V0.5.2*, 2018, DOI: 10.5281/zenodo.1207017.
- 38 M. T. Patel, M. R. Khan, X. Sun and M. A. Alam, *Appl. Energy*, 2019, 247, 467–479.
- 39 S. Sánchez-Carbajal and P. M. Rodrigo, *Int. J. Photoenergy*, 2019, 2019, 1–14.



## Chapter 8

# Conclusion

Bifacial operation and perovskite/silicon tandem solar cells are two very promising approaches to improve the power generation per land area, a figure of merit that is especially important to reduce the BOS costs of PV systems. Compared to traditional monofacial silicon solar cells, both concepts require more sophisticated simulation tools and power ratings from standardized indoor measurements are less useful to predict the power generation for outdoor conditions. Instead, energy yield calculations that consider the effects of varying spectral irradiance, solar position, cloud coverage and temperature are required for reliable power generation forecasts. In this thesis, several simulation tools were developed to evaluate the performance with focus on optical considerations for bifacial single junction and tandem solar cells. Many of these tools are driven by weather data to accurately model the impact of realistic outdoor conditions.

Utilising FEM simulations with Bayesian optimisation helps to improve the light-trapping performance of a metal grating reflector used in a record-efficiency multijunction device. Good agreement between the existing structure and the simulations was shown and the geometry of the device was improved to yield a higher photocurrent in the silicon junction of  $0.37 \text{ mA/cm}^2$ , which corresponds to a relative increase of 2.8 %.

A detailed illumination model for bifacial solar cells was developed for solar panels that are mounted in large PV arrays. The model assumes infinitely many and infinitely wide rows of solar panels, which allows simplifying the problem to calculations in 2 dimensions. The light on the backside mostly originates from reflections on the ground and therefore a crucial step in the modelling is the radiance from the ground. In typical operation conditions, significant portions of the ground under the solar panels will be shaded from direct sunlight and partially shaded from diffuse irradiance. This is considered by the model and subsequently, the irradiance on the backside is calculated considering inhomogeneity along the module height. The strength of the model lies in fast computations and that it allows to consider the current matching constrains for the series connected cell integrated in a solar panel.

In the next step, the illumination model was used to perform energy yield calculations for idealised solar cells placed in Seattle, USA. The focus of the investigation was the effect of luminescent coupling and bifacial operation. It was found, that both luminescent coupling and bifacial operation enables to reduce the bandgap of the perovskite cell in a tandem device. Luminescent coupling allows the recycling of excess current from the top cell by radiative recombination and subsequent absorption in the bottom cell for tandems in 2T configuration. Due to the refractive index contrast between the two subcells and the surrounding air, this process is very efficient from an optical perspective, with over 76 % for a modeled device architecture. However, the electronic quality of the perovskite cell which determines the ratio of radiative to non-radiative recombination is a critical parameter in assessing the relevance of

luminescent coupling in perovskite/silicon tandem solar cells. The electronic quality of perovskite solar cells has been constantly improving over the last few years; however, there is still further research required to evaluate the practical relevance of luminescent coupling.

Bifacial operation of a tandem solar cell increases the photocurrent in the bottom cell. Due to the lower bandgap of the bottom cell, all light will exclusively be absorbed there. In a 2T tandem that requires current matching for best performance, this has implications for the ideal bandgap of the perovskite. For realistic illumination scenarios and assuming a ground albedo of 30 %, the optimum bandgap of the perovskite was shifted from 1.74 to 1.66 eV in energy yield calculations for Seattle.

Manufacturing perovskites with an ideal bandgap of around 1.70 eV for monofacial tandem solar cells has been challenging, and higher quality perovskites have been demonstrated in the 1.60 eV range. Both luminescent coupling and bifacial operation were demonstrated to enable lower optimal perovskite bandgaps and overall more relaxed conditions for current matching. These findings can therefore lead to a paradigm change in the development of perovskite materials with potentially improved stability and higher energy yields.

To increase the confidence in the simulation results, the models were validated against experimental measurements of solar cell performance with the corresponding solar irradiance and temperature data. The model chain was compared to measurements of monofacial and bifacial silicon panels mounted on a rooftop installation in Jerusalem, Israel. Excellent agreement between simulation and measurements was demonstrated when the module current was used as a proxy for the irradiance. A simple temperature-dependent one-diode model was used to simulate the *IV*-characteristics of the solar panels. These simulations were compared to the measured fill factor, open circuit voltage, and maximum power and excellent agreement was found over the course of the day, except for situations early in the morning or late in the afternoon when the light intensity is very low. The validated model chain was used to estimate the gain when “upgrading” from a standard monofacial silicon solar cell. A bifacial silicon solar panel showed a 20 % higher energy yield, for monofacial tandems a gain of 42 % and 43 % was simulated for 2T and 4T configurations, respectively, and finally 55 % and 61 % for 2T and 4T bifacial tandem solar cells. This shows that 4T tandem solar cells can potentially better utilize bifacial operation, however it should be noted that the optimal bandgap for 4T was found to be 1.70 eV, the upper limit that was considered to be manufacturable. The 2T bifacial tandem on the other hand has an optimal bandgap of 1.56 eV and should therefore be easier to manufacture with currently known synthesis routes for perovskite top cells.

The practical bifacial gain by using bifacial instead of monofacial solar cells strongly depends on the geometry of a particular installation. While using larger distances between rows of solar panels increases the backside illumination, it will also increase the land usage, which will increase the cost of the power plant. In order to achieve the lowest possible LCOE, a tradeoff between energy yield and land consumption needs to be found. A simple economic model was developed that distinguishes between the cost of solar panels and the cost area usage. With this model, the trade-off can be optimised and it was shown that the best geometry in terms of LCOE depends on the location’s climate and the cost per square meter of land usage. Using location-specific optimisation of the power plant geometry can yield up to 23 % lower LCOE compared to typical rule-of-thumb design strategies.

In summary, several tools have been developed to evaluate and optimise solar cells with an emphasis on bifacial operation and tandem designs. The tools cover illumination of the solar cell, optimisation of optical components within the cell and

---

simulation of the power output. The impact of bifacial operation on the bandgap of the perovskite bandgap was demonstrated and quantified in some case studies. Weather and operation conditions vary greatly around the world and solar panels are installed in all these different environments. This work showed that already for bifacial solar cells the individual optimisation of solar power plant layouts can greatly reduce the cost of the generated electricity. In the future it might prove beneficial to optimise the design of solar cells in order to achieve a tailor-made setup for the individual operation location and conditions. The tools developed in this thesis allows to optimise the design based on weather data that is available in global databases for many regions around the world. This will help to further reduce LCOE of PV power plants to accelerate the transition of our carbon-based economy towards renewable energy systems.



## *Danksagung*

An dieser Stelle möchte ich meinen ganz herzlichen Dank an Klaus Jäger und Christiane Becker ausdrücken, die es mir ermöglicht haben meine Promotion mit diesem spannenden Thema durchzuführen und die mich während meiner Forschung betreut, beraten und unterstützt haben. Die sich immer die Zeit genommen haben meine Fragen zu beantworten, meine Forschung zu diskutieren und meine Texte mit ihren vielen Rechtschreibfehlern Korrektur zu lesen. Ich danke auch Sven Burger für seine Beratung und Betreuung, die besonders in FEM-Projekten willkommene Hilfe war. Ich danke Christof Schütte für die Übernahme der offiziellen Betreuung am Mathematik-Institut der FU Berlin. And I would also like to thank Eugene Katz for his time and effort to write a third review of my doctoral thesis.

Ich möchte mich außerdem bei meinen Kollaborationspartnern und Mitautoren Asher Karsenti, Lev Kreinin, Benedikt Bläsi, Oliver Höhn und Eugene Katz für die gute Zusammenarbeit und wissenschaftliche Beratung bedanken. Vielen Dank an meinen Freund Felix Reisbeck für das Korrekturlesen von weiten Teilen der Doktorarbeit. Shoutout an “meine Firma” für die Unterstützung beim Drucken.

Ich danke Martin Hammerschmidt für seine Zeit und Geduld, meine Probleme mit JCMSuite mit mir zu debuggen und mit mir die Mysterien der Finite Elemente Methode zu diskutieren. Des Weiteren möchte ich mich bei allen Kollegen sowohl aus der Gruppe am Helmholtz-Zentrum als auch den Kollegen aus der Computational Nano Optic-Gruppe am Zuse Institut bedanken, die sich immer wieder die Zeit genommen haben meine Fragen und Probleme mit hilfreichen Diskussionen und wissenschaftlichem Rat zu lösen. Die außerdem immer eine angenehme Arbeitsatmosphäre geschaffen haben, in der ich mich wohl gefühlt und gerne gearbeitet habe. Vielen Dank an Philipp Schneider für die Beratung beim Thema Bayes’sche Optimierung.

Ein besonderer Dank geht an meinen Kollegen Dunbi, der immer bereit war meine vielen Ideen mit mir zu diskutieren. Ich hoffe du verzeihst mir, dass ich immer noch manchmal deinen Namen falsch schreibe.

Ich danke meinen Freunden und meiner Familie, die mich in all meinen Lebenslagen begleitet haben. Mein ganz besonderer Dank gebührt meiner Frau Hanna für ihre ganze Unterstützung während all der Zeit und das Aushalten meiner Launen, besonders in der Schreibphase meiner Doktorarbeit.

Ich bedanke mich außerdem bei meiner Graduiertenschule HEIBRiDS, die über weite Teile meine Doktorarbeit finanzierten, mich in Kontakt mit vielen tollen Wissenschaftlern aus dem Bereich Data-Science gebracht und unsere Arbeit mit Workshops und Training unterstützt hat.





# Selbstständigkeitserklärung

Name: Tillmann

Vorname: Peter

Ich erkläre gegenüber der Freien Universität Berlin, dass ich die vorliegende Dissertation selbstständig und ohne Benutzung anderer als der angegebenen Quellen und Hilfsmittel angefertigt habe. Die vorliegende Arbeit ist frei von Plagiaten. Alle Ausführungen, die wörtlich oder inhaltlich aus anderen Schriften entnommen sind, habe ich als solche kenntlich gemacht. Diese Dissertation wurde in gleicher oder ähnlicher Form noch in keinem früheren Promotionsverfahren eingereicht.

Mit einer Prüfung meiner Arbeit durch ein Plagiatsprüfungsprogramm erkläre ich mich einverstanden.

Datum:

---

Signed:

---



# Bibliography

- [1] G. Team, *Data.giss: Giss surface temperature analysis (gistemp v4)*. [Online]. Available: <https://data.giss.nasa.gov/gistemp/>.
- [2] UNFCCC, *The Paris Agreement - Publication | UNFCCC*, 2018. [Online]. Available: <https://unfccc.int/documents/184656>.
- [3] P. Friedlingstein, M. W. Jones, M. O’Sullivan, *et al.*, “Global Carbon Budget 2021,” *Earth System Science Data*, vol. 14, no. 4, pp. 1917–2005, Apr. 2022, ISSN: 18663516. DOI: 10.5194/ESSD-14-1917-2022.
- [4] Y. Yao, J. H. Xu, and D. Q. Sun, “Untangling global levelised cost of electricity based on multi-factor learning curve for renewable energy: Wind, solar, geothermal, hydropower and bioenergy,” *Journal of Cleaner Production*, vol. 285, p. 124827, Feb. 2021, ISSN: 0959-6526. DOI: 10.1016/J.JCLEPRO.2020.124827.
- [5] IRENA, “Rethinking energy 2017: Accelerating the global energy transformation,” International Renewable Energy Agency, Tech. Rep., 2017. [Online]. Available: [https://www.irena.org/-/media/Files/IRENA/Agency/Publication/2017/IRENA\\_REthinking\\_Energy\\_2017.pdf](https://www.irena.org/-/media/Files/IRENA/Agency/Publication/2017/IRENA_REthinking_Energy_2017.pdf).
- [6] IRENA, “Renewable power generation costs in 2020,” International Renewable Energy Agency, Tech. Rep., 2017. [Online]. Available: <https://www.irena.org/publications/2021/Jun/Renewable-Power-Costs-in-2020>.
- [7] S. Philipps, “Photovoltaics Report,” Fraunhofer ISE, Freiburg, Tech. Rep., 2022. [Online]. Available: <https://www.ise.fraunhofer.de/content/dam/ise/de/documents/publications/studies/Photovoltaics-Report.pdf>.
- [8] A. Louwen, M. Junginger, and A. Krishnan, “Technological Learning in Energy Modelling: Experience Curves Bibliographical data,” Tech. Rep., 2018.
- [9] C. Kost, S. Shammugam, V. Fluridominik, P. Davoodi, and M. Schlegl, “Levelized Cost of Electricity- Renewable Energy Technologies,” Fraunhofer ISE, Freiburg, Tech. Rep., 2021. [Online]. Available: [www.ise.fraunhofer.de](http://www.ise.fraunhofer.de).
- [10] L. Oberbeck, K. Alvino, B. Goraya, and M. Jubault, “IPVF’s PV technology vision for 2030,” *Progress in Photovoltaics: Research and Applications*, vol. 28, no. 11, pp. 1207–1214, Nov. 2020, ISSN: 1099-159X. DOI: 10.1002/PIP.3305. [Online]. Available: <https://onlinelibrary.wiley.com/doi/full/10.1002/pip.3305>  
<https://onlinelibrary.wiley.com/doi/abs/10.1002/pip.3305>  
<https://onlinelibrary.wiley.com/doi/10.1002/pip.3305>.
- [11] Maxeon Solar Technologies, “MAXEON 6 AC SOLAR PANEL Datasheet,” Tech. Rep., Jan. 2022. [Online]. Available: [www.sunpower.maxeon.com/int/InstallGuideACModules](http://www.sunpower.maxeon.com/int/InstallGuideACModules).

- [12] A. Richter, M. Hermle, and S. W. Glunz, "Reassessment of the Limiting Efficiency for Crystalline Silicon Solar Cells," *IEEE Journal of Photovoltaics*, vol. 3, no. 4, pp. 1184–1191, Oct. 2013, ISSN: 2156-3381. DOI: 10.1109/JPHOTOV.2013.2270351. [Online]. Available: <http://ieeexplore.ieee.org/document/6557081/>.
- [13] Y. Chen, D. Chen, C. Liu, *et al.*, "Mass production of industrial tunnel oxide passivated contacts (i-TOPCon) silicon solar cells with average efficiency over 23% and modules over 345 W," *Progress in Photovoltaics: Research and Applications*, vol. 27, no. 10, pp. 827–834, Oct. 2019, ISSN: 1099-159X. DOI: 10.1002/PIP.3180. [Online]. Available: <https://onlinelibrary.wiley.com/doi/full/10.1002/pip.3180> <https://onlinelibrary.wiley.com/doi/abs/10.1002/pip.3180> <https://onlinelibrary.wiley.com/doi/10.1002/pip.3180>.
- [14] D. Muñoz, C. Voz, M. Fonrodona, *et al.*, "Characterization of bifacial heterojunction silicon solar cells obtained by hot-wire CVD," *Journal of Non-Crystalline Solids*, vol. 352, no. 9-20, pp. 1953–1957, Jun. 2006, ISSN: 0022-3093. DOI: 10.1016/J.JNONCRY SOL.2005.09.043.
- [15] G. Galbiati, V. D. Mihailetchi, R. Roescu, *et al.*, "Large-area back-contact back-junction solar cell with efficiency exceeding 21%," pp. 1–6, Oct. 2014. DOI: 10.1109/PVSC-VOL2.2012.6656742.
- [16] ITRPV, "13th edition of the international technology roadmap photovoltaics," VDMA, Tech. Rep., 2022, (accessed on 2022/06/20). [Online]. Available: [itrpv.vdma.org](http://itrpv.vdma.org).
- [17] ITRPV, "11th edition of the international technology roadmap photovoltaics," VDMA, Tech. Rep., 2020, (accessed on 2020/08/31). [Online]. Available: [itrpv.vdma.org](http://itrpv.vdma.org).
- [18] A. R. Bowman, F. Lang, Y.-H. Chiang, *et al.*, "Relaxed Current Matching Requirements in Highly Luminescent Perovskite Tandem Solar Cells and Their Fundamental Efficiency Limits," *ACS Energy Letters*, vol. 14, pp. 612–620, Jan. 2021, ISSN: 2380-8195. DOI: 10.1021/acseenergylett.0c02481. [Online]. Available: <https://pubs.acs.org/doi/10.1021/acseenergylett.0c02481>.
- [19] F. Dimroth, "High-efficiency solar cells from III-V compound semiconductors," *physica status solidi c*, vol. 3, no. 3, pp. 373–379, Mar. 2006, ISSN: 1862-6351. DOI: 10.1002/pssc.200564172. [Online]. Available: <https://onlinelibrary.wiley.com/doi/10.1002/pssc.200564172>.
- [20] C. Fetzer, R. R. King, D. C. Law, *et al.*, *Multijunction Solar Cell Development and Production at Spectrolab*, 2007. [Online]. Available: <https://ntrs.nasa.gov/citations/20090022292>.
- [21] H. J. Snaith, "Present status and future prospects of perovskite photovoltaics," *Nature Materials* 2018 17:5, vol. 17, no. 5, pp. 372–376, Apr. 2018, ISSN: 1476-4660. DOI: 10.1038/s41563-018-0071-z. [Online]. Available: <https://www.nature.com/articles/s41563-018-0071-z>.
- [22] A. W. Ho-Baillie, J. Zheng, M. A. Mahmud, F. J. Ma, D. R. McKenzie, and M. A. Green, "Recent progress and future prospects of perovskite tandem solar cells," *Applied Physics Reviews*, vol. 8, no. 4, p. 041307, Oct. 2021, ISSN: 19319401. DOI: 10.1063/5.0061483. [Online]. Available: <https://aip.scitation.org/doi/abs/10.1063/5.0061483>.

- [23] A. Kojima, K. Teshima, Y. Shirai, and T. Miyasaka, "Organometal halide perovskites as visible-light sensitizers for photovoltaic cells," *Journal of the American Chemical Society*, vol. 131, no. 17, pp. 6050–6051, May 2009, ISSN: 00027863. DOI: 10.1021/JA809598R/SUPPL{\\_}FILE/JA809598R{\\_}SI{\\_}001.PDF. [Online]. Available: <https://pubs.acs.org/doi/full/10.1021/ja809598r>.
- [24] M. A. Green, E. D. Dunlop, J. Hohl-Ebinger, *et al.*, "Solar cell efficiency tables (Version 60)," *Progress in Photovoltaics: Research and Applications*, vol. 30, no. 7, pp. 687–701, Jul. 2022, ISSN: 1062-7995. DOI: 10.1002/pip.3595. [Online]. Available: <https://onlinelibrary.wiley.com/doi/10.1002/pip.3595>.
- [25] *IEC:60904-3: Photovoltaic devices - Part 3: Measurement principles for terrestrial photovoltaic (PV) solar devices with reference spectral irradiance data*, 2008.
- [26] S. Akhil, S. Akash, A. Pasha, *et al.*, *Review on perovskite silicon tandem solar cells: Status and prospects 2T, 3T and 4T for real world conditions*, Dec. 2021. DOI: 10.1016/j.matdes.2021.110138.
- [27] F. Fu, J. Li, T. C. J. Yang, *et al.*, "Monolithic Perovskite-Silicon Tandem Solar Cells: From the Lab to Fab?" *Advanced Materials*, vol. 34, no. 24, p. 2106540, Jun. 2022, ISSN: 1521-4095. DOI: 10.1002/ADMA.202106540. [Online]. Available: <https://onlinelibrary.wiley.com/doi/full/10.1002/adma.202106540> <https://onlinelibrary.wiley.com/doi/abs/10.1002/adma.202106540> <https://onlinelibrary.wiley.com/doi/10.1002/adma.202106540>.
- [28] C. U. Kim, E. D. Jung, Y. W. Noh, *et al.*, "Strategy for large-scale monolithic Perovskite/Silicon tandem solar cell: A review of recent progress," *EcoMat*, vol. 3, no. 2, e12084, Apr. 2021, ISSN: 2567-3173. DOI: 10.1002/EOM2.12084. [Online]. Available: <https://onlinelibrary.wiley.com/doi/full/10.1002/eom2.12084> <https://onlinelibrary.wiley.com/doi/abs/10.1002/eom2.12084> <https://onlinelibrary.wiley.com/doi/10.1002/eom2.12084>.
- [29] E. Köhnen, M. Jošt, A. B. Morales-Vilches, *et al.*, "Highly efficient monolithic perovskite silicon tandem solar cells: analyzing the influence of current mismatch on device performance," *Sustainable Energy & Fuels*, vol. 3, no. 8, pp. 1995–2005, Jul. 2019, ISSN: 23984902. DOI: 10.1039/C9SE00120D. [Online]. Available: <https://pubs.rsc.org/en/content/articlehtml/2019/se/c9se00120d> <https://pubs.rsc.org/en/content/articlelanding/2019/se/c9se00120d>.
- [30] G. Pezarz, G. Siefer, and A. W. Bett, "A simple method for quantifying spectral impacts on multi-junction solar cells," *Solar Energy*, vol. 83, no. 9, pp. 1588–1598, Sep. 2009, ISSN: 0038092X. DOI: 10.1016/j.solener.2009.05.009.
- [31] E. Aydin, T. G. Allen, M. De Bastiani, *et al.*, "Interplay between temperature and bandgap energies on the outdoor performance of perovskite/silicon tandem solar cells," *Nature Energy*, vol. 5, no. 11, pp. 851–859, Nov. 2020, ISSN: 20587546. DOI: 10.1038/s41560-020-00687-4. [Online]. Available: <https://www.nature.com/articles/s41560-020-00687-4>.

- [32] P. S. Schulze, A. J. Bett, M. Bivour, *et al.*, “25.1% High-Efficiency Monolithic Perovskite Silicon Tandem Solar Cell with a High Bandgap Perovskite Absorber,” *Solar RRL*, vol. 4, no. 7, p. 2000152, Jul. 2020, ISSN: 2367-198X. DOI: 10.1002/SOLR.202000152. [Online]. Available: <https://onlinelibrary.wiley.com/doi/full/10.1002/solr.202000152><https://onlinelibrary.wiley.com/doi/abs/10.1002/solr.202000152><https://onlinelibrary.wiley.com/doi/10.1002/solr.202000152>.
- [33] S. Abdul Hadi, E. A. Fitzgerald, and A. Nayfeh, “Theoretical efficiency limit for a two-terminal multi-junction “step-cell” using detailed balance method,” *Journal of Applied Physics*, vol. 119, no. 7, p. 073104, Feb. 2016, ISSN: 10897550. DOI: 10.1063/1.4942223. [Online]. Available: <http://aip.scitation.org/doi/10.1063/1.4942223>.
- [34] M. T. Hörantner and H. J. Snaith, “Predicting and optimising the energy yield of perovskite-on-silicon tandem solar cells under real world conditions,” *Energy & Environmental Science*, vol. 10, no. 9, pp. 1983–1993, 2017, ISSN: 1754-5692. DOI: 10.1039/C7EE01232B. [Online]. Available: <http://xlink.rsc.org/?DOI=C7EE01232B>.
- [35] R. Schmager, M. Langenhorst, J. Lehr, U. Lemmer, B. S. Richards, and U. W. Paetzold, “Methodology of energy yield modelling of perovskite-based multi-junction photovoltaics,” *Optics Express*, vol. 27, no. 8, A507, Apr. 2019, ISSN: 10944087. DOI: 10.1364/oe.27.00a507. [Online]. Available: <https://doi.org/10.1364/OE.27.00A507>.
- [36] C. Gueymard, “SMARTS2, A Simple Model of the Atmospheric Radiative Transfer of Sunshine,” Florida Solar Energy Center, 1995, Tech. Rep. [Online]. Available: <http://www.fsec.ucf.edu/en/publications/pdf/fsec-pf-270-95.pdf>.
- [37] R. E. Bird and C. Riordan, “Simple solar spectral model for direct and diffuse irradiance on horizontal and tilted planes at the earth’s surface for cloudless atmospheres,” *Journal of Climate & Applied Meteorology*, vol. 25, no. 1, pp. 87–97, Jan. 1986, ISSN: 0733-3021. DOI: 10.1175/1520-0450(1986)025<0087:SSSMFD>2.0.CO;2. [Online]. Available: [https://journals.ametsoc.org/view/journals/apme/25/1/1520-0450\\_1986\\_025\\_0087\\_ssmfd\\_2\\_0\\_co\\_2.xml](https://journals.ametsoc.org/view/journals/apme/25/1/1520-0450_1986_025_0087_ssmfd_2_0_co_2.xml).
- [38] M. Sengupta, Y. Xie, A. Lopez, A. Habte, G. Maclaurin, and J. Shelby, “The National Solar Radiation Data Base (NSRDB),” *Renewable and Sustainable Energy Reviews*, vol. 89, pp. 51–60, Jun. 2018, ISSN: 1364-0321. DOI: 10.1016/J.RSER.2018.03.003. [Online]. Available: <https://www.sciencedirect.com/science/article/pii/S136403211830087X>.
- [39] T. Huld, R. Müller, and A. Gambardella, “A new solar radiation database for estimating PV performance in Europe and Africa,” *Solar Energy*, vol. 86, no. 6, pp. 1803–1815, Jun. 2012, ISSN: 0038092X. DOI: 10.1016/j.solener.2012.03.006.
- [40] U. Rau, “Reciprocity relation between photovoltaic quantum efficiency and electroluminescent emission of solar cells,” *Physical Review B - Condensed Matter and Materials Physics*, vol. 76, no. 8, p. 085303, Aug. 2007, ISSN: 10980121. DOI: 10.1103/PhysRevB.76.085303.

- [41] X. Gao, Y. Cui, J. Hu, G. Xu, and Y. Yu, "Lambert W-function based exact representation for double diode model of solar cells: Comparison on fitness and parameter extraction," *Energy Conversion and Management*, vol. 127, pp. 443–460, Nov. 2016, ISSN: 01968904. DOI: 10.1016/j.enconman.2016.09.005.
- [42] A. Jain and A. Kapoor, "Exact analytical solutions of the parameters of real solar cells using Lambert W-function," *Solar Energy Materials and Solar Cells*, vol. 81, no. 2, pp. 269–277, Feb. 2004, ISSN: 09270248. DOI: 10.1016/j.solmat.2003.11.018.
- [43] A. A. El Tayyan, "An approach to extract the parameters of solar cells from their illuminated I - V curves using the Lambert W function," *Turkish Journal of Physics*, vol. 39, no. 1, pp. 1–15, Jan. 2015, ISSN: 13036122. DOI: 10.3906/fiz-1309-7. [Online]. Available: <https://doi.org/10.3906/fiz-1309-7>.
- [44] L. Zhu, T. Mochizuki, M. Yoshita, *et al.*, "Conversion efficiency limits and bandgap designs for multi-junction solar cells with internal radiative efficiencies below unity," *Optics Express*, vol. 24, no. 10, A740, May 2016, ISSN: 10944087. DOI: 10.1364/oe.24.00a740. [Online]. Available: <https://opg.optica.org/viewmedia.cfm?uri=oe-24-10-A740&seq=0&html=true%20https://opg.optica.org/abstract.cfm?uri=oe-24-10-A740%20https://opg.optica.org/oe/abstract.cfm?uri=oe-24-10-A740>.
- [45] N. N. Lal, Y. Dkhissi, W. Li, Q. Hou, Y.-B. Cheng, and U. Bach, "Perovskite Tandem Solar Cells," *Advanced Energy Materials*, vol. 7, no. 18, p. 1602761, Sep. 2017, ISSN: 16146832. DOI: 10.1002/aenm.201602761. [Online]. Available: <https://onlinelibrary.wiley.com/doi/10.1002/aenm.201602761>.
- [46] G. E. Eperon, M. T. Hörantner, and H. J. Snaith, "Metal halide perovskite tandem and multiple-junction photovoltaics," *Nature Reviews Chemistry*, vol. 1, no. 12, pp. 1–18, Dec. 2017. DOI: 10.1038/s41570-017-0095. [Online]. Available: <https://www.nature.com/articles/s41570-017-0095>.
- [47] M. H. Futscher and B. Ehrler, *Efficiency Limit of Perovskite/Si Tandem Solar Cells*, Oct. 2016. DOI: 10.1021/acsenerylett.6b00405. [Online]. Available: <http://pubs.acs.org/journal/aelccp>.
- [48] W. E. McMahon, D. J. Friedman, and J. F. Geisz, "Multijunction solar cell design revisited: disruption of current matching by atmospheric absorption bands," *Progress in Photovoltaics: Research and Applications*, vol. 25, no. 10, pp. 850–860, Oct. 2017, ISSN: 10627995. DOI: 10.1002/pip.2899. [Online]. Available: <https://onlinelibrary.wiley.com/doi/10.1002/pip.2899>.
- [49] P. Tockhorn, H.-Z. Berlin, J. Sutter, *et al.*, "Nano-optical designs enhance monolithic perovskite/silicon tandem solar cells toward 29.8% efficiency," Mar. 2022. DOI: 10.21203/RS.3.RS-1439562/V1. [Online]. Available: <https://www.researchsquare.com%20https://www.researchsquare.com/article/rs-1439562/v1>.
- [50] A. Al-Ashouri, E. Köhnen, B. Li, *et al.*, "Monolithic perovskite/silicon tandem solar cell with >29% efficiency by enhanced hole extraction," *Science*, vol. 370, no. 6522, pp. 1300–1309, Dec. 2020, ISSN: 10959203. DOI: 10.1126/science.abd4016. [Online]. Available: <https://www.science.org>.

- [51] A. Rohatgi, K. Zhu, J. Tong, *et al.*, “26.7% Efficient 4-Terminal Perovskite-Silicon Tandem Solar Cell Composed of a High-Performance Semitransparent Perovskite Cell and a Doped Poly-Si/SiO<sub>x</sub> Passivating Contact Silicon Cell,” *IEEE Journal of Photovoltaics*, vol. 10, no. 2, pp. 417–422, Mar. 2020, ISSN: 21563403. DOI: 10.1109/JPHOTOV.2019.2963564.
- [52] S. Chauhan and R. Singh, “A Review on Perovskite/Silicon Tandem Solar Cells,” May 2021. DOI: 10.20944/PREPRINTS202105.0188.V1. [Online]. Available: <https://www.preprints.org/manuscript/202105.0188/v1>.
- [53] R. Perez, R. Stewart, R. Seals, and T. Guertin, “The development and verification of the Perez diffuse radiation model,” Sandia National Laboratories (SNL), Albuquerque, NM, and Livermore, CA (United States), Tech. Rep., Oct. 1988. DOI: 10.2172/7024029. [Online]. Available: <http://www.osti.gov/servlets/purl/7024029/>.
- [54] B. Y. Liu and R. C. Jordan, “The long-term average performance of flat-plate solar-energy collectors: With design data for the U.S., its outlying possessions and Canada,” *Solar Energy*, vol. 7, no. 2, pp. 53–74, Apr. 1963, ISSN: 0038-092X. DOI: 10.1016/0038-092X(63)90006-9.
- [55] B. LeBaron and I. Dirmhirn, “Strengths and limitations of the Liu and Jordan model to determine diffuse from global irradiance,” *Solar Energy*, vol. 31, no. 2, pp. 167–172, Jan. 1983, ISSN: 0038-092X. DOI: 10.1016/0038-092X(83)90078-6.
- [56] A. P. Brunger and F. C. Hooper, “Anisotropic sky radiance model based on narrow field of view measurements of shortwave radiance,” *Solar Energy*, vol. 51, no. 1, pp. 53–64, Jul. 1993, ISSN: 0038-092X. DOI: 10.1016/0038-092X(93)90042-M. [Online]. Available: <https://www.sciencedirect.com/science/article/pii/0038092X9390042M>.
- [57] R. Perez, R. Seals, P. Ineichen, R. Stewart, and D. Menicucci, “A new simplified version of the perez diffuse irradiance model for tilted surfaces,” *Solar Energy*, vol. 39, no. 3, pp. 221–231, Jan. 1987, ISSN: 0038092X. DOI: 10.1016/S0038-092X(87)80031-2.
- [58] F. Abelès, “La théorie générale des couches minces,” *Journal de Physique et le Radium*, vol. 11, no. 7, pp. 307–309, Jul. 1950, ISSN: 0368-3842. DOI: 10.1051/JPHYSRAD:01950001107030700. [Online]. Available: <http://dx.doi.org/10.1051/jphysrad:01950001107030700>.
- [59] T. G. Mackay and A. Lakhtakia, *The Transfer-Matrix Method in Electromagnetics and Optics The Transfer-Matrix Method in Electromagnetics and Optics Synthesis Lectures on Electromagnetics*. Morgan & Claypool, 2020, ISBN: 9781681737928. [Online]. Available: <http://store.morganclaypool.com>.
- [60] R. Santbergen, T. Meguro, T. Suezaki, G. Koizumi, K. Yamamoto, and M. Zeman, “GenPro4 Optical Model for Solar Cell Simulation and Its Application to Multijunction Solar Cells,” *IEEE Journal of Photovoltaics*, vol. 7, no. 3, pp. 919–926, May 2017, ISSN: 21563381. DOI: 10.1109/JPHOTOV.2017.2669640.
- [61] F. Enrichi and G. C. Righini, *Solar cells and light management : materials, strategies and sustainability*, 1st. Elsevier, 2019, ISBN: 9780081027622.



- [62] M. R. Islam, Y. Wu, K. Liu, Z. Wang, S. Qu, and Z. Wang, "Recent Progress and Future Prospects for Light Management of All-Perovskite Tandem Solar Cells," *Advanced Materials Interfaces*, vol. 9, no. 4, p. 2101144, Feb. 2022, ISSN: 2196-7350. DOI: 10.1002/ADMI.202101144. [Online]. Available: <https://onlinelibrary.wiley.com/doi/full/10.1002/admi.202101144><https://onlinelibrary.wiley.com/doi/abs/10.1002/admi.202101144><https://onlinelibrary.wiley.com/doi/10.1002/admi.202101144>.
- [63] S. H. Zaidi, D. S. Ruby, and J. M. Gee, "Characterization of random reactive ion etched-textured silicon solar cells," *IEEE Transactions on Electron Devices*, vol. 48, no. 6, pp. 1200–1206, 2001, ISSN: 00189383. DOI: 10.1109/16.925248.
- [64] S. Winderbaum, O. Reinhold, and F. Yun, "Reactive ion etching (RIE) as a method for texturing polycrystalline silicon solar cells," *Solar Energy Materials and Solar Cells*, vol. 46, no. 3, pp. 239–248, Jun. 1997, ISSN: 0927-0248. DOI: 10.1016/S0927-0248(97)00011-1.
- [65] V. Magnin, J. Harari, M. Halbwx, S. Bastide, D. Cherfi, and J. P. Vilcot, "Angle-dependent ray tracing simulations of reflections on pyramidal textures for silicon solar cells," *Solar Energy*, vol. 110, pp. 378–385, Dec. 2014, ISSN: 0038-092X. DOI: 10.1016/J.SOLENER.2014.09.025.
- [66] S. A. Boden and D. M. Bagnall, "Optimization of moth-eye antireflection schemes for silicon solar cells," *Progress in Photovoltaics: Research and Applications*, vol. 18, no. 3, pp. 195–203, May 2010, ISSN: 1099-159X. DOI: 10.1002/PIP.951. [Online]. Available: <https://onlinelibrary.wiley.com/doi/full/10.1002/pip.951><https://onlinelibrary.wiley.com/doi/abs/10.1002/pip.951><https://onlinelibrary.wiley.com/doi/10.1002/pip.951>.
- [67] C. H. Sun, P. Jiang, and B. Jiang, "Broadband moth-eye antireflection coatings on silicon," *Applied Physics Letters*, vol. 92, no. 6, p. 061112, Feb. 2008, ISSN: 0003-6951. DOI: 10.1063/1.2870080. [Online]. Available: <https://aip.scitation.org/doi/abs/10.1063/1.2870080>.
- [68] B. Rech, C. Becker, D. Eisenhauer, G. Köppel, H. Sai, and T. Matsui, "Honeycomb micro-textures for light trapping in multi-crystalline silicon thin-film solar cells," *Optics Express*, Vol. 26, Issue 10, pp. A498-A507, vol. 26, no. 10, A498–A507, May 2018, ISSN: 1094-4087. DOI: 10.1364/OE.26.00A498. [Online]. Available: <https://opg.optica.org/viewmedia.cfm?uri=oe-26-10-A498&seq=0&html=true><https://opg.optica.org/abstract.cfm?uri=oe-26-10-A498><https://opg.optica.org/oe/abstract.cfm?uri=oe-26-10-A498>.
- [69] D. Eisenhauer, G. Köppel, K. Jäger, *et al.*, "Smooth anti-reflective three-dimensional textures for liquid-phase crystallized silicon thin-film solar cells on glass," *Optics Express*, Vol. 25, Issue 12, pp. A467-A472, vol. 25, no. 12, A467–A472, Sep. 2016. [Online]. Available: <http://arxiv.org/abs/1609.06997>.
- [70] E. Vazsonyi, K. De Clercq, R. Einhaus, *et al.*, "Improved anisotropic etching process for industrial texturing of silicon solar cells," *Solar Energy Materials and Solar Cells*, vol. 57, no. 2, pp. 179–188, Feb. 1999, ISSN: 0927-0248. DOI: 10.1016/S0927-0248(98)00180-9.

- [71] R. Cariou, J. Benick, F. Feldmann, *et al.*, “III–V-on-silicon solar cells reaching 33% photoconversion efficiency in two-terminal configuration,” *Nature Energy*, vol. 3, no. 4, pp. 326–333, Apr. 2018, ISSN: 2058-7546. DOI: 10.1038/s41560-018-0125-0. [Online]. Available: <http://www.nature.com/articles/s41560-018-0125-0>.
- [72] M. Hammerschmidt, D. Lockau, S. Burger, *et al.*, “FEM-based optical modeling of silicon thin-film tandem solar cells with randomly textured interfaces in 3D,” <https://doi.org/10.1117/12.2001789>, vol. 8620, pp. 323–331, Mar. 2013, ISSN: 0277786X. DOI: 10.1117/12.2001789. [Online]. Available: <https://www.spiedigitallibrary.org/conference-proceedings-of-spie/8620/86201H/FEM-based-optical-modeling-of-silicon-thin-film-tandem-solar/10.1117/12.2001789.full%20https://www.spiedigitallibrary.org/conference-proceedings-of-spie/8620/86201H/FEM-based-optical-modeling-of-silicon-thin-film-tandem-solar/10.1117/12.2001789.short>.
- [73] A. Naqavi, A. Naqavi, A. Naqavi, *et al.*, “An RCWA Analysis of Solar Cell Back Reflectors: Comparison between Modelling and Experiment,” *Advanced Photonics & Renewable Energy (2010)*, paper PTuC3, PTuC3, Jun. 2010. DOI: 10.1364/PV.2010.PTuC3. [Online]. Available: <https://opg.optica.org/abstract.cfm?uri=PV-2010-PTuC3>.
- [74] A. S. Mohsin, M. Mobashera, A. Malik, M. Rubaiat, and M. Islam, “Light trapping in thin-film solar cell to enhance the absorption efficiency using FDTD simulation,” *Journal of Optics (India)*, vol. 49, no. 4, pp. 523–532, Dec. 2020, ISSN: 09746900. DOI: 10.1007/S12596-020-00656-W/TABLES/1. [Online]. Available: <https://link.springer.com/article/10.1007/s12596-020-00656-w>.
- [75] A. W. Smith and A. Rohatgi, “Ray tracing analysis of the inverted pyramid texturing geometry for high efficiency silicon solar cells,” *Solar Energy Materials and Solar Cells*, vol. 29, no. 1, pp. 37–49, Feb. 1993, ISSN: 0927-0248. DOI: 10.1016/0927-0248(93)90090-P.
- [76] A. W. Blakers, A. Wang, A. M. Milne, J. Zhao, and M. A. Green, “22.8% efficient silicon solar cell,” *Applied Physics Letters*, vol. 55, no. 13, p. 1363, Dec. 1989, ISSN: 0003-6951. DOI: 10.1063/1.101596. [Online]. Available: <https://aip.scitation.org/doi/abs/10.1063/1.101596>.
- [77] R. Kopecek and J. Libal, *Towards large-scale deployment of bifacial photovoltaics*, Jun. 2018. DOI: 10.1038/s41560-018-0178-0. [Online]. Available: <https://www.nature.com/articles/s41560-018-0178-0>.
- [78] C. K. Lo, Y. S. Lim, and F. A. Rahman, “New integrated simulation tool for the optimum design of bifacial solar panel with reflectors on a specific site,” *Renewable Energy*, vol. 81, pp. 293–307, Sep. 2015, ISSN: 18790682. DOI: 10.1016/j.renene.2015.03.047.
- [79] S. Ayala Pelaez and C. Deline, “bifacial\_radiance: a python package for modeling bifacial solar photovoltaic systems,” *Journal of Open Source Software*, vol. 5, no. 50, p. 1865, Jun. 2020. DOI: 10.21105/joss.01865. [Online]. Available: <https://doi.org/10.21105/joss.01865>.

- [80] M. Ernst, G. E. Conechado, and C. A. Asselineau, “Accelerating the simulation of annual bifacial illumination of real photovoltaic systems with ray tracing,” *iScience*, vol. 25, no. 1, p. 103698, Jan. 2022, ISSN: 25890042. DOI: 10.1016/j.isci.2021.103698.
- [81] U. A. Yusufoglu, T. H. Lee, T. M. Pletzer, *et al.*, “Simulation of energy production by bifacial modules with revision of ground reflection,” in *Energy Procedia*, vol. 55, Elsevier Ltd, Jan. 2014, pp. 389–395. DOI: 10.1016/j.egypro.2014.08.111.
- [82] W. Shockley and H. J. Queisser, “Detailed balance limit of efficiency of p-n junction solar cells,” *Journal of Applied Physics*, vol. 32, no. 3, pp. 510–519, 1961, ISSN: 00218979. DOI: 10.1063/1.1736034.
- [83] J. Jia, Y. Miao, Y. Kang, *et al.*, “Bias-dependence of luminescent coupling efficiency in multijunction solar cells,” *Optics Express*, vol. 23, no. 7, A219, Apr. 2015, ISSN: 1094-4087. DOI: 10.1364/oe.23.00a219.
- [84] M. A. Steiner and J. F. Geisz, “Non-linear luminescent coupling in series-connected multijunction solar cells,” *Applied Physics Letters*, vol. 100, no. 25, p. 251106, Jun. 2012, ISSN: 00036951. DOI: 10.1063/1.4729827. [Online]. Available: <http://aip.scitation.org/doi/10.1063/1.4729827>.
- [85] M. Hammerschmidt, “Optical simulation of complex nanostructured solar cells with a reduced basis method,” Ph.D. dissertation, Freie Universität Berlin, 2016.
- [86] J. Pomplun, S. Burger, L. Zschiedrich, and F. Schmidt, “Adaptive Finite Element Method for Simulation of Optical Nano Structures,” Tech. Rep. 10, 2007, pp. 3419–3434.
- [87] P. A. Kelly, *Lecture Notes: An introduction to Solid Mechanics*. [Online]. Available: <https://pkel015.connect.amazon.auckland.ac.nz/SolidMechanicsBooks/index.html>.
- [88] B. Shahriari, K. Swersky, Z. Wang, R. P. Adams, and N. de Freitas, “Taking the Human Out of the Loop: A Review of Bayesian Optimization,” *Proceedings of the IEEE*, vol. 104, no. 1, pp. 148–175, Jan. 2016, ISSN: 0018-9219. DOI: 10.1109/JPROC.2015.2494218. [Online]. Available: <https://ieeexplore.ieee.org/document/7352306/>.
- [89] A. Cully, J. Clune, D. Tarapore, and J.-B. Mouret, “Robots that can adapt like animals,” *Nature*, vol. 521, no. 7553, pp. 503–507, May 2015, ISSN: 0028-0836. DOI: 10.1038/nature14422. [Online]. Available: <http://www.nature.com/articles/nature14422>.
- [90] J. Snoek, H. Larochelle, and R. P. Adams, *Practical Bayesian Optimization of Machine Learning Algorithms*, 2012. [Online]. Available: <http://papers.nips.cc/paper/4522-practical-bayesian-optimization>.
- [91] P.-I. Schneider, X. Garcia Santiago, C. Rockstuhl, and S. Burger, “Global optimization of complex optical structures using Bayesian optimization based on Gaussian processes,” B. C. Kress, W. Osten, and H. P. Urbach, Eds., vol. 10335, International Society for Optics and Photonics, Jun. 2017, 103350O. DOI: 10.1117/12.2270609. [Online]. Available: <http://proceedings.spiedigitallibrary.org/proceeding.aspx?doi=10.1117/12.2270609>.
- [92] P. I. Frazier, “A tutorial on bayesian optimization,” Jul. 2018. DOI: 10.48550/arxiv.1807.02811. [Online]. Available: <https://arxiv.org/abs/1807.02811v1>.

- [93] R. L. Riche and V. Picheny, “Revisiting Bayesian Optimization in the light of the COCO benchmark,” Mar. 2021. [Online]. Available: <http://arxiv.org/abs/2103.16649>.
- [94] O. S. Steinholtz, “A Comparative Study of Black-box Optimization Algorithms for Tuning of Hyper-parameters in Deep Neural Networks,” Tech. Rep., 2018. [Online]. Available: <http://urn.kb.se/resolve?urn=urn:nbn:se:ltu:diva-69865>.
- [95] C. Balázs, M. van Beekveld, S. Caron, *et al.*, “A comparison of optimisation algorithms for high-dimensional particle and astrophysics applications,” *Journal of High Energy Physics 2021 2021:5*, vol. 2021, pp. 1–46, 5 May 2021, ISSN: 1029-8479. DOI: 10.1007/JHEP05(2021)108. [Online]. Available: [https://link.springer.com/article/10.1007/JHEP05\(2021\)108](https://link.springer.com/article/10.1007/JHEP05(2021)108).
- [96] P. I. Schneider, X. Garcia Santiago, V. Soltwisch, M. Hammerschmidt, S. Burger, and C. Rockstuhl, “Benchmarking Five Global Optimization Approaches for Nano-optical Shape Optimization and Parameter Reconstruction,” *ACS Photonics*, vol. 6, no. 11, pp. 2726–2733, Nov. 2019, ISSN: 23304022. DOI: 10.1021/acsp Photonics.9b00706. [Online]. Available: <https://pubs.acs.org/sharingguidelines>.
- [97] R. Santbergen, M. R. Vogt, R. Mishima, *et al.*, “Ray-optics study of gentle non-conformal texture morphologies for perovskite/silicon tandems,” *Optics Express, Vol. 30, Issue 4, pp. 5608-5617*, vol. 30, no. 4, pp. 5608–5617, Feb. 2022, ISSN: 1094-4087. DOI: 10.1364/OE.448545. [Online]. Available: <https://opg.optica.org/viewmedia.cfm?uri=oe-30-4-5608&seq=0&html=true%20https://opg.optica.org/abstract.cfm?uri=oe-30-4-5608%20https://opg.optica.org/oe/abstract.cfm?uri=oe-30-4-5608>.
- [98] R. Guerrero-Lemus, R. Vega, T. Kim, A. Kimm, and L. E. Shephard, *Bifacial solar photovoltaics - A technology review*, Jul. 2016. DOI: 10.1016/j.rser.2016.03.041.
- [99] X. Sun, M. R. Khan, C. Deline, and M. A. Alam, “Optimization and performance of bifacial solar modules: A global perspective,” *Applied Energy*, vol. 212, pp. 1601–1610, Feb. 2018, ISSN: 03062619. DOI: 10.1016/j.apenergy.2017.12.041.
- [100] S. A. Pelaez, C. Deline, B. Marion, *et al.*, “Field-Array Benchmark of Commercial Bifacial PV Technologies with Publicly Available Data,” in *Conference Record of the IEEE Photovoltaic Specialists Conference*, vol. 2020-June, Institute of Electrical and Electronics Engineers Inc., Jun. 2020, pp. 1757–1759, ISBN: 9781728161150. DOI: 10.1109/PVSC45281.2020.9300379.
- [101] S. Wang, O. Wilkie, J. Lam, *et al.*, “Bifacial Photovoltaic Systems Energy Yield Modelling,” in *Energy Procedia*, vol. 77, Elsevier Ltd, Aug. 2015, pp. 428–433. DOI: 10.1016/j.egypro.2015.07.060.
- [102] K. Yoshikawa, H. Kawasaki, W. Yoshida, *et al.*, “Silicon heterojunction solar cell with interdigitated back contacts for a photoconversion efficiency over 26%,” *Nature Energy*, vol. 2, no. 5, pp. 1–8, Mar. 2017, ISSN: 20587546. DOI: 10.1038/nenergy.2017.32. [Online]. Available: <https://www.nature.com/articles/nenergy201732>.

- [103] M. Jošt, L. Kegelmann, L. Korte, and S. Albrecht, “Monolithic Perovskite Tandem Solar Cells: A Review of the Present Status and Advanced Characterization Methods Toward 30% Efficiency,” *Advanced Energy Materials*, vol. 10, no. 26, p. 1904102, Jul. 2020, ISSN: 1614-6832. DOI: 10.1002/aenm.201904102. [Online]. Available: <https://onlinelibrary.wiley.com/doi/10.1002/aenm.201904102>.
- [104] S. H. Lim, J.-J. Li, E. H. Steenbergen, and Y.-H. Zhang, “Luminescence coupling effects on multijunction solar cell external quantum efficiency measurement,” *Progress in Photovoltaics: Research and Applications*, vol. 21, no. 3, pp. 344–350, May 2013, ISSN: 10627995. DOI: 10.1002/pip.1215. [Online]. Available: <http://doi.wiley.com/10.1002/pip.1215>.
- [105] M. A. Steiner, J. F. Geisz, I. Garcia, *et al.*, “Effects of internal luminescence and internal optics on Voc and Jsc of III-V solar cells,” *IEEE Journal of Photovoltaics*, vol. 3, no. 4, pp. 1437–1442, 2013, ISSN: 21563381. DOI: 10.1109/JPHOTOV.2013.2278666.
- [106] M. De Bastiani, A. J. Mirabelli, Y. Hou, *et al.*, “Efficient bifacial monolithic perovskite/silicon tandem solar cells via bandgap engineering,” *Nature Energy*, pp. 1–9, Jan. 2021. DOI: 10.1038/s41560-020-00756-8. [Online]. Available: <https://www.nature.com/articles/s41560-020-00756-8>.
- [107] K. Jäger, P. Tillmann, E. A. Katz, and C. Becker, “Perovskite/Silicon Tandem Solar Cells: Effect of Luminescent Coupling and Bifaciality,” *Solar RRL*, p. 2000628, Jan. 2021, ISSN: 2367-198X. DOI: 10.1002/solr.202000628. [Online]. Available: <https://onlinelibrary.wiley.com/doi/10.1002/solr.202000628>.
- [108] A. Onno, N. Rodkey, A. Asgharzadeh, *et al.*, “Predicted Power Output of Silicon-Based Bifacial Tandem Photovoltaic Systems,” *Joule*, vol. 4, no. 3, pp. 580–596, Mar. 2020, ISSN: 25424351. DOI: 10.1016/j.joule.2019.12.017. [Online]. Available: <https://asu.pure.elsevier.com/en/publications/predicted-power-output-of-silicon-based-bifacial-tandem-photovolt>.
- [109] T. J. Jacobsson, A. Hultqvist, A. García-Fernández, *et al.*, “An open-access database and analysis tool for perovskite solar cells based on the FAIR data principles,” *Nature Energy* 2021 7:1, vol. 7, no. 1, pp. 107–115, Dec. 2021, ISSN: 2058-7546. DOI: 10.1038/s41560-021-00941-3. [Online]. Available: <https://www.nature.com/articles/s41560-021-00941-3>.
- [110] R. Kopecek and J. Libal, “Bifacial Photovoltaics 2021: Status, Opportunities and Challenges,” *Energies*, vol. 14, no. 8, p. 2076, Apr. 2021, ISSN: 1996-1073. DOI: 10.3390/en14082076. [Online]. Available: <https://www.mdpi.com/1996-1073/14/8/2076>.